1

CERAMIC GAS TURBINE ENGINE DEMONSTRATION PROGRAM

May 1982

Final Report, January 1976 to May 1981

Prepared under Contract Number N00024-76-C-5352

David W. Richerson

Keith M. Johansen

SPONSORED BY

THE DEPARTMENT OF DEFENSE
ADVANCED RESEARCH PROJECTS AGENCY
DARPA ORDER 3155

PREPARED FOR

DEPARTMENT OF THE NAVY
NAVAL AIR SYSTEMS COMMAND
WASHINGTON, D.C. 20362

BY

GARRETT TURBINE ENGINE COMPANY
A DIVISION OF THE GARRETT CORPORATION
P.O. BOX 5217, PHOENIX, AZ 85010

DISTRIBUTION STATEMENT A
Approved for public release;
Distribution Unlimited

Garrett Report 21-4410

693

SECURITY CLASSIFICATION OF THIS PAGE (When Data Entered)

REPORT DOCUMENTATION PAGE

READ INSTRUCTIONS
BEFORE COMPLETING FORM

1. REPORT NUMBER

2. GOVT ACCESSION NO. AD-A117088

3. RECIPIENT'S CATALOG NUMBER

4. TITLE (and Subtitle)
Ceramic Gas Turbine Engine
Demonstration Program

5. TYPE OF REPORT & PERIOD COVERED
Final Report
1-2-76 to 5-31-81

6. PERFORMING ORG. REPORT NUMBER
21-4410

7. AUTHOR(s)
David W. Richerson
Keith M. Johansen

8. CONTRACT OR GRANT NUMBER(s)
N00024-76-C-5352

9. PERFORMING ORGANIZATION NAME AND ADDRESS
Garrett Turbine Engine Company
P.O. Box 5217
Phoenix, AZ 85010

10. PROGRAM ELEMENT, PROJECT, TASK AREA & WORK UNIT NUMBERS
DARPA Order 3155

11. CONTROLLING OFFICE NAME AND ADDRESS
Department of the Navy
Naval Air Systems Command
Washington, D.C. 20362

12. REPORT DATE
May 1982

13. NUMBER OF PAGES
215

14. MONITORING AGENCY NAME & ADDRESS (if different from Controlling Office)

15. SECURITY CLASS. (of this report)
Unclassified

15a. DECLASSIFICATION/DOWNGRADING SCHEDULE

16. DISTRIBUTION STATEMENT (of this Report)

Approved for public release; distribution unlimited.

17. DISTRIBUTION STATEMENT (of the abstract entered in Block 20, if different from Report)

18. SUPPLEMENTARY NOTES

19. KEY WORDS (Continue on reverse side if necessary and identify by block number)

Gas Turbine Engine
Ceramics
Nondestructive Evaluation
Silicon Nitride
Mechanical Properties
Probabilistic Design

20. ABSTRACT (Continue on reverse side if necessary and identify by block number)

(See Reverse Side)

DD FORM 1 JAN 73 1473 EDITION OF 1 NOV 65 IS OBSOLETE

Unclassified

SECURITY CLASSIFICATION OF THIS PAGE (When Data Entered)

ABSTRACT

Ceramics, because of their stability at high temperature, have the potential to improve the power and fuel efficiency of gas turbine engines by allowing engine operation at higher temperature with minimum cooling penalty. The DARPA/NAVY/Garrett Ceramic Gas Turbine Engine Demonstration Program was begun in 1976 with the objective of demonstrating that ceramics could be designed, fabricated, and built into a gas turbine engine and that the engine could be operated with higher power and lower specific fuel consumption than a baseline metallic engine.

Extensive design, ceramic component processing development, material property evaluation, proof testing, nondestructive evaluation development, and rig and engine testing were conducted. An engine containing first-stage ceramic rotor blades (with the other components metallic) was successfully operated at design speed (41,730 rpm) and at an average turbine inlet temperature of 2200°F under severe cyclic conditions for 15 hours. An engine containing a ceramic hot section consisting of two full turbine stages (102 separate ceramic parts) was successfully operated in single cycles at design speed and at 2200°F producing 30 percent greater power and consuming 7 percent less fuel than the baseline metallic engine. Cyclic testing of the all-ceramic hot section was not successful because of a contact stress problem that would have required engine redesign.

The feasibility and benefits of using ceramic components have been demonstrated in this program. Further development and engine testing will be required to achieve cyclic durability and reliability.

FOREWORD

This is the final technical report of the Ceramic Turbine Engine Demonstration Program initiated through the foresight of Dr. E. C. Van Reuth of the Defense Advanced Research Projects Agency (DARPA). The program was funded under Contract Number N00024-76-C-5352 and was initially monitored by C. Miller and J. Fairbanks for the Naval Sea Systems Command (NAVSEA) and later by J. Horan and A. Rezetta for the Naval Air Systems Command.

The authors would like to thank DARPA, NAVSEA, and NASC for support of this work. Appreciation is also extended to the following individuals from other organizations who actively supported the program through technical reviews: R. Ashbrook (NASA), D. Campbell (AFAPL), S. Freiman (NRL), P. Genalis (NSRDC), K. Jakus (U. of Mass.), H. Graham (AFML), R. N. Katz (AMMRC), E. N. Lenoe (AMMRC), H. B. Probst (NASA), R. W. Rice (NRL), R. Ruh (AFML), N. Tighe (NBS), B. Wagner (NAPC), and S. Wiederhorn (NBS).

Special thanks are also due the subcontractors, expecially the AiResearch Casting Company and the Norton Company, and the many contributors at the Garrett Turbine Engine Company to the performance of the program: G. G. Austin, A. S. Bogus, W. E. Boon, D. W. Boone, W. D. Carruthers, E. B. Coleman, J. M. Dahn, P. Damiani, C. R. Dins, C. K. Dunlap, R. J. Evershed, B. J. Flager, S. K. Gupta, J. E. Harper, W. Hudson, K. P. Johnson, B. H. Johnston, H. L. Kington, L. N. Kloster, K. Kmetko, H. J. Krasnow, A. D. Lane, J. Lee, L. J. Lindberg, H. C. Liu, T. A. Marshall, W. P. McCullough, L. J. Meyer, H. C. Mongia, N. R. Nelson, M. W. Robare, J. W. Sanborn, R. E. Sas, J. J. Schuldies, R. A. Solomon, W. H. Spaulding, A. J. Stone, D. J. Tree, F. B. Wallace, J. M. Wimmer, L. P. Wynn, T. M. Yonushonis, and J. G. Zimmerer.

TABLE OF CONTENTS

TABLE OF CONTENTS (CONTD)

TABLE OF CONTENTS (CONTD)

TABLE OF CONTENTS (CONTD)

1.0 INTRODUCTION AND SUMMARY

1.1 PROGRAM OBJECTIVES

The use of ceramic materials for high-temperature components in gas turbine engines offers significant payoffs for a broad range of commercial and military applications. Some of the primary payoffs include improved performance (since the engine can operate at high turbine inlet temperature without cycle penalties for component cooling), reduced cost, reduced weight, improved corrosion and erosion resistance, and reduced dependence on critical imported metals required in current superalloys.

The Ceramic Gas Turbine Engine Demonstration Program was initiated in February 1976, based on the belief that sufficient progress had been made in ceramic properties and manufacturing processes and in advanced analysis techniques that a successful engine demonstration could be achieved. The program was conducted by the Garrett Turbine Engine Company (formerly AiResearch Manufacturing Company of Arizona) and was sponsored by the Defense Advanced Research Projects Agency (DARPA). During the first two years, the program was monitored by the Department of Navy, Naval Sea Systems Command (NAVSEA) and subsequently by the Naval Air System Command (NASC).

The program objectives included

- Demonstrate the use of ceramic components in a gas turbine engine with peak turbine inlet temperature (TIT) up to 2500°F, average TIT up to 2200°F
- Demonstrate significant engine performance improvements
- Demonstrate a reduction in the use of strategic materials

The program was to use 1976 state-of-the-art ceramic materials, and thus the program did not include efforts to achieve major materials improvements.

The engine selected for this demonstration was the Garrett Model T76 turboprop engine (see Figure 1-1)--a 715-horsepower engine whose various derivatives are used for military and civil aircraft propulsion and as an

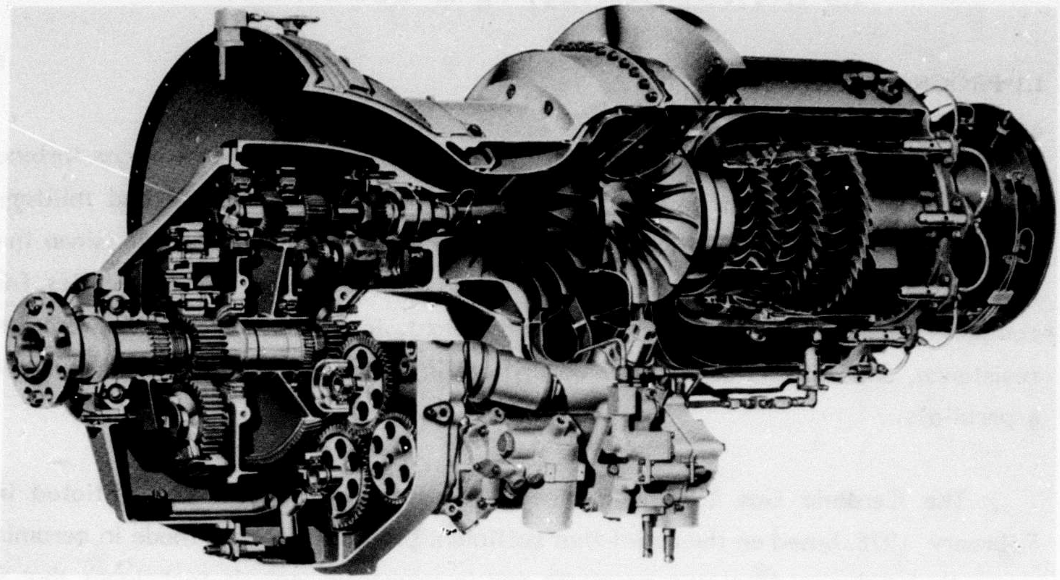

POWER OUTPUT	715 SHP
SPECIFIC FUEL CONSUMPTION	0.60 LB/HP-HR

Figure 1-1. Model T76 Turboprop Used for Ceramic Turbine Demonstration Program.

industrial and marine engine. The gearbox and compressor sections were used without change; however, the combustor and turbine sections were redesigned to use ceramic gas-path components. An increase of approximately 350°F in turbine inlet temperature was projected to increase engine output power to 1000 horsepower and decrease specific fuel consumption (SFC) by 10 percent. For this program, the engine designation was TSE331C-1.

The ceramic engine hot-end cross section as initially defined is shown in Figure 1-2. Ceramic materials were reaction-bonded and hot-pressed silicon nitride. The initial design included 124 ceramic parts.

1.2 PROGRAM SCHEDULE

The program was originally defined as a three-year effort as shown in Figure 1-3. As the program progressed, the objectives, scope, and component design changed based upon rig and engine test results and changes in priority. Specifically, the development efforts on the ceramic combustor and transition liners were terminated midway through the program so that the effort could be

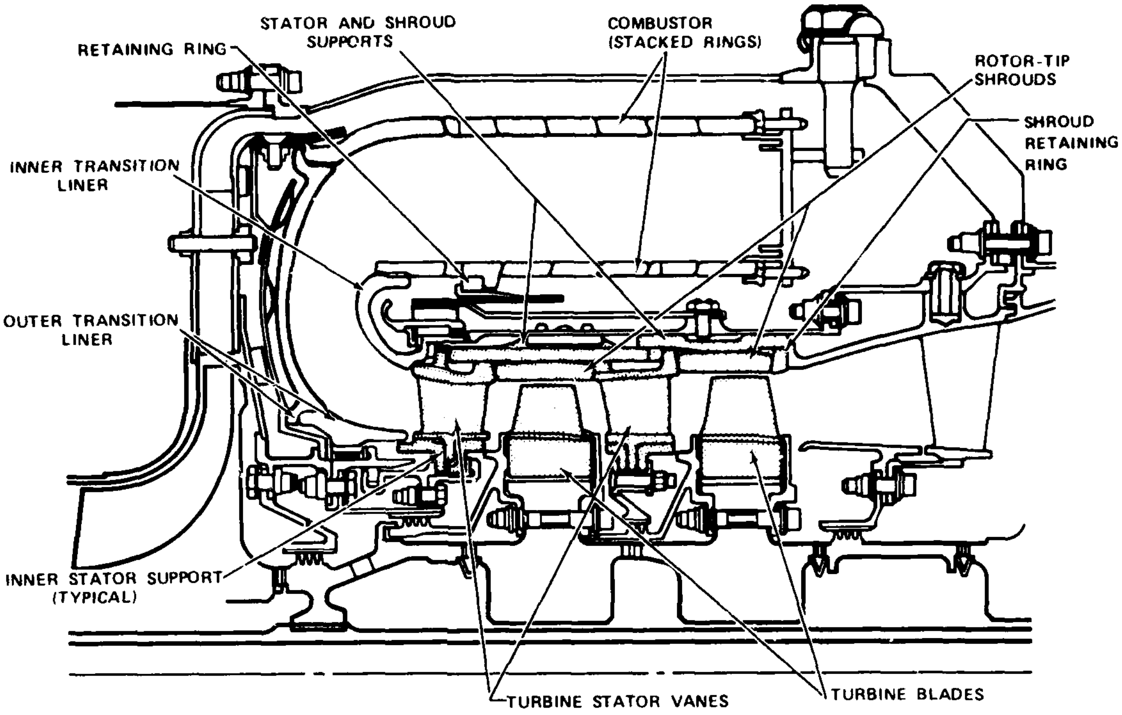

23-SVG401-2A

Figure 1-2. Initial TSE331C-1 Ceramic Engine.

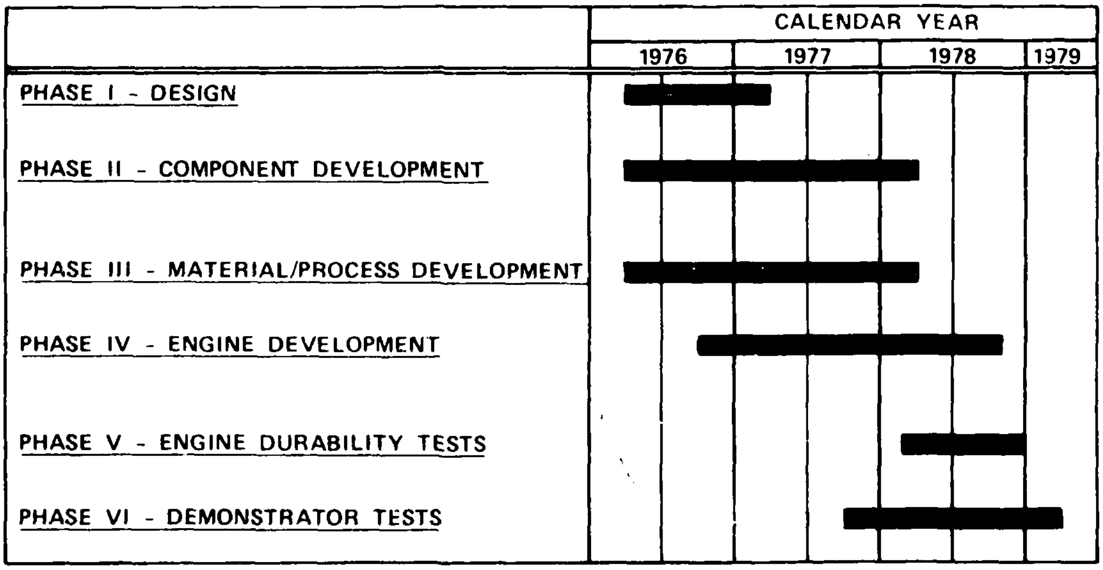

33-ART00223-48

Figure 1-3. Initial DARPA-NAVSEA Ceramic Engine Program Schedule.

concentrated on rotor and stator component development. This modification was made possible by the availability of metal combustor and transition liner components of suitable design to survive the required temperatures of the rig and engine testing. The final TSE331C-1 engine hot-section consisted of 102 ceramic parts and is shown schematically in Figure 1-4.

The engine demonstration objectives were also changed as the program progressed. The initial plan was to integrate the engine into a boat and conduct a vehicle demonstration. However, midway through the program it was decided that the ceramic technology was more urgently needed for applications such as remotely piloted vehicles where light weight and higher performance were particularly important. At this point, program management was transferred from the Naval Sea Systems Command (NAVSEA) to the Naval Air Systems Command (NASC). The new objective of the program was to conduct a 50-hour engine test on a test stand rather than in a vehicle.

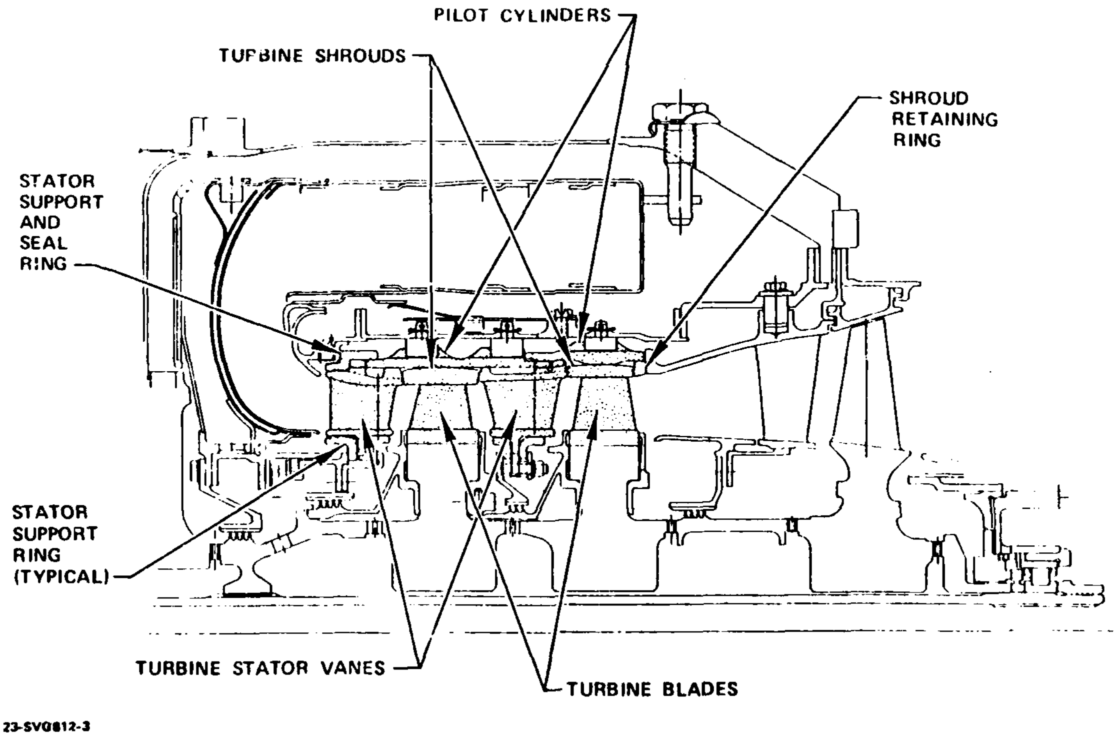

Figure 1-4. TSE331C-1 Ceramic Turbine Section.

As the program progressed, a contact stress problem was identified which limited static structure component life and prevented successful cyclic engine operation. This led to a further program redirection, summarized in Figure 1-5, in which the program was stretched out with no increase in budget to study the mechanisms of the contact stress problem.

This was followed by an add-on effort to demonstrate cyclic durability of a ceramic-bladed first-stage rotor operating in an engine at an average turbine inlet temperature of 2200°F. The objective of this add-on was 15 hours of engine operation over a severe cycle representative of a cruise missile engine cycle.

This report will summarize the activities identified in Figure 1-5. Detailed program progress was previously reported in limited-distribution Quarterly Interim reports[1-17]* and in a published mid-program review.[18] In addition, several less-detailed summary reviews have been published.[19-23]

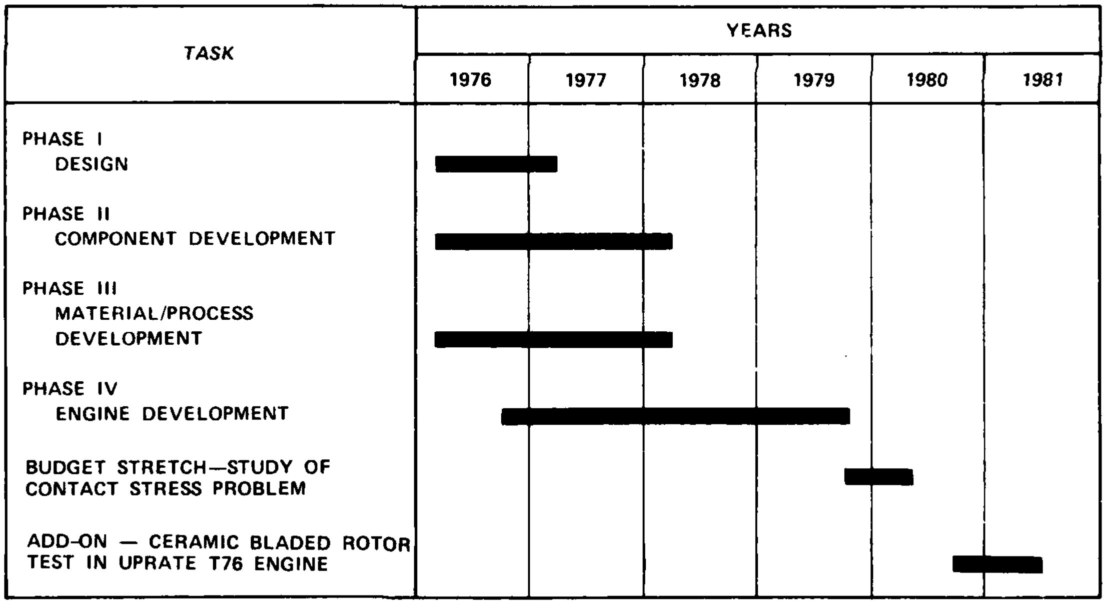

Figure 1-5. Modified DARPA-NASC Ceramic Engine Development Schedule.

---

*Designates references that are included at the end of this report.

1.3 COMPONENT DESIGN

Due to the unique properties of the candidate ceramic materials (negligible ductility, low fracture toughness, and area and volume effect on strength), a probabilistic design approach was required to guide the design iterations of the components. Component design was conducted with finite-element and finite-difference techniques. A Weibull model was used to relate the strength distribution of the ceramic to the stress distribution in the components to obtain an analytical assessment of component reliability. Each component configuration was iteratively modified until an acceptable level of aerodynamic performance (goal: 40-percent power increase and 10-percent SFC decrease over the baseline metal engine) and component survival probability (goal: 0.998) were achieved.

These objectives were achieved and resulted in an engine configuration consisting of two ceramic turbine stages and one metallic stage as shown schematically in Figure 1-4.

The viability of the probabilistic design methodology implemented under this program was verified qualitatively by survival of the various ceramic components under engine operating conditions. In the case of the rotor blades, it was verified quantitatively by spin-pit proof testing each blade to 130-percent overspeed. For example, the analysis predicted a 3-percent failure rate for second-stage rotor blades under the overspeed operating conditions; six out of 205 failed during the test. Similar correlation was obtained for analytical modeling and experimental testing of blade-attachment specimens and four-point bend test bars.

Section 2.0 of this report provides a detailed description of the design methodology and preliminary and detailed design of the TSE331C-1 ceramic engine components.

1.4 CERAMIC COMPONENT PROCESS DEVELOPMENT

The ceramic engine design resulted in a requirement for over 100 individual ceramic parts per engine, ranging from small complex stator vanes and rotor blades to large but simple cylindrical shrouds and pilot structures. Parts of comparable complexity or size were not available from commercial sources for the candidate ceramic materials. This fabrication technology had to be developed as part of the program.

A hybrid rotor concept consisting of ceramic rotor blades inserted into a superalloy disk resulted from 3-D finite-element design analysis. NC-132 hot-pressed silicon nitride (Si_3N_4) manufactured by the Norton Company was selected as the rotor blade material due to its high strength (4-point bend strength consistently over 100 ksi) and relatively good record of reproducibility.

Rotor blade machining development was conducted at Garrett and Norton Company. Blades having the required close dimensional tolerances and strength consistent with the design requirements were successfully machined by both Garrett and Norton. In addition, substantial cost reductions were demonstrated through the use of ultrasonic machining and form wheel grinding.

The stator configuration was defined by aerodynamic, thermal, and stress analysis and consisted of individual vane segments of reaction-bonded Si_3N_4 (RBSN) assembled into a ring and piloted on the OD and ID by other RBSN support structures. Three sources were selected for stator fabrication development:

- AiResearch Casting Company (ACC) - slip casting and injection molding
- Ford Motor Company - injection molding
- Norton Company - isostatic pressing and machining.

Parallel development at more than one source was deemed necessary because of the short development time available in the program and because the two potential commercial sources (Norton and ACC) had not previously fabricated complex shaped stator vanes. Ford Motor Company had previously developed the capability to fabricate individual stator vanes and integral stators but did not wish to become a major supplier of development parts under the Garrett program.

The stator component development subcontracts were completely successful. Stators of acceptable quality were produced by all three suppliers with the use of three different fabrication approaches. In each case, fixed process specification and certification procedures were established to ensure continued quality control.

Development of other static structure components was conducted successfully by ACC and Norton. Figure 1-6 shows a complete engine set of 102 ceramic components ready for assembly into an engine.

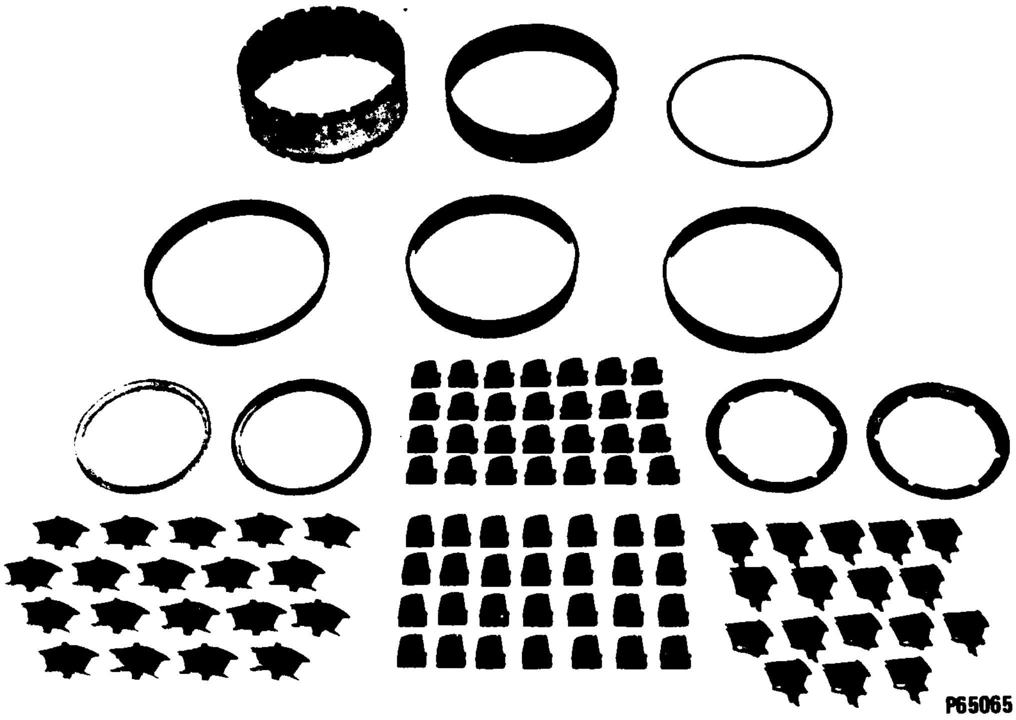

Figure 1-6. Complete Engine Set of Ceramic Components.

A detailed description of ceramic component development is included in Section 3.0 of this report.

1.5 MATERIAL CHARACTERIZATION

Material characterization was conducted under Phase III of the program and was required for the following reasons: (a) to provide statistical material property data for design, (b) to define specification and certification procedures to monitor lot-to-lot fabrication of specimens and components, (c) to provide fracture data under controlled conditions that would aid in interpretating component fractures, (d) to aid in improvement of materials if necessary, and (e) to help determine the capabilities of nondestructive evaluation (NDE) strength by defining the interrelationships of flaw size, detectability and effect on material. Some of the key interactions are shown in Figure 1-7.

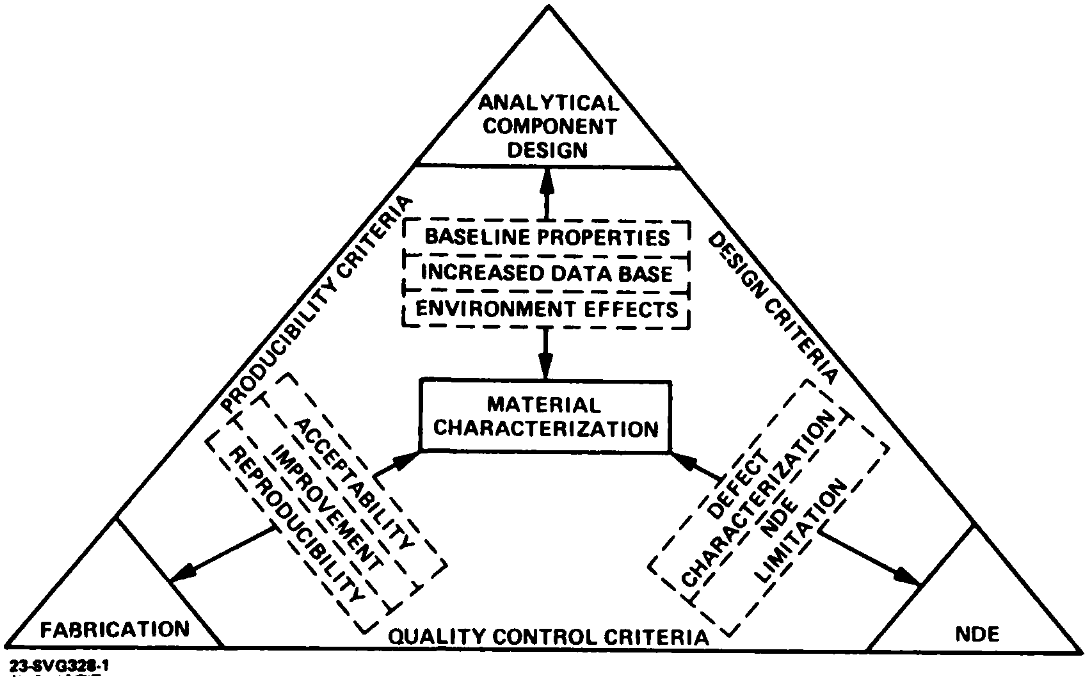

Figure 1–7. Interaction of Material Characterization with Other Program Tasks and Objectives.

The emphasis of the material characterization effort was to obtain data relevant to the engine duty-cycle requirement and the component fabrication processes. The following data were obtained:

- 4-point flexure strength versus temperature for each candidate material with both machined and as-fabricated surfaces
- Tensile strength versus temperature for NC-132 hot-pressed silicon nitride
- Strength versus exposure to static oxidation, cyclic oxidation,and sea-salt corrosion
- Strength versus machining
- Strength after cyclic fatigue and stress-rupture testing
- Compatibility of ceramic-ceramic and ceramic-metal couples under high-temperature oxidizing conditions

- Impact tolerance of hot-pressed Si_3N_4 rotor blades
- Effects of contact stress and vibration on strength

The characterization testing determined that the NC-132 hot-pressed Si_3N_4 was reproducible and had adequate properties for the rotor blade design requirements. The reaction-bonded Si_3N_4 was less reproducible and had marginal strength, oxidation resistance, and contact stress resistance. Preoxidation treatments were developed which improved oxidation resistance and strength. For instance, the strength of transverse machined NC-132 was increased by 50 percent by a 50-hour, 1800°F oxidation exposure.

Further discussion of the material characterization effort is included in Section 4.0.

1.6 NONDESTRUCTIVE EVALUATION

Due to the low fracture toughness and lack of ductility, the strength of ceramics is very sensitive to small internal and surface defects such as cracks, voids, inclusions, and scratches. An important task in the program was to evaluate nondestructive evaluation (NDE) techniques for detection of strength-limiting flaws in the candidate ceramic materials. Initially, flat-plate specimens seeded with various types of flaws of known size were inspected by state-of-the-art NDE techniques including conventional X-ray radiography, ultrasonic C-scan, neutron radiography, and dye penetrants. These inspections indicated that improved capability was necessary.

Substantially improved X-ray radiography resolution was developed at Garrett using microfocus radiography with computerized image enhancement. Other emerging technologies including higher frequency ultrasonics (45 MHz), ultrasonic shear waves, microwaves, and scanning laser acoustic microscopy (SLAM) were evaluated using the standards containing known defects.

Component shape standards were prepared containing known defects and were used to define inspection criteria. NDE was then successfully used along with proof testing and property certification testing to qualify components for rig and engine testing.

The NDE development effort is discussed in further detail in Section 5.0.

1.7 RIG AND ENGINE TESTING

1.7.1 RIG TESTING

Rotor blades were proof-tested by spin testing to 130 percent of design speed prior to rig and engine testing. Simple proof tests of stator vanes and static structures were not as straightforward, so verification of these designs was dependent upon rig testing prior to engine testing. Static structure component development and design verification were conducted using rig tests where substantial instrumentation could be incorporated and where flow and temperature conditions could be monitored and controlled more closely than in an engine. The second-stage stator and its supporting ceramic structure were evaluated first, followed by equivalent first-stage stator testing. In each case, the severity of conditions was increased in stepwise fashion, with disassembly and inspection of the components occurring after each test, until full design conditions of 1975°F for the second-stage stator and 2200°F for the first-stage stator were achieved.

Some ceramic parts cracked or fractured during these tests, leading to modifications of some clearances, tightening of some tolerances, and addition of metallic compliant layers at some ceramic-ceramic and ceramic-metal interfaces.

After successful demonstration of individual stages, the complete static structure was assembled and rig tested. The same stepwise procedure was employed, culminating in a 10-hour cyclic endurance demonstration at 120 percent of design gas loads at 1700°F with no fractured ceramic components. Figure 1-8 shows the ceramic components after this successful 10-hour demonstration.

The next step was to test the static structure with a rotor to provide dynamic airflow and vibration conditions not simulated by the static rig. A series of seven dynamic rig tests were conducted. These tests identified a redesign requirement to solve a rotor blade vibration condition but culminated in a successful 24-cycle demonstration at 1700°F and speeds to 41,730 rpm (100-percent design speed).

The static and dynamic rig structure tests verified that the design methodology, material properties, component fabrication quality, and design configuration were suitable to progress to the next stage of development--engine testing.

1.7.2 ENGINE TESTING

A total of 27 engine tests were conducted, highlighted by a one-hour test at full design conditions (41,730 rpm, 2200°F average turbine inlet temperature) which

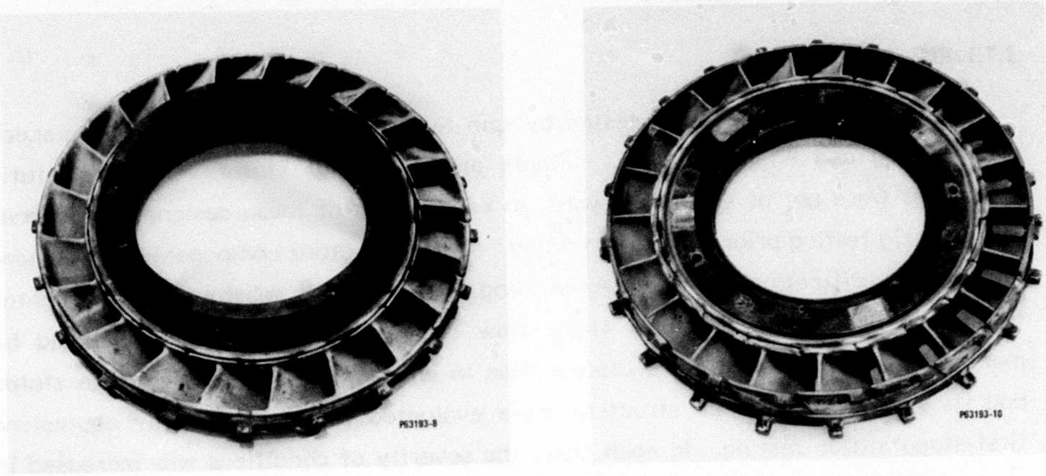

FIRST STAGE **SECOND STAGE**

Figure 1–8. First–Stage and Second–Stage Stator Assemblies after 10 Hours Endurance Testing in the Full Static Structure Rig.

produced 930 shp and an SFC of 0.56 lb/hp-hr. None of the 102 ceramic parts fractured. This success clearly demonstrated the feasibility of using ceramic components to achieve increased power and decreased fuel consumption. The 930 shp represented a 30-percent increase in power and the 0.56 lb/hp-hr represented a 6.7-percent decrease in fuel consumption compared to the baseline metal engine.

Although the TSE331C-1 engine could be operated with no apparent problems for a single cycle, problems arose during multi-cycle, transient operation. Chipping and cracking occurred at several ceramic-ceramic static structure interfaces and in several cases resulted in engine failure. A variety of minor design modifications such as changes in contact contour and utilization of compliant metallic interface layers were not consistently effective. Near the end of the program, engine testing was suspended, and all program resources were concentrated on achieving an understanding of the mechanism of interface damage and in developing a solution.

Engine testing is discussed in more detail in Section 6.0

1.8 CERAMIC CONTACT STRESS INVESTIGATION

An apparatus was designed and built to evaluate material strength degradation as a function of load, coefficient of friction, temperature, contact geometry, sliding versus static contact, surface condition, and interface compliant layers. Both reaction-bonded and hot-pressed Si_3N_4 were shown to have high resistance to normal (uniaxial) contact loads but sustained surface damage under sliding or biaxial contact loads. Under the latter stressing condition, a tensile stress spike was determined to be present locally at the material surface at the trailing edge of the contact.

Utilizing data from the contact tests apparatus and computer analysis, the worst-case tensile stress at a static-structure reaction-bonded Si_3N_4 interface was estimated to be 85 ksi. This would be high enough to produce surface damage since the baseline flexural strength of the RBSN static-structure materials was 45 ksi or less.

The surface damage due to biaxial contact stress was very shallow, typically under 0.004 inch. At the time the damage resulted, the surrounding region was in compression and prevented cracks from extending deeper into the material. However, subsequent tensile loading did cause crack extension and resulted in fracture of the test bar.

The contact stress study led to a reasonable hypothesis for chipping and cracking at static structure interfaces in the engine:

(1) High-contact tensile stress was present at some ceramic-ceramic interfaces due to localized biaxial stress distribution

(2) The unwanted biaxial stress distribution resulted from two sources: (a) component deflection due to a combination of tolerance mismatch and cantilevering of the static structure from the OD and (b) a combination of axial aerodynamic loads and thermal deflections

(3) Contact-induced surface damage was produced during the initial engine run, probably during peak aerodynamic load and temperature or due to restraints during cooldown

(4) Transient thermal tensile stresses during subsequent engine runs then resulted in crack extension.

The contact stress studies suggested that a major redesign of the TSE331C-1 engine was necessary to resolve the interface problem. A parallel ceramic development program (AFML/APL Contract F33615-77-C-5171 Ceramic Components for Turbine Engines) using the same T76 baseline engine was in progress at Garrett. The decision was made not to redesign the TSE331C-1 but rather to incorporate the experience gained through engine testing of the TSE331C-1 and through the contact studies into the AFML/APL engine design and to test that engine as a second-generation design.*

The contact stress studies are described in more detail in Section 7.0 of this report.

1.9 CERAMIC-BLADED ROTOR ENGINE DEMONSTRATION

Except for an initial blade vibration problem, which was quickly identified and resolved, no test rig or engine failures were attributed to a ceramic rotor blade failure. An add-on task was initiated late in the program to conduct cyclic engine durability testing of a ceramic-bladed rotor. An Uprate T76 engine** was modified to permit engine testing at a 2200°F average turbine inlet temperature*** of a ceramic-bladed first-stage rotor with an all-metal, cooled static structure.

The contract add-on required two 7-1/2 hour engine tests with a normal fast lightoff and with a simulated cruise missile duty cycle as shown in Table 1-1 below.

The two 7-1/2 hour duty-cycle tests were successfully conducted in May 1981 and clearly demonstrated that ceramic rotor blades can operate under normal engine lightoff and cyclic conditions. The second test was more severe than the contractual requirement. It included two 12-minute intervals at the maximum power condition at a temperature range of 2210°F to 2264°F average turbine inlet temperature. During this test, the engine produced 1184 shaft horsepower with an SFC of 0.523 lb/hp-hr

---

*The AFML/APL design substantially reduced contact loads and minimized the potential for biaxial stress states by using a simplified load path with support at the ID and OD.[24] The static structure has been successfully operated under cyclic conditions to an average turbine inlet temperature in excess of 2300°F with no evidence of contact problems.[25]

**The Uprate T76 engine is a military version of the Garrett model TPE331 rated at 1040 shp.

***Average turbine inlet temperature (TIT) is the gas temperature entering the first-stage stator. Since the metallic stator was cold, temperature at the first-stage rotor was approximately 70°F lower. Peak TIT was approximately 2500°F.

TABLE 1-1. CYCLE FOR CERAMIC-BLADED ROTOR ENGINE TESTING.

TOTAL TIME PER TEST:	7-1/2 HOURS
TIME AT CRUISE (60 PERCENT POWER):	5-1/2 HOURS
RAPID TRANSIENTS:	8 CYCLES FROM 50-PERCENT TO 75-PERCENT POWER
TIME AT MAXIMUM TEMPERATURE (2200^0F AVERAGE [TIT]):	12 MINUTES

compared to the Uprate T76 specification of 1040 shp and 0.558 lb/hp-hr. Wide turbine-blade tip clearances were used to be conservative. Performance could be further improved by reducing the tip clearance to normal metal turbine levels.

The Uprate T76 modifications and ceramic-bladed rotor tests are described in detail in Section 8.0 of this report.

1.10 CONCLUSIONS AND RECOMMENDATIONS

Substantial technology advancement was achieved in this program in the areas of brittle material design, ceramic component processing, understanding of material properties (particularly processing and environmental effects), proof testing and NDE, identifying and resolving critical rig and engine failure modes, and increasing the understanding of the role and mechanisms of contact stress. Although the original goal of 50 hours cyclic engine testing was not achieved due to the static structure contact stress problem, the first successful operation of a ceramic engine demonstrating substantial improvements in power and specific fuel consumption was achieved. This was followed by 15 hours of cyclic engine operation with first-stage ceramic rotor blades, also demonstrating improved power and SFC.

The DARPA/NAVY/Garrett Ceramic Engine Demonstration Program has demonstrated the feasibility and potential benefits of the use of ceramic components in gas turbine engines. Further work is necessary to develop durability and reliability. The following near-term tasks are recommended:

- Continue ceramic-bladed rotor tests in the Uprate T76 to further evaluate material and design durability and reliability.

- Reduce the tip clearances in the ceramic-bladed Uprate T76; identify clearance minimum and evaluate rub tolerance; develop and demonstrate an abradable shroud with the ceramic blades.

- Continue static structure and rotor development and engine testing under the AFML/APL Ceramic Components for Turbine Engines Program.

- Initiate a development program for static structure materials processes to achieve improved properties and reliability.

If started immediately, the near-term tasks could be completed successfully within two years. At that point the technology will be ready for development of a reliable ceramic engine for a specific limited-life application, such as an advanced cruise missile.

2.0 ENGINE AND COMPONENT DESIGN

The design of gas turbine engines is an iterative process, from thermodynamic cycle selection through engine development testing. In the analytical phases of preliminary and detailed design, an optimum concept and configuration is achieved through a complex interfacing of a multi-disciplined team in a cycle that requires many decisions and compromises to be made. This process evaluates and integrates the parameters of the thermodynamic cycle, component performance, mechanical configuration, manufacturing processes, material selection, vibrational characteristics, and temperature and stress distributions. The iterative design cycle continues until analytic predictions indicate that the configuration constraints and goals for performance and reliability have been achieved.

In the Garrett program, the primary departure from the methodology employed in metallic design was in the portion of the design criteria dealing with analytic design goals, the depth of the analysis, and component risk-evaluation technique. The lack of previous engine-based experience with ceramic components required concept and configuration decisions to be more dependent on analytic evaluation than in comparable metallic designs.

This section presents a description of the TSE331C-1 engine and cycle, a summary of the design criteria and methodology used, and detailed description of the design analysis of each ceramic component.

2.1 TSE331C-1 ENGINE CYCLE SELECTION

In order to concentrate on the design, development, and demonstration of ceramics, the use of an existing engine was appropriate to minimize design work that would not contribute to the basic objectives. The Model T76-G-10 Engine, a state-of-the-art engine rated at 715 shp for sea-level, standard-day conditions, was selected as the baseline for this program. It contains uncooled metal turbine components and produced maximum power at a peak turbine inlet temperature of 2050°F (average turbine inlet temperature = 1840°F). The engine flow path consists of a two-stage centrifugal compressor, a reverse-flow annular combustor, and a three-stage axial turbine as previously shown in Figure 1-1. A gearbox, mounted at the forward end of the engine, drives the engine accessories and provides a 20.9:1 gear ratio to produce a maximum output shaft speed of 2,000 rpm.

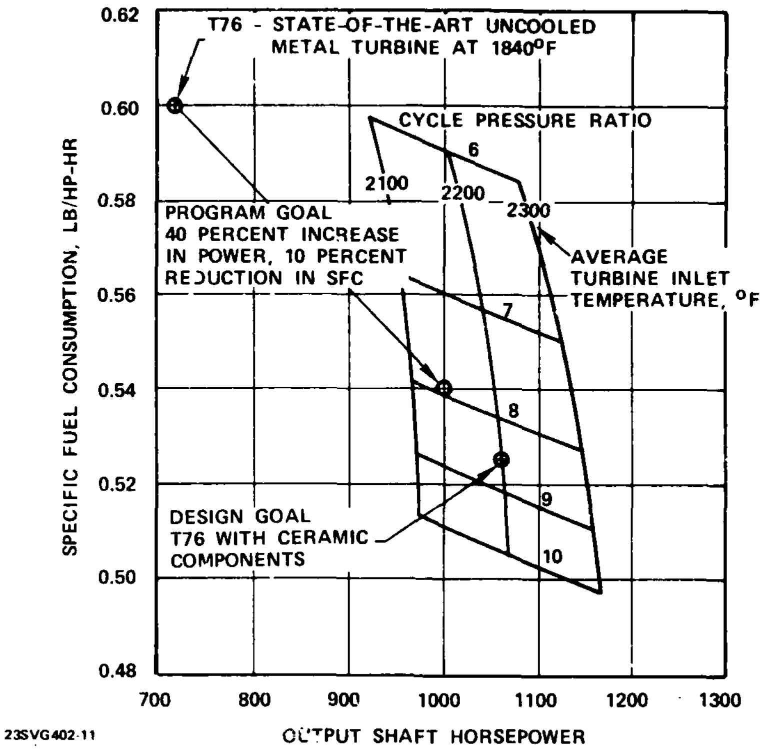

Figure 2-1. TSE331C-1 Engine Cycle Selection.

In order to establish the turbine and combustor-section thermodynamic design point for the ceramic engine, a parametric engine cycle study was conducted.[1,26] This study established the engine performance design goals as shown in Figure 2-1. These design goals reflect a greater improvement in performance than that required to meet the program objectives of a 40-percent increase in power (1,000 versus 715 shp) and a 10-percent decrease in SFC (0.54 versus 0.6 lb/hp-hr), thus providing some margin for compromises during the development program.

Since the engine employed an existing compressor section, parameters such as speed, airflow, and combustor inlet conditions were fixed, and the parameters of immediate interest (combustor and turbine-section design point) that were derived from the study were as shown in Table 2-1 below.

The selected design point turbine efficiency was over one percent lower than the metal turbine efficiency in order to provide a performance margin for possible design compromises, engine-development contingencies, and hardware tolerance contributions. Table 2-2 is a summary of the engine cycle parameters established for the engine.

TABLE 2-1. ENGINE DESIGN POINT PARAMETERS.

COMBUSTOR EFFICIENCY	– 99.5 PERCENT
COMBUSTOR PRESSURE DROP ($\Delta P/P_{IN}$)	– 4.0 PERCENT
AVERAGE TURBINE INLET TEMPERATURE	– 2200°F
MAXIMUM TURBINE HOT-SPOT TEMPERATURE	– 2500°F
TURBINE EFFICIENCY (TOTAL-TO-DIFFUSER EXIT STATIC)	– 85.0 PERCENT

TABLE 2-2. TSE331C-1 ENGINE DESIGN POINT CYCLE PARAMETERS.

ROTOR SPEED, RPM	41,730
INLET TEMPERATURE, T_{t2}, °F	59
INLET TOTAL PRESSURE, P_{t2}, PSIA	14.696
INLET AIRFLOW, W_a, LBS/SEC	6.16
COMPRESSOR TOTAL PRESSURE RATIO, P_{t3}/P_{t2}	8.58
COMPRESSOR EFFICIENCY, PERCENT	0.803
LEAKAGE AND COOLING AIRFLOW, $W_L + W_c$, PERCENT	3.1
COMBUSTOR AIRFLOW, W_{a3}, LBS/SEC	5.911
COMBUSTOR INLET TOTAL PRESSURE, P_{t3}, PSIA	126.15
COMBUSTOR INLET TOTAL TEMPERATURE, T_{t3}, °F	597.3
COMBUSTOR TOTAL PRESSURE LOSS, $\frac{P_{t3}-P_{t4}}{P_{t3}}$	0.04
COMBUSTION EFFICIENCY	0.995
FUEL-AIR RATIO, f/a	0.0259
AVERAGE TURBINE INLET TOTAL TEMPERATURE, T_{t4}, °F	2200
TURBINE INLET CORRECTED FLOW, $\frac{W_{g4}/\theta_{t4}}{\delta_{t4}}$	1.683
TURBINE TOTAL-STATIC PRESSURE RATIO, P_{t4}/P_{s5}	8.242
TURBINE EFFICIENCY, η_t	0.85
PARASITIC POWER LOSS, HP	12.0
REDUCTION GEAR EFFICIENCY, η_g	0.98
OUTPUT SHAFT POWER, HP	1064.0
SPECIFIC FUEL CONSUMPTION, SFC, LBS/HP/HR	0.524

2.2 DESIGN METHODOLOGY

Metal turbine components are designed utilizing a deterministic approach of comparing the maximum component stress with a single value of material strength. This cannot be done with ceramics due to their unique properties: (a) high scatter in strength data compared to metals, (b) criticality of small flaws and (c) a pronounced size effect (i.e., strength dependence on the volume and area under stress in addition to the magnitude of the applied load). For ceramics, a probabilistic design methodology is required in which component failure risk is assessed based upon a comparison of the stress distribution throughout the component and the statistical strength distribution of the ceramic material (as a function of stress, volume and area).[27,28]

Garrett finite-element analysis programs ISOPDQ and ISO3DQ were utilized to model the stress distribution of the ceramic turbine components. Weibull statistics were utilized to characterize the baseline strength and flaw-size distribution of the ceramic materials. Where possible, strength data was obtained by both flexure testing and tensile testing to provide surface and volume inputs to the Weibull analysis. To further increase the validity of the data, every effort was made to fabricate the test specimens in the same fashion as the component (i.e., same processing, machining, inspection, and preoxidation treatment) to ensure that both had the same statistical flaw distribution.

The output processors of the ISOPDQ and ISO3DQ finite-element programs were modified to integrate stress fields over both surface area and volume.[1,29] The two-parameter Weibull distribution function (Equation 1) was used to compare the calculated stress field with the material strength and strength distribution parameters:

$$P_F = 1 - e^{-\left(\frac{\sigma_a}{\sigma_\theta}\right)^m} \qquad (1)$$

where: P_F = Probability-of-failure

σ_a = Applied stress

σ_θ = Characteristic strength

m = Weibull slope

Equation (1) can be used to calculate the probability of failure for a particular volume or surface represented in a finite-element analysis. The following describes how local probabilities are combined to get an overall probability for an entire structure and to relate the material constants σ_θ, and m, obtained from appropriate material test data, to the component stress distribution.

Assuming independence, the probability of survival of an entire structure can be found by combining individual local probabilities of survival according to Equation (2):

$$(1-P_{F_T}) = \sum_{L=1}^{n} (1-P_{F_i})_i \tag{2}$$

where: P_{F_T} = Probability of failure for the entire structure

P_{F_i} = Probability of failure for a local element i

If "s" local volumes of homogenous structure have the same flaw distribution, applied stress, and volume, the individual probabilities of survival are equal. The probability of survival, R, of the total volume is thus the product of the probabilities of survival of the local volume, as in Equation (3):

$$(1-P_{F_T}) = (1-P_{F_i})^s \tag{3}$$

The probability of failure of the entire structure is then

$$P_{F_T} = 1-e^{-s\ell n(1-P_{F_i})} \tag{4}$$

At this point, a necessary relation with test data is introduced. The number of unit volumes "s" can be treated as the volume of the uniformly stressed structure or finite element (v) divided by the stressed volume of the applicable test specimen, (V_t). The strength distribution of the test volume is expressed in the form of the three-parameter or the two-parameter Weibull expression of Equation (1).

The probability of survival of the portion of the structure represented by a given finite element having an applied principal stress can thus be written in the form:

$$R = e^{-\frac{v}{V_t}\left(\frac{\sigma_1}{\sigma_{\theta_1}}\right)^{m_1} - \frac{a}{A_t}\left(\frac{\sigma_2}{\sigma_{\theta_2}}\right)^{m_2}} \tag{5}$$

where: σ_1 and σ_2 are the appropriate stress values integrated over the volume and surface area, and θ_1, θ_2, m_1, m_2 are appropriate material constants.

"a" is the surface area of the component (if greater than zero) represented in a particular finite element, and A_t is the effective stressed-surface area of the test specimen from which property data was obtained.

An estimate of the probability of survival of a local volume or surface (i.e., a particular finite element) must consider the three principal stresses. The system probability of survival is assumed to be equal to the product of the individual probabilities associated with each principal stress. Considering the brittle nature of ceramic materials, the principal stresses are considered to be a better measure of failure than equivalent or octahedronal shear stresses.

Since compressive stresses contribute little to crack growth (and thus failure) and constitute a less well-known family of properties for ceramics, it has been assumed that compressive stress can be neglected. The probability of survival of the total structure may thus be taken to be the product of two Weibull distributions of the probabilities of survival of all the local volumes and surface areas, which are obtained during the finite-element process.

Two points require comment. First, the stress solution must be accurate (3-D is essential), and the modeling must not introduce local perturbations in the stress field, as sometimes happens at boundaries between substructures. Secondly, a mesh structure and integration method adequate for stress calculation may be inappropriate for a probability calculation.

In performing a probabilistic evaluation calculation of a finite-element model, it was apparent that a mesh size sufficient to represent the stresses is not sufficient to accurately represent the failure probability. To overcome this mathematically, the probabilistic evaluation programs WESTAC2 and WESTAC3 incorporated a refined integration calculation:

$$\int \sigma^n \, dv = \sum_{i=1}^{\ell} \sum_{j=1}^{\ell} \sum_{k=1}^{\ell} H_i H_j H_k \sigma^n(\xi_i, \eta_j, \zeta_k) \, J(\xi_i, \eta_j, \zeta_k) \tag{6}$$

where: ℓ is the number of Gauss points

H is the weight function

J is the determinant of Jacobian of the transformation between X, Y, Z and ξ, η, ζ coordinates

ξ, η, ζ are the Gauss point coordinates

To ensure the accuracy of the probability calculation, a variation of the number of Gauss points was performed for each element. Initially, the probability of the element was calculated with 3 and 4 integration points and the results of both calculations were computed. If there is a significant change between the two calculations, the integration is performed for 7 Gaussian points, which is then compared to the results of the 4-point calculation. It was determined that 15 Gaussian points would accurately represent the probability of an element with even the most severe stress gradients.

2.3 PRELIMINARY DESIGN

The initial phase of detailed design analysis established turbine section aerodynamics, mechanical arrangement for support of turbine structural members, and material temperature levels throughout the hot section.[1,2]

The turbine aerodynamic design point was selected to match the existing T76 two-stage centrifugal compressor (rotating at 41,730 rpm), and is defined in Table 2-3. To achieve the desired efficiency, three turbine stages were necessary.

Also, the definition of how much work should be extracted from each turbine stage was investigated. Two specific work splits were evaluated. These were: (a) an equal division of work between all three stages, and (b) a division whereby the first two stages equally shared 52 percent of the turbine work, and the third stage supplied the remaining 48 percent. A comparison presented in Table 2-4 shows that the aerodynamic efficiency of the equal-work turbine has an advantage of 0.4 points. However, this advantage is offset by a substantial (28 percent) reduction in the number of ceramic blades that would be required both for the first and second stages of the unequal work-split turbine.

TABLE 2-3. TSE331C-1 TURBINE DESIGN POINT.

INLET PRESSURE, PSIA	121.1
INLET TEMPERATURE, °R	2659.7
FLOW, LB/SEC	6.125
SPEED, RPM	41,730
PRESSURE RATIO (TOTAL-TO-DIFFUSER STATIC)	8.242
WORK, BTU/LB	258.7
PREDICTED EFFICIENCY (TOTAL-TO-DIFFUSER STATIC)	0.85
CORRECTED FLOW, LB/SEC	1.683
CORRECTED SPEED, RPM	18,429
CORRECTED WORK, BTU/LB	50.46

TABLE 2-4. RESULTS OF TURBINE WORK-SPLIT STUDY.

STAGE	EQUAL WORK			HIGH 3RD STAGE WORK**		
	1ST	2ND	3RD	1ST	2ND	3RD*
WORK, BTU/LB	89.7	89.7	89.7	70.0	70.0	129.2
CORRECTED WORK, BTU/LB	17.5	19.8	22.7	13.7	15.0	30.3
NO. OF VANES	22	23	27	21	21	24
NO. OF BLADES	39	39	39	28	28	34
INLET PRESSURE, PSIA	121.1	67.5	34.6	121.1	76.9	46.6
INLET TEMPERATURE, °R	2660	2355	2050	2660	2425	2213
RELATIVE TEMPERATURE (HUB) °R	2448	2144	1839	2515	2281	1943
OVERALL EFFICIENCY (TOTAL-TO-DIFFUSER STATIC)		0.863			0.859	

*REQUIRES 23 DESWIRL VANES
**FLOW-PATH III

The basic program commitment to establish the feasibility of using ceramics in a gas turbine and to achieve that goal in three years resulted in the decision to employ ceramic blades installed in a superalloy disk as opposed to an integral ceramic turbine wheel. Early calculations indicated bore stress levels too high for the current ceramic materials for an integral turbine wheel, and review of fabrication technology suggested that the required development was not within the scope of the program.

Certain aspects of designing a ceramic component are not significantly different from designing metallic components. Achieving an optimum design requires an iterative compromise between system reliability, cycle efficiency, component performance, manufacturing processes, and mechanical design. However, the design criteria and the depth of analysis required to make design compromises and configuration decisions are significantly different due to the characteristics of ceramic materials. Constraints imposed by ceramic material characteristics, which required configuration compromises and innovative design in the TSE331C-1 and are not normally required in metallic designs, were

(a) Lack of fracture toughness provided an incentive to strive for low levels of both local and average stresses in ceramic components.

(b) The degree of scatter in strength data and the pronounced size effect required that special techniques and criteria for risk evaluation be applied to complex shapes and stress distributions.

(c) Metal-to-ceramic interfaces were needed that were capable of compensating for large differences of thermal expansion.

(d) Low density and high elastic modulus in ceramics result in high natural frequencies in comparison to metal blades. In the TSE331C-1, the fundamental frequencies were close to rotor blade/stator vane passing frequencies. Tuning of frequencies was thus required to avoid interference in the operating range.

(e) Lack of data at high frequencies and temperatures for internal damping was an incentive to provide blade damping externally, and influenced disk coverplate design.

(f) Designs had to be selected that could be fabricated from 1976 vintage ceramic materials and process technology.

(g) At the time of blade conceptual design, NDE methods were not considered capable of detecting the extremely small critical flaw sizes of the higher strength ceramics with sufficient certainty. Thus blade configurations were influenced by the need to be compatible with proof-testing methods.

2.4 TURBINE ROTOR SYSTEM DESIGN

This section summarizes the preliminary design and detailed design of the two stages of ceramic-bladed rotors for the TSE331C-1 engine.[1,2,30] Emphasis will be on description of the flow path and configuration iterations implemented to minimize stress in the ceramic blades.

2.4.1 PRELIMINARY ROTOR DESIGN

The unequal work split shown previously in Table 2-4 was selected to reduce the stresses on the two ceramic stages. This had the further advantage of minimizing the number of blades, which provided additional design flexibility as well as slightly easing the manufacturing requirements. A single-tang dovetail configuration rather than a multi-tang firtree configuration was selected for blade attachment. Although lower attachment stresses could theoretically be achieved with the firtree, the increased complexity would make manufacturing much more difficult. Furthermore, to provide low stresses, centrifugal loads would have to be shared over each contact surface of the firtree. This occurs readily with metal blades because of their ability to deform locally and their thermal expansion match with the disk. Since ceramics do not deform locally and have much lower thermal expansion than the metal disk, the load sharing would have to be achieved through very close tolerance and compliant layers. Therefore, for these reasons and the manufacturing considerations, a single-tang dovetail was selected.

A series of four flow-path variations were investigated in terms of their effects on airfoil and blade-attachment stresses, airfoil natural frequencies, cooling supply configurations, aerodynamic efficiency, and stator-to-rotor spacing and its effect on aerodynamic excitation of blade resonance.[1] In each case, the third-stage rotor exit critical Mach number was held constant at 0.5 and the principal variations were introduced into the first two stages. The initial velocity diagrams for the four flow paths assumed constant stator-exit and rotor-exit angles. The four flow path variations evaluated in the preliminary analysis are shown schematically in Figure 2-2.

Flow-path I had a 3.2-inch radius (compared to 2.95 inches for the baseline T76 engine) with 28 blades, which provided increased rim space permitting additional flexibility for optimizing the blade attachment. The blade was a high-reaction, low-Mach-number configuration with relatively low airfoil twist. The airfoil stress distribution and the blade natural frequencies were calculated using finite-element analysis techniques. Results of the analysis indicated potential stress problems in the first- and second-stage airfoils as well as in the blade attachments. A possible first-mode frequency interference with the stator count was also indicated for the first-stage rotor blades near design operating speed. Several possible alternatives were then evaluated.

A configuration having the same hub radius of the Model T76 and the same blade height as Flow-path I, was selected for further detailed evaluation. Analysis of this configuration, Flow-path II, indicated a reduction in airfoil stress, but it maintained the possible frequency interference. The attachment stress was virtually unchanged, and although the pull of each rotor blade was decreased, it was counteracted by (a) the increased number of rotor blades and (b) the decreased rim diameter.

It became apparent that the larger hub radius and lower blade number of Flow-path I would be requried, but that a lower blade load would also be required. Flow-path III, similar to Flow-path I but with the rotor exit Mach number levels of Flow-path II, was evaluated. Relative to Flow-path II, a reduction in airfoil stresses was achieved, the attachment stress was reduced, and first-mode frequencies of both stage were increased. The frequency increase for the first stage was favorable, but the second stage was moved closer to a potential excitation at stator passing frequency at design point. An additional reduction in attachment stress level was required along with an improved blade natural frequency position for the second-stage blading.

Flow-path IV further decreased the blade height by a 20-percent reduction of the first-stage area while maintaining the hub radius at 3.2 inches. This resulted in

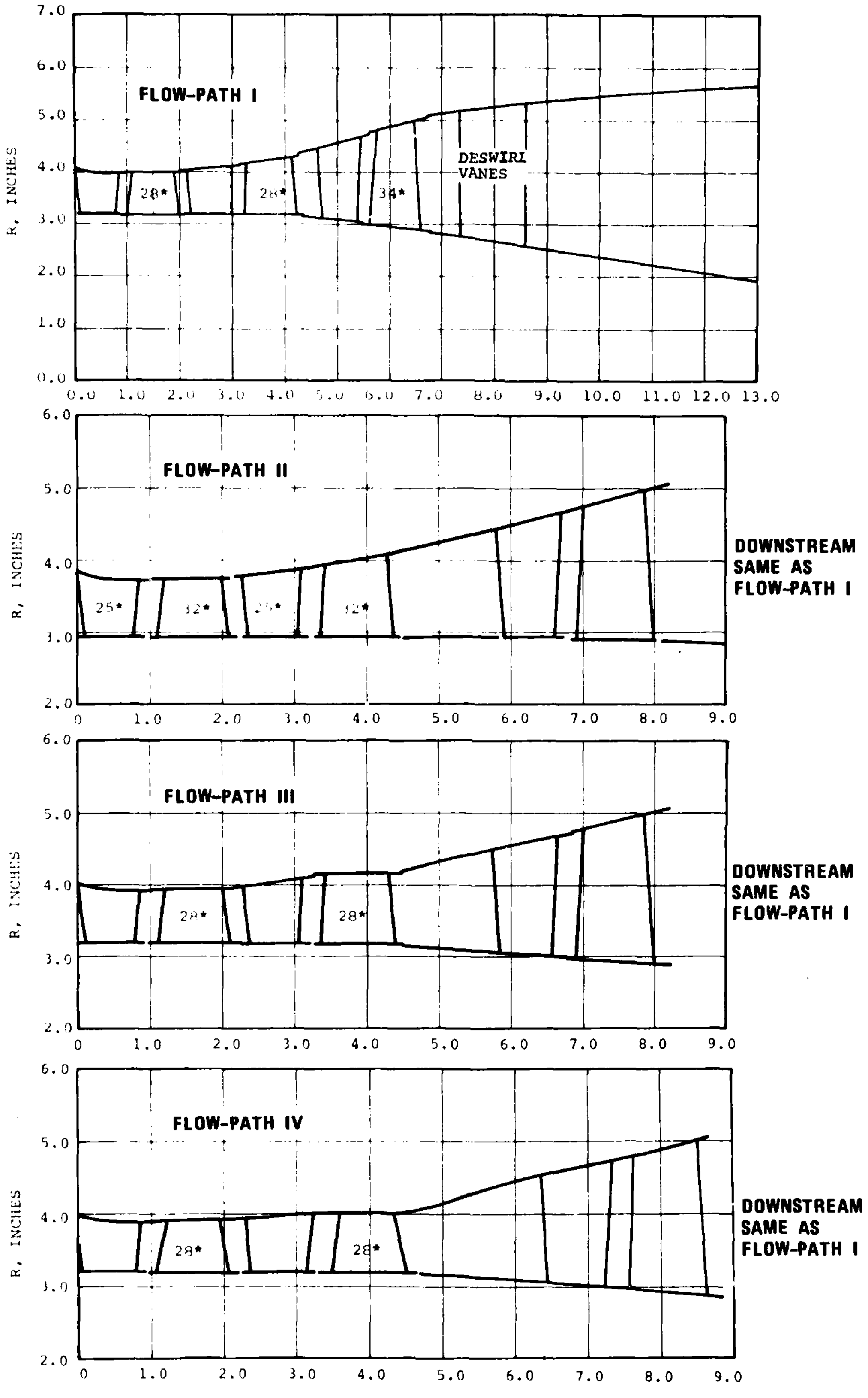

*NO. OF BLADES

Figure 2-2. Preliminary Design Flow-Path Variations.

reduced attachment stresses and moved the fundamental frequencies of both first- and second-stage rotor blades above an interference with stator passing. Flow-path IV was selected for further optimization as the turbine flow path for the TSE331C-1.

The pertinent turbine aerodynamic parameters are presented in Table 2-5, showing the variations due to the flow-path change. As shown in this table, predicted efficiency for the turbine with Flow-path IV still provides a performance level that is greater than the design goal of 85 percent.

Flow-path selection was based primarily on the two types of airfoils shown in Figure 2-3. One was designed for slight positive incidence, which reduced the level of airfoil peak stresses by minimizing airfoil twist. The other was designed for negative incidence, which reduced peak attachment stresses through decreased stagger and broach angles, while increasing airfoil natural frequencies resulting from increased root section camber. Both airfoils were aerodynamically equivalent from a performance standpoint.

The negative incidence configuration was selected for detailed design. This selection was based on the requirements for lower attachment stresses and higher natural frequencies. Attachment stress levels were considerably higher than those of the airfoils, and an additional increase in flexural frequency was required to avoid frequency interference in the operating range.

At the end of the preliminary design phase, a significant reduction in component risk had been achieved, and adequate visibility was available to provide confidence that the configuration could be successful. The largest gains were in average stress levels with further reduction of concentrated stresses being accomplished later in the detailed design phase. The average airfoil root-section stress was reduced by 18 percent in the first stage and 34 percent in the second stage, with reductions of 13 and 26 percent in airfoil peak stress. Average attachment stresses had been reduced by 19 percent in the first stage and 31 percent in the the second stage. Design modification aimed at driving the first flexural frequency above that of stator passing at design speed resulted in a 28-percent frequency increase for the first-stage airfoil and 64 percent for the second-stage airfoil.

The reductions in stress and increases in fundamental blade frequencies were attained at a cost of 0.7 percent turbine efficiency loss; however, the predicted performance level still remained greater than the design goal of 85 percent.

TABLE 2-5. AERODYNAMIC PARAMETER VARIATION DUE TO FLOW PATH CHANGE.

FLOW PATH	STAGE	ROTOR EXIT TIP RADIUS IN.	ROTOR EXIT HUB RADIUS IN.	MEAN WORK COEFF. $\frac{Jg\Delta H}{U_m^2}$	MEAN FLOW COEFF. $\frac{V_x}{U_m}$	ROTOR EXIT CRITICAL MACH NO. V/a'_{cr}	ZERO CLEARANCE EFFICIENCY	EFFICIENCY
	1ST	4.02	3.2	1.01	0.44	0.25	0.925	0.862
I	2ND	4.32	3.15	0.995	0.43	0.27	0.91	0.865
	3RD	5.0	2.9	1.543	0.518	0.50	0.90	0.828*
							OVERALL	0.863*
	1ST	3.76	2.95	1.18	0.511	0.29	0.92	0.856
II	2ND	4.09	2.93	1.11	0.50	0.31	0.905	0.860
	3RD	5.0	2.9	1.543	0.518	0.50	0.90	0.828*
							OVERALL	0.859*
	1ST	3.96	3.20	1.02	0.49	0.30	0.923	0.856
III	2ND	4.18	3.17	1.0	0.52	0.35	0.915	0.861
	3RD	5.0	2.9	1.543	0.518	0.50	0.90	0.828*
							OVERALL	0.859*
	1ST	3.915	3.20	1.05	0.524	0.316	0.925	0.854
IV	2ND	4.02	3.17	1.01	0.686	0.442	0.907	0.848
	3RD	5.0	2.9	1.543	0.518	0.50	0.90	0.828*
							OVERALL	0.856*

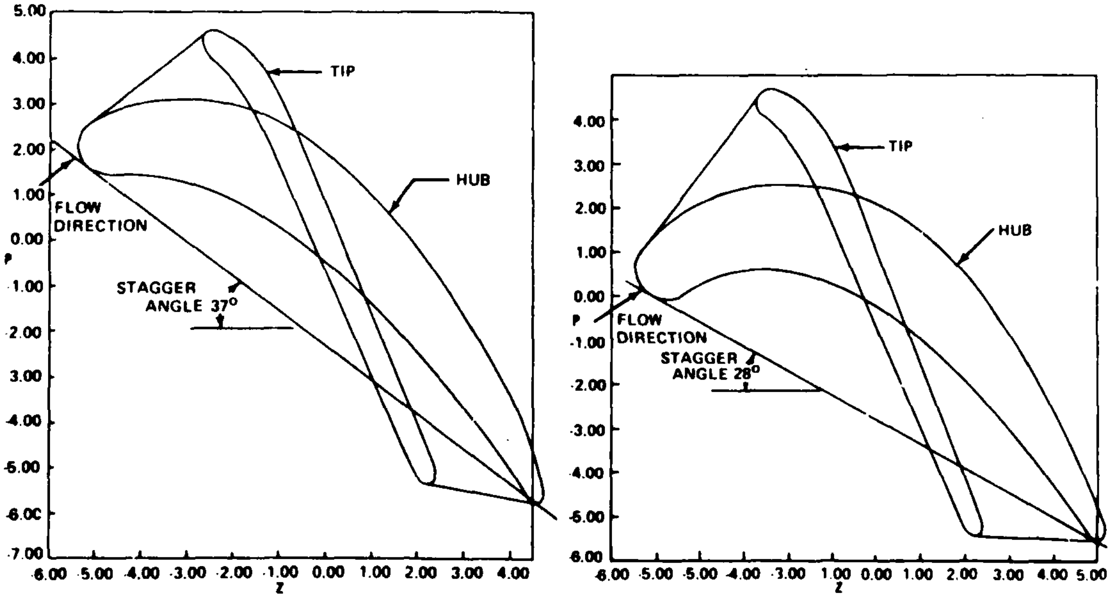

POSITIVE INCIDENCE HUB DESIGN

NEGATIVE INCIDENCE HUB DESIGN

Figure 2-3. Candidate Rotor Blade Configuratons for the Second-Stage Turbine.

Preliminary thermal analysis was conducted in parallel with preliminary stress analysis to determine whether the selected engine cycle would impose critical structural constraints. Figure 2-4 shows the results of the preliminary thermal analysis conducted assuming hot-pressed Si_3N_4 for the rotor blades, Waspaloy for the disk, reaction-bonded Si_3N_4 for the stator, shrouds, and support structure, and siliconized SiC for the combustor and transition liners. The temperature levels were estimated based upon gas-path thermal boundary conditions, secondary flow-circuit design, baseline thermal analysis of the stator support and first-stage rotor, and a general knowledge of Model T76 engine temperatures. The temperatures shown in Figure 2-4 represent average circumferential values and do not reflect the presence of hot streaks.

The preliminary thermal analysis indicated that the primary area of concern was the metal disk and that circulation of the high-temperature mainstream gas would have to be prevented by a disk cavity purge flow. This purge flow could readily be achieved through natural disk pumping of the rotors using compressor discharge air for cooling. The preliminary cooling circuit along with pumping flows (in percent of core flow) are shown in Figure 2-5. The cooling flow usage is compared with uncooled and cooled standard metal engine designs in Table 2-6.

To provide better use of cooling air and to assure acceptably low temperature at the disk rim, sealing plates for the first and second stages were incorporated into the design to direct the cooling flow to provide convective cooling, reducing the heat generated by the high airfoil temperatures.

2.4.2 DETAILED ROTOR DESIGN

The detailed design phase provided a final level of component and configuration optimization as well as detailed analytical component evaluation and risk assessment. If, in the final assessment, predicted risk had been too high and could not have been reduced to an acceptable level within the scope of the planned development testing, reevaluation and a redirected preliminary design effort would have been necessary.

Examples of the analytical models employed in the design of first and second stage ceramic rotor blades are shown in Figure 2-6. The 3-D blade model (A) was used to tie together information provided by the simpler models, to evaluate three-dimensional stress concentrations and [in conjunction with the 3-D disk model (C)]

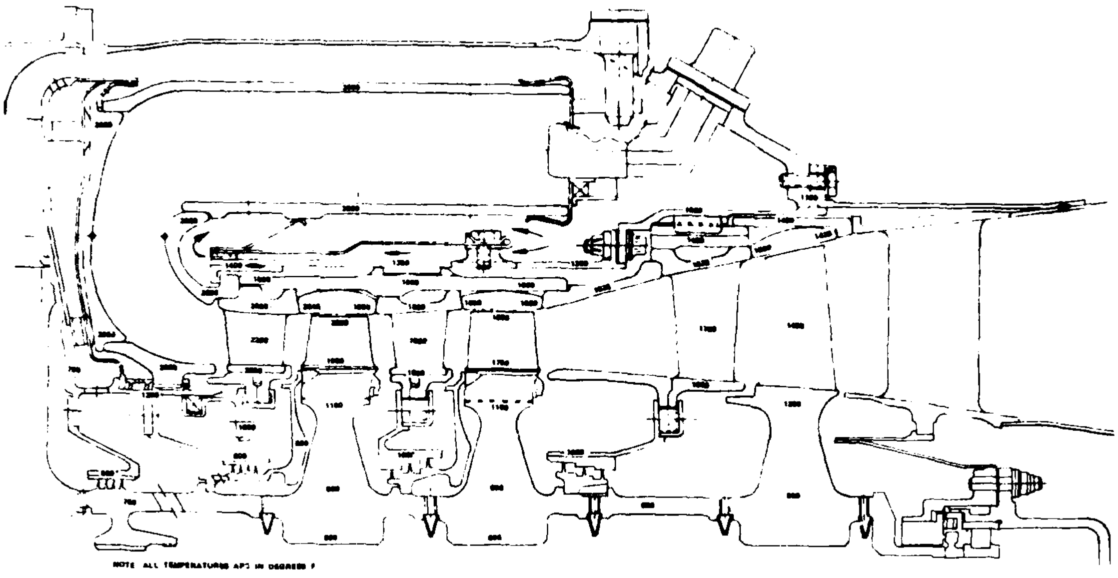

Figure 2-4. TSE331C-1 Turbine Temperature Levels for Preliminary Design.

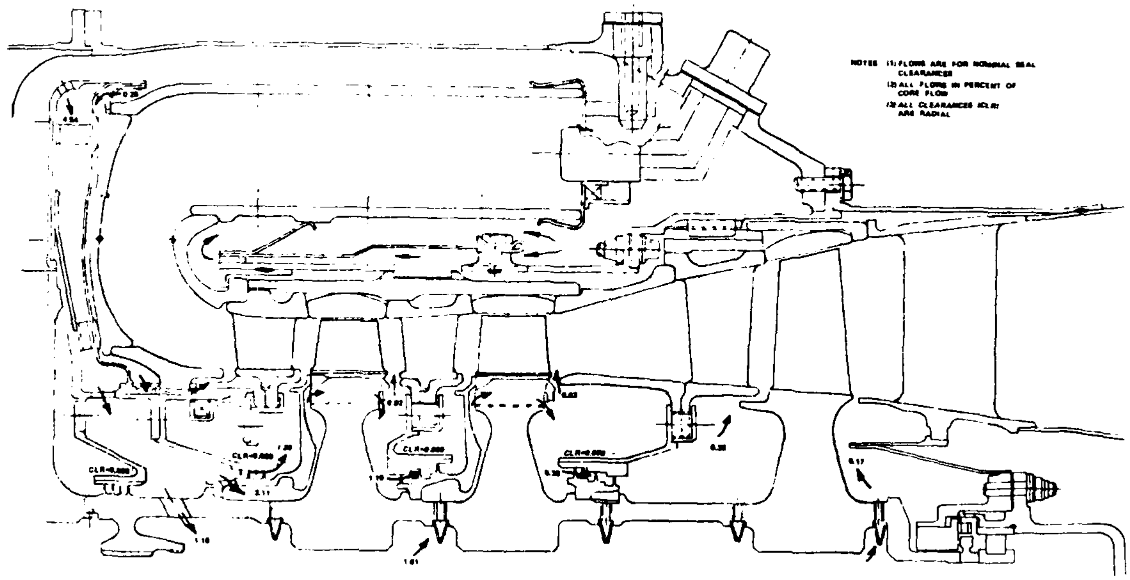

Figure 2-5. TSE331C-1 Preliminary Secondary Flow Circuit.

TABLE 2-6. COOLING FLOW USAGE COMPARISON.

	GARRETT TURBOPROP ENGINE MODELS		
	TPE331-8-401	T76-G-420	TSE331C-1
T.I.T. AVERAGE	1830°F	2027°F	2200°F
POWER OUTPUT	856 SHP	1040 SHP	1000 SHP
A – COMPONENT COOLING PERCENT OF CORE FLOW	6.4	12.0	3.3
B – SEAL LEAKAGE PERCENT OF CORE FLOW	0.7	1.3	1.2
TOTAL A + B	7.1	13.3	4.5

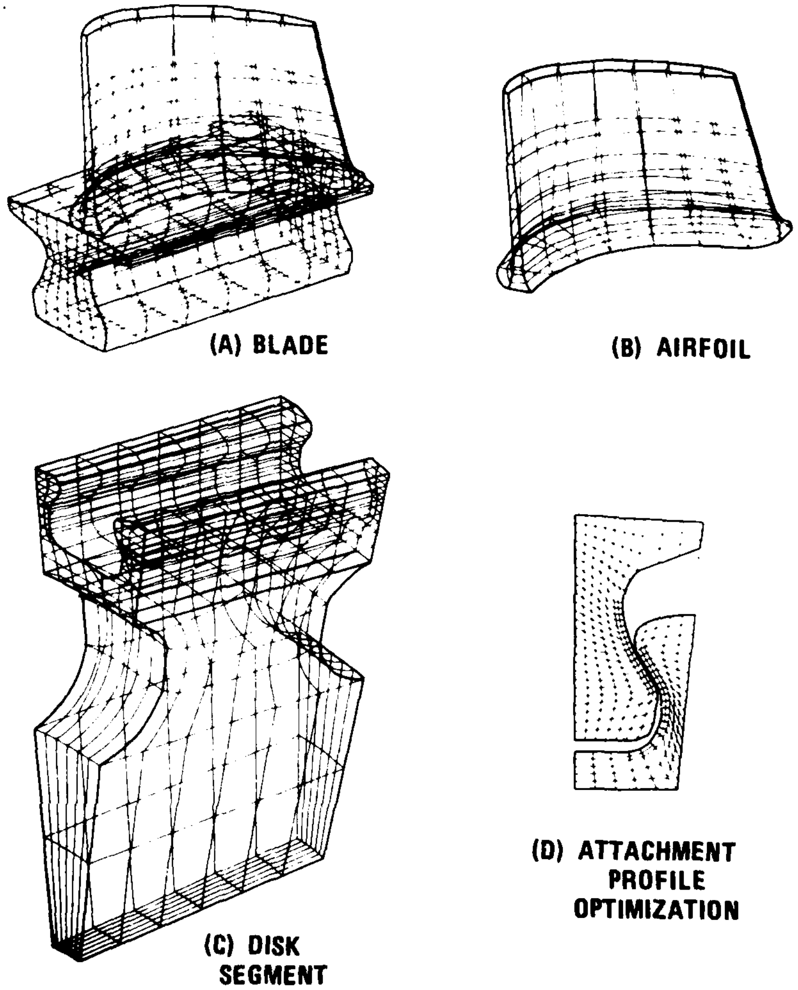
(A) BLADE

(B) AIRFOIL

(C) DISK SEGMENT

(D) ATTACHMENT PROFILE OPTIMIZATION

Figure 2-6. Examples of Analytical Models Utilized For Rotor Design.

to evaluate the effects of broach angle and disk axial stiffness. It was also used with material Weibull data to calculate probability of survival for the various blade configurations evaluated. The 3-D airfoil model (B) was used to optimize the airfoil configuration with respect to twist, tilt, lean, airfoil height,and pressure loading. A similar 3-D model was used to predict natural frequencies. The 2-D attachment model was used to optimize the profile of the attachment, to select the attachment specimen for material fabrication studies, and for spin pit testing.

Initial detailed analysis was conducted for conditions of maximum aerodynamic loading and the maximum design speed of 41,730 rpm. During this stage of the analysis, trade-off studies of important parameters such as airfoil tilt, lean and fairing, airfoil-to-platform contour transition, and broach angle effects were completed. Later, as thermal boundary information became available, the analysis was refined to include transient thermal stresses in addition to aerodynamic and rotational stresses.

A significant reduction in airfoil peak stresses was achieved by optimizing the airfoil section stack. This process, commonly referred to as leaning and tilting the airfoil, moves the center of gravity of the airfoil sections in a manner that will result in a centrifugal restoring moment, which counteracts aerodynamic loading. Tilt and lean were optimized in the ceramic blades to position the maximum stresses in the interiors of the airfoil rather than at the leading- or trailing-edges where failure most frequently occurs. Optimized stress distributions for steady-state conditions at the maximum operating speed of 41,730 rpm are shown in Figure 2-7.

Linear and nonlinear tilt, lean, and fairing were compared. The nonlinear configuration provided a slight decrease in stress but not enough to outweigh the additional complexity of manufacturing and inspection.

An elliptical transition contour between the airfoil and platform was selected. This elliptical form provided minimum stress concentration and improved thermal compatibility between the airfoil and platform.

A three-dimensional blade analysis was required to minimize stresses due to broach angle effects and blade overhang. The broach angle was decreased by slightly increasing airfoil twist. The first-stage blade with its higher reaction-angle airfoil required an axial length increase to 1.14 inches along with a broach angle decrease to

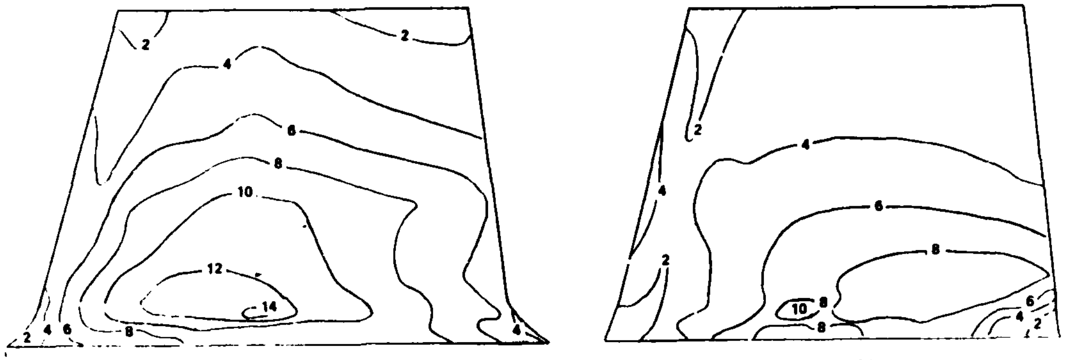

SUCTION SIDE PRESSURE SIDE

FIRST-STAGE ROTOR

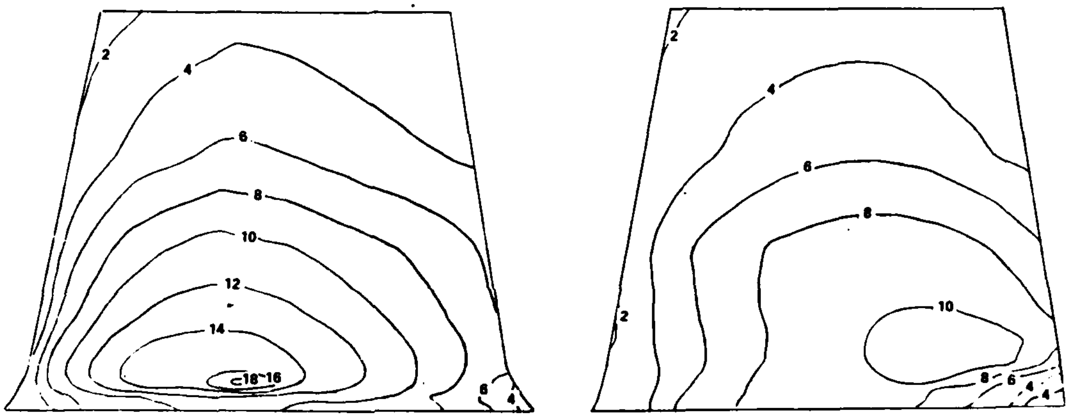

SUCTION SIDE PRESSURE SIDE

SECOND-STAGE ROTOR

Figure 2-7. TSE331C-1 Rotor Blade Airfoil Maximum Principal Stresses at 41,730 RPM (Stress Contours Labeled in KSI).

23 degrees. The second-stage axial length could be held to 1.1 inches with a broach angle of 17 degrees. Broach angle with a constant attachment profile would force obtuse platform corners to be much thicker than acute corners. In the TFE331C-1 design, the platform edge thickness was held constant resulting in a reduction in platform load and additional reduction in stress concentration for the obtuse corners of the attachment. The airfoil trailing-edge region was allowed to overhang the attachment neck, lowering stress in this critical zone of the airfoil. Concentrations of stress due to the overhanging regions of the airfoil and the platform itself were minimized by a 20-degree platform relief angle.

2.4.2.1 ROTOR BLADE ATTACHMENT DESIGN

A straight, single-tang dovetail configuration employing a metallic compliant layer between the ceramic blade and the metal disk was selected based upon prior Garrett and industry experience.[31] Design effort was directed to avoid stress concentration or local superposition of stresses. Initial analysis included aerodynamic and centrifugal stress but not thermal stress. Three-dimensional finite-element analysis was required.

Contact pressure angles of 45° and 60°, as illustrated in Figure 2-8, were evaluated. The 60° configuration was selected for its lower average neck stresses, higher neck stiffness and resulting higher natural frequencies, and lower probability of failure.

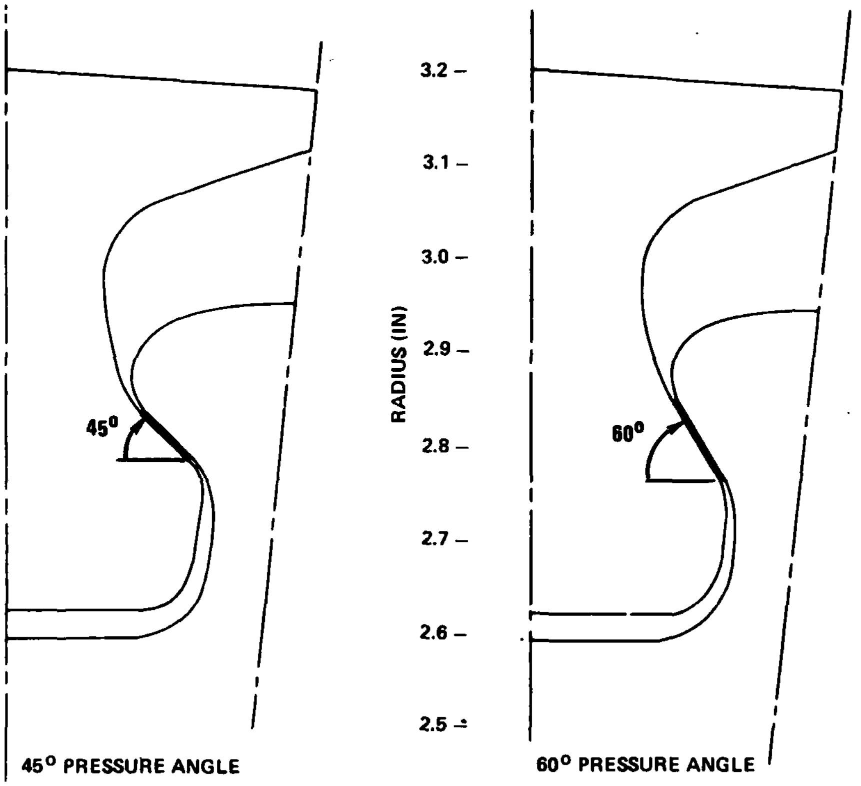

Figure 2-8. Attachment Contact Pressure Angle Comparison TSE331C-1 First-Stage Rotor.

Large compound radii were utilized in the attachment neck to minimize stress concentration. A 0.250-inch radius tangent to the contact surface was blended into a 0.090-inch radius tangent to the platform relief angle. This helped separate bending, concentrated tensile and overhang stresses, and provided a relatively uniform radial stress distribution. The amount of airfoil overhang, the neck profile, and the angle on the underside of the platform were all optimized to minimize stress concentration in the neck.

Spin pit tests on simplified rotor blade attachment specimens were conducted to support the attachment design effort. Initial tests showed that the platinum compliant layer thinned during cyclic testing. The blade configuration was modified to decrease contact stress, resulting in some increase in neck stress. In addition, the compliant layer material was changed to HS-25 and the thickness reduced from 0.010 to 0.005 inch.

Figures 2-9 through 2-12 present the stress distribution at maximum power steady-state conditions for the first- and second-stage rotor blades after optimization. The peak stresses in the first-and second-stage blades were respectively 43.8 ksi and 41.9 ksi and occurred above the contact zone at the leading edge on the pressure side, obtuse corner. The high stress concentration in this region was due to broach angle effects.

2.4.2.2 Blade Vibration Considerations

Design efforts were directed towards keeping blade natural frequency excitations outside the engine operating range. Natural frequencies of ceramic rotor blades are much higher than those of metal blades because of the low density and high elastic modulus of the hot-pressed Si_3N_4. Figure 2-13 compares the critical flexural mode (first mode) identified during the design study[2] for first- and second-stage Si_3N_4 blades with engine operating conditions. The interference diagram indicates a minimum margin of 26 percent above the strongest excitation source (stator passing frequency) in the operating range.

2.4.2.3 Transient Thermal and Stress Analysis

Detailed thermal analyses of steady-state and transient conditions were performed for the rotors using 3-D finite-difference techniques.[2,4,30] The model

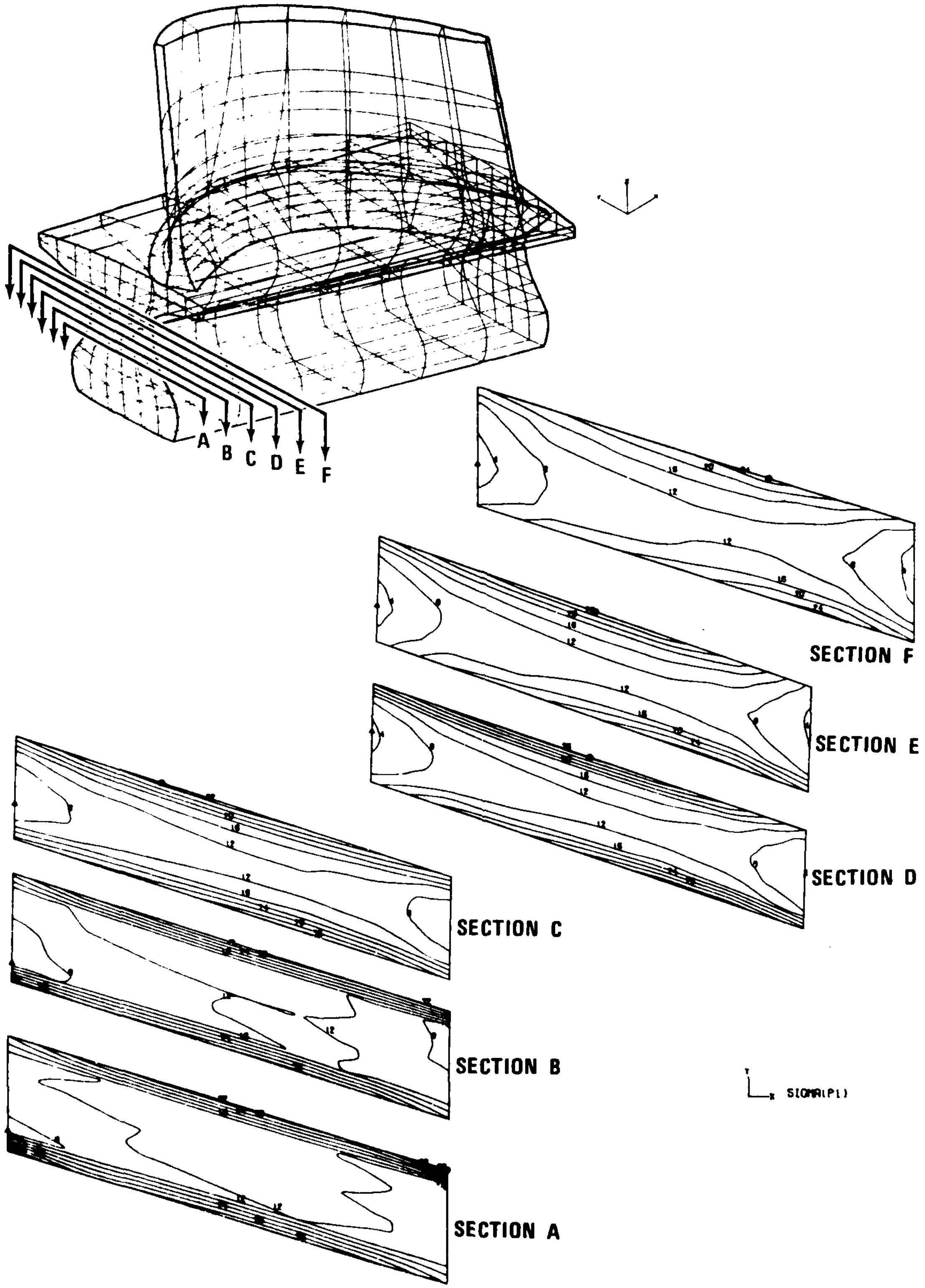

Figure 2-9. TSE331C-1 First-Stage Blade Attachment Maximum Principal Stress at 41,730 RPM, Horizontal Sections, Stress in KSI.

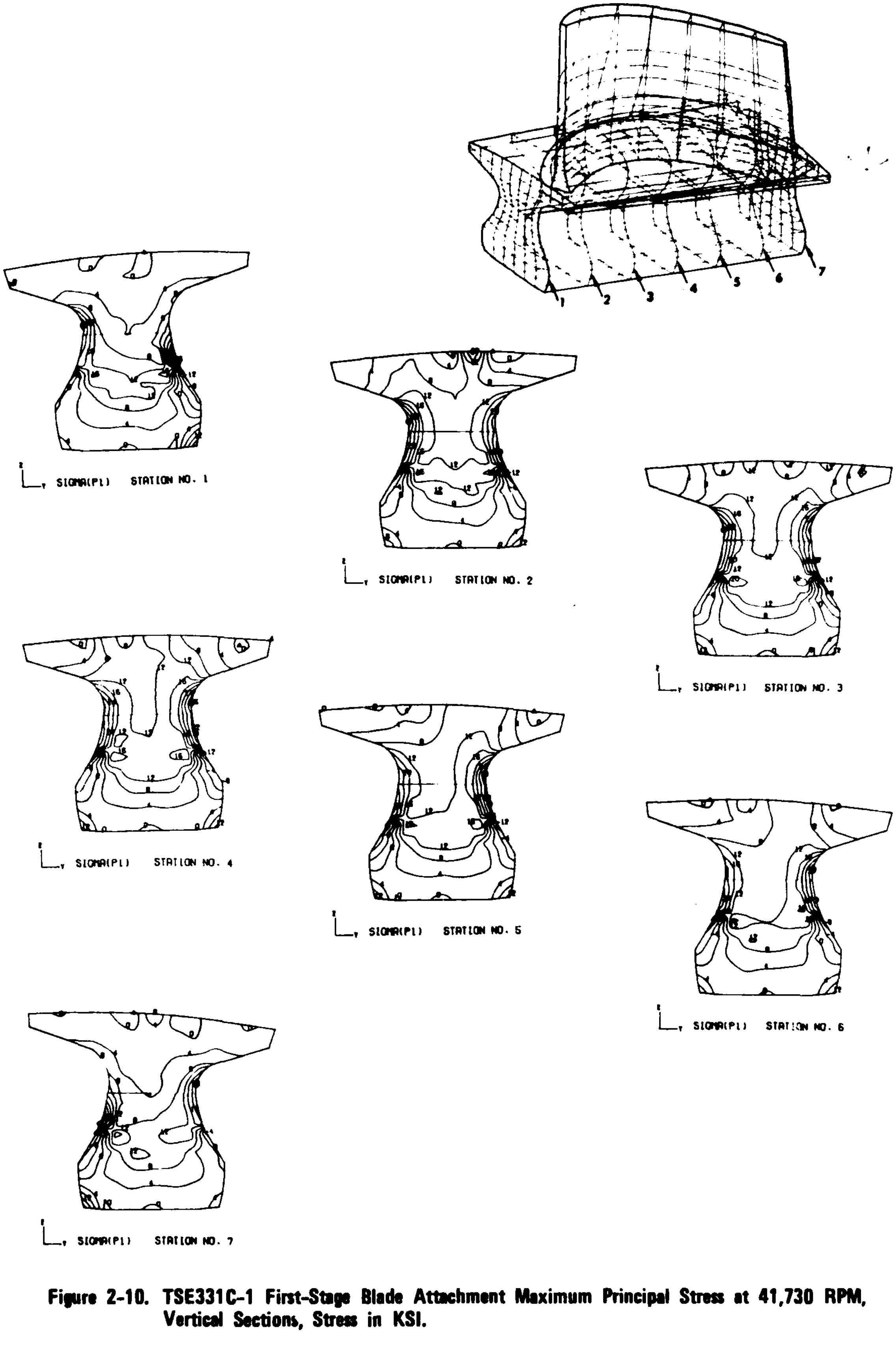

Figure 2-10. TSE331C-1 First-Stage Blade Attachment Maximum Principal Stress at 41,730 RPM, Vertical Sections, Stress in KSI.

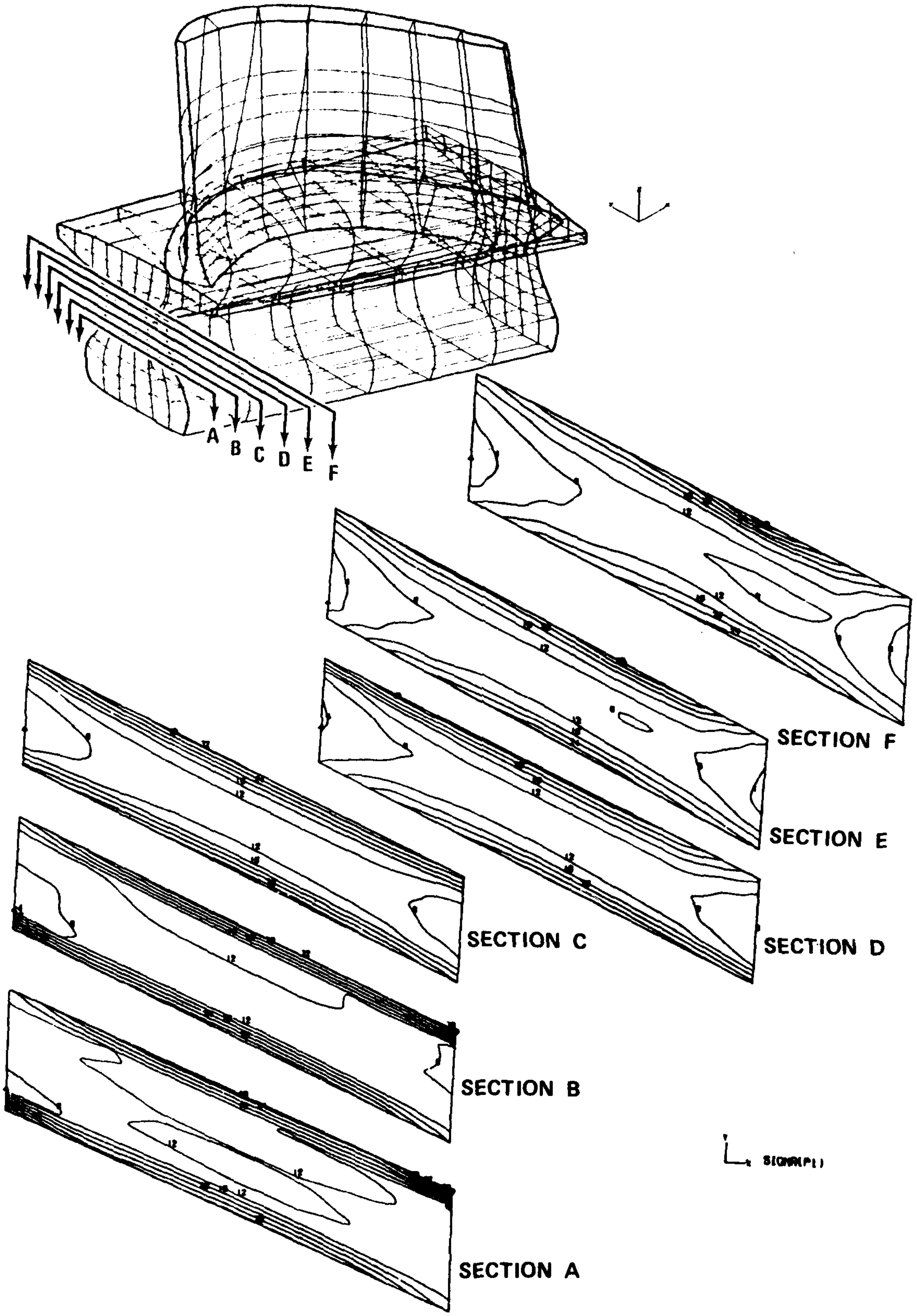

Figure 2-11. TSE331C-1 Second-Stage Blade Attachment Maximum Principal Stress at 41,730 RPM, Vertical Sections, Stress in KSI.

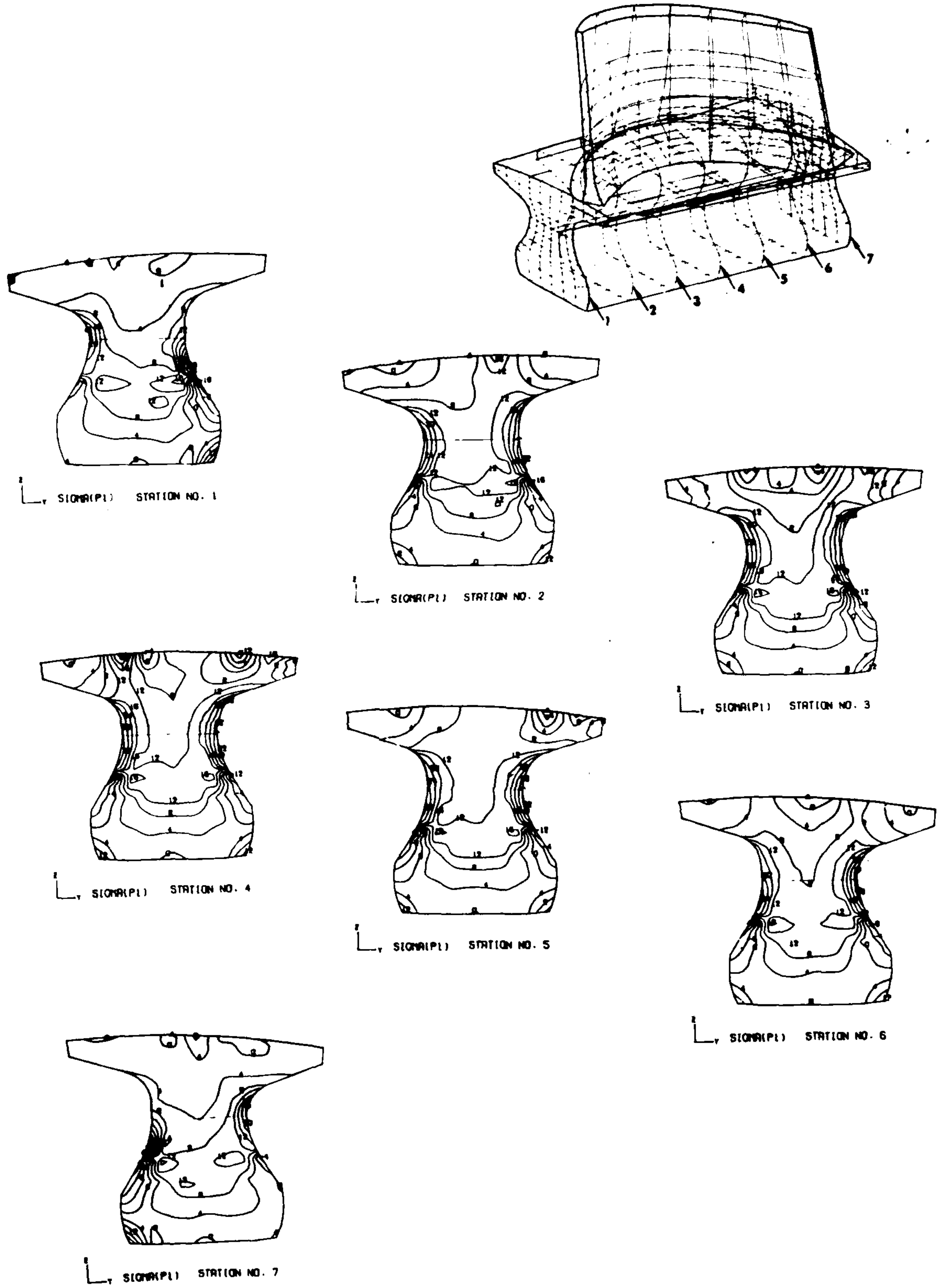

Figure 2-12. TSE331C-1 Second-Stage Blade Attachment Maximum Principal Stress at 41,730 RPM, Vertical Sections, Stress in KSI.

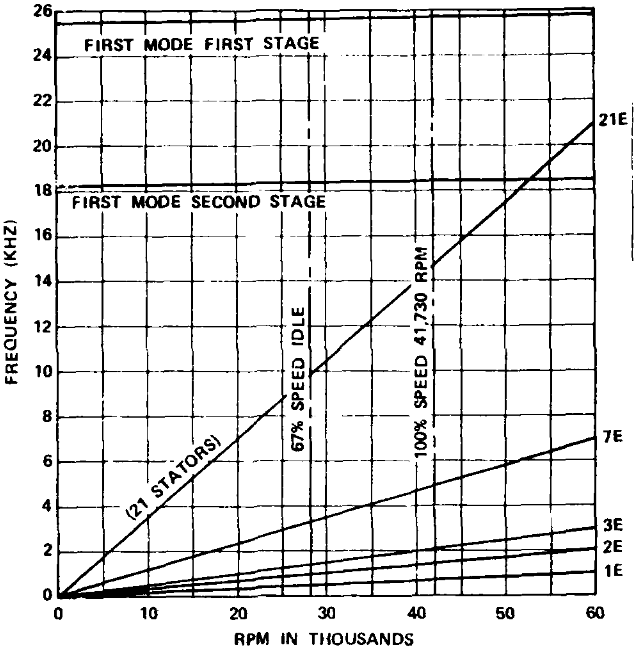

	FREQUENCY (Hz)	
MODE	**1ST STAGE**	**2ND STAGE**
FIRST	**26,700**	**18,400**
SECOND	**41,000**	**29,800**
THIRD	**53,000**	**44,900**
FOURTH	**76,000**	**57,800**

Figure 2-13. First- and Second-Stage Rotor Blade Natural Frequencies and TSE331C-1 Interference Diagram.

included a blade, a symmetric disk sector, the front cover plate, and portions of surrounding static structure appropriate for determining fluid temperatures which would influence the rotor temperature distribution.

Thermal analysis results for maximum-power steady-state conditions are illustrated in Figure 2-14. The analysis predicted maximum airfoil temperatures of 2065°F and 1820°F respectively for the first- and second-stage rotors. Attachment temperatures were in the range of 1300-1400°F.

The maximum principal stress distribution for the first-stage rotor blade at maximum power (TIT = 2200°F, rpm = 41,730) is shown in Figure 2-15 in comparison with the stress distribution at maximum speed without thermal stresses. Airfoil stress for this condition was dominated by a small pressure-to-suction-side thermal gradient rather than the slightly larger axial thermal gradient. Tensile thermal stress occurred on the suction side and at the trailing edge because of the lower temperature on the suction side. The stress increase on the suction side was straightforward, but the resulting stresses at the trailing edge were more subtle. These midspan tensile trailing-edge stresses resulted from the airfoil geometry, the distance from the minimum inertia axis of the trailing edge and its lower relative stiffness, as well as the thermal gradient. The suction-to-pressure-side displacement differential

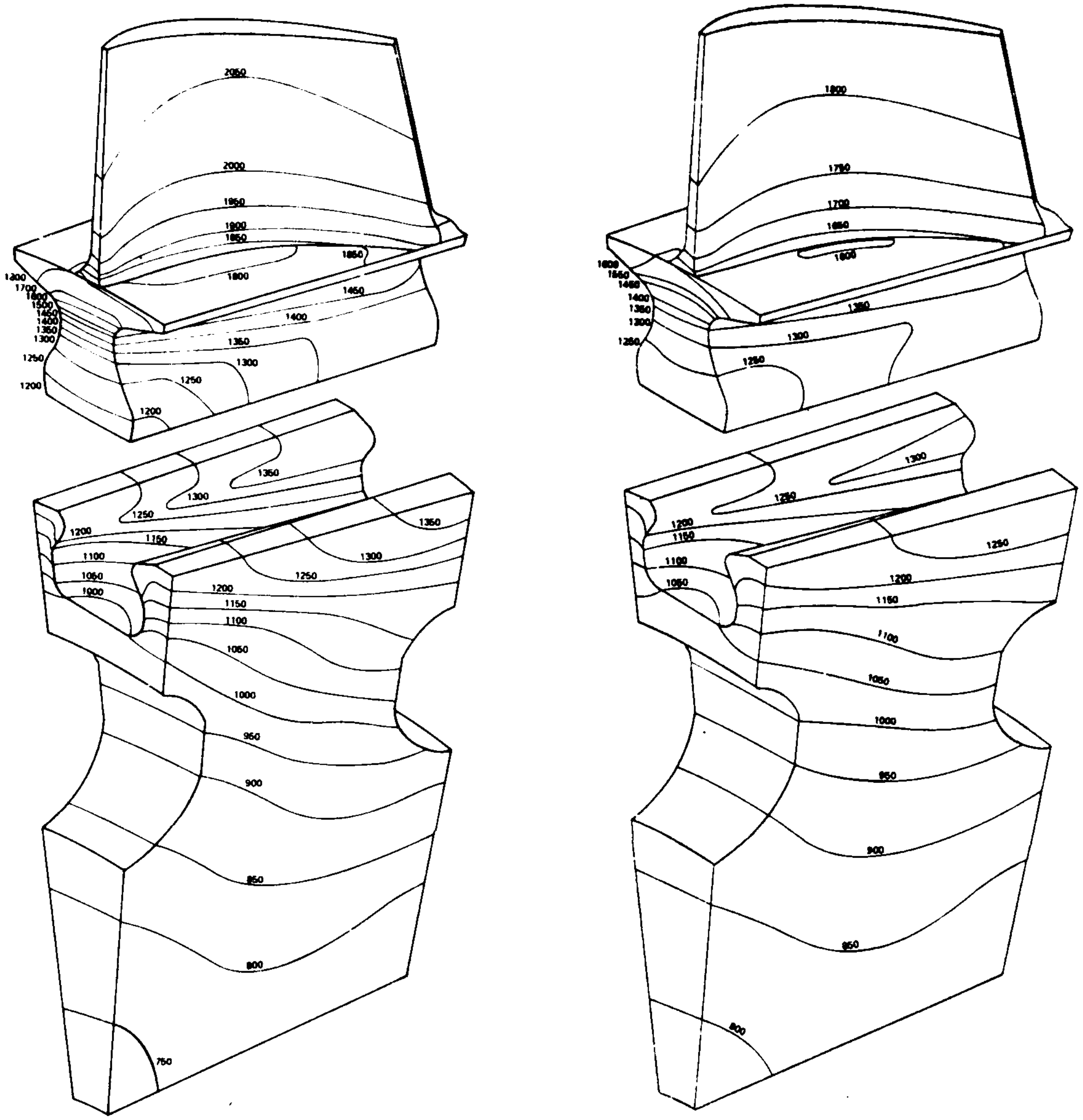

FIRST STAGE **SECOND STAGE**

Figure 2-14. TSE331C-1 First-Stage and Second-Stage Rotor Temperature Distribution for Maximum Power Steady-State Condition.

in the stiffer centerbody of the blade was amplified by the distance to the trailing edge, thereby forcing significant tensile stresses. These pronounced trailing-edge stresses were not present in the second-stage airfoil due to lower thermal gradients and lower airfoil cambers. Tensile thermal stresses in the second stage were considerably lower and more uniform than those in the first stage.

The elliptical airfoil platform transition provided good thermal compatibility and low concentration of stress. In the attachment area, the temperature distribu-

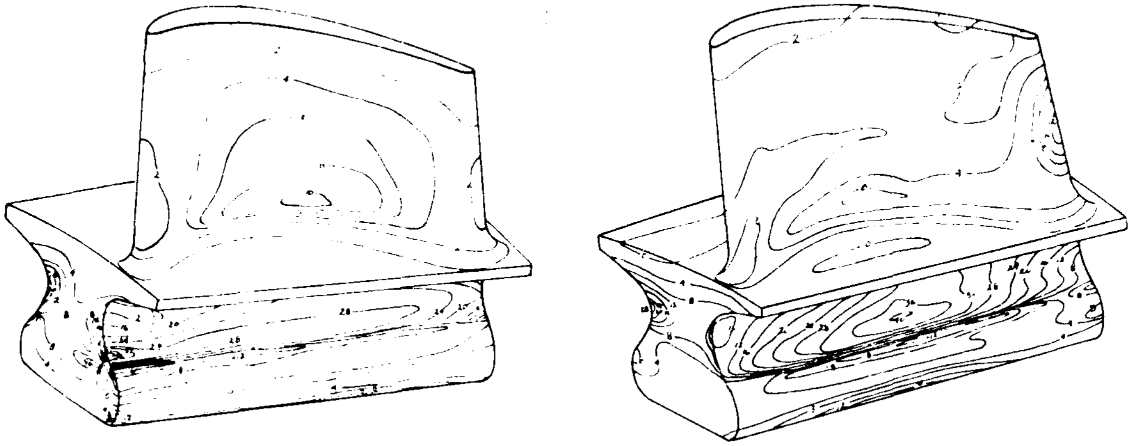

STRESS IN KSI

41,730 RPM CONDITION
(NOT INCLUDING THERMAL STRESSES)

MAXIMUM POWER CONDITION
(INCLUDING THERMAL STRESSES)

Figure 2-15. Comparison of the Maximum Principal Stress Distribution for the First-Stage Rotor Blade at 41,730 RPM and at Full Power Illustrating the Shift in Stress Distribution by Thermal Effects.

tion resulted in unloading of the ends of the attachment causing an increase in stress at the acute corner fillets. Conditions in the acute corners were dominated by convection cooling rather than conduction, resulting in tensile thermal stresses immediately under the platform.

Transient analyses were performed for normal acceleration and deceleration. The rotor speed and inlet temperature dependent variables were simulated to the schedules shown in Figure 2-16. The acceleration transient consisted of a cold start and run-up to idle speed, hold at idle speed for one minute, accelerate to maximum power and maximum speed in 18 seconds, hold at idle for one minute, followed by shutdown and rolldown to zero speed in 20 seconds. A thermal soakback period was also included following the shutdown.

The acceleration transient maximum power was achieved in 123 seconds, and based on experience with rotor-response rates, a period of 300 seconds was selected for study. The deceleration transient to zero-speed was achieved in 98 seconds after initiation, and based on experience and the simulation capabilities of the analysis, a 200-second period was selected for study.

The critical transient conditions of the ceramic rotor blades were determined to be at 125 seconds into the acceleration and 15 seconds into the deceleration. Surface isotherm maps for these conditions are shown in Figure 2-17 for the first-stage rotor.

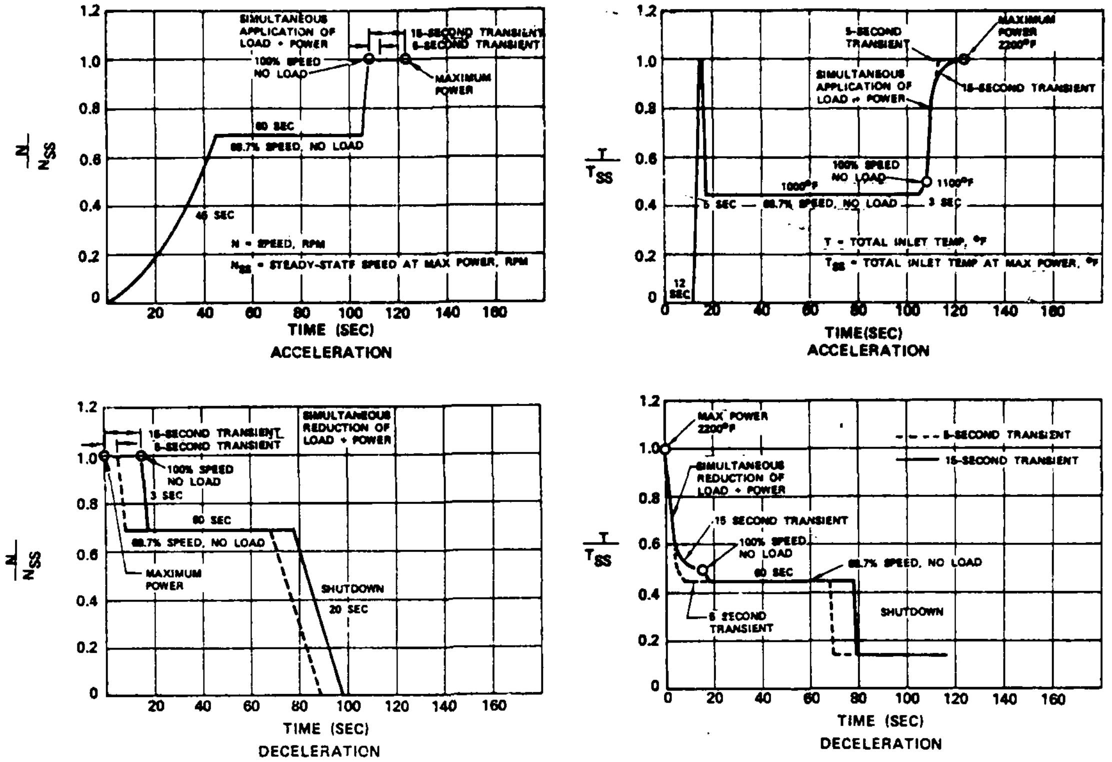

Figure 2-16. Rotor Speed and Inlet Temperature Schedules Used to Conduct Transient Analyses.

The maximum stresses were predicted for the rotor blade 125 seconds into the acceleration schedule. The maximum principal stress distribution for this condition is shown in Figure 2-18A. At this time the engine is at full speed, and maximum thermal gradients occur in the lower portion of the airfoil and in the platform attachment neck region. The central core of the blade is cooler with significant tensile thermal stresses in the centerbody of the airfoil and attachment neck near the midpoint. A peak attachment neck surface stress of 50 ksi is predicted on the suction side near mid-cord. Trailing-edge stresses are slightly increased over those of steady-state maximum power. The peak trailing-edge stress of 15.5 ksi occurs near mid-span.

As shown in Figure 2-18B, deceleration stresses are less severe than those of acceleration. The engine is still at full speed 15 seconds into the deceleration schedule. The leading and trailing edges are cooler and have relatively low tensile stresses. The attachment stresses are dominated by rotational stresses.

2.4.2.4 ROTOR DESIGN ASSESSMENT

Substantial stress reduction was achieved during analytical design. Analytical

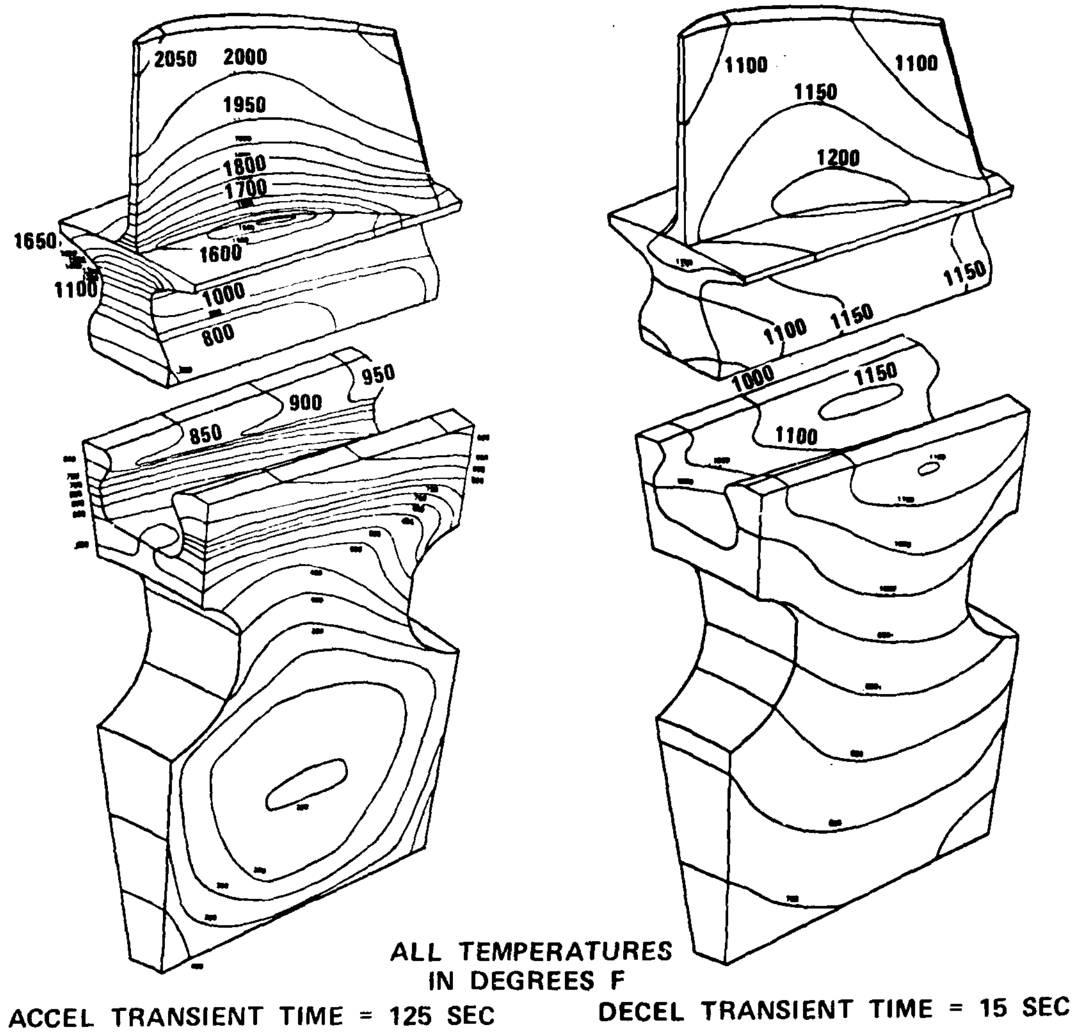

Figure 2-17. Surface Isotherm Maps for the First-Stage Rotor Blade at Critical Transient Conditions.

assessment of the cumulative probability of survival (CPS), using properties as they became available from the material characterization program, indicated that for all evaluated conditions, the final rotor design exceeded the 99.8-percent CPS goal. At full operating temperature and speed, CPS values of 99.989 percent for the first-stage blades, and 99.983 percent for the second-stage blades were calculated. The minimum predicted CPS occured at 125 seconds into acceleration for the first-stage rotor blade. Based upon this assessment, prints were released to initiate rotor blade procurement.

2.5 CERAMIC STATIC STRUCTURE DESIGN

This paragraph describes the preliminary and final design of the ceramic static structure components. A complete heat-transfer analysis of all these components

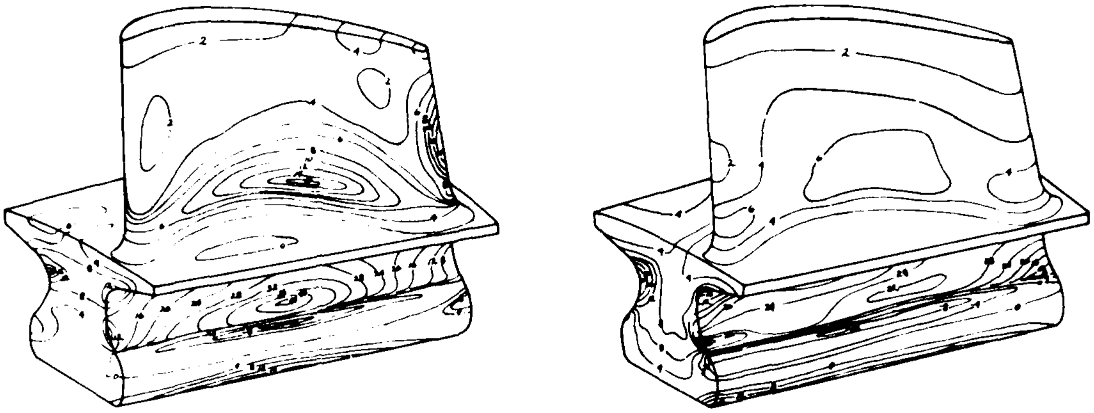

A. LIMITING ACCELERATION CONDITION

B. LIMITING DECELERATION CONDITION

STRESS IN KSI

Figure 2-18. First-Stage Rotor Blade Maximum Principal Stress Distributions at Limiting Transient Conditions.

was performed to determine temperature distributions during steady-state, start-up, normal shutdown, and emergency shutdown conditions. The results of these analyses were used along with calculated gas loads to accomplish two- and three-dimensional finite-element stress analyses of all items. Results of stress analyses were evaluated using a probabilistic approach that compared local stress fields to available material characteristics. Reaction-bonded silicon nitride was the material chosen for all static components discussed.

2.5.1 PRELIMINARY STATIC STRUCTURE ANALYSIS

The primary objectives during preliminary analysis were to select candidate materials, conduct an aerodynamic analysis to define a flow path consistent with the performance requirements, and to complete an initial thermal analysis.[1,2,32] The flow path selection was discussed earlier in Paragraph 2.3. It consisted of an unequal work split design with 21 ceramic vanes in both the first- and second-stage stator.*

---

*A stator-passing excitation problem was identified during rig testing, leading to a redesign of the stators to configurations containing only 19 first-stage and 17 second-stage vanes. This will be discussed in Paragraph 2.5.2.4 and Section 6.0.

The thermal model and the materials and components used for the initial static structure thermal analysis are illustrated in Figure 2-19. The resulting temperatures calculated for the steady-state maximum power condition are shown in Figure 2-20.

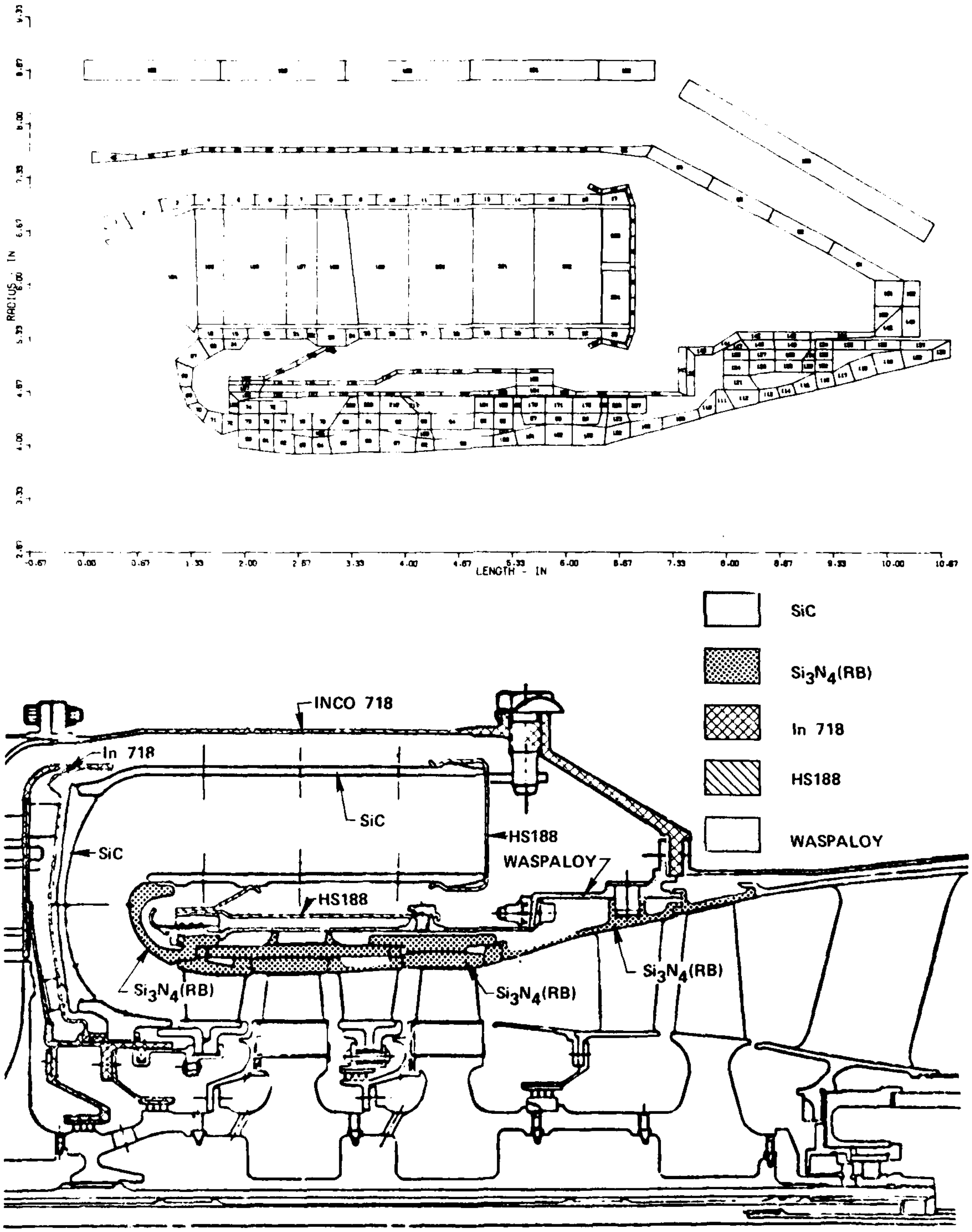

Figure 2-19. The Model and Materials Used For the Preliminary Static Structure Thermal Analysis.

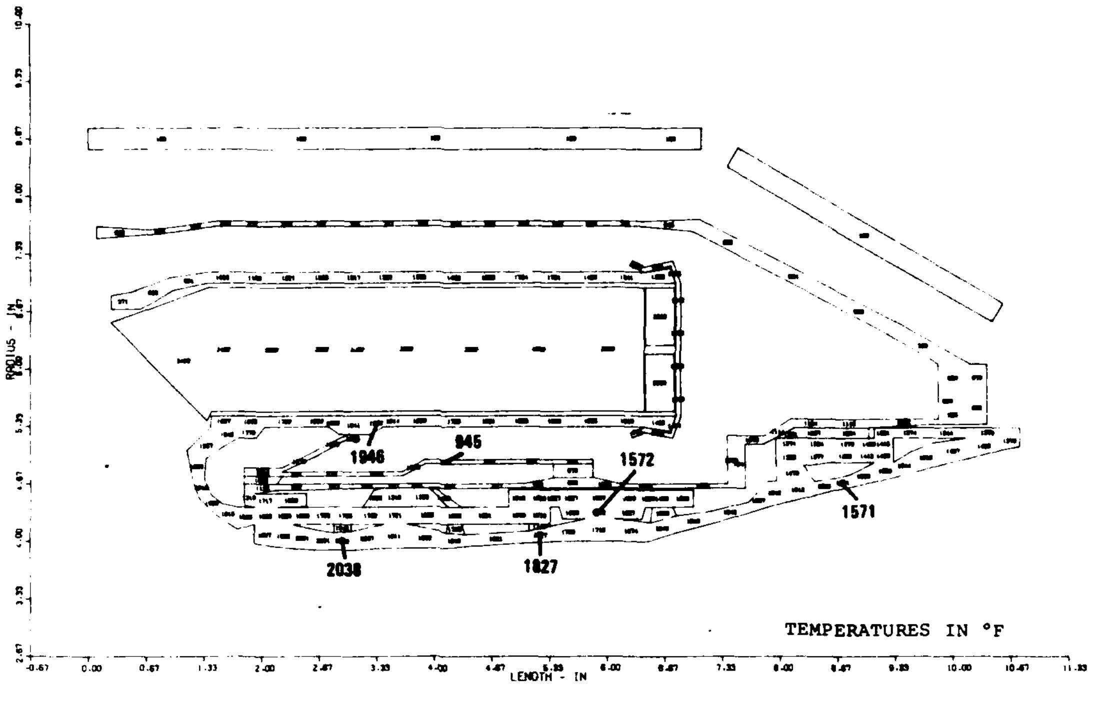

Figure 2-20. Turbine Structure Temperatures At Steady-Stage Maximum Power.

A transient thermal analysis was conducted for the same engine operation schedules shown in Figure 2-16. It determined that maximum temperature response in the flow path components occurred during and shortly after acceleration from idle to maximum power, approximately 110 to 120 seconds into the cycle. Maximum temperature response for the combustor was during lightoff and acceleration to idle. During deceleration the maximum temperature response of the flow path components was shortly after deceleration from maximum power to idle at approximately 75-90 seconds.

2.5.2 DETAILED STATOR THERMAL AND STRESS ANALYSIS

Three stator design approaches were considered; (1) integral (one-piece) with vanes attached rigidly to the inner and outer rings but with one ring slotted to reduce thermal stresses, (2) an assembly of segments consisting of two or more vanes attached to the ring segments, and (3) single-vane segments, each with inner and outer platforms to form a continuous ring during assembly. The first approach was rejected due to high predicted stresses and manufacturing considerations. The single-vane approach was selected for detailed design.

The primary stresses in the stators were thermal. Three-dimensional thermal analysis with a fine-mesh model was required to account for chordwise and spanwise conduction. The model selected is shown in Figure 2-21. Chordwise conduction arose due to the nonuniform thickness of the vane along the chord from the leading to the trailing edge, as well as from variations in heat-transfer boundary conditions in the chordwise direction. The chord length was much greater than the thickness, and a grid of two elements through the thickness and ten elements along the chord was selected. Radial or spanwise conduction occurred because both inner and outer shrouds were at a lower temperature than the vane. Turbine inlet gas temperature radial profiles also caused radial thermal gradients in the vane. Six sections of elements were included in the spanwise direction to account for these radial aspects. The grid geometry in the platforms was governed by the vane grid, and conduction paths from the vane to the platforms were appropriately simulated. Platform thickness is small compared to other dimensions, thus a grid of one element through the thickness was considered adequate.

Heat-transfer boundary conditions were obtained using specialized Garrett computer programs and test data. Correlations for cylinders in crossflow were combined with turbulent flat-plate boundary-layer correlations to obtain heat-transfer coefficients over the external surface of the vane and platforms.

Outer platform thermal boundary conditions were obtained from a separate analysis which included the inner platform, stator support ring, and piston ring. The influence of cavity air temperature on structure temperatures was determined. Radiation and conduction boundary conditions were included to account for these effects.

Steady-state temperature distributions for the maximum-power condition were obtained for several turbine inlet temperature radial profiles. An average turbine inlet temperature of 2200°F was assumed for profiles A and B, shown in Figure 2-22. Profile A is parabolic and symmetric about the mid-span, with a peak temperature of 2250°F and a minimum of 2120°F at the platforms. Profile B is flat at a constant value of 2200°F. Peak vane temperatures, which occurred at the mid-span trailing edge, were 2220°F for profile A, and 2183°F for profile B. Hot-spot profiles similar to A and B, with a peak temperature of 2500°F were also considered. The radial and chordwise temperature distributions are summarized in Figure 2-23.

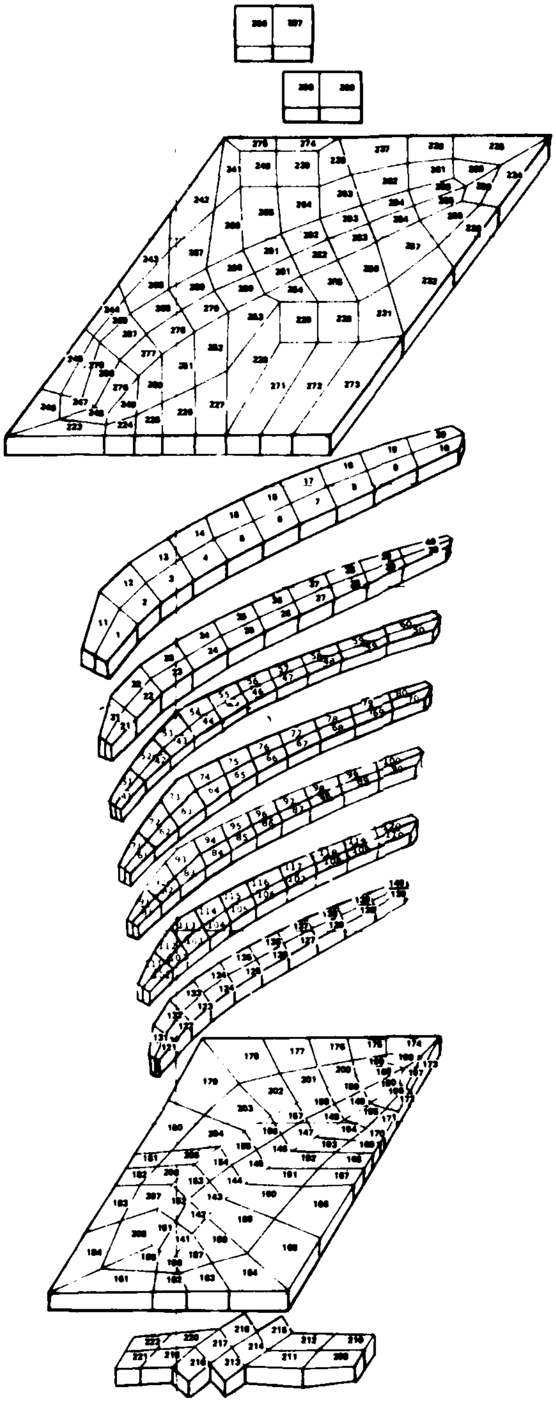

Figure 2-21. TSE331C-1 First-Stage Stator Thermal Analysis Model.

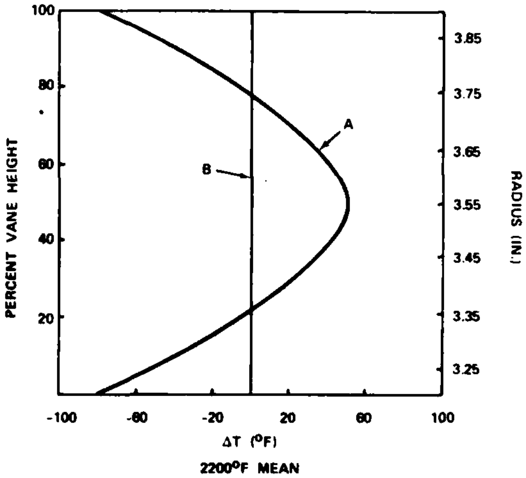

Figure 2-22. Combustor Exit Gas Temperature Profiles for T_{ave} = 2200°F Assumed During Thermal Analysis.

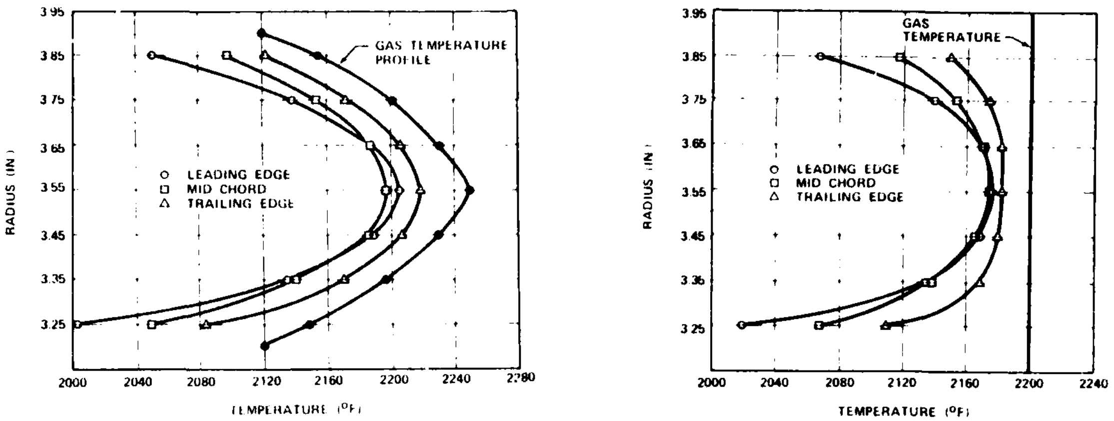

RADIAL TEMPERATURE DISTRIBUTION. PROFILE A

RADIAL TEMPERATURE DISTRIBUTION. PROFILE B

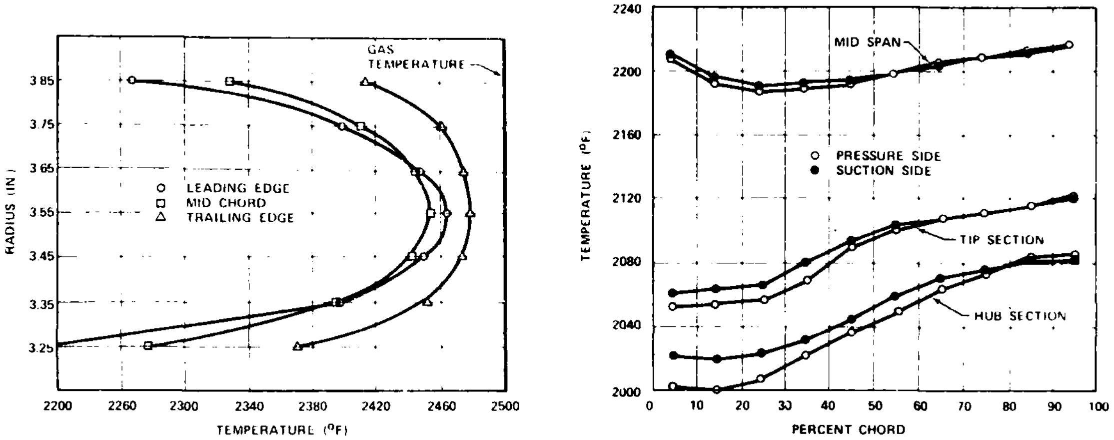

RADIAL TEMPERATURE DISTRIBUTION. 2500°F HOT-SPOT

CHORDWISE TEMPERATURE DISTRIBUTION. PROFILE A

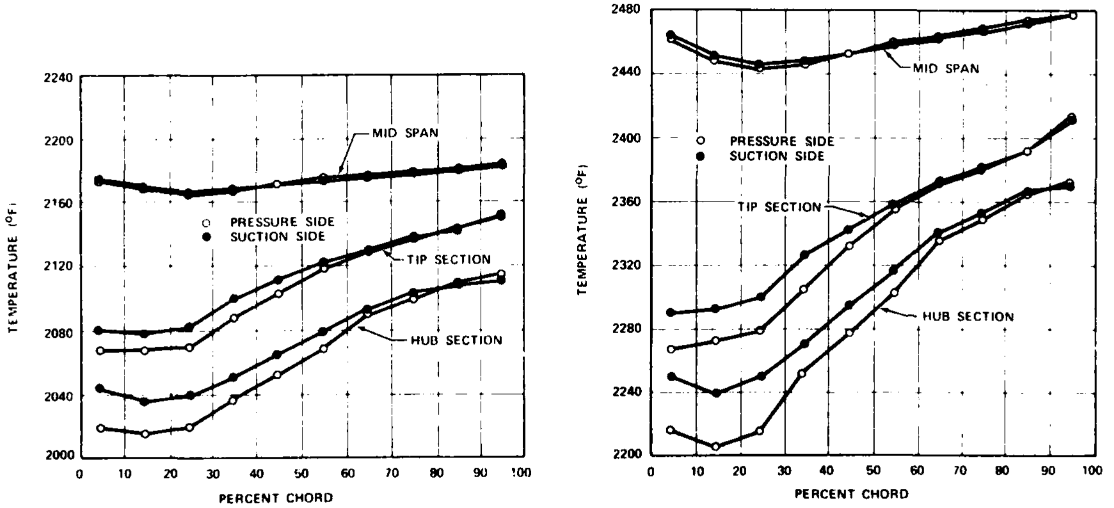

CHORDWISE TEMPERATURE DISTRIBUTION. PROFILE B

CHORDWISE TEMPERATURE DISTRIBUTION. 2500°F HOT-SPOT

Figure 2-23. First-Stage Vane Radial and Chordwise Temperature Distributions at Steady-State for Parabolic and Flat 2200°F Gas Temperature Profiles and for the 2500°F Hot Spot Condition.

Combustor rig testing indicated that the flat temperature profile (B) best represented engine conditions. Therefore, this profile was used to evaluate steady state and transient thermal stresses.

The primary 3-D stress analysis model used for the stator vanes is depicted in Figure 2-24. The stator is supported by four primary contact surfaces which react against the thermal and pressure loads. For this particular stator, thermal stresses are substantially higher than pressure stresses. The stator is axially restrained by the first-stage rotor shroud. Anti-rotation tabs on the outer platform provide rotational restraint. In addition to the four primary contact surfaces, the tab below the inner platform is used to retain the inner platform in the event that a vane fractures during engine testing.

This 3-D model utilized 1163 nodes to construct 290 isoparametric parabolic conoid elements. Both vane pressure and thermal loads were considered. A flat temperature profile across the vane span for a steady-state turbine inlet temperature of 2200°F was assumed. The boundary conditions assumed line contact along the radial restraints at inner and outer platforms.

Thermal stresses for steady state maximum power operation at 2200°F and with a 2500°F hot spot are shown in Figure 2-25. The peak stresses are substantially higher for the 2500°F condition.

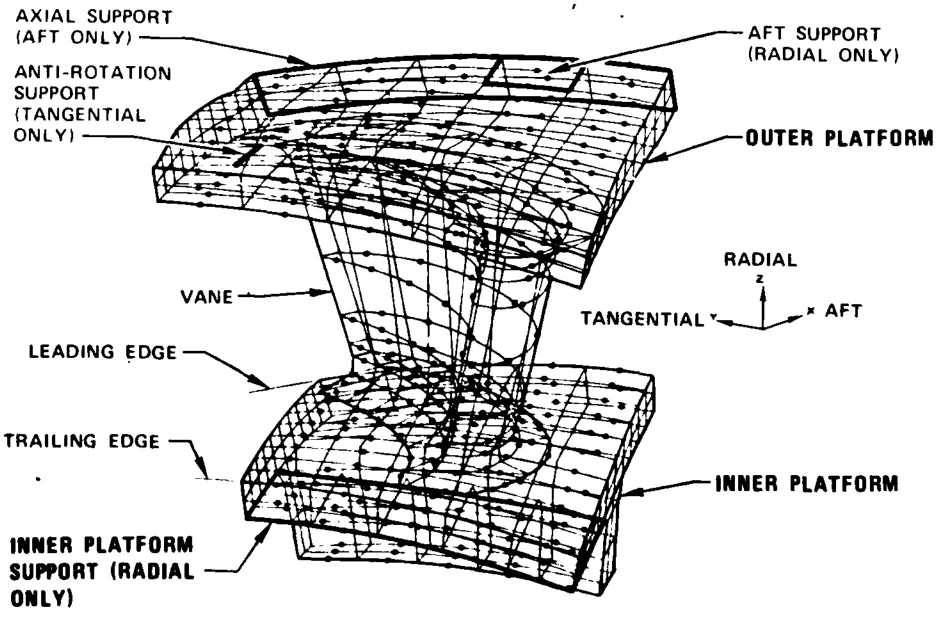

Figure 2-24. First-Stage Stator Single Vane Model with Boundary Conditions.

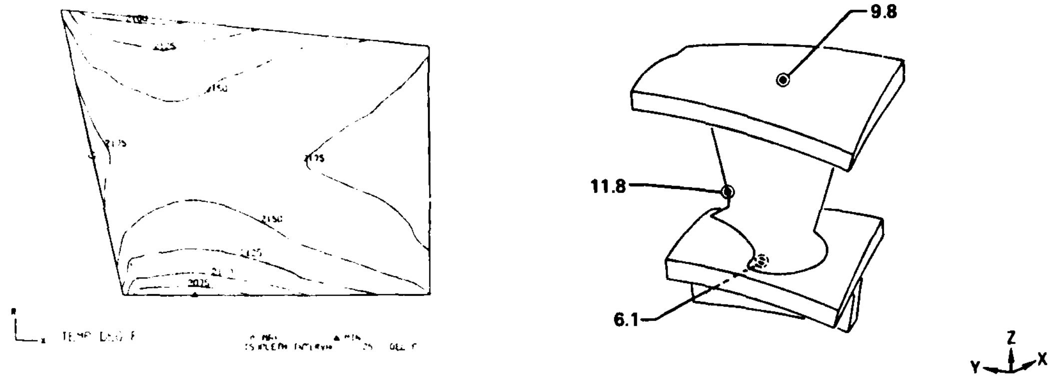

2200°F TURBINE INLET TEMPERATURE

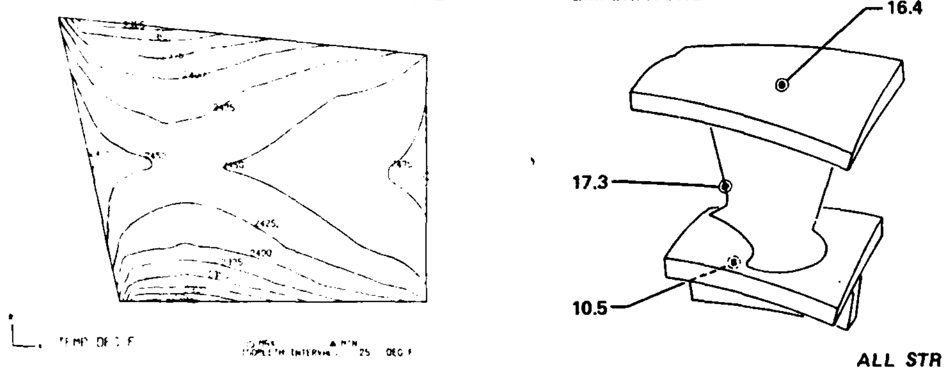

2500°F TURBINE INLET TEMPERATURE

Figure 2-25. First-Stage Stator Stresses Versus Turbine Inlet Temperature for Steady-State Maximum Power.

2.5.2.1 First-Stage Stator Transient Stress Analysis

The most severe thermal gradients during the start-up cycle were calculated to occur at 115 seconds after engine start. The analysis of the single-vane model at this transient condition revealed a peak principal tensile stress of 23.9 ksi at the vane trailing edge.[3] This corresponded to a calculated probability of success of 99.76 percent. This design was judged marginal and a stress reduction effort was initiated.

The high stresses were determined to be due to interactions between the stator airfoil and platforms. A high radial thermal gradient existed through the thickness of the inner and outer platforms. This gradient caused the platforms to curve toward the cool side; i.e., the inner platform curved radially upward and the outer platform curved downward. Consequently, radial tensile stresses were created at the leading and trailing edges of the vane, and radial compressive stresses were created in the mid-section of the vane. The thermal gradients through the vane fillets created stresses within the vane in the same manner as the platforms. For example, on the lower trailing edge of the pressure side of the vane, a vane-only model showed a tensile stress of 0.6 ksi. With the addition of the vane fillets, this tensile stress increased to 6.2 ksi, and, with the additional effect of the platforms, this stress increased to 23.9 ksi.

Two approaches were taken to reduce the stress levels in the stator: (1) increase the flexibility of the platforms by decreasing their thickness and (2) reduce the thermal gradient in the platforms by reducing contact with mating surfaces to minimize conduction heat loss.

Table 2-7 and Figure 2-26 summarize the results of the analyses to reduce the stress in the first-stage stator. By decreasing the size of the large inner platform tab to 0.4 inch, decreasing the inner and outer platform thickness from 0.1 inch to 0.06 inch, and reducing the inner platform contact area to 0.125 inch and the outer platform contact area to the aft tab, the trailing edge and the anti-rotation tab, the critical peak stress for 2200°F inlet temperature was reduced from 23.9 ksi to 16.1 ksi. Superimposing pressure loads increased the stress to 17.6 ksi. Including the 2500°F hot-spot condition increased the peak stress to 21.6 ksi. This was judged to be an acceptable level. Prints for this design were released for ceramic stator manufacturing development.

2.5.2.2 Second-Stage Stator Analysis

The second stage stator configuration analyzed consisted of 21 reaction-bonded Si_3N_4 single-vane segments trapped axially between the first- and second-stage turbine rotor shrouds and supported in the same manner as the first-stage stator. Tangential motion was prevented by the use of an antirotation tang on the outer band which engaged a mating slot in the main pilot cylinder (also referred to as the turbine vane and shroud support).

In order to expedite stress analyses for the second-stage stator, the steady-state temperatures predicted for the second-stage stator were applied to the 3-dimensional finite-element model developed for the first-stage stator. Although this did not produce an exact analysis, the high degree of similarity between the two stators assured that the calculated stresses were sufficiently accurate to allow an initial evaluation of the problems that could be expected with the proposed design.

TABLE 2-7. FIRST-STAGE STATOR ANALYTICAL OPTIMIZATION SUMMARY.

START-UP TRANSIENT CONDITION, T = 115 SECONDS								
				PEAK PRINCIPAL TENSILE STRESS			CALCULATED PROBABILITY OF SUCCESS (%)	
CASE NO	CONFIGURATION	TYPE LOADING	TURBINE INLET TEMP (°F)	LOCATION*	VALUE (KSI)	REDUCTION FROM BASELINE (KSI)	SINGLE VANE	21-VANE ASSEMBLY
01	BASELINE (DWG NO. 3551326)	THERMALS ONLY	2200	LOWER VANE TRAILING EDGE	23.9	--	99.756	94.998
02	VANE ONLY MODEL			LOWER VANE MID-CHORD	6.7	17.2	>99.999	>99.99
03	VANE WITH FILLETS MODEL			LOWER FILLET MID-CHORD	14.0	9.9	99.996	99.925
04	CASE 1 WITH NO INNER BAND TAB			LOWER VANE TRAILING EDGE	20.9	3.0	99.832	96.522
05	CASE 1 WITH 0.05 INCH THICK INNER BAND			UPPER VANE TRAILING EDGE	20.2	3.7	99.932	98.588
06	CASE 1 WITH REDUCED CONTACT SURFACES			LOWER VANE TRAILING EDGE	22.4	1.5	99.889	97.687
07	CASE 1 WITH 0.06 INCH THICK INNER BAND, 0.40 INCH LONG TAB, AND REDUCED CONTACT SURFACES			UPPER VANE TRAILING EDGE	17.1	6.8	99.989	99.764
08	CASE 1 WITH 0.06 INCH THICK INNER AND OUTER BAND, 0.40 INCH LONG TAB, AND REDUCED CONTACT SURFACES			INNER BAND LEADING EDGE	16.1	7.8	99.998	99.962
09	SAME AS CASE 8 (PRESSURES INCLUDED)	THERMALS AND PRESSURE		OUTER BAND ANTI-ROTATION TAB	17.6	6.3	99.973	99.433
10	SAME AS CASE 7 (HOT-SPOT ANALYSIS)	THERMALS ONLY	2500	UPPER VANE TRAILING EDGE	21.6	2.3	99.861	97.120

*FILLET REFERS TO FILLET RADIUS BETWEEN VANES AND PLATFORMS.

Because the thermal gradients were lower in the second-stage stator than in the first-stage stator, the corresponding stresses were lower. Using the case 01 model (shown previously in Figure 2-26), a maximum principal tensile stress of 17.8 ksi was calculated for the outer platform antirotation tab. The thermal and stress maps are illustrated in Figure 2-27. This resulted in a calculated probability of success of 99.91 percent for a 21-vane assembly. Based on this result, second-stage stator prints were released for ceramic component fabrication development.

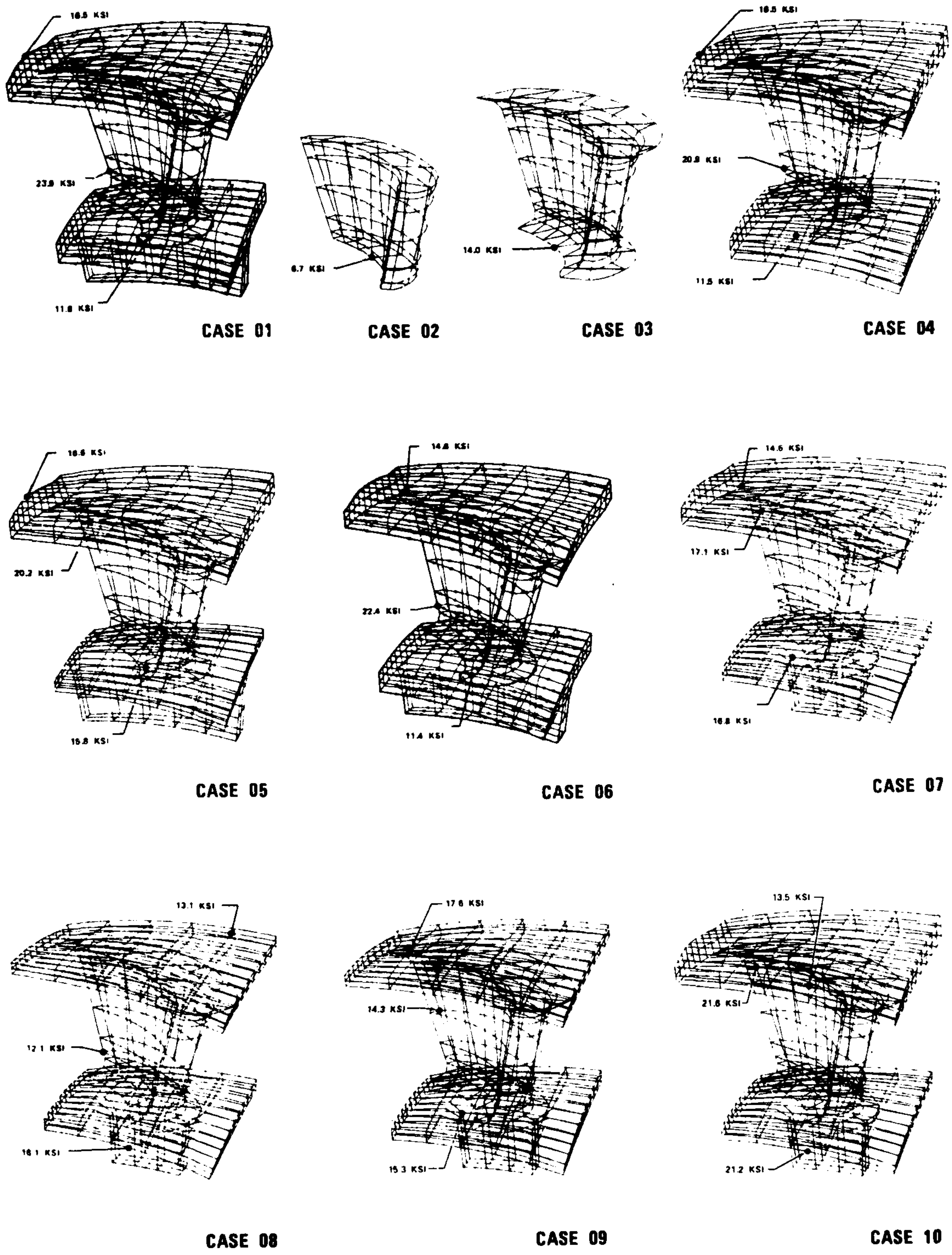

Figure 2-26. First-Stage Stator Analytical Optimization Studies for Normal Start-Up Transient Condition.

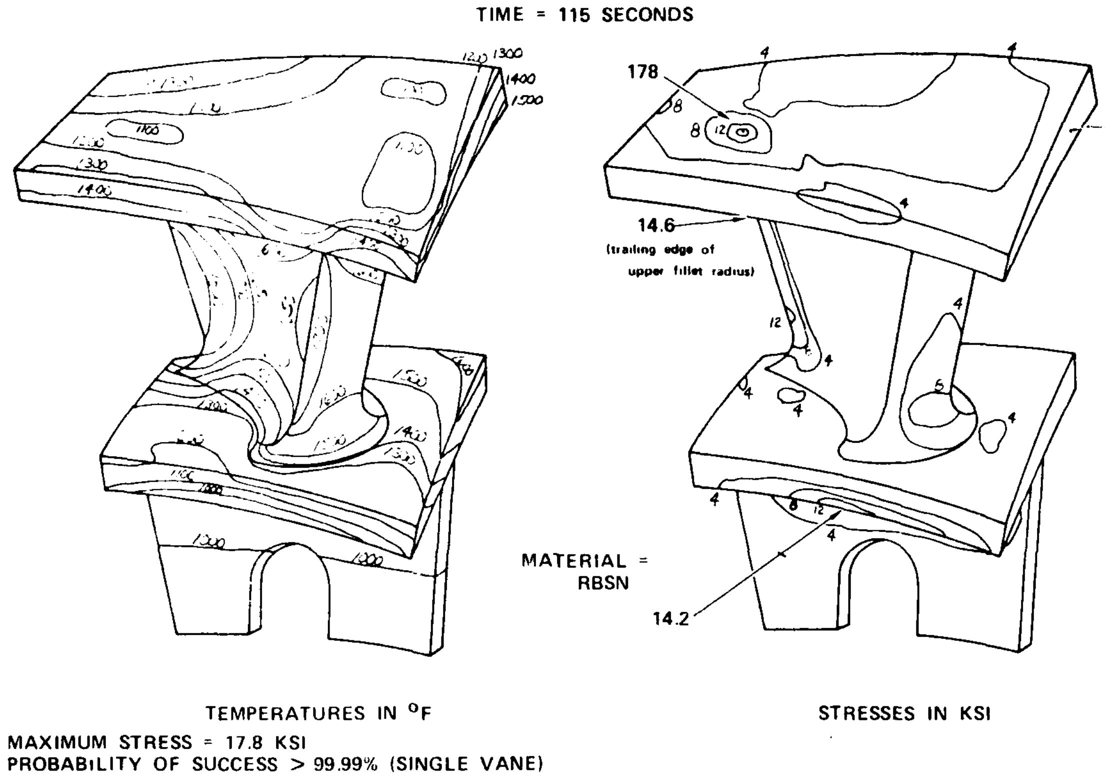

Figure 2-27. Second-Stage Stator Temperature and Stress Results for the Typical Start Condition.

2.5.2.3 Stator Design Summary

Table 2-8 summarizes the design parameters for the first- and second-stage stators as they were initially released for fabrication.

2.5.2.4 Stator Redesign

In the first rig operated with a ceramic rotor, a blade resonance problem was encountered due to excitation from the stators. This was resolved by reducing the stator vane count to 19 for the first stage and 17 for the second stage. Thermal and stress models similar to those previously described were used.

A second problem requiring design modification was encountered during static structure rig testing. Chipping occurred at component interfaces indicating the presence of high contact stress. Therfore, during the redesign to achieve the 19-vane and 17-vane configurations, effort was included to decrease localized contact stresses and to improve mechanical load sharing.

Table 2-8. Stator Design Point Summary.

PARAMETER	FIRST STAGE		SECOND STAGE	
	HUB	TIP	HUB	TIP
RADIUS (INCH)	3.200	3.900	3.2	3.99
CHORD (INCH)	1.2757	1.7689	1.155	1.4277
AXIAL CHORD (INCH), C_x	0.760	0.900	0.77	0.9
SPACING (INCH), S	0.957	1.167	0.957	1.194
L.E. THICKNESS (INCH)	0.100	0.100	0.08	0.08
T.E. THICKNESS (INCH)	0.040	0.040	0.04	0.04
L.E. HALF-WEDGE ANGLE (DEG)	11	11	7	10
T.E. HALF-WEDGE ANGLE (DEG)	4	4	5	5
SOLIDITY, C_x/S	0.794	0.771	0.8046	0.7538
ZWEIFEL	0.918	0.751	1.247	0.946
THROAT (INCH^2)	0.4008	0.3433	0.4606	0.5140
BLOCKAGE (PERCENT)	8.98	11.33	8.32	7.93
SECTION AREA (INCH^2)	0.1033	0.2036	0.0975	0.1480
EXIT BLADE ANGLE (DEG)	62.245	72.383	59.84	65.02
INLET BLADE ANGLE (DEG)	20.00	13.500	0.0	-2.0
STAGGER ANGLE (DEG)	53.433	59.417	48.19	50.92
DEL BP (BLADE PARAMETER)	60.00	35.00	20	120
$\Delta P/P$	0.0149	0.0241	0.019	0.027
Re x 10^{-5}	4.226	5.751	2.86	4.02
P′ (PSIA)	121.104	121.104	76.296	80.304
T′ (^{0}R)	2659.7	2659.7	2417.08	2440.88
VANE OR BLADE NUMBER		21		21
ASPECT RATIO $(\bar{R}_T-\bar{R}_H)/\bar{C}_x$		0.921		1.018
HUB/TIP RATIO		0.8205		0.802
THROAT AREA (INCH^2)		5.465		8.084

The free-body diagram and predicted load reactions for the first stage stator is shown in Figure 2-28. All reactions were assumed to be acting at either one or two points to eliminate the redundancies of a distributed load along a surface. The analysis was done for four different seal load conditions, the applicable case depending upon the accuracy of controlling dimensions between contact surfaces. The seal load is the axial pressure load across the first-stage stator seal plate.

The idealized condition corresponds to Case 2, which assumed that an equal share of the seal load was transmitted to each stator. Case 4 assumed that only three stators carried the complete seal loads. Under this condition the corresponding stresses were marginal. Rather than designing to this condition with a thicker platform and thereby decreasing the chances for survival due to thermal loading,

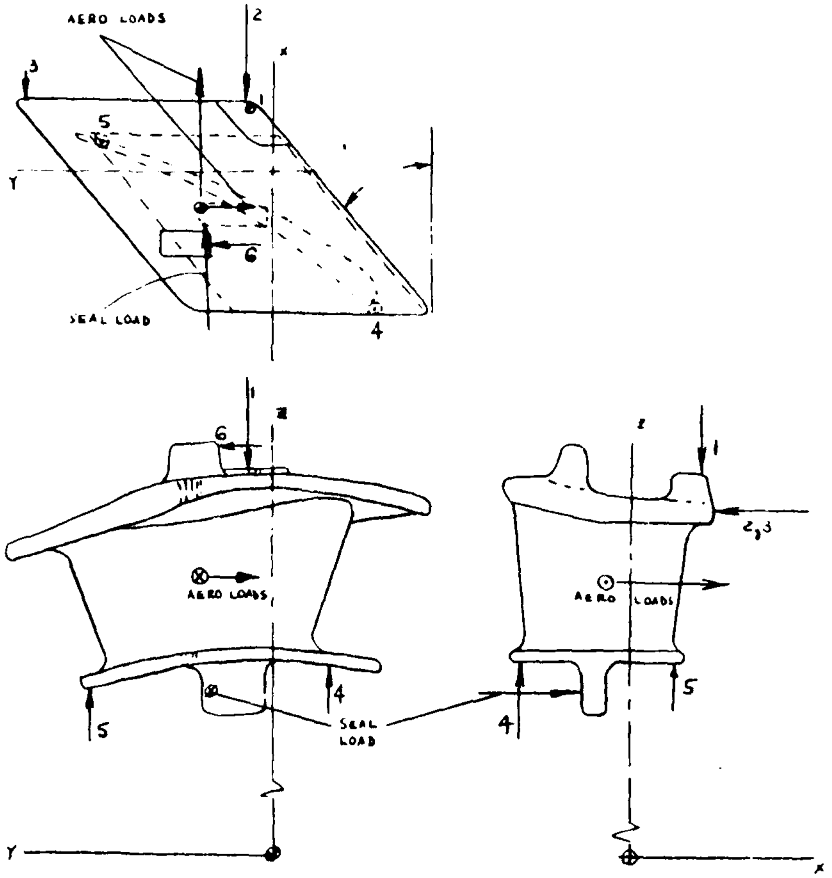

	LOCATION	LOADS, Lb (*)			
	LOAD CASE →	1	2	3	4
APPLIED LOADS	AERO LOAD (X)	34.21	34.21	34.21	34.21
	AERO LOAD (Y)	13.05	13.05	13.05	13.05
	SEAL LOAD	0	16.00	60.80	101.33
REACTIONS	1	17.79	45.61	98.16	145.70
	2	26.85	43.89	85.51	123.18
	3	5.55	6.31	9.49	12.36
	4	3.67	21.76	55.92	86.82
	5	14.11	23.85	42.24	58.88
	6	13.05	13.05	13.05	13.05

(*) LOAD DIRECTIONS AS SHOWN

CASE 1: AERO LOAD ONLY
CASE 2: AERO LOAD + EQUAL SEAL LOAD
CASE 3: AERO LOAD + 1/5 TOTAL SEAL LOAD
CASE 4: AERO LOAD + 1/3 TOTAL SEAL LOAD

Figure 2-28. Free-Body Diagram and Load Reactions for the First-Stage Stator.

emphasis was placed on obtaining an equal load-sharing distribution between the stators.

To accomplish this, the dimensioning and tolerances were tightened on controlling datum surfaces, and the complete stator assembly was specified to be set up in a fixture so that the critical contact surfaces were machined as an assembly. As a further safeguard, compliant material was used to improve the load distribution.

Two other design changes were made, based primarily on results from the static structure rig tests. The first change was to increase the effective contact length of the antirotation lugs from 0.040-inch to 0.105-inch to help eliminate chipping problems and to increase the load-carrying capability of the lugs. The second change was to increase the inner-platform thickness from 0.070 inch to 0.090 inch to increase the load-carrying capability.

The free-body diagram and load reactions for the second stage stator are shown in Figure 2-29 and Table 2-9. Very high contact loads could occur at the interface of the stator platform and the turbine shroud if the full load were carried by only three vanes. The second-stage stator vanes were modified similarly to the first-stage vanes, including machining of the assembly and use of a compliant interface material to decrease the risk of three vanes supporting the whole axial load.

2.5.3 TURBINE STATOR AND SHROUD SUPPORT DESIGN

The purpose of the turbine stator and shroud support (shown in Figure 1-2) is to radially position the turbine vanes and turbine shrouds in the engine and to prevent rotation of the stator vanes. Tabs on the outer platform of the vanes fit into slots in each end of the turbine stator and shroud support.

The turbine stator and shroud support is positioned radially by the metal structure of the engine. A radial pin joint was designed to position the ceramic cylinder in the metal cylinder without restricting thermal expansion in the radial direction.[3,8]

Peak tensile stress for the turbine stator and shroud support structure was determined analytically to be 11.5 ksi. Peak tensile stresses under several operating conditions are summarized in Figure 2-30.

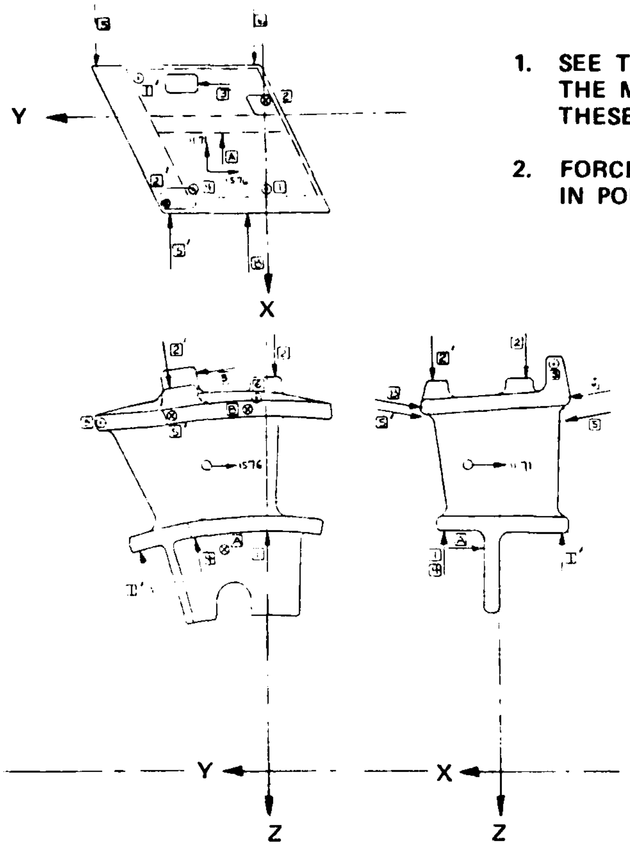

1. SEE TABLE 2-2 FOR THE MAGNITUDES OF THESE REACTIONS
2. FORCES SHOWN ARE IN POUNDS FORCE

Figure 2-29. Free-Body Diagram for the Second-Stage Stator.

Table 2-9. Load Reactions for the Second-Stage Stator.

		NO SEAL LOAD			EQUAL SEAL LOAD			1/3 SEAL LOAD		
		NO STACK LOAD	EQUAL STACK LOAD	1/3 STACK LOAD	NO STACK LOAD	EQUAL STACK LOAD	1/3 STACK LOAD	NO STACK LOAD	EQUAL STACK LOAD	1/3 STACK LOAD
LOADS	VANE AXIAL	11.7	11.7	11.7	11.7	11.7	11.7	11.7	11.7	11.7
	VANE TANGENTIAL	15.8	15.8	15.8	15.8	15.8	15.8	15.8	15.8	15.8
	SEAL (A)	0	0	0	21.6	21.6	21.6	122.2	122.2	122.2
	STACK (B)	0	56.1	317.8	0	56.1	317.8	0	56.1	317.8
REACTIONS	1	–	6.9	80.5	16.5	22.0	81.0	127.7	133.1	158.7
	2	5.4	–	–	23.0	13.5	–	123.7	114.1	69.7
	3	12.6	11.7	5.9	12.6	11.3	5.4	10.7	9.5	3.4
	4	7.9	34.1	142.5	15.2	20.9	10.5	23.2	28.9	55.5
	5	–	2.5	21.7	1.4	6.8	27.8	16.6	22.0	47.1
	6	17.0	66.5	31.3	32.4	84.1	329.2	119.6	171.2	412.3
	1′	4.2	–	–	–	–	–	–	–	–
	2′	–	15.5	100.8	–	–	59.4	–	–	–
	5′	5.1	–	–	–	–	–	–	–	–

- ALL LOADS AND REACTIONS ARE IN POUNDS FORCE

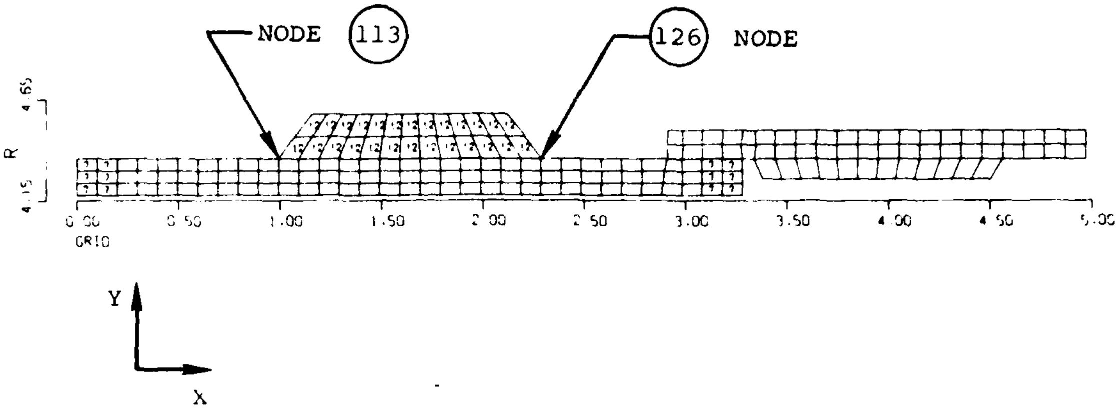

CONDITION	MAXIMUM PRINCIPAL STRESS (KSI)	NODE LOCATION	PROBABILITY OF SUCCESS
STEADY-STATE	11.5	126	99.99
TYPICAL START-UP TIME = 121.14 SEC	4.3	126	99.99
TYPICAL SHUT DOWN TIME = 5 SEC	10.8	113	99.94

MATERIAL: REACTION-BONDED SILICON NITRIDE

Figure 2-30. Thermal Stress Analysis Results for the Turbine Stator and Shroud Supports.

2.5.4 TURBINE SHROUD DESIGN

The turbine shrouds provide the tip seal for the rotor blades. Several configurations were considered, including a solid ring, a segmented ring, and a ring with a single slot.[32] The multi-segment ring was deleted to avoid the problem of retention. The other two configurations were analyzed using properties for typical reaction-bonded Si_3N_4.

The highest tensile stresses occurred during the start-up transient 122 seconds after lightoff and resulted from the interference with the shroud support, the radial gradient through the shroud, and the temperature differential between the shroud and the support. The predicted peak tensile stresses were 13.9 and 6.6 ksi, respectively, for the solid and slotted-ring configurations. The slotted configuration was selected. Analysis for the most severe case anticipated in the engine--the start-up transient with a hot streak 400°F above the average--predicted a peak stress of 9.1 ksi. This was considered acceptable, and prints were released for fabrication.

2.5.5 TURBINE STATOR INNER SUPPORT DESIGN

The turbine stator inner supports grip the tangs on the inner platform of the stator vanes to provide positioning and support. Both start up and shutdown transients were evaluated. The most severe stress was found to occur 130 seconds after light-off. Peak tensile stresses for several conditions are shown in Figure 2-31. These stresses were low in each case, and the probability of success for the component was high.

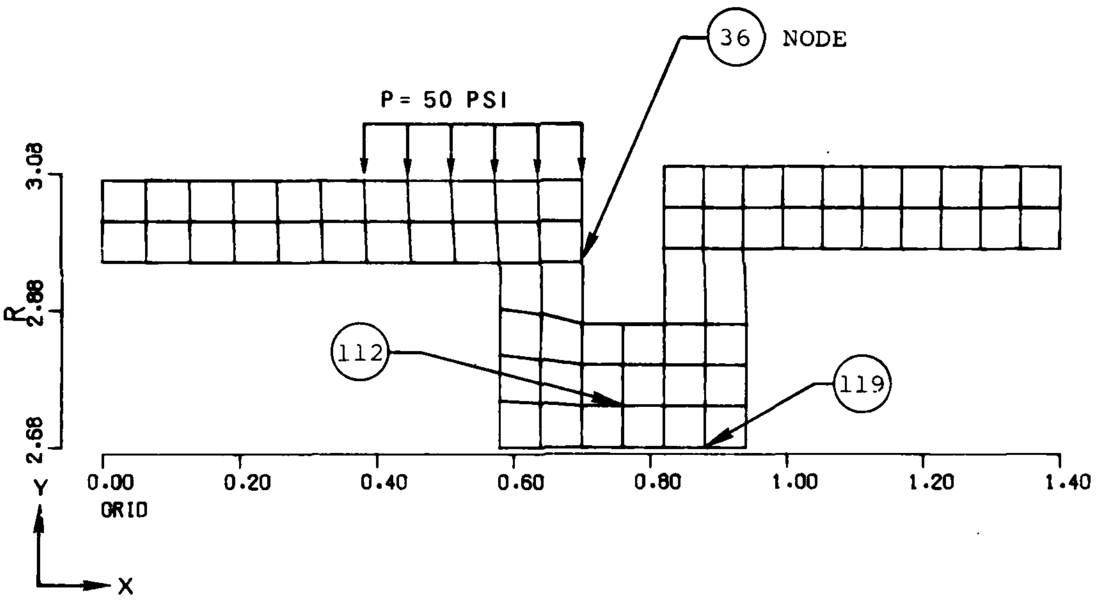

CONDITION	MAXIMUM PRINCIPAL STRESS (KSI)	NODE LOCATION	PROBABILITY OF SUCCESS
STEADY-STATE	6.1 (TANGENTIAL)	112	99.99
TYPICAL START-UP TIME = 130 SEC	8.4 (TANGENTIAL)	119	99.99
TYPICAL SHUT DOWN TIME = 5 SEC	5.9 (RADIAL)	36	100.00

MATERIAL: REACTION-BONDED SILICON NITRIDE

Figure 2-31. Thermal Stress Analysis Results for the First-Stage Stator Inner Support.

2.5.6 CERAMIC COMBUSTOR AND TRANSITION LINERS

The initial design specified ceramics for the combustor and transition liners of the TSE331C-1 engine. However, as the program progressed, it was determined that metal components could be used with less program risk. Before changing to metal, considerable design was conducted on the ceramic configurations. This work will not be discussed here, but is detailed in the references.[3,4,33]

2.5.7 EMERGENCY SHUTDOWN ANALYSIS

Due to the possibility of a component failure or inadvertent fuel stoppage, the effect of an extremely rapid or emergency shutdown on the thermal stress magnitude of all the static ceramic components was investigated.[4] Figure 2-32 shows the rotor speeds and first-stage stator inlet temperatures used in the investigation. Shown for comparison is the typical shutdown schedule. A 15-second rolldown to zero speed and virtually instantaneous decrease in turbine inlet temperature was assumed for the emergency shutdown based upon baseline metal engine characteristics. These parameters were used in the thermal computer programs for all of the ceramic structure components to predict component temperatures throughout the shutdown

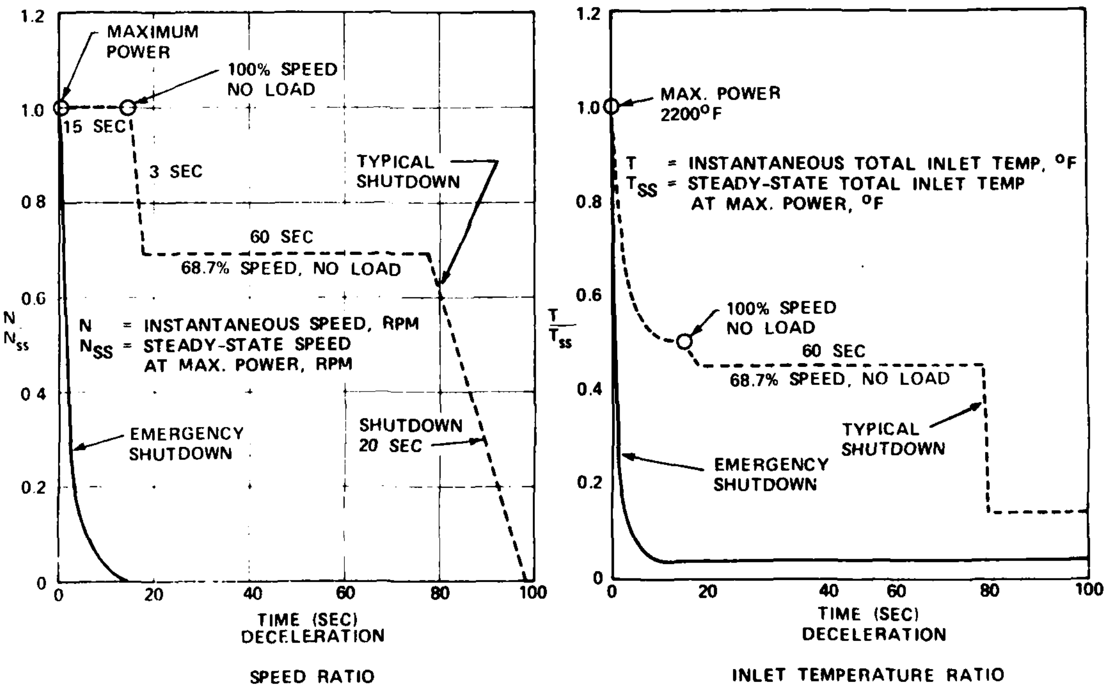

Figure 2-32. Emergency Shutdown Schedule.

period. The most severe thermal gradients were then used to compute thermal stresses for each of the ceramic components.

The most severe stresses were found to occur in the first stage stator at 5.7 seconds after shutdown. At this condition the vane temperatures dropped below the platform temperatures, creating a radial thermal gradient opposite to that occurring during the start-up or steady-state condition. As a consequence, the maximum tensile stresses within the vane were no longer at the trailing edge but occurred at the midchord region and at the leading edge of the vane outer fillet radii. The maximum principal tensile stress predicted was 18.6 ksi and resulted in a probability of success >99.99 percent. Thermal gradients in the second-stage stator were lower and resulted in a peak stress of only 14.9 ksi.

Thermal stresses in all the other components during the emergency shutdown were calculated to be less than for the normal startup transient condition. Therefore, the emergency shutdown was determined not to be a limiting condition for the operation of the TSE331C-1 engine.

476 +/

3.0 CERAMIC COMPONENT PROCESS DEVELOPMENT

The ceramic engine design resulted in a requirement for more than 100 separate ceramic parts per engine build, ranging from small complex stator vanes and rotor blades to large but simple cylindrical shrouds and pilot structures. Silicon nitride parts of comparable complexity or size were not available from commercial sources. This section describes the development efforts conducted at subcontractors and at Garrett. To assure the best chance for obtaining qualified engine components within the time constraints of the program, multiple sources and processing approaches were pursued for each component.

3.1 CERAMIC ROTOR BLADE FABRICATION DEVELOPMENT

A hybrid rotor concept consisting of ceramic rotor blades inserted into a superalloy disk resulted from the 3-D finite element design analyses. Several factors were considered in selection of rotor blade material and the fabrication approach:

1. The blade was the highest stress (~44 ksi in the attachment) ceramic part in the engine

2. Only hot-pressed ceramic material had the required strength

3. Technology was not available to make complexly shaped blades by hot pressing

Based on these factors, a minimum-risk approach of machining rotor blades from strength-certified flat plate billets of hot pressed Si_3N_4 was selected. NC-132 hot pressed Si_3N_4 manufactured by the Norton Company, Worcester, MA was chosen as the blade material due to its high strength (reported 4-point bend strength consistently over 100 ksi) and relatively good record of reproducibility.

Rotor blade development was conducted in two stages. The first stage consisted of machining of the attachment region and conducting spin tests to evaluate the material capability in the as-machined configuration to withstand design rotational stresses. The second stage was to develop the tooling and procedures to machine the airfoil and platform.

3.1.1 ROTOR BLADE ATTACHMENT MACHINING

Attachment machining was conducted at Norton Company by form wheel grinding, at Arthur Crafts Company by contour grinding (under contract to Norton Co), and at Western Gold and Platinum Company (WESGO) and at Garrett by profile grinding. Ultrasonic machining was implemented at Garrett as a roughing operation to decrease labor time and cost.

Contour grinding was performed with a manual machine equipped with a shadow lamp which projected an enlarged image of the work piece and grinding wheel on a screen. By matching this projection to a mylar print of the required contour, the operator was able to achieve very close tolerances. Rough machining was conducted at a downfeed of 0.0005 inch per pass and finishing at 0.0002 inch per pass with a finer grit diamond wheel. Residual grinding grooves were aligned in the axial direction of the attachment and would be perpendicular (transverse) to the maximum tensile stress during engine operation. As discussed in a later paragraph (4.1.1), perpendicular alignment of grinding grooves to the stress direction results in decreased strength because a larger surface flaw is present in this orientation. In an effort to minimize the size of the residual machining flaws, contour-ground blade attachments were lapped using very fine diamond powder and a shaped balsa wood form. Test bars (0.125 by 0.125 inch in cross-section) were machined using the contour grinding setup and were strength tested in 4-point bending with an outer span of one inch and an inner span of 0.5 inch. The as-machined specimens had a measured strength of 63.5 ksi compared to 72.1 ksi for lapped specimens.*

The Norton Company conducted form wheel grinding studies. A series of shaped grinding wheels were used in a sequence operation to achieve the final dimensional tolerances and surface finish of test samples. The sequence ranged from rough machining with a 60-grit diamond wheel where approximately 0.080-inch depth of material could be removed per pass to finish machining with a 900-grit wheel where only about 0.0002 inch could be removed per pass. Feasibility was demonstrated, but delays were caused by some tooling problems. To meet program timing requirements, the contour machining approach was selected for blade machining by Norton.

---

*An oxidation treatment of 50 hours at 1800°F was developed, which increased the strength of transverse machined NC-132 to approximately 95.0 ksi. This is discussed in Paragraph 4.1.2.

WESGO machined attachment spin-test specimens and blade attachments using a combination of form-wheel grinding and single-spindle, numerically-controlled profile grinding. With profile grinding, the machining grooves were in the radial direction, parallel to the maximum stress, and were less detrimental to strength. To be conservative, though, the attachment area was also lapped and exposed to the beneficial oxidation treatment.

Garrett conducted both attachment and airfoil machining process development studies using a Gorton P2-3 Pantograph Profile Grinder. The pantograph was modified to operate at high tool speed in order to achieve an improved cutting rate, reduced tool wear, and higher as-machined strength of the ceramic material. The modification consisted of replacing the mechanically driven spindle, capable of 12,000 rpm, with an airturbine-driven spindle, capable of 60,000 rpm. This resulted in an increase in as-machined strength from 73 to 84.5 ksi. Later, the spindle capability was increased to 100,000 rpm, further increasing the bend strength to 98.8 ksi. An additional 20 percent improvement was achieved by the 1800°F/50 hour oxidation-treatment.

The Garrett setup for grinding the attachment and bottom surface of the blade platform is shown in Figure 3-1. The 8:1 master made it possible to achieve the required tolerances of ±0.0002 inch.

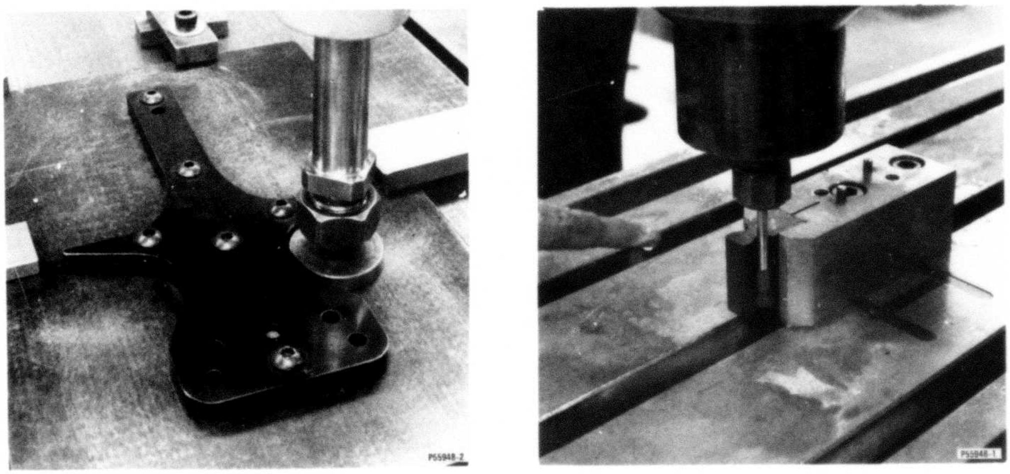

Figure 3-1. Blade-Attachment Grinding at Garrett.

3.1.2 ROTOR AIRFOIL MACHINING

Rotor airfoil machining development was conducted at Garrett and at Norton Company.

Initial airfoil machining studies by Norton were conducted at Excello Company using the same cam-grinding techniques previously employed to produce the large Westinghouse 3-D stator airfoils under contract DAAF-46-72-C-0162.[37] By modifying the setup to a cantilevered configuration, feasibility was demonstrated. However, due to their workload in other areas, Excello chose not to continue. Norton then selected Jarvis Company to machine the airfoil with a spindle-type profile grinder. Jarvis was successful and became a qualified source for rotor blades.

Complete rotor blades were successfully machined at Garrett using the pantograph profile grinder. Figure 3-2 shows a blade airfoil being machined and a group of completed blades.

Blade machining by profile grinding was slow and expensive. Ultrasonic trepanning was evaluated at Garrett to rough out the attachment and airfoil and

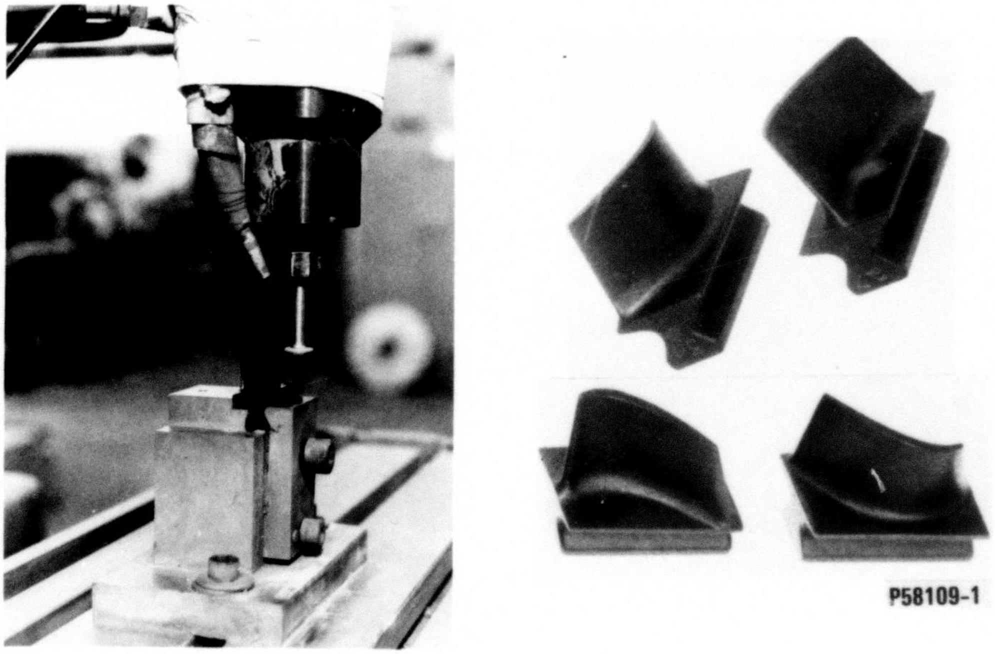

Figure 3-2. Rotor Blade Machining at Garrett.

minimize the stock removal required by profile grinding. A schematic for ultrasonic machining is shown in Figure 3-3. The ultrasonic transducer vibrates a thin-walled tool (having the shape of the desired cut) at a high frequency. A slurry of carefully sized boron carbide abrasive in water is sprayed onto the vibrating tool. Cavitation effects distribute the slurry uniformly over the surface of the tool. When the tool is moved into contact with the ceramic workpiece, the individual boron carbide particles are accelerated by the ultrasonic frequency to high velocity impact against the ceramic at the tool tip. A cutting rate of about 0.010 inch per minute was achieved with the hot-pressed Si_3N_4.

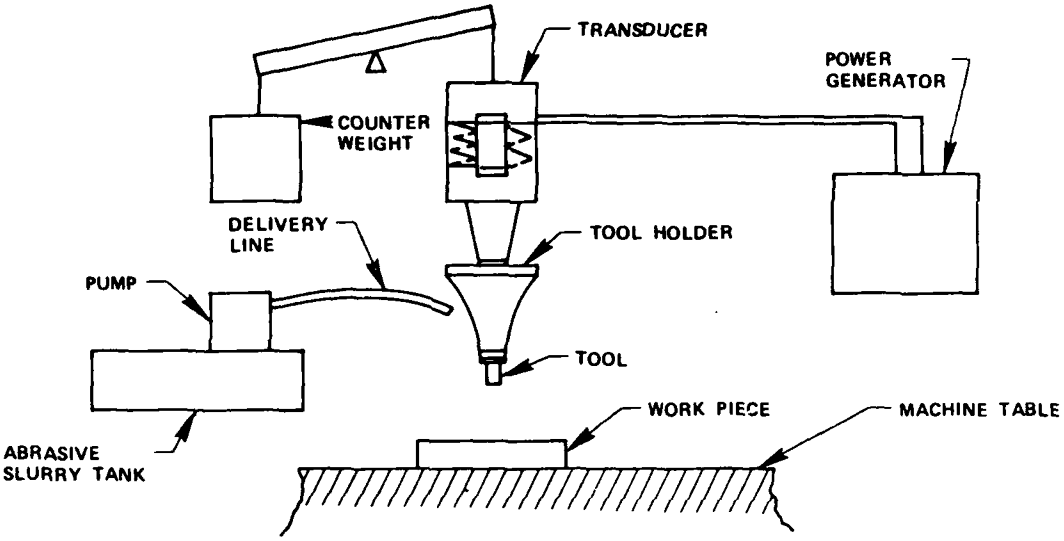

Figure 3-3. Schematic Illustrating Ultrasonic Machining.

Ultrasonic trepanning was successfully used to decrease the time and cost of both attachment and blade machining as illustrated in Figure 3-4. First, the blade attachment region was ultrasonically machined to within 0.010 inch of final dimensions. Then, in a second pass with a different tool contour, the blade airfoil envelope was ultrasonically machined.

3.1.3 ROTOR BLADE SPIN TESTING

Room temperature and 1300°F spin-pit tests were conducted in parallel with the blade fabrication development.[3,38] These tests had several critical objectives:

1. Evaluate the material capability in the component configuration exposed to a stress distribution simulating that of the engine

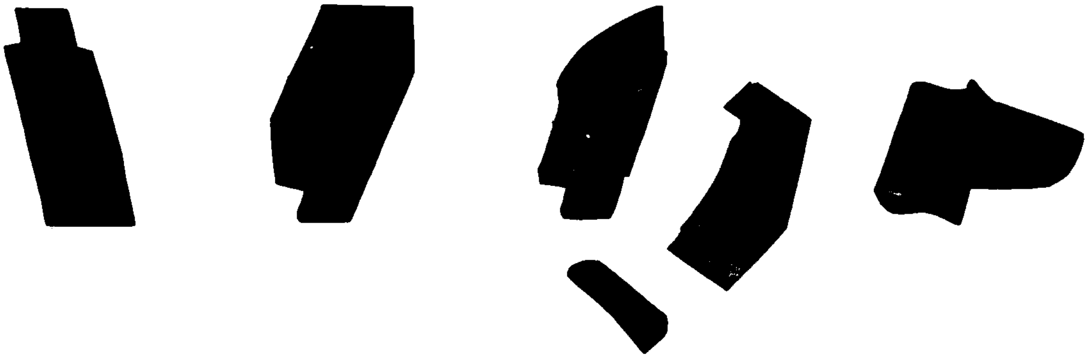

Figure 3-4. Reduced-Cost Blade Machining Using Ultrasonic Trepanning and Pantograph Profile Grinding.

2. Evaluate the validity of the probabilistic design approach

3. Evaluate metallic compliant layers for use between the ceramic blade and the metal disk

4. Proof test blades prior to their use in rig and engine testing

Spin testing was conducted in the Garrett spinpit facility using an air-motor drive and a rigid shaft. The ceramic test specimen was inserted into a superalloy disk mounted on the shaft as shown in Figure 3-5. Dummy weights were mounted adjacent to the blade to simulate the stress distribution of a fully bladed rotor. Testing was conducted at room temperature and 1300°F using several test specimen configurations. Heating was achieved with six 100 watt quartz lamps. Results of testing are summarized in Table 3-1.

Only two failures occurred during the 36 tests. To obtain data on the limitation of the hot-pressed Si_3N_4 and to better evaluate the accuracy of the probabilistic design, the -2 specimen configuration was modified by machining the attachment axial length from 1.0 inch to 0.5 inch. This -2C configuration is shown schematically in Figure 3-6. Analysis indicated that this configuration could be spin tested to failure routinely within the 60,000 rpm operation limit of the spinpit. The test results are compared in Figure 3-6 with probabilistic predictions based upon baseline material property data. The correlation is excellent, providing strong evidence that the

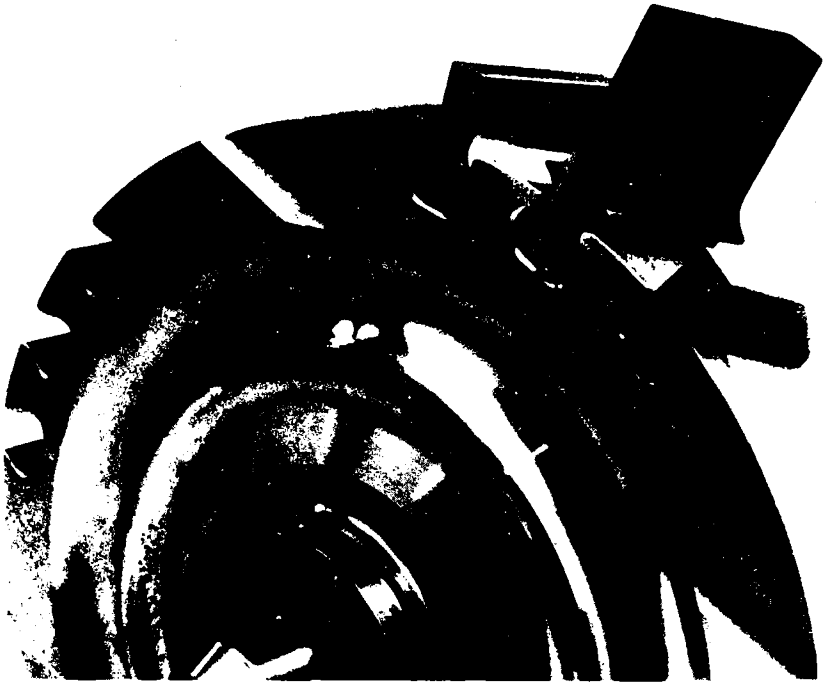

P57316-2

Figure 3-5. Attachment Assembly for Spin Testing.

TABLE 3-1. SUMMARY OF ATTACHMENT TEST RESULTS.

					% ENGINE DESIGN STRESS*		
NUMBER OF SPECIMENS TESTED/FAILED	SPECIMEN TYPE	MAXIMUM RPM	TEMP. °F	% EQUIV. DESIGN SPEED*	AVE.	PEAK	CRUSHING
10/0	–2	48,500	RT	135	230	180	224
18/2	–2	45,300	1300	134	200	155	170
8/0	–2B	48,500	RT	145	230	251	224

*BASED ON SECOND STAGE BLADE ATTACHMENT AT 41,730 RPM DESIGN SPEED WHICH WOULD HAVE AN AVERAGE NECK STRESS OF 14.1 KSI, A PEAK NECK STRESS OF 41.9 KSI AND A COMPLIANT LAYER CRUSHING STRESS OF 55 KSI.

probabilistic design approach developed at Garrett was appropriate for rotor blade design. Peak stresses in the -2C attachment ranged from 98.8 ksi to 133.7 ksi (236 to 319 percent of engine design stress) and clearly demonstrated that the ceramic material had adequate strength margin.

As rotor blades became available from the process development efforts, they were oxidized at 1800°F for 50 hours and then proof-tested in the spin pit at room temperature at 130-percent design speed (169 percent design stress). The results are

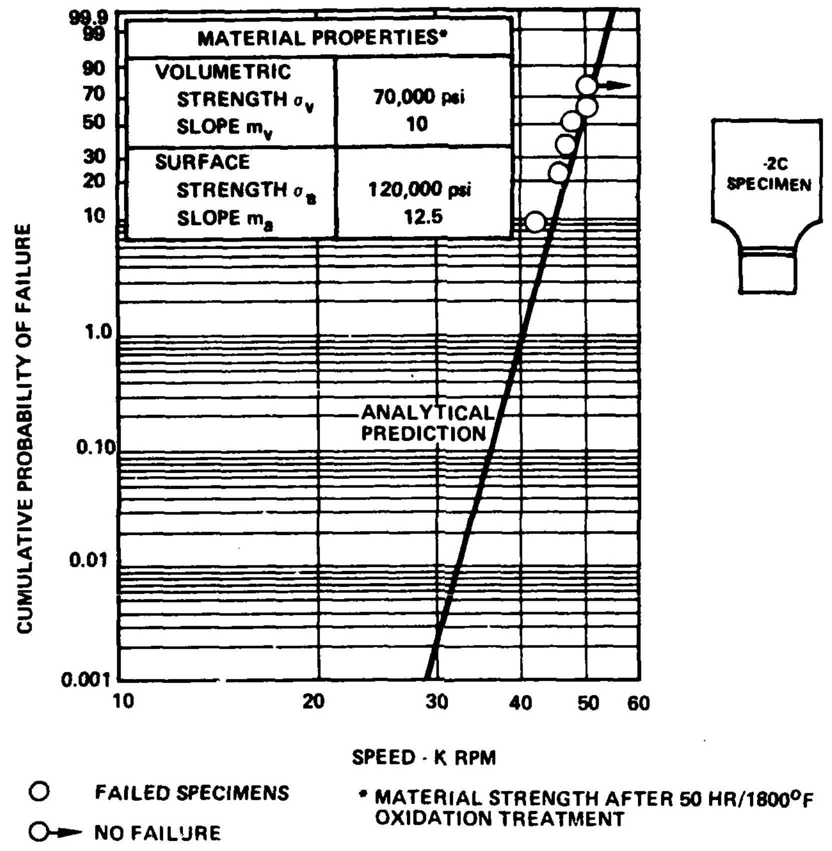

Figure 3-6. Results of -2C Specimen Spin Testing.

summarized in Figure 3-7. Six blades out of 205 failed the proof test. Analysis had predicted a 3-percent failure rate. This provided further verification of the probabilistic design approach and qualified rotor blades for rig and engine testing.

Attachment testing identified some potential problems with blade compliant layers. Platinum was initially selected as the prime candidate based upon successful testing at Pratt and Whitney Aircraft Company.[31] However, during attachment tests, the platinum decreased in thickness, especially under cyclic testing and at 1300°F. At 1300°F and 130 percent of the crushing load expected on the compliant layer in the engine, the platinum reduced in thickness from 0.0048 inch to 0.0015 inch after 8 cycles to 51,500 rpm. An alternate material, HS25 cobalt-base alloy, only reduced in thickness from 0.0059 to 0.0054 inch in 25 cycles under the same conditions. In another cyclic test at higher contact stress, the platinum compliant layer thinned to zero thickness during the 49th cycle and resulted in blade fracture. Based on these tests, HS25 was selected as the compliant layer for initial rig tests.

3.1.4 ROTOR BLADE PROCESSING SUMMARY

Figure 3-8 shows the flow chart that was identified for successful material certification, blade fabrication and blade spin-pit proof testing. By following the procedures outlined in this chart, high quality rotor blades were routinely qualified for rig and engine testing.

3.2 CERAMIC STATOR FABRICATION DEVELOPMENT

The stator configuration was defined by aerodynamic, thermal, and stress analyses and consisted of single vane segments of reaction-bonded Si_3N_4 (RBSN) assembled into a ring and piloted on the OD and ID by other RBSN support structures. Three sources were selected for stator fabrication development:

- AiResearch Casting Company (ACC) - slip casting, injection molding,and process improvement
- Ford Motor Company - injection molding
- Norton Company - isostatic pressing and machining, and process improvement

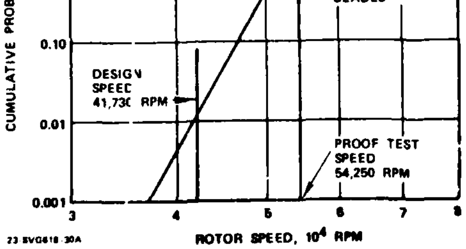

Figure 3-7. Results of Rotor Blade Proof Testing at 130 Percent Overspeed Condition.

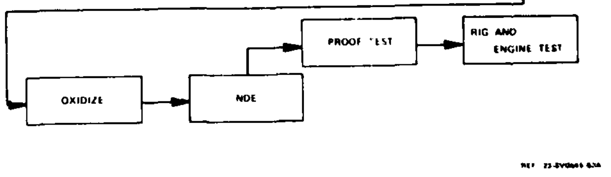

Figure 3-8. Flow Chart for Rotor Blade Processing and Qualification for Rig and Engine Testing.

Parallel development at more than one source was deemed necessary because of the limited development time available in the program and because the two potential commercial sources (Norton and ACC) had not previously fabricated complex shaped stator vanes. Ford Motor Company had previously developed the capability to fabricate single stator vanes and integral stators[39] but decided not to become a major supplier of development parts under the Garrett program.

3.2.1 ACC SLIP CASTING STATOR DEVELOPMENT

Slip casting is a process wherein a material is prepared in powder form and mixed in a liquid medium, usually aqueous. Other ingredients are added in small quantities and serve as deflocculents to keep the solid particles in suspension. The slip is then poured into a mold that provides the shape the part is to assume and also provides a means of extracting the liquid. After drying in the mold, the part is removed and subjected to thermal treatment to achieve its final form. Figure 3-9 is the ACC flow chart showing the pertinent steps in the slip casting of silicon and production of their RBN-101 reaction-bonded silicon nitride components.[7,40]

Starting silicon powders were obtained from Kawecki Berylco Industries Inc. and Union Carbide Corporation and subjected to chemical analysis, particle size

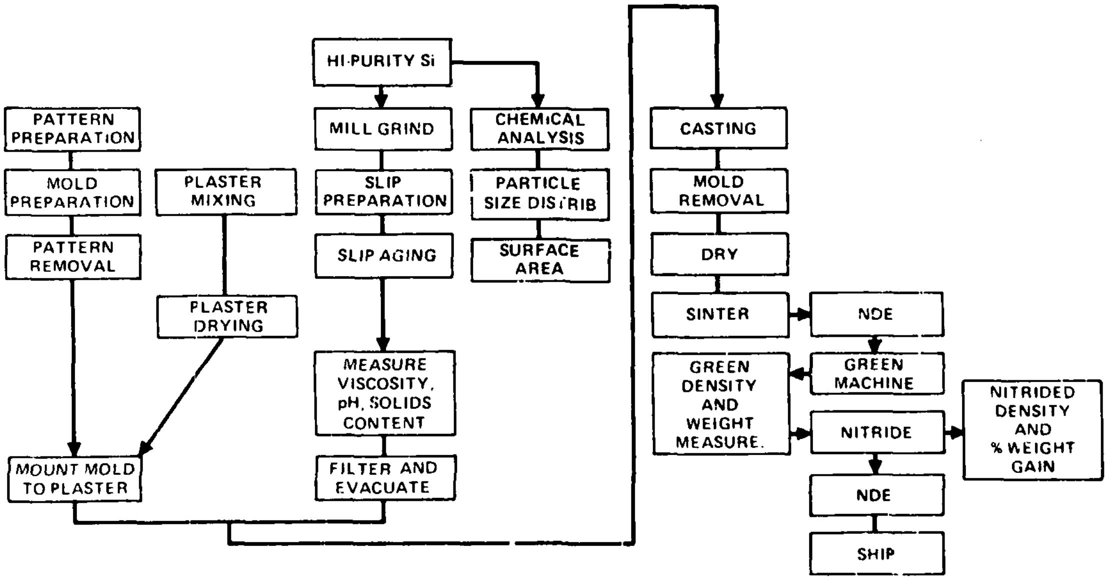

Figure 3-9. Process Steps at ACC for Slip Casting of Silicon to Produce Reaction-Bonded Si_3N_4.

distribution analysis and surface area determination. To obtain optimum particle size distribution for slip casting, the silicon powder was milled dry in an Al_2O_3 ball mill with high purity Al_2O_3 grinding media for 12 to 24 hours. Three percent iron oxide or chromium oxide was added during milling to act as a nitriding aid during the later step of converting the silicon to Si_3N_4.

Milled silicon powder was mixed with de-ionizd water to produce a slip containing 75 percent by weight of solids. One cc per liter of water of monoethanolamine was added as a deflocculent. The slip was thoroughly mixed and allowed to age for appproximately five days. The aging was necessary to complete outgassing that occurred due to chemical reaction between the silicon and water.

Stator vanes were cast into wax molds made by the fugitive wax process developed at Ford Motor Company.[41,42] The mold-making procedure for a second stage TSE331C-1 vane at ACC is illustrated in Figure 3-10. A water-soluble wax in the shape of the stator vane was injection molded. This pattern was attached to a cone shape and dipped in a non-water-soluble wax. The water-soluble wax was dissolved, leaving a hollow mold of the stator and a funnel into which the slip could be poured. The edge of the vane shroud opposite the funnel was trimmed open and mounted against a plaster block. Slip was poured into the stator mold via the funnel. Water was extracted by capillary action through the plaster resulting in a buildup of silicon particles in the mold. When the casting was complete, the mold was removed by dissolving in a solvent such as trichlorethylene, leaving the fragile silicon shape. This was then dried, sintered, and nitrided to produce a near-net-shape reaction bonded Si_3N_4 stator vane.

Parametric process development was conducted parallel to component fabrication development in an effort to improve the strength and oxidation resistance of the RBSN. Progress was monitored through strength testing, fracture analysis, and microstructure examination. Test bars were cast and processed with each batch of components to provide a means of material certification. As the program progressed, a fixed process was defined and a specification written. Four-point bend strength of the RBN-101 RBSN material was typically in the range of 30-35 ksi, and density was approximately 2.7 $g/cm.^3$

3.2.2 ACC INJECTION MOLDED STATOR DEVELOPMENT

Injection molding studies were just beginning at AiResearch Casting Company (ACC) at the start of the program, so a longer development effort was required to

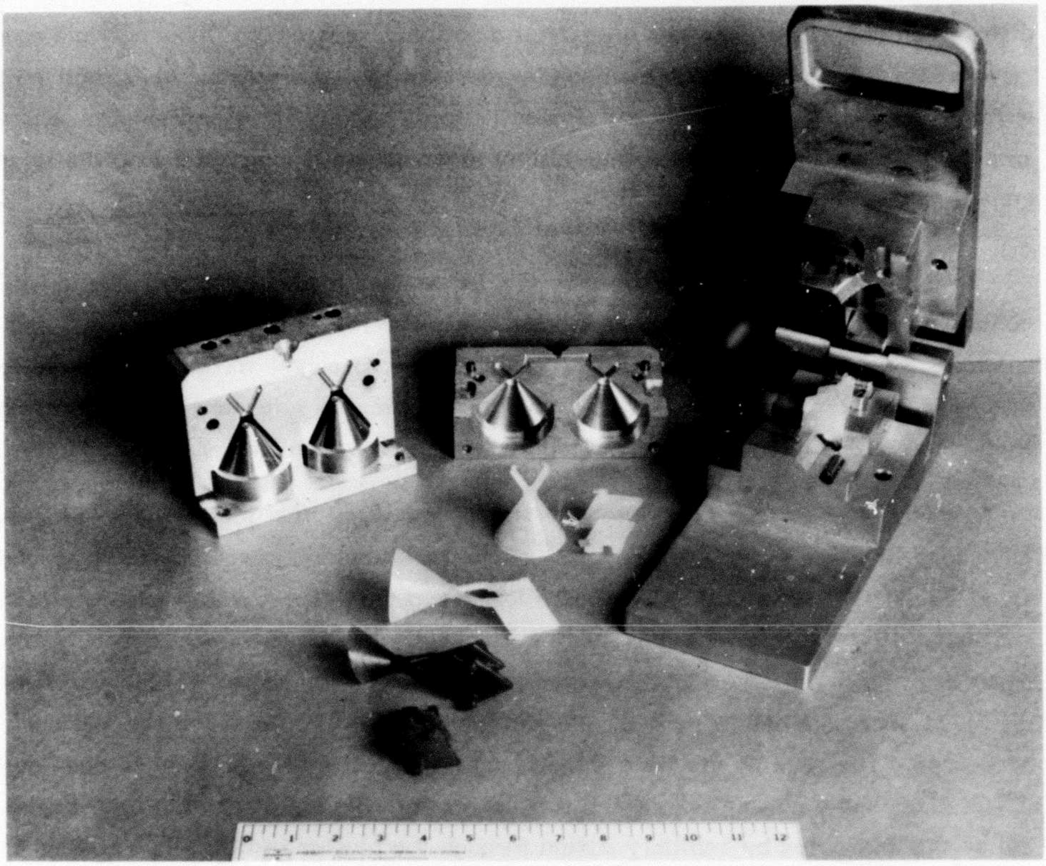

Figure 3-10. Tooling and Steps in the Fabrication of a Wax Mold for a TSE331C-1 Stator Vane at ACC.

achieve quality stator vanes, acceptable properties, and a fixed-process specification. However, the effort was successful and resulted in high quality stator vanes of an RBSN designated RBN-122, having average strength typically over 30 ksi.[7,40]

Injection molding is a process wherein a material in a plastic state is injected under pressure into a cavity of a desired configuration. When set, the injected material is rigid, and the shape may be removed from the mold. The process for making a ceramic turbine component by injection molding, while not simple, is less complicated than the slip-casting method. The flow chart in Figure 3-11 shows the various steps that are taken at ACC to injection-mold and nitride RBN-122 RBSN.

ACC systematically varied the major injection-molding parameters in an effort to produce the complex TSE331C-1 stator vane configuration and simultaneously to achieve acceptable properties. The major injection-molding parameters considered

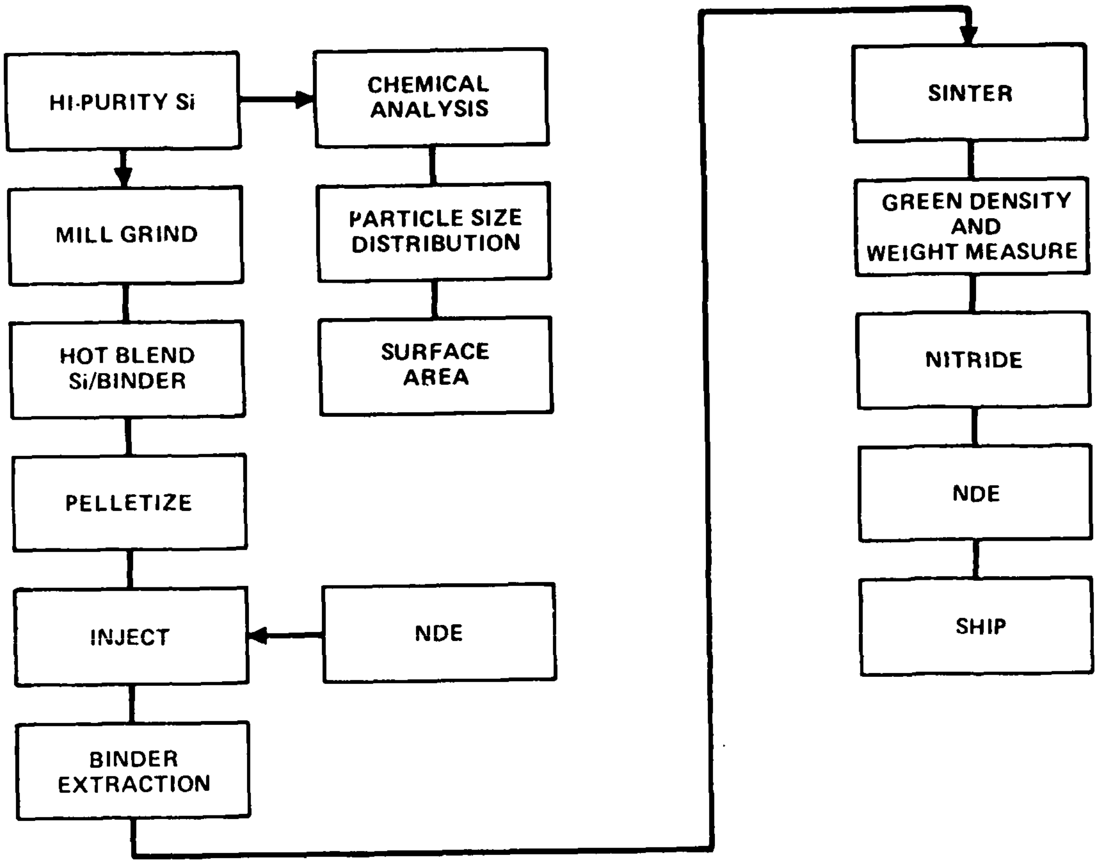

Figure 3-11. Process Chart Showing the Steps in Fabrication of RBN122 RBSN at ACC by Injection Molding.

included the ratio of solids to organic carrier, powder characteristics, injection temperature, injection speed, injection pressure, holding time, and holding pressure.

Temperature control was particularly important during the injection-molding cycle. Temperature had to be controlled in the feed chamber, in the plasticizing chamber, in the injection nozzle, and in the mold. For example, temperature in the nozzle was varied from 150°F to 200°F. Below ~170°F the solid-plastic mix was not fluid enough to properly fill the mold, resulting in pores and knit lines. In the range of ~170°F to 185°F, void-free parts were successfully injection molded. Above ~185°F, voids and blistering began to appear.

Injection speed and pressure were also important. A high injection rate was selected. This helped avoid chilling of the mix by the mold and allowed complete filling of the mold before solidification. High pressure was also beneficial in achieving complete mold fill and helping to heal flow lines before solidification of the plastic binder.

Test bars for strength measurement and other property characterization studies were injection molded with each stator vane. The tooling is shown in Figure 3-12. A group of vanes and test bars is shown in Figure 3-13.

The quality of the injection-molded stator vanes was as excellent as with vanes produced by slip casting. A complete engine set of injection-molded stator vanes is shown in Figure 3-14.

3.2.3 FORD MOTOR COMPANY INJECTION MOLDED STATOR DEVELOPMENT

Ford Motor Company was also selected to fabricate stator vanes by injection molding. Ford had substantial prior injection-molding experience of RBSN and a well-defined composition. Therefore, this effort was essentially a "parts buy" and was not of a scope to allow much development. Its purpose was to provide an additional backup to assure that some components would be available for early initiation of rig testing. Although some initial problems were encountered involving very small platform cracks and metallic contamination, Ford was successful in delivering high quality stator vanes.[43]

Temperature control was identified as the cause of the cracking. A study was made varying both material and tool temperature over a range of 205-285°F for the material and 80-100°F for the tool. Best results were obtained at a material

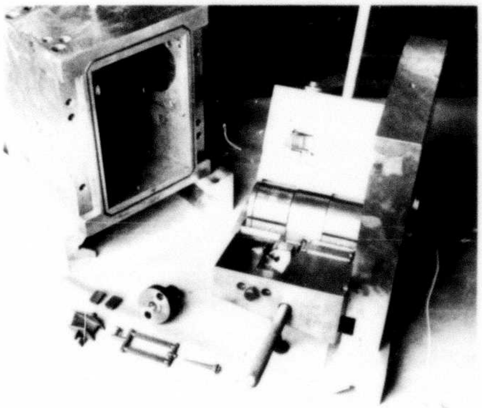

Figure 3-12. TSE331C-1 Stator Vane Injection Molding Tooling from ACC.

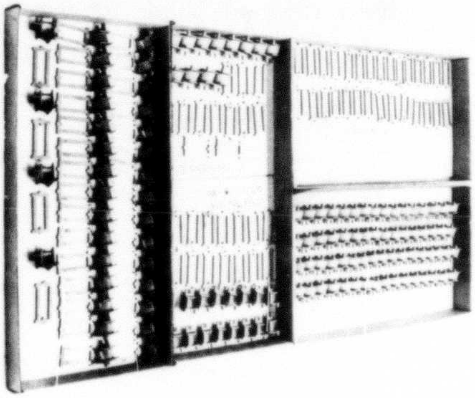

Figure 3-13. Injection Molded Stator Vanes and Test Bars from ACC.

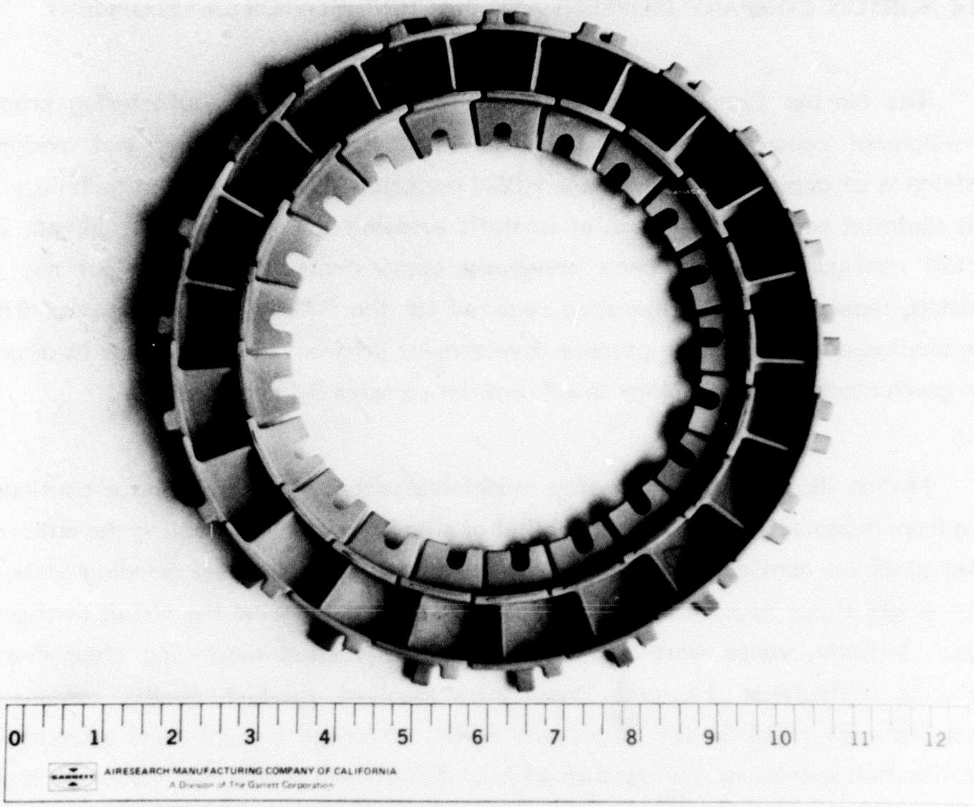

temperature of 195°F and a tool temperature of 80°F. Cracking decreased as these parameters were approached, with only one fine crack persisting at the trailing-edge inner platform. Measurements indicated that the tool temperature was lower in this region than in the rest of the tool. Heaters were installed in this area and another series of tests conducted holding the material temperature at 245°F. The best results were obtained with most of the tool operated at 80°F but with the rear platform area held at 90°F. A yield of about 20-percent crack-free vanes was achieved. Since funding was not available for further optimization these parameters were used to fabricate the 44 vanes needed for delivery to Garrett.

The injection molded stator vanes and representative strength test bars were nitrided (after binder extraction) using the nitrogen demand cycle shown in Figure 3-15. The characteristic strength ranged from 39.8 ksi with a Weibull slope of 12.1 to 43 ksi with a Weibull slope of 8.6.

4/6 +6

3.2.4 NORTON COMPANY ISOPRESS AND MACHINE STATOR DEVELOPMENT

The Norton Company was selected for stator vane manufacturing process development because their NC-350 RBSN had the best strength and oxidation resistance of commercially available RBSN materials. The fabrication technique for this material was a combination of isostatic pressing and machining.[36] Simple 2-D airfoil configurations had been previously demonstrated by Norton but not the twisted, tapered, 3-D configuration required for the DARPA/Navy program. Thus, the challenge of the stator process development program at Norton was to develop the green machining technology to achieve the complex 3-D contours.

Norton developed a multi-step machining process: (1) machine a continuous ring from an isostatically compacted billet of silicon powder, duplicating the outer and inner platform configurations with diamond-coated, formed-wheel grinding tools, (2) slice single stator segments from the ring, and (3) profile grind the airfoil configuration. Initially, vanes were damaged during the various machining steps due to fixturing difficulties. However, these were resolved and high quality vanes were produced with yields in the 90 percent range. Average 4-point bend strengths of certification specimens averaged 40-45 ksi. As-nitrided first-stage vanes are shown in Figure 3-16.

3.3 CERAMIC STATIC STRUCTURE PROCESS DEVELOPMENT

The term "static structure" will be used in this section to refer to all the ceramic parts other than the rotor blades and stator vanes. In the later sections on rig and engine testing, "static structure" will include the stator vanes. Ceramic combustor and transition liner development will not be discussed, even though considerable effort was expended prior to the decision to use metal hardware for these components.

Initial development of static structure hardware was conducted by ACC, Ceramic Systems, Inc. (CSI), and Norton. ACC and CSI supplied components of slipcast RBSN for evaluation of strength, uniformity, and oxidation stability. Norton supplied components of isopressed/machined RBSN. Norton and ACC were selected to fabricate hardware for rig and engine testing. Examples of completed ceramic hardware are shown in Figure 3-17.

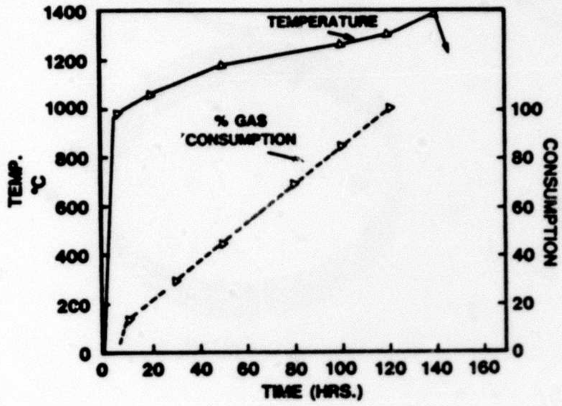

Figure 3-15. Ford Motor Company Nitrogen Demand Nitriding Cycles Used for TSE331C-1 First-Stage Vane Processing.

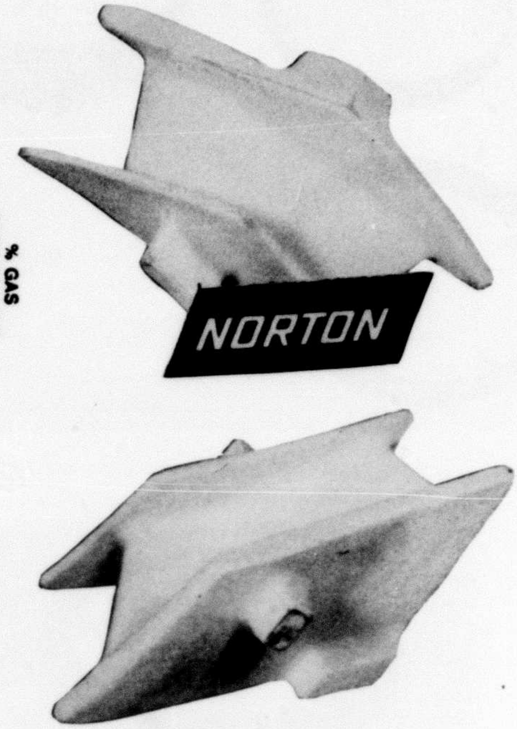

Figure 3-16. First-Stage Stator Vanes Fabricated Successfully at Norton Company by Isostatic Pressing and Machining.

3.4 MATERIAL IMPROVEMENT

In parallel to component fabrication development, effort was conducted at ACC and Norton to improve the properties of RBSN. Goals were to (1) achieve an average room-temperature 4-point bend strength of 40 ksi, (2) improve oxidation stability by increasing density, and (3) investigate methods of surface treating to reduce oxidation.

Strengths of the ACC and Norton materials were improved by systematic variation of key process parameters.[7,40,44] The ACC materials did not meet the 40 ksi goal but were consistently above 30,000 psi. The Norton NC-350 RBSN improved during the program and exceeded the 40 ksi goal. Strength data for component certification specimens is plotted versus date of fabrication in Figure 3-18.

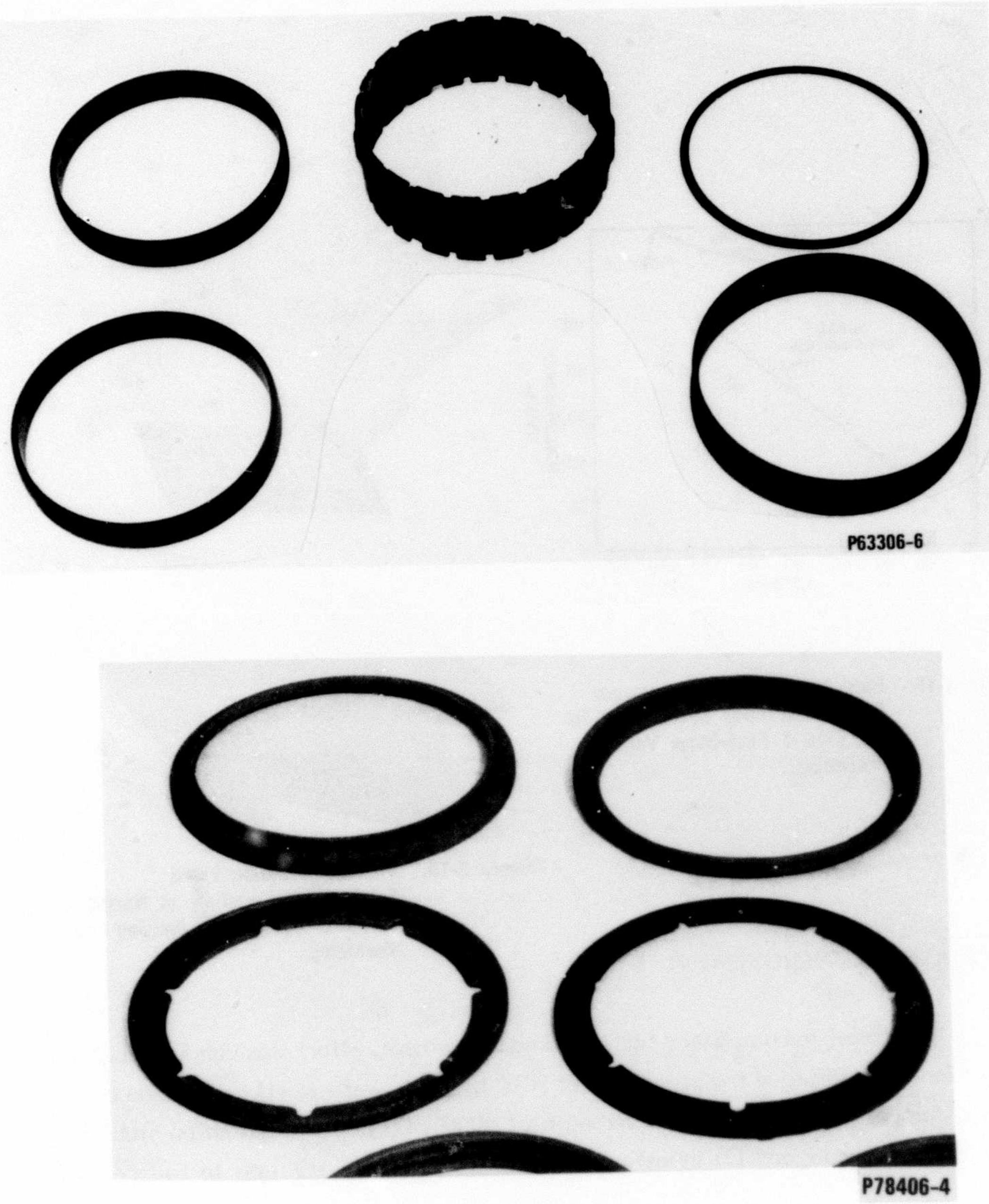

P63306-6

P78406-4

Figure 3-17. RBSN Static-Structure Components.

Both ACC and Norton successfully increased the bulk density of their RBSN materials. ACC materials were consistently above 2.65 g/cm.[3] The Norton NC-350 was increased from a typical value of 2.4 or 2.45 to greater than 2.5 g/cm.[3] A very fine-grained microstructure was maintained by Norton which resulted in excellent oxidation resistance.[15,45]

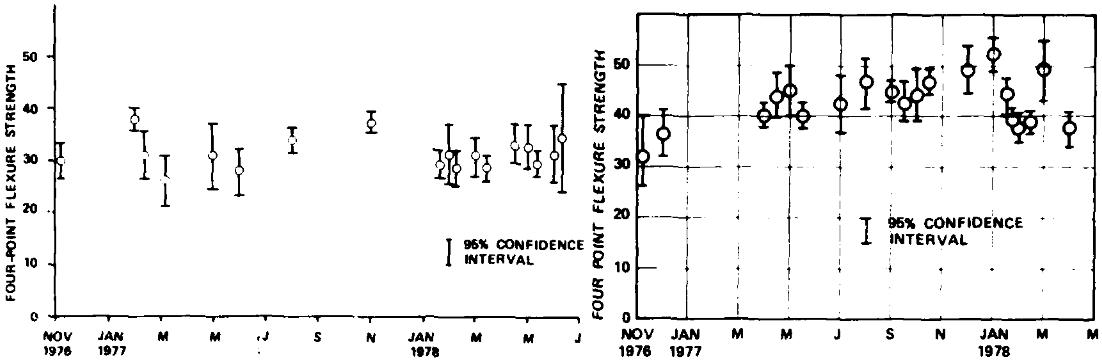

ACC RBN-101 Slip Cast RBSN

Norton NC-350 Isopressed and Machined RBSN

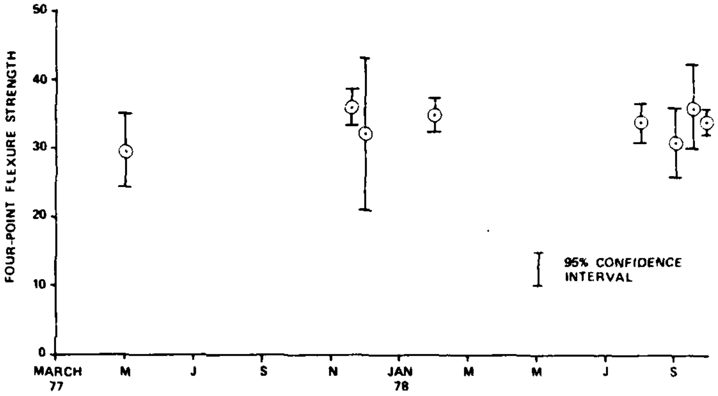

ACC RBN-122 Injection Molded RBSN

Figure 3-18. Summary of Component Certification Strength Data for ACC and Norton RBSN Materials.

Norton attempted further improvements by densifying the surface of their NC-350 RBSN by impregnation with salts followed by thermal treatment. This effort was not successful in improving strength or oxidation resistance.[9]

4.0 MATERIAL CHARACTERIZATION

Emphasis of the materials characterization effort was on obtaining property data on as-fabricated material specimens under time/temperature/environment conditions relevant to the 50-hour 2200°F average TIT engine test requirement.[1] This is illustrated in the material characterization logic charts shown in Figure 4-1 for the rotor and static structure candidate materials.[46] These logic charts were prepared at the start of the program to identify a test philosophy and to provide a road map. As the program progressed, the scope was narrowed to several of the best materials. New tests (such as duty-cycle oxidation, friction, and contact stress) were added as their need became apparent from rig and engine testing.

4.1 ROTOR MATERIALS CHARACTERIZATION

Key concerns for the rotor material were strength after machining and oxidation, stress-rupture life, and cyclic fatigue. These were evaluated as defined in Figure 4-1 for Norton NC-132 hot-pressed Si_4N_4. In addition, key properties of an alternate material, Norton NCX-34 (Si_4N_4 + 8% Y_2O_3), were measured. Later in the program, based upon rig test results, some impact and contact/vibration tests were conducted with NC-132.

4.1.1 STRENGTH VERSUS MACHINING FOR NC-132

Specimens of NC-132 (0.125 by 0.250 by 2.0 inches) were surface machined using the techniques that would be used on various portions of the rotor blades. These specimens were then strength tested at room temperature on an Instron test machine using a self-aligning fixture having an outer span of 1.5 inch and an inner span of 0.75 inch. The results are summarized in Figure 4-2.[2,20] Alignment of the surface grooves perpendicular to the tensile stress axis, as occurred in the transverse machined specimen (and in an axially-machined rotor blade attachment), resulted in an average strength of only 63 ksi. This was half the typical published strength for NC-132 hot-pressed Si_3N_4 (HPSN) and well below design expectations.

Profile grinding produced grinding grooves parallel to the tensile stress and resulted in less strength reduction. By increasing the spindle speed on the profile grinder, strengths comparable to longitudinal surface-ground test bars were achieved.

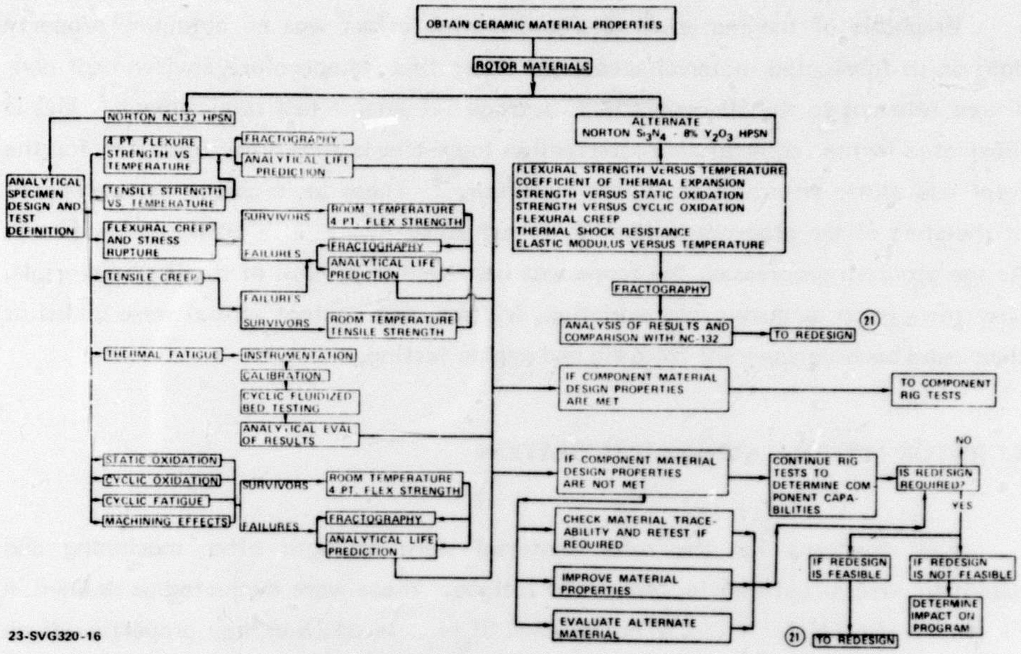

23-SVG320-16

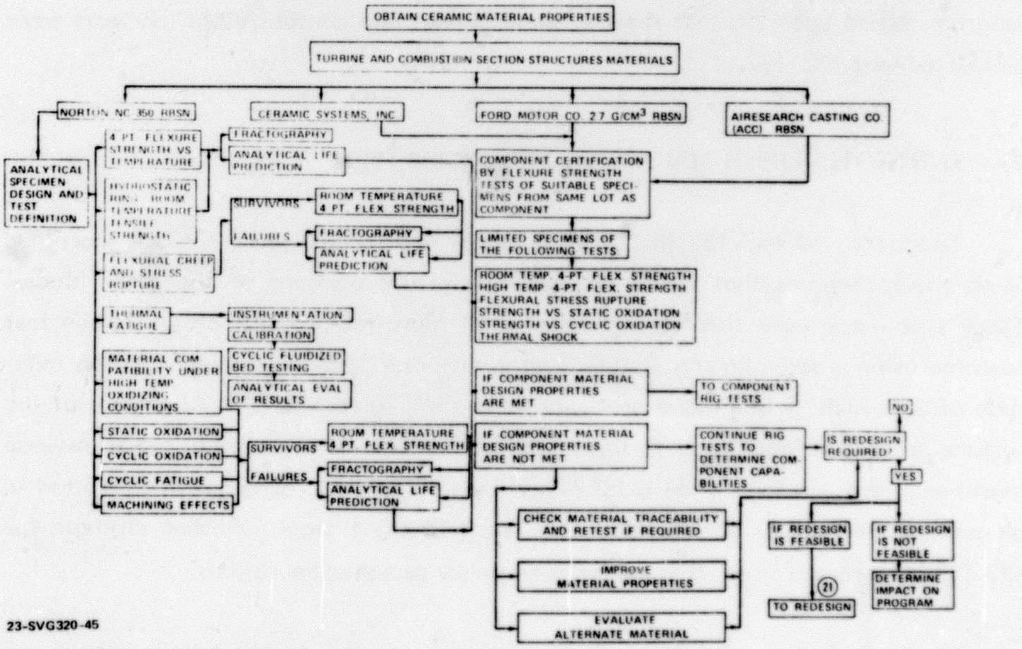

23-SVG320-45

Figure 4-1. Material Characterization Logic Charts.

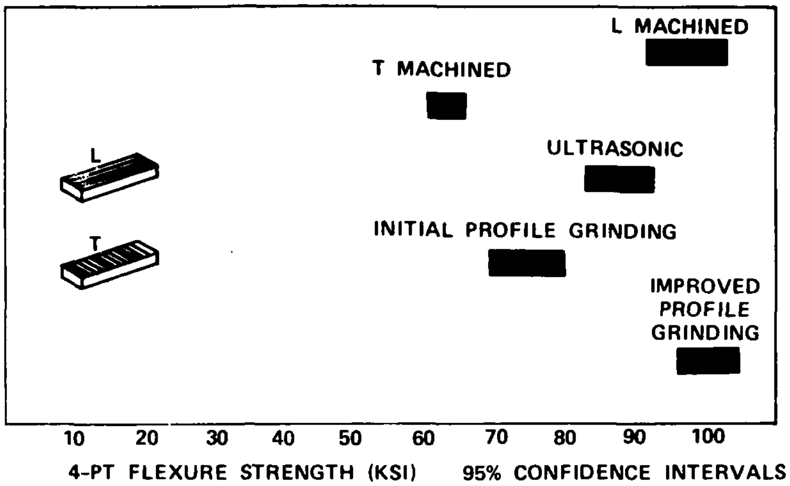

Figure 4-2. Results of 4-Point Bend Strength Versus Surface Condition Evaluation of NC-132 Hot Pressed Si_3N_4.

4.1.2 STATIC OXIDATION OF NC-132

Four-point bend strength testing was conducted for NC-132 specimens exposed to oxidation in static air.[2,20,47] There were two objectives to this testing; first, to determine if an oxidation treatment could decrease the severity of surface machining damage and increase the strength and, second, to determine if 50-hour exposure at projected engine temperature would affect material strength.

The results of the oxidation-strengthening study are summarized in Figures 4-3 and 4-4. Exposure at 1800°F for 24 and 50 hours increased the strength. Examination of the specimen surface showed that the grinding grooves were nearly eliminated and were replaced by a smooth oxide layer. Transverse ground specimens exposed at 2200°F for 24 hours were also stronger than the transverse machined control specimens. However, longitudinally, ground specimens exposed at the same time were substantially lower in strength than the longitudinally machined control specimens. The machining grooves were no longer visible, but new strength-limiting flaws (pits) were present. Examination of these pits by energy dispersive X-ray analysis showed a concentration of Mg, Al, Ca, and Fe. The presence of these impurity concentrations plus the morphology of the pits suggested that impurities in the Si_3N_4 were combining with the SiO_2 surface layer to produce a silicate liquid

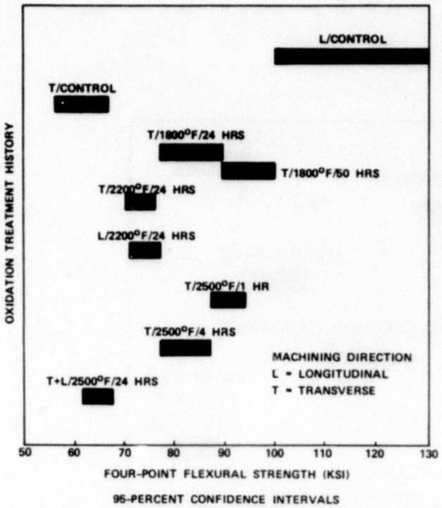

Figure 4-3. Four-Point Flexure Strength of NC-132 HPSN After Static Oxidation Exposures.

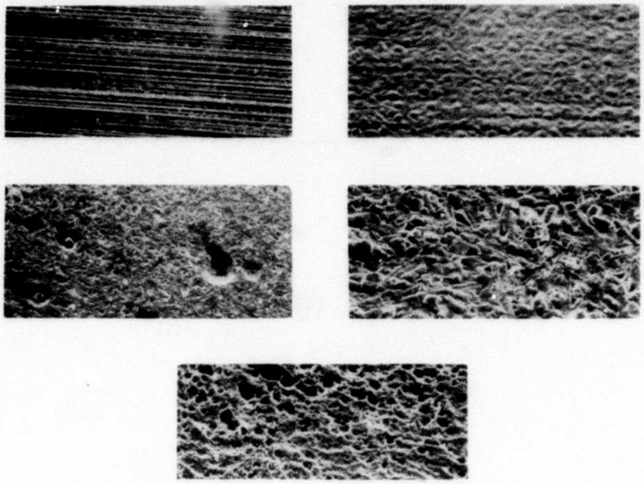

Figure 4-4. Surfaces of NC-132 HPSN As-Machined and After Static Oxidation Exposures.

which was either directly dissolving Si_3N_4 or allowing an increased rate of oxygen diffusion to the $Si_3N_4 - SiO_2$ interface.

Static oxidation exposures at 2500°F for 24 hours produced a thick oxide scale and an average strength of only 63 ksi. Fracture analysis showed that each specimen failed at a surface pit hidden by the oxide scale. A typical example is shown in Figure 4-5. Removal of the oxide scale revealed many pits, most of which were nearly spherical and were wetted with a glass containing impurities such as Mg and Ca.

The oxidation study successfully identified an oxidation treatment that could be utilized for machined HPSN to increase the strength. A treatment of 1800°F/50 hours was selected. It increased the strength from 63 ksi in the as-machined condition to 95 ksi. To determine the reproducibility of the treatment, six test bars were machined from each of five HPSN billets and oxidized for 50 hours at 1800°F in three different furnaces.[2] The resulting average strengths ranged from 91 ksi to 100 ksi compared to 62 ksi for the as-machined specimens.

The oxidation study also identified pit formation as the strength-limiting mechanism for exposures at 2200°F and 2500°F. However, these temperatures were higher than the rotor material would be exposed to in the engine. Peak temperature

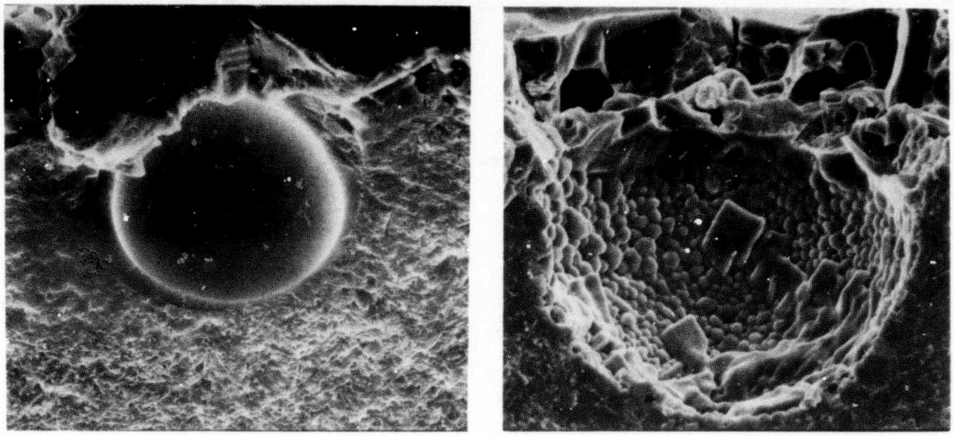

Figure 4-5. Typical Fracture Surface of NC-132 HPSN After 2500°F/24 Hour Static Oxidation Exposure Showing Oxidation Pit at the Fracture Origin.

for the first-stage rotor was estimated by thermal analysis to be 2065°F. Therefore, exposures were conducted at 2065°F. After 140 hours exposure, the four-point flexure strength was 83 ksi. After 240 hours, it was 62 ksi. All fractures initiated at surface pits.

The strength reduction at 2065°F was not considered to be a problem to engine testing. Peak stresses in the rotor blade region that would see 2065°F were determined by finite-element stress analysis to be only 2000 psi.

4.1.3 STRENGTH VERSUS TEMPERATURE FOR NC-132

Strengths over the engine operating temperature range were determined for NC-132 HPSN in four-point flexure and in uniaxial tension.[9,20,47] The high-temperature flexure tests were conducted at California State University at Long Beach using a self-aligning SiC fixture provided by Garrett having an outer span of 1.5 inch and an inner span of 0.75 inch. Tests were conducted with specimens 0.125 by 0.250 by 2 inches at a displacement rate of 0.02-inch per minute with an MTS test unit. Tensile tests were conducted at Southern Research Institute using a gas bearing load train to minimize parasitic bend stresses.[48] The tensile test specimen shown in Figure 4-6 has a typical cylindrical configuration with a gauge diameter and length of 0.188 inch and 1.25 inch, respectively. Overall specimen length was six inches.

All test specimens were machined in the transverse direction with a 320-grit diamond finishing wheel and exposed to the 1800°F/50 hours oxidation treatment. These conditions were selected to simulate the surface of the rotor blade and provide more realistic strength data than was previously available. The test results are summarized in Figure 4-7 and Table 4-1.

4.1.4 STRESS RUPTURE LIFE OF NC-132

At the beginning of this program, stress rupture life was identified as a potential limitation for NC-132 HPSN and was the primary reason the NCX-34 alternate material was selected for evaluation. Stress rupture testing and creep testing were conducted at IIT Research Institute under a Garrett subcontract.[49]

The stress rupture and creep tests were conducted in four-point flexure using the standard 0.125 by 0.250 by 2 inch Garrett test specimen pre-oxidized at 1800°F for 50 hours. The stress rupture tests were typically conducted for 50 hours since a 50-hour test at maximum stress would result in conservative data. The creep data were obtained in a stepwise fashion at three different stresses. The total time for each creep test was approximately 40 hours.

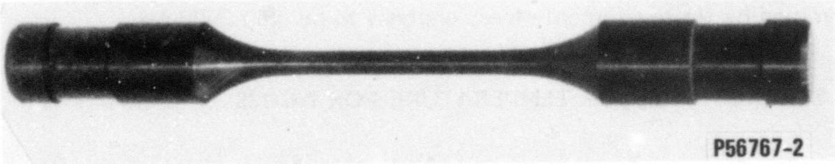

Figure 4-6. NC-132 HPSN Tensile Test Specimen (Six Inches Long).

535 +8

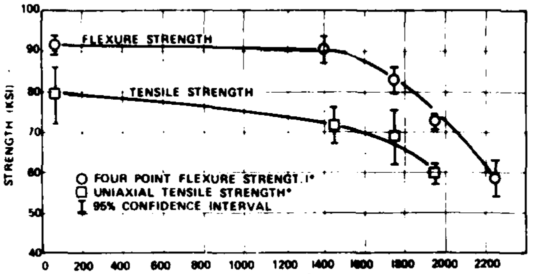

*ALL SPECIMENS MACHINED WITH 320 GRIT DIAMOND IN THE TRANSVERSE DIRECTION AND OXIDIZED AT 1800°F FOR FIFTY HOURS PRIOR TO TESTING

Figure 4-7. NC-132 HPSN Strength Versus Temperature Data.

TABLE 4-1. FOUR-POINT FLEXURE STRENGTH OF NC-132 HPSN.

	TEMPERATURES				
	70°F	1400°F	1750°F	1950°F	2250°F
NUMBER OF SAMPLES	50	30	30	30	6
AVERAGE (KSI)	91.6	90.3	82.7	72.6	58.6
STANDARD DEVIATION (KSI)	8.6	9.2	8.8	5.3	4.3
CHARACTERISTIC STRENGTH (KSI)	95.4	94.3	86.5	75.0	60.7
WEIBULL SLOPE	12.6	11.3	10.8	15.9	13.4
WEIBULL AVG. (KSI)	91.5	90.2	82.6	72.6	58.4
ELASTIC MODULUS ($X10^6$ PSI)	--	44.0	40.0	39.0	--

The stress rupture and creep tests were conducted in four-point flexure with an outer span of 1.75 inch and an inner span of 0.875 inch using dead-weight loading. Fixtures were made from Refrax 20 SiC.

Deflection during creep tests was monitored with a three-point deflectometer. The deflection was determined from the relative movement of the middle rod with respect to the mean position of the outer rods, eliminating the need to consider fixture deformation.

The stress rupture and creep data for NC-132 HPSN is summarized in Table 4-2. Stresses of 40 - 45 ksi at 1950°F were required to cause failure. These stresses were about five times greater than the stress in the engine at the base of the airfoil where stress rupture would be of concern.

The stress rupture results varied dramatically between HPSN billets. Specimens from Billet GR 29195850 fractured after 0.2 and 0.46 hours at 1950°F/45 ksi while specimens from other billets survived 50 hours at 1950°F/45 ksi. The creep data showed the same comparison. Chemical analysis identified that this billet had unusually high Ca and Al content.

NC-132 specimens tested at 2000°F and 40,000 psi underwent substantial deformation and slow crack growth as shown in Figure 4-8.

TABLE 4-2. SUMMARY OF STRESS RUPTURE AND CREEP RESULTS FOR NC-132 HPSN (OXIDIZED AT 1800°F/50 HRS. PRIOR TO TEST).

STRESS RUPTURE					CREEP				
SERIAL NO.	BILLET OR SERIAL NO.	TEMP (°F)	STRESS (KSI)	TIME (HRS)	SERIAL NO.	BILLET OR SERIAL NO.	TEMP (°F)	STRESS (KSI)	$(HR^{-1}x10^{-5})$
364	GR29195850	1950	20	50	362	GR29195850	1950	40	5.7
365		1950	20	50			1950	50	14.5*
366		1950	20	50					
367		1950	20	50					
370		1950	45	0.2*	363	GR29195850	2000	30	2.9
371		1950	45	0.46*			2000	40	7.9
372		1950	50	0.007*			2000	50	37.7
373		1950	50	0.12*					
1529	7-14191-109	1950	45	50	1523	7-14191-109	1950	40	0.4
1530		1950	45	50			1950	50	0.7
							1950	55	*
					1525	7-14191-109	1950	40	0.8
							1950	50	1.7
							1950	55	2.1
1319	6-14191-707	2000	40	50					
1320		2000	40	2 MIN.*					
1714	7-14191-111	1950	45	50	1717	7-14191-111	1950	40	--
1716		1950	45	50			1950	50	0.6
							1950	55	0.5
							1950	50	0.7
							1950	55	1.0

*FRACTURED

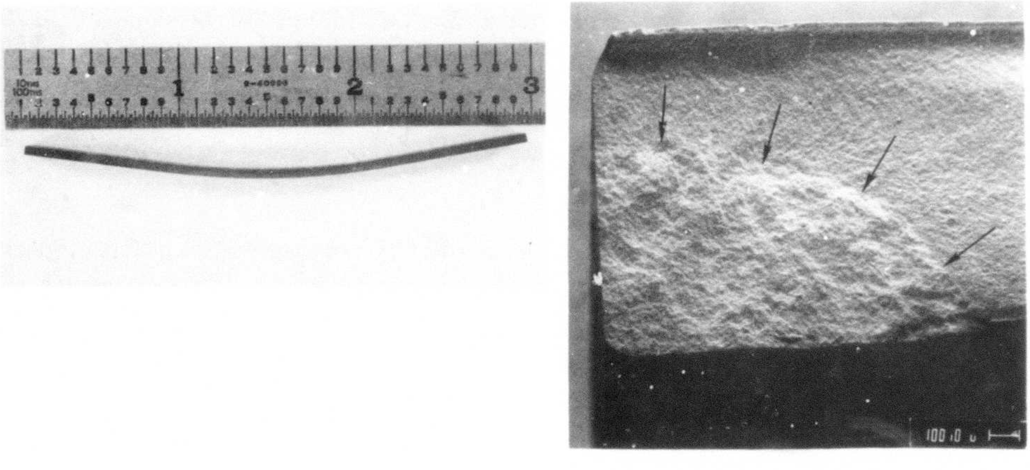

Figure 4-8. Deformation and Slow Crack Growth in NC-132 HPSN.

4.1.5 CYCLIC FATIGUE OF NC-132 HPSN

Cyclic fatigue testing was conducted at IIT Research Institute under subcontract to Garrett.[49] Testing was conducted in four-point flexure with a 0.125 by 0.250 by 3 inch specimen configuration with an outer span of 2.5 inches and an inner span of 1.0 inch. The specimens were preoxidized at 1800°F for 50 hours prior to fatigue testing. Tension-tension mode tests were conducted at 1400°F (attachment neck temperature), 1750°F (temperature at the peak stress region of the second-stage airfoil) and 1950°F (temperature at the peak stress region of the first-stage airfoil). Several tests were also conducted at 2200°F. The mechanical loads were controlled by a servo valve that received and transmitted hydraulic fluid (remote pump source) to the actuator on command from the servo-controller. The load cell provided the closing loop element by monitoring the load on the sample and transmitting the signals to the servac. A function generator with a sinusoidal output wave form was used as the comparator signal, wherein the servac interpreted the difference between intended stress and feedback stress and relayed open/close messages to the servo valve.

The fatigue test results for NC-132 are summarized in Table 4-3. At temperatures up to 1950°F, no fractures occurred outside the 95-percent confidence interval of the fast-fracture data for the material.[5,50] The fracture surfaces of fatigue specimens were indistinguishable from those of fast-fracture specimens. Cyclic stressing did not appear to degrade the NC-132 strength up to 1950°F and 10^6 cycles. At 2200°F, stress and time dependency were evident but could not be distinguished from stress rupture effects.

Although the data was limited, the cyclic fatigue tests indicated that NC-132 would not be significantly degraded by cyclic loading within the time/temperature/stress operating conditions of the TSE331C-1 engine demonstration.

4.1.6 DYNAMIC OXIDATION STUDY OF NC-132 HPSN

Static oxidation of test bars in a furnace does not provide a close simulation of dynamic oxidation in an engine. To more closely simulate the engine environment, the Garrett hot corrosion test facility shown in Figure 4-9 was used. The facility consists of a combustor which burns jet A aircraft fuel with a gas discharge velocity of Mach 0.4. The test specimens are mounted in a carousel and rotated in the high velocity combustor gases. The temperature is measured by an infrared pyrometer

TABLE 4-3. SUMMARY OF CYCLIC FATIGUE DATA FOR NC-132 HPSN

SPECIMEN NO.	PEAK STRESS (KSI)	TEMPERATURE (^{0}F)	CYCLES	TOTAL TIME (HRS)	STATUS
189	70	1400	306,500	23	S*
190	70		316,200	23	S
191	70		314,900	23	S
200	85.5		50,600	7	F*
201	90		17,000	2	F
202	94		203,200	23	S
186	61	1750	271,400	21	S
187	61		320,300	23	S
188	61		915,600	71	S
192	70		311,000	23	
193	80		384,000	23	
194	87		--	--	FL*
183	40	1950	700,000	158	S
184	40		281,000	20	S
185	40		315,000	22	S
319	40		1,130,000	69	S
321	45	1950	1,050,000	65	S
320	50		2,500	0.1	F
1322	62		293	0.1	FL
318	62		34	0.1	FL
199	66		217,000	23	S
198	70		13,000	1.5	F
1323	70		60	0.01	F
197	75		56	0.03	F
316	30	2200	305,000	19.5	S
317	30		301,800	19	S
1317	35		502,400	35	F
315	35		369	0.05	F
314	40		61	0.01	FL
313	47.5		79	0.01	FL
1315	49		75	0.01	FL
1314	51.5		25	0.01	FL

S = SURVIVED   F = FAILED   FL = FAILED DURING LOADING

535 +2

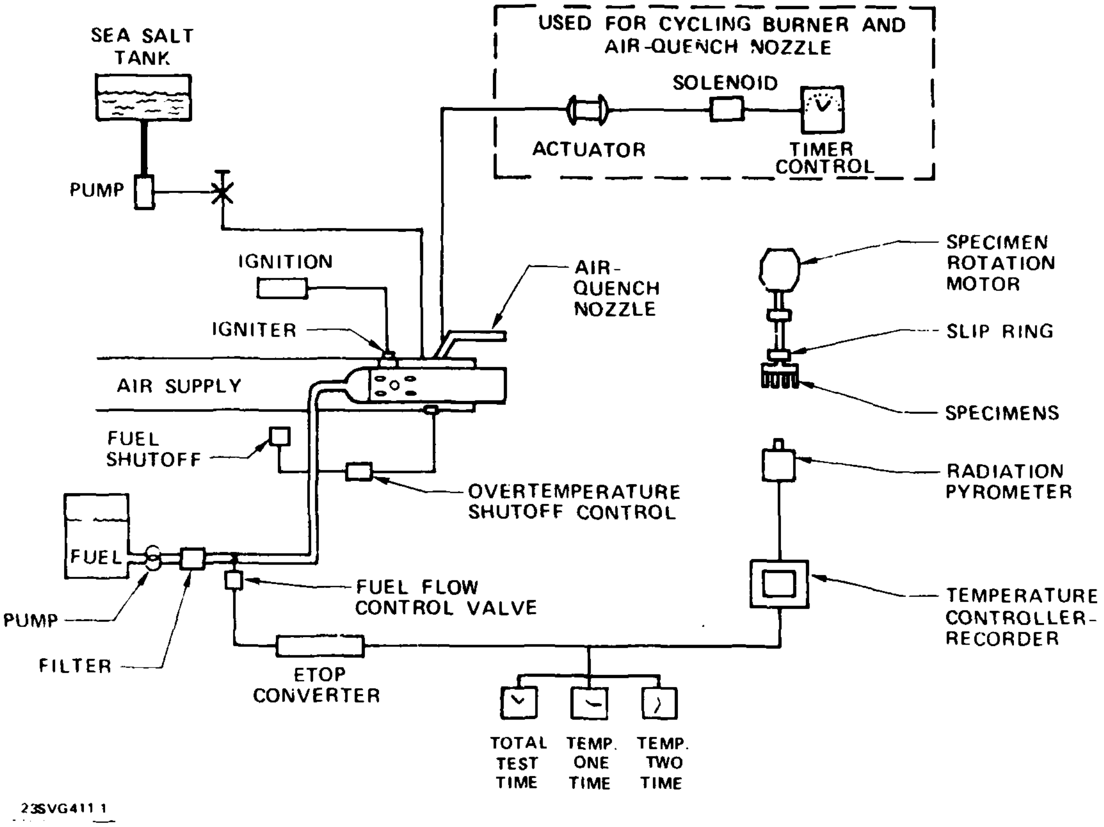

Figure 4-9. Schematic of Garrett Hot Corrosion Test Rig.

focused on the specimens. The output from the pyrometer compared to a temperature set point provides an input to a fuel-air control which modulates valves to automatically maintain the set-point temperature. A timer-controlled actuator moves the combustor away from the specimens and replaces it with an airblast nozzle to rapidly quench the test specimens from the exposure temperature to approximately 300°F. The hot corrosion rig can operate automatically with a cycle containing two set-point temperatures and a quench. It can also operate with an oxidizing atmosphere produced by air-rich burning of the fuel or can operate with controlled corrosive impurity additions such as sea salt.

The hot corrosion rig was slightly modified for evaluation of ceramics. The fuel nozzle was changed to increase the temperature capability to 2050°F. The metal venturi nozzle at the combustor exit was replaced by ceramic to provide longer life at the higher test temperature. The specimen carousel was modified to hold 16

0.125 by 0.25 by 3 inch ceramic flexure test bars so that strength after dynamic oxidation exposure could be measured.

Tests on NC-132 HPSN were conducted with several types of cycles with and without sea salt addition.[6,51] The specific cycles and the results are summarized in Table 4-4. The strength of NC-132 HPSN was increased by dynamic oxidation exposure at temperatures of 1950°F and 2050°F for combustion gases containing no sea salt additions. Oxide layers were typically smooth and glassy and the strength of transverse machined specimens was approximately 100 ksi. However, when sea salt was present, surface corrosion was visible and the strength was reduced to 70 to 80 ksi. Figure 4-10 compares specimens exposed to combustion products with and without sea salt additions. The presence of the sea salt resulted in significantly more wetting of the Si_3N_4 surface and a heavy buildup of glassy material. Scanning electron micrographs of typical fracture surfaces are included in Figure 4-11 and show the glassy buildup and the surface corrosion. Energy dispersive X-ray analysis for the base Si_3N_4 material and the glass are also shown in Figure 4-11. High levels of Na, Al, Fe Mg and S are present in the glass. The presence of these impurities and

TABLE 4-4. DYNAMIC OXIDATION RESULTS FOR NC-132 HPSN.

SURFACE CONDITIONS, EXPOSURE	AVERAGE STRENGTH (KSI)	STANDARD DEVIATION	SAMPLES TESTED	PREDOMINANT FRACTURE ORIGIN
L, CONTROL, NO EXPOSURE	97.0	16.8	38	SURFACE, AT VARIETY OF FLAWS
T, CONTROL, NO EXPOSURE	63.0	5.0	12	SURFACE, AT GRIND GROOVES
T, 1950°F/1 HR, AIR QUENCH/ 5 MIN, 50 CYCLES	99.0	12.0	4	SURFACE, FLAWS NOT OBVIOUS
L, 2050°F/5 MIN, AIR QUENCH/ 3 MIN, 100 CYCLES	108.0	7.0	8	SURFACE, FLAWS NOT OBVIOUS
L, 1650°F/1.5 HRS, 2050°F/ 0.5 HR, AIR QUENCH/5 MIN, 25 CYCLES	100.0	20.0	4	SURFACE, FLAWS NOT OBVIOUS
L, SAME CYCLE AS ABOVE WITH 5 PPM SEA SALT	71.0	2.4	4	SURFACE CORROSION
L AND T, 1950°F/3 MIN, 1650°F/ 5 MIN, AIR QUENCH/3 MIN, 135 CYCLES, 5 PPM SEA SALT	81.0	--	4	SURFACE CORROSION

L = 320-GRIT LONGITUDINAL
T = 320-GRIT TRANSVERSE

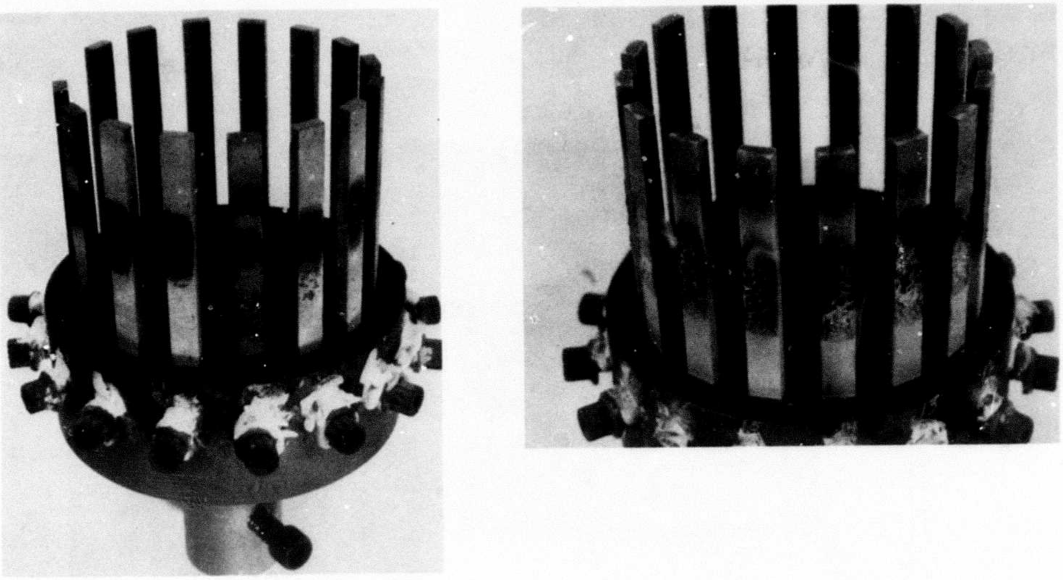

Figure 4-10. Hot Corrosion Rig Test Fixtures With Hot-Pressed and Reaction-Bonded Silicon Nitride Specimens. (A) No Sea Salt (B) 5 ppm Seal Salt.

the appearance of the Si_3N_4 surface suggested that the molten glass was either dissolving or reacting with the Si_3N_4 or in some other fashion was accelerating the rate of oxidation. The dynamic oxidation testing, although limited in scope, indicated that NC-132 HPSN was not likely to degrade significantly during the rig and engine testing planned for the engine demonstration program and that an alternate material or design was not required.

4.1.7 IMPACT STUDY OF NC-132 HPSN

The tolerance of ceramic rotor blades to foreign object damage (FOD) has always been a concern. Initial FOD testing was conducted to investigate if carbon particles generated in the combustor would damage a ceramic rotor blade.[11] As illustrated in Figure 4-12, the whirlpit was modified to allow controlled injection of carbon particles in the path of a rotating ceramic blade.

Carbon particles up to 0.9 gram and an equivalent diameter of 0.48 inch were evaluated at 16,000 and 32,000 rpm. The hot-pressed ceramic blade was not damaged, suggesting that carbon from the combustor did not pose an FOD problem. Damage from RBSN was evaluated next. Rotor blades had previously been damaged in dynamic rig Build 5 in which pieces of the RBSN static-structure had

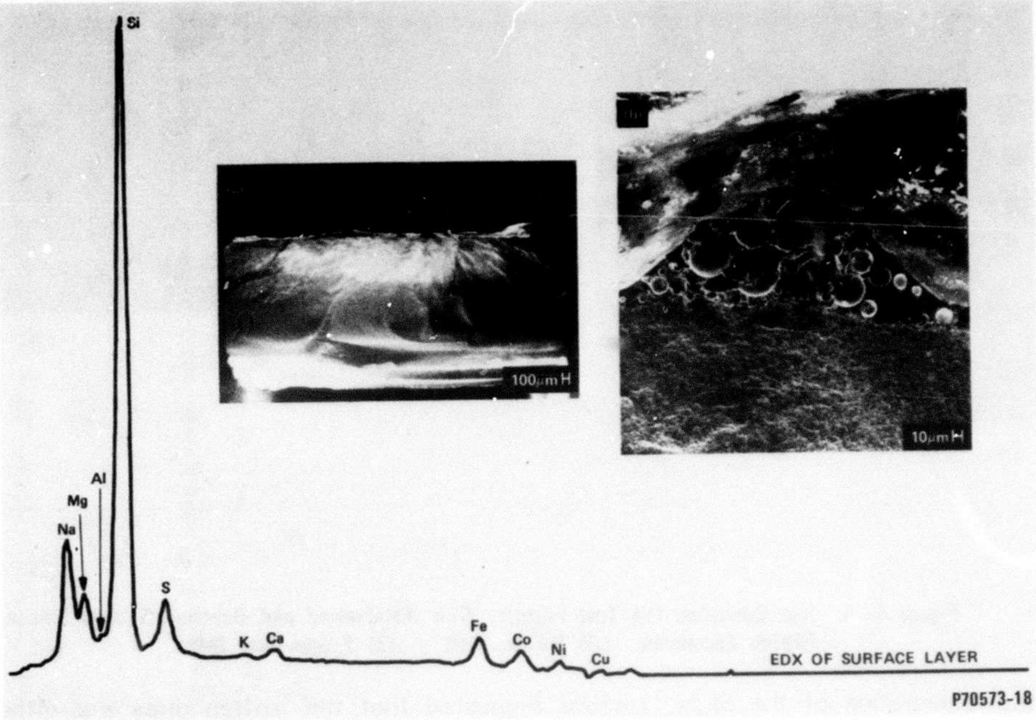

Figure 4-11. Scanning Electron Photomicrographs and Energy Dispersive X-Ray Analysis for NC-132 After Dynamic Oxidation With Sea Salt Additions.

apparently gone through the turbine. Two whirlpit tests were conducted, one with a 0.6 gram RBSN piece (equivalent diameter 0.3 inch) dropped into the blade at 16,000 rpm and one with a similar 0.6 gram RBSN at 32,000 rpm. The blade was not damaged in the former case but fractured at the airfoil in the latter case. These tests demonstrated that the ceramic rotor blades do have some tolerance to impact.

To further evaluate FOD tolerance of NC-132 blades, cast steel shot of various sizes was used. Initially, a set weight of 0.55 gram of shot sizes of 0.007, 0.010/0.012, 0.018/0.023, 0.033, and 0.055 inch diameter were dropped into the path of a second-stage blade spinning at 32,000 rpm. Only 0.055-inch diameter shot fractured the blade airfoil. The smaller shot produced impact marks with a visible trace of metal but no scuffing, cracking, or chipping of the ceramic. This is illustrated in Figure 4-13 for the 0.033 inch diameter shot. Additional tests were conducted with discrete shot particles. Individual pieces of 0.033-inch diameter shot were dropped on a blade at 32,000 rpm with no damage. This was repeated with

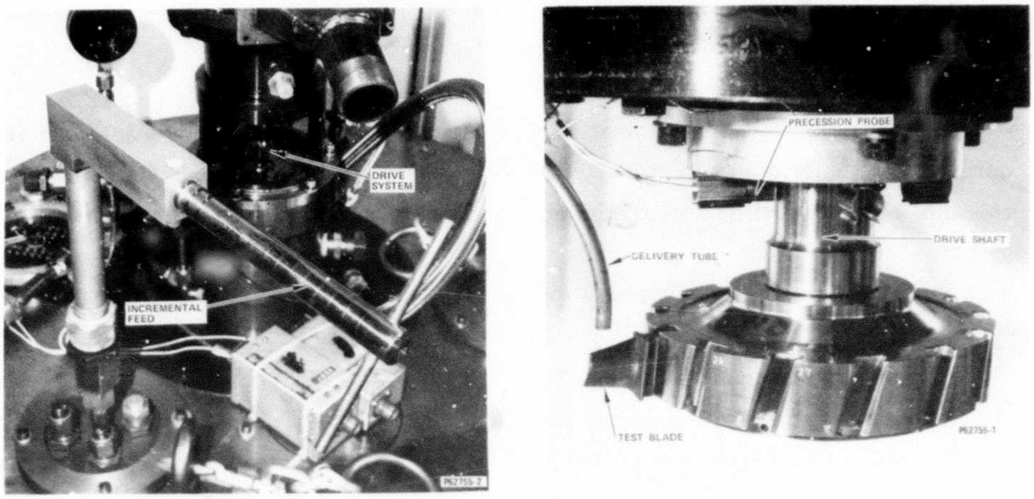

Figure 4-12. Whirlpit Modification to Permit Impact Testing of Particles of Carbon, RBSN and Steel Shot Against a Rotating NC-132 HPSN Ceramic Rotor Blade.

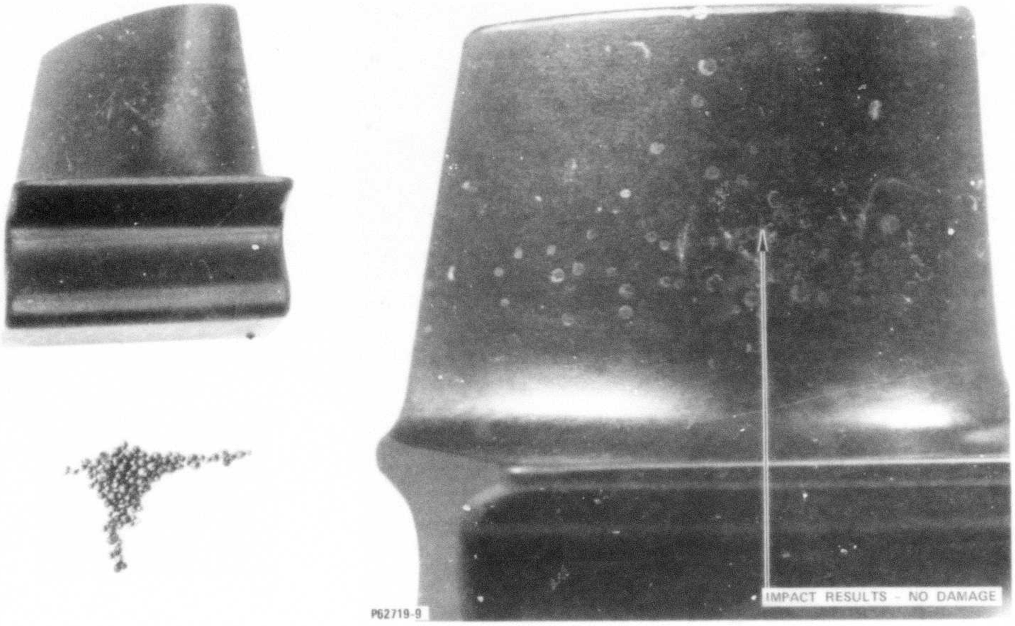

Figure 4-13. Results of Impact Testing at 32,000 rpm with 0.55 Grams of 0.033 Inch Diameter Steel Shot.

0.055-inch shot. The third 0.055-inch particle caused airfoil fracture. Testing was continued at 45,000 rpm. Fracture occurred with 0.033-inch shot with the third particle. Next, ten pieces of 0.018/0.023 inch diameter shot were individually dropped in the blade path at 45,000 rpm with no damage.

The results of the steel shot FOD tests are summarized in Figure 4-14. The ceramic blades have substantial impact damage tolerance and should be capable of reliable engine operation with a minimum of foreign object ingestion protection.

4.1.8 CONTACT-VIBRATION STUDY OF NC-132 HPSN

This study was initiated to explain a rotor blade failure that occurred during the first dynamic rig test (to be discussed in Paragraph 6.4). The rotor blade failed at 37,000 rpm in the attachment at the edge of the contact between the blade and the disk. The failure origin was not in the region identified analytically to have the peak stress. Blades that failed previously in overspeed proof tests had all fractured in the attachment neck precisely at the point of predicted peak stress. Furthermore, the fracture surface for the dynamic rig failure was different from any seen previously. Thus, the evidence suggested that either a material flaw or a fracture mode

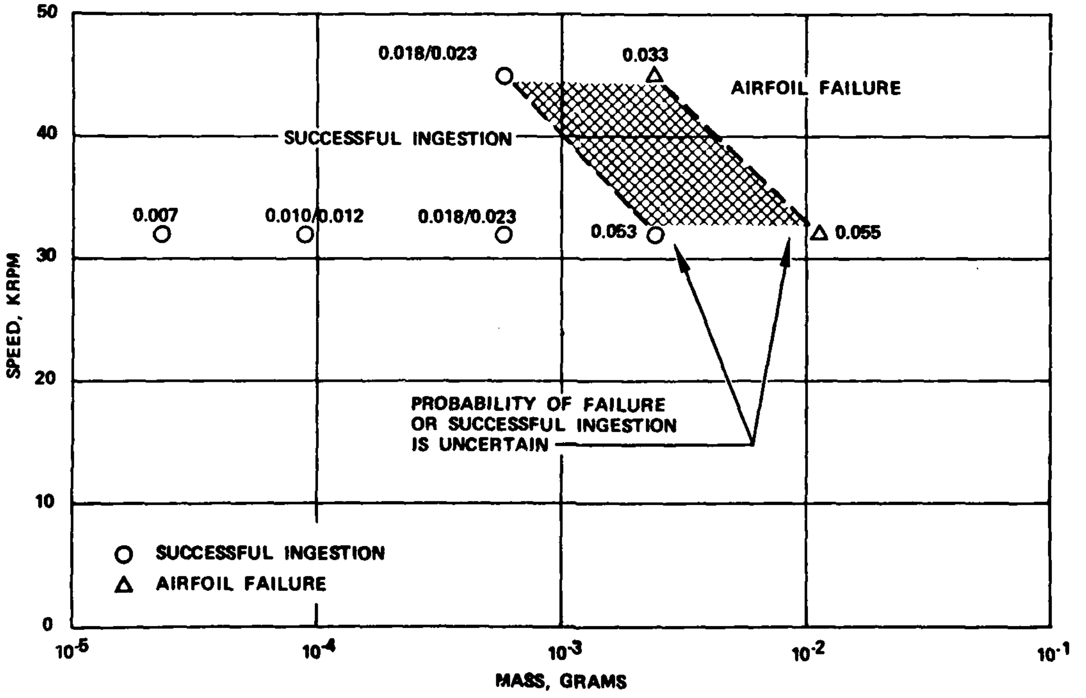

Figure 4-14. Summary of Steel Shot FOD Testing of NC-132 HPSN Rotor Blades in the Whirlpit.

previously not encountered was responsible. Contact stress and vibration were the two variables selected for evaluation.

A test was designed to evaluate both the independent and combined effects of contact stress and vibration with and without compliant layers.[7] Schematics of the test fixture and specimen configurations are shown in Figure 4-15. A rectangular specimen was clamped in a fixture with the bolts torqued to produce an average contact load of 35-40 ksi. This fixture was attached to a Bullen ultrasonic unit, and the specimen was driven at resonant frequencies from 6 to 18 kHz (frequency dependent upon specimen length). The amplitude, measured with a Bently probe, was increased until the specimen fractured. Two specimen configurations were evaluated: 1) a simple cantilevered rectangular beam that would allow evaluation of the combined effects of contact and vibration and would best simulate the conditions of a rotor blade during engine operation, and 2) a tapered beam (shown in Figure 4-15)

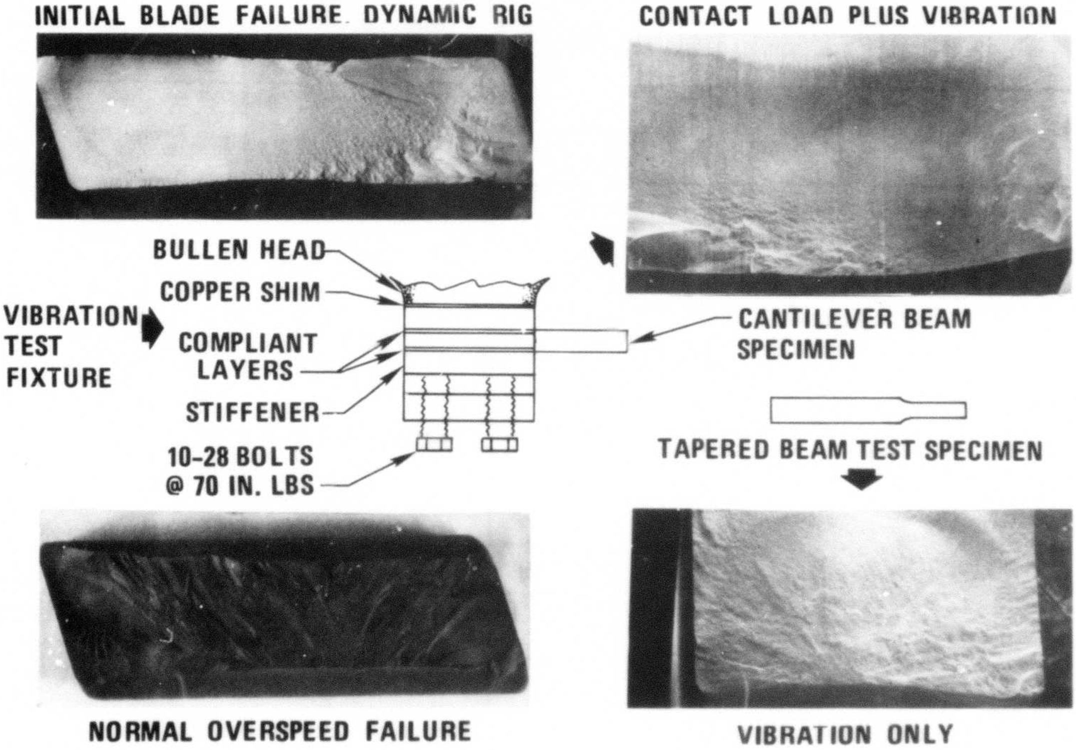

Figure 4-15. Schematic of the Test Fixture and Specimen Configuration for Contact-Vibration Evaluation and Scanning Electron Micrographs Comparing the Fracture Surfaces for the Various Failure Conditions.

that would minimize the contact effect and isolate the effect of high frequency vibration.

The results are summarized in Table 4-5. The cantilevered beam specimens without a compliant layer and most of those with an HS25 compliant layer fractured at much lower apparent stress (~20 ksi) than the baseline flexure strength of the material (95 ksi) and had a fracture surface identical to the failed rotor blade. The scanning electron photomicrographs in Figure 4-15 compare the fracture surfaces of the rig-tested blade, the cantilevered beam specimen, a typical overspeed proof test blade, and a tapered beam specimen. The latter two have a small fracture mirror and indicate initiation of fracture at a small flaw at high stress. The former two have a large fracture mirror and indicate fracture initiation at a large flaw at low stress.

Cantilever beam specimens that were vibration tested with platinum compliant layers fractured at higher apparent stress (47 ksi) but still well below the baseline

TABLE 4-5. SUMMARY OF CONTACT-VIBRATION TESTING OF NC-132 HPSN.

TEST TYPE	COMPLIANT LAYER	APPARENT FAILURE STRESS (KSI)	FREQUENCY (Hz)
CANTILEVER RECTANGULAR BEAM 0.125 X 0.025 X3 INCH	NONE	20	6,000
	NONE	20	6,400
	NONE	23	6,400
	HS25	20	6,500
	HS25	20	6,300
	HS25	11	11,500
	HS25	40	11,700
	PLATINUM	47	6,300
STATIC	HS25	77	0
FLIP-FLOP	HS25	76	0
	HS25	78	0
	PLATINUM	89	0
	PLATINUM	83	0
	PLATINUM	83	0
TAPERED BEAM	HS25	90	15,600
	PLATINUM	77	15,100
	PLATINUM	103	15,200
	PLATINUM	78	15,900
	PLATINUM	84	15,500

strength of the material. To evaluate contact effects only, cantilever beams with the 35-40 ksi contact load were fractured by a single-cycle mechanical load application (referred to in the Table as static) and by a low-cycle mechanical load application (flip-flop) where the load was applied at one-pound increments sequentially from opposite directions until the specimen fractured. The apparent stress varied from 76-89 ksi, higher than for the combined contact-vibration case, but still slightly lower than the baseline strength of the material.

The final tests were conducted with the tapered beam. A peak flexure stress could be produced in the thin cross section adjacent to the step by increasing the vibration amplitude. By measuring the strain at fracture, the local stress could be calculated. Peak contact stress would be in a separate area (thick section of beam), allowing the separation of contact and vibration effects. As shown in Table 4-5, fracture stresses due to vibration only were comparable to the baseline flexure strength of the NC-132 HPSN material. The fracture surface (Figure 4-15) was also comparable to that of the baseline flexure strength tested specimens.

The contact-vibration tests were very helpful in developing an understanding of the blade failure in the dynamic rig test and in identifying an area of technology requiring further study. The tests showed that vibration and contact loading could interact to cause fracture at a low apparent tensile stress* and that a soft compliant layer was beneficial. Platinum was selected as the blade attachment compliant layer for future rig and engine tests. Disk slots were lapped to decrease vibration amplitude and load concentration, and the stators were redesigned to decrease vibration by avoiding the stator's passing excitation.

4.2 ALTERNATE ROTOR MATERIAL

An experimental Norton material (NCX-34 HPSN) containing 8 percent Y_2O_3 as the hot pressing aid was selected as an alternate rotor blade material. Preliminary data generated by Norton[53] for this material suggested that it had higher strength at temperature, improved stress-rupture life, and at least equivalent oxidation-resistance compared to NC-132 HPSN. To provide a better comparison with NC-132 and to assess the capability of NCX-34 to meet the TSE331C-1 engine design requirements, the following properties were evaluated: strength versus temperature,

---

*Further study conducted under an ONR program and reported in Reference 52 showed that localized high tensile stresses could occur at the edge of a contact zone and that these could add to the applied flexural load to cause fracture.

coefficient of thermal expansion, elastic-modulus versus temperature, strength versus oxidation and corrosion, and thermal shock resistance.[47] Most of the NCX-34 property measurements were conducted by Norton Company.

4.2.1 STRENGTH OF NCX-34

The strength of NCX-34 HPSN with 8 percent Y_2O_3 was measured on longitudinally machined specimens in three-point flexure at Pennsylvania State University. The results are plotted in Figure 4-16 and compared to three-point data previously generated at Penn State for Norton NC-130 Si_3N_4.[54] A comparison with NC-132 would have been preferable, but comparable three-point data was not available. However, the strength-versus-temperature curves for NC-130 and NC-132 are similar. Room-temperature, four-point flexure data for longitudinal and transverse machined NCX-34 specimens is also included in Figure 4-16. NCX-34 had higher strength than NC-130 or NC-132, especially at temperatures above 1500°F. This was attributed to increased refractoriness of the grain boundary regions when Y_2O_3 was used as a sintering aid rather than MgO[55,56] as used in NC-130 and NC-132.

Two room-temperature, four-point flexure data points are also included in Figure 4-16, one for longitudinal machined NCX-34 (139 ksi) and one for transverse machined NCX-34 (105 ksi). Orientation of the machining grooves (and the associated subsurface machining damage) with respect to the stress direction appeared to

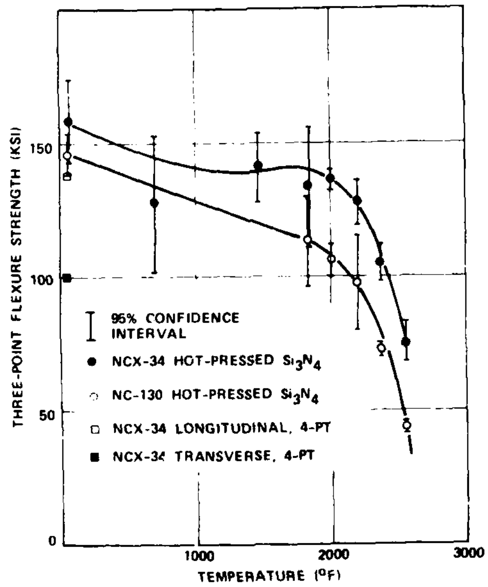

Figure 4-16. Strength Versus Temperature Comparison for NC-130 and NCX-34 HPSN Materials.

have less effect on the strength of NCX-34 than it did on NC-132 (see Paragraph 4.1.1). This supported the contention of Freiman and Rice* that NCX-34 has a higher fracture toughness than NC-132.

4.2.2 ELASTIC MODULUS AND THERMAL EXPANSION OF NCX-34

The elastic modulus of NCX-34 was measured at Norton Company from room temperature to 1900°F. The curve was statistically indistinguishable from that for NC-132.

The coefficient of thermal expansion was also determined by Norton Company under subcontract to Garrett. The average expansion over the range of 72° to 2300°F was 1.9×10^{-6} in./in./°F compared to 1.7×10^{-6} in./in./°F over the same temperature range for NC-132.

4.2.3 STRENGTH VERSUS OXIDATION/CORROSION

Static oxidation tests on NCX-34 were conducted at both Norton Company and Garrett. Norton exposed 0.125 by 0.125-inch cross-section specimens for 300 hours over the range of 1830°F to 2370°F and measured the strength in four-point flexure with an outer span of one inch and an inner span of 0.5 inch. Exposures above 2000°F resulted in an initial strength decrease from 159 ksi to 92 ksi within the first 100 hours, followed by very little additional decrease in strength for exposure up to 300 hours. At 1830°F, the strength only decreased from 159 ksi to about 143 ksi.**

Static oxidation tests at Garrett were conducted with the standard 0.125 by 0.25-inch cross-section specimen. NCX-34 retained a strength of 117,000 psi for longitudinal machined specimens and 105,000 psi for tranverse machined specimens after 240 hours of static oxidation at 2065°F.

---

*Personal communication from S. Freiman and R. Rice of the Naval Research Laboratories, Washington, D.C.

**Some other studies have shown good oxidation resistance of NCX-34 at high temperatures, but catastrophic oxidation at the intermediate temperature of 1830°F.[57] This was not observed for the billets of NCX-34 evaluated in the DARPA/NAVY program. However, some of this material has subsequently been tested at lower temperatures and found to be susceptible to the catastrophic oxidation.[58]

Three tranverse machined test bars of NCX-34 were exposed to 50 cycles of dynamic oxidation in the Garrett hot-corrosion test rig. The cycle consisted of one hour at 1950°F followed by a five minute airblast quench. The average four-point flexture strength after exposure was 150,000 psi, compared to a baseline of 100,000 psi.

4.2.4 THERMAL SHOCK RESISTANCE

The thermal shock resistance of NCX-34 was evaluated using the technique described by Davidge and Tappin[59] and Hasselman.[60] These tests were conducted at Norton under subcontract to Garrett using 0.125 by 0.125 by 4-inch specimens. This study investigated the effects of increasingly severe thermal shock on strength and specific-damping capacity (internal friction). Thermal shock was perfomed by suspending a specimen in a vertical tube furnace (controlled to ±5°F) for 15 minutes at the desired temperature, followed by quenching in a large room-temperature water bath. Specific-damping-capacity measurements were obtained before and after quenching using a Nametre Model XII acoustic spectrometer and the bandwidth method discussed by Zener.[61]

Following the thermal shock treatment and specific-damping-capacity measurement, the flexure strength of each specimen was measured. The data for NCX-34 is summarized in Figure 4-17. The dashed line represents the four-point flexure strength after thermal-shock quenching as a function of the ΔT between the furnace and the water bath. The dotted lines represent the change in specific-damping capacity before and after quenching, as a function of ΔT for NCX-34 and NC-132 (obtained on the same equipment during a previous study.[62] NCX-34 appears to be capable of withstanding approximately a 400°F more severe quench than NC-132.

4.3 REACTION BONDED Si_3N_4 MATERIALS CHARACTERIZATION

Reaction bonded Si_3N_4 (RBSN) was selected as the material for the stator vanes and other static structure components. Key property concerns were strength versus fabrication approach and machining, strength after static and dynamic oxidation exposure, stress rupture life, and cyclic fatigue. Evaluations were conducted relevant to engine operating temperature and time. Fractography was used to identify the property-limiting flaw or characteristic of each material and to provide feedback to the fabricator that might aid in material improvement during subsequent development.

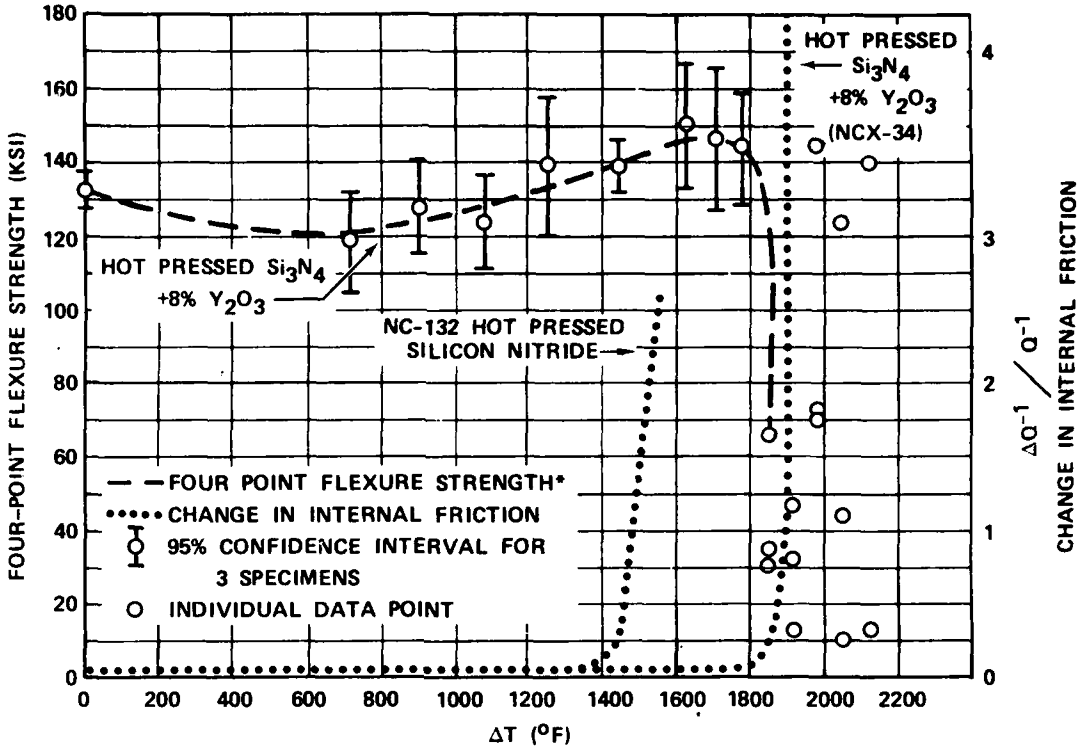

*FOUR-POINT FLEXURE STRENGTH 1.0 IN. OUTER SPAN 0.5 IN. INNER SPAN

23SVG408-11

Figure 4-17. Thermal Shock Comparison of NCX-34 (Si_3N_4 + 8 Percent Y_2O_3) and NC-132.

4.3.1 STRENGTH OF AS-FABRICATED RBSN

Flexure strength testing was conducted using the same specimen configuration and fixtures described in Paragraph 4.1.1. Tensile tests were conducted at Stanford Research Institute using hydrostatic-loading of thin-walled rings.

The flexure strength results are summarized in Table 4-6. Additional room-temperature data showing batch-to-batch variations were shown previously in Figure 3-18 (Paragraph 3.4). Several observations were made from the strength data in Table 4-6: (1) the strength increased with increasing test temperatures, (2) orientation of the grinding direction perpendicular to the stress direction (the transverse machining case) substantially decreased strength, and (3) the strength was similar for longitudinal machined and as-nitrided material. Fracture analysis determined that transverse machined specimens all fractured at machining damage

TABLE 4-6. FLEXURE STRENGTH VERSUS TEMPERATURE AND SURFACE CONDITION OF RBSN MATERIALS.

MATERIAL	SURFACE CONDITION	TEMPERATURE (°F)	QUANTITY	AVERAGE STRENGTH (KSI)	STANDARD DEVIATION KSI)
NORTON NC-350	320-GRIT, LONGITUDINAL MACHINED	70	6	31.2	2.7
		1950	6	46.9	6.2
		2250	6	53.0	3.4
		2450	6	51.7	2.3
	AS-NITRIDED (LONGITUDINAL MACHINING PRIOR TO NITRIDING)	70	12	31.3	4.0
		1950	12	48.0	2.7
		2250	12	53.8	4.8
		2450	12	56.7	3.6
	AS-NITRIDED (TRANSVERSE MACHINING PRIOR TO NITRIDING)	70	7	31.1	5.0
		1950	4	45.7	7.4
		2250	5	45.4	6.9
		2450	4	45.1	3.3
	320-GRIT TRANSVERSE MACHINED	70	8	15.4	0.5
	320-GRIT LONGITUDINAL MACHINED	70	10	26.5*	3.6
		70	9	35.3**	6.3
		2250	6	43.3	4.3
ACC RBN-101	AS-NITRIDED	70	6	22.5*	1.2
		70	5	33.5*	7.0
		2450	4	31.5	4.3
FORD	AS-NITRIDED	70	17	31.5	5.1
		70	43	41.2***	5.7

*EARLY MATERIAL **IMPROVED MATERIAL ***FORD CERTIFICATION DATA

and that as-nitrided specimens fractured at microstructural pores. Longitudinal machined specimens fractured due to machining damage and at pores.

Hydrostatic ring tensile tests were conducted in an attempt to obtain volumetric strength data.[9] Tests were conducted on one-inch diameter rings with an approximate volume of 0.12 inch^3 and two-inch diameter rings with an approximate volume of 0.4 inch.^{3} Rings were fabricated by diamond-machining sections of hollow cylinders of NC-350 RBSN. All tests were conducted at room temperature. Eighteen small-diameter rings with as-nitrided ID and OD had an average burst strength of 15.0 ksi with a standard deviation of 2.4 ksi. Eighteen large-diameter rings with as-nitrided ID and OD had an average burst strength of 12.9 ksi with a standard deviation of 1.9 ksi. Twelve large-diameter rings with machined surface had an average burst strength of 12.8 ksi with a standard deviation of 2.5 ksi. All ring fractures initiated at the flat machined surfaces at machining grooves perpendicular to the stressing direction. The strengths are comparable to those reported in Table 4-6 for transverse machined specimens tested in four-point flexure. Since all the fractures were surface initiated, no volumetric data was obtained.

4.3.2 STATIC AND DYNAMIC OXIDATION OF RBSN

Initial static and dynamic oxidation tests were conducted with NC-350 RBSN because of its early availability in the program. These tests had several objectives: (1) improve the strength of transverse machined RBSN, (2) evaluate the material stability for 50 hours static exposure at 2250°F, and (3) evaluate the material stability under cyclic conditions in a burner rig including sea salt additions to the combustion gases. The results are summarized in Table 4-7.[51]

The strength of machined specimens increased after both static and cyclic oxidation exposure (without sea salt additions). As-machined specimens typically failed at grinding marks on the specimen surface while oxidized specimens typically

TABLE 4-7. RESULTS OF INITIAL STATIC AND DYNAMIC OXIDATION STUDIES OF NORTON NC-350 RBSN.

TEST TYPE	SURFACE CONDITION, EXPOSURE	AVERAGE STRENGTH (KSI)	STANDARD DEVIATION	SAMPLES TESTED
CONTROL	A	31.0	4.0	12
	L	31.0	2.7	6
	T	23.0	4.4	6
STATIC OXIDATION	A, 1800°F/50 HRS	30.0	4.0	6
	A, 2250°F/50 HRS	20.0	3.6	12
	L, 2250°F/50 HRS	33.0	5.6	6
	T, 2250°F/50 HRS	37.0	3.0	6
CYCLIC OXIDATION	A, 1950°F/1 Hr, AIR QUENCH/5 MIN, 50 CYCLES	36.0	–	6
	L, (SAME AS ABOVE)	43.0	4.2	6
	T, (SAME AS ABOVE)	42.0	5.7	6
	T, 1950°F/3 MIN, 1650°F/5 MIN, AIR QUENCH/ 3 MIN, 135 CYCLES, 5 PPM SEA SALT	26.0	–	5
	A, 2250°F/5 MIN, AIR QUENCH/3 MIN, 70 CYCLES	34.0	2.8	6
	T, (SAME AS ABOVE)	35.0	1.1	4
	A, 1650°F/1.5 HRS, 2050°F/0.5 HR AIR QUENCH/ 5 MIN, 25 CYCLES	30.0	1.6	4
	A, SAME CYCLE AS ABOVE WITH 5 PPM SEA SALT	17.0	1.7	4

L - 320 - GRIT LONGITUDINAL
T - 320 - GRIT TRANSVERSE
A - AS-NITRIDED

failed at internal pores or inclusions of unreacted silicon. Evidently the oxidation was decreasing the surface damage.

Only limited quantities of as-nitrided NC-350 specimens were available to test. The data for these specimens suggested that the strength decreased after static oxidation. High magnification of the fracture surface showed a network of small surface and subsurface oxide-coated pores which acted as fracture initiation sites. Comparison of this surface with the surface of machined and oxidized NC-350 specimens helped to explain why as-nitrided specimens decreased in strength and machined specimens increased in strength. Oxidation of machined specimens resulted in a uniform, smooth protective surface layer which diminished surface defects during its formation. Oxidation of as-nitrided specimens did not result in a smooth protective surface but instead resulted in surface and subsurface pores which acted as more severe flaws than originally existed.

Cyclic oxidation without sea salt addition tended either to increase the strength of NC-350 RBSN or to have no effect. Cyclic oxidation/corrosion with sea salt addition resulted in buildup of a glassy layer and recession of the surface. Depending upon exposure time and original surface condition, cyclic oxidation/corrosion with sea salt resulted in increased, decreased, or unaffected strength. The testing with 5-ppm sea salt represented an accelerated test compared to the typical engine environment. However, long-term exposure would undoubtedly result in strength degradation and would probably be the life-limiting factor for NC-350 RBSN.

4.3.3 FLASH-OXIDATION TREATMENT OF RBSN

The static-oxidation tests demonstrated that a suitable oxidation exposure could increase the strength of machined RBSN specimens. Therefore, a study was conducted to optimize exposures for the various RBSN materials[14,45] and to determine if the resulting surface oxide layers would protect the material against further oxidation. Specimens of NC-350, RBN122, and RBN101 RBSN materials were "flash" oxidized at various temperatures above 2000°F and then exposed for longer times at 1650 and 2010°F (temperatures shown previously to result in excessive oxidation weight gain and strength reduction for some RBSN materials). Weight change and 4-point flexure strength were measured for each specimen. The strength results are summarized in Table 4-8.

TABLE 4-8. FLASH-OXIDATION TEST RESULTS.

FLASH OXIDATION TREATMENT SOURCE AND CONDITIONS	FLASH OXIDATION TREATMENT ONLY			FLASH OXIDATION TREATMENT FOLLOWED BY EXPOSURE AT 1650°F			FLASH OXIDATION TREATMENT FOLLOWED BY EXPOSURE AT 2010°F		
	NC-350	ACC I.M.	ACC S.C.	NC-350	ACC I.M.	ACC S.C.	NC-350	ACC I.M.	ACC S.C.
CONTROL - NO FLASH OXIDATION	41.7*	35.0	40.8	43.2 (10 HRS)**	23.9 (10 HRS)	32.4 (10 HRS)	34.4 (10 HRS)	40.1 (10 HRS)	35.9 (10 HRS)
FISHER HEAT TREAT, 2010°F/7 HRS	34.6	--	--	42.0 (10 HRS)	--	--	39.7 (10 HRS)	--	--
GARRETT, 2010°F/2 HRS	45.3	--	--	--	--	--	(40.7) (50 HRS)	--	--
FISHER HEAT TREAT, 2190°F/7 HRS	34.9	--	--	44.5 (10 HRS)	--	--	40.9 (10 HRS)	--	--
ACC***, 2410°F/2 HRS	--	34.7	32.5	--	24.5 (50 HRS)	28.0 (50 HRS)	--	32.2 (50 HRS)	31.9 (50 HRS)
FORD, 2650°F/2 HRS	34.9	36.7	34.6	34.3 (50 HRS)	28.5 (50 HRS)	27.7 (50 HRS)	31.3 (50 HRS)	34.1 (50 HRS)	30.2 (50 HRS)
GARRETT, 2460°F/2 HRS	42.8	35.1	38.0	40.6 (10 HRS)	36.5 (50 HRS)	34.3 (10 HRS)	40.0 (10 HRS)	36.0 (10 HRS)	36.8 (10 HRS)

ACC I.M. = ACC INJECTION-MOLDED RBSN (RBN 122)

ACC S.C. = ACC SLIP-CAST RBSN (RBN 101)

*4-POINT FLEXURE STRENGTH IN KSI
**DURATION OF EXPOSURE
***FURNACE BACK-FILLED WITH ARGON DURING HEATUP

Specimens exposed at 1650°F without a prior flash-oxidation treatment showed a continuous weight gain as did the ACC RBSN materials at 2010°F. The flash-oxidation treatments minimized weight gain during 1650°F and 2010°F exposure so that the weight gain versus exposure time curves were nearly flat. For example, as-received NC-350 oxidized 10 hours at 1650°F gained 0.7 percent, whereas flash-oxidized NC-350 gained only 0.02 percent. Visual and SEM examinations indicated that flash-oxidized specimens had a coherent surface oxide layer which apparently provided a passive diffusion barrier to further oxidation. Specimens not flash-oxidized and exposed only at 1650°F did not form a coherent surface layer and were thus susceptable to internal oxidation along open pore channels. The amount of open porosity as well as the size of the interconnected open porosity affected the oxidation behavior. NC-350 had the largest amount of open porosity (10-20 percent) but also the smallest diameter porosity ($\ll 1\mu m$). As a result, the surface of NC-350 was easily sealed by flash oxidation at 2010°F. The RBN101 and RBN122 had less open porosity (8-10 percent) but substantially larger pores ($>15\mu m$) and interconnection channel size ($\sim 1\mu m$). Higher temperature flash-oxidation treatments were required to seal the surface porosity.

Flash oxidation at excessive temperatures resulted in the formation of a thick glassy layer and surface pits, which reduced the four-point flexure strength. The thick surface layer tended to crack during cooling, lessening its effectiveness as a barrier to subsurface oxidation.

Based upon the above study, the following flash-oxidation treatments were selected:

- NC-350 - 2010°F for 2 hours
- RBN 101 and RBN 122 - 2460°F for 2 hours.

4.3.4 DUTY CYCLE OXIDATION

A gas-fired furnace containing eight stress-rupture fixtures was used to determine how the properties of NC-350 and RBN 122 would be affected by cyclic exposure to simulated engine operating temperatures under a 15-ksi load.[15] The two cycles identified in Table 4-9 were evaluated. Cycles A and B, respectively, simulated second-stage and first-stage stator temperatures for a typical engine cycle.

TABLE 4-9. THERMAL CYCLES FOR FURNACE DUTY-CYCLE TESTING.

CYCLE A, RBN 122		CYCLE B, NC-350	
TIME (MIN)	TEMPERATURE (°F)	TIME (MIN)	TEMPERATURE (°F)
10	1200	10	1400
20	1500	20	1700
20	1800	20	2000
20	2000	20	2200
40	1500	40	1700
10	1200	10	1400
45	300	45	300

The results of the duty cycle oxidation study are summarized in Table 4-10. No stress reputure failures were observed at 15-ksi. The material strengths after duty cycle oxidation were equivalent to or higher than the strengths of as-received test bars. The duty cycle tests indicated that the RBSN materials were acceptable from an oxidation-stability point of view for rig and engine testing.

4.3.5 STRESS RUPTURE OF RBSN

Stress rupture and creep tests were conducted at IIT Research Institute using the procedures described previously in Section 4.1.4. The results are summarized in Table 4-11.[10] The majority of the specimens survived the required 50 hours at 150- to 200-percent design stress at temperatures ranging from 1950°F to 2450°F. Specimens that fractured did so at pre-existing surface and internal flaws. No slow crack growth or deformation were observed except for NC-350 specimens 1333-1337, which came from a single batch.

Creep rate was evaluated in four-point flexure at outer fiber stresses up to 35 ksi for RBN 101, 40 ksi for Ford RBSN, and 45 ksi for NC-350 at temperatures up to 2450°F. The creep rate was consistently below the detection limit of the apparatus $(< 0.5 \times 10^{-5}\ \dot{\epsilon}\ hr^{-1})$.

TABLE 4-10. RESULTS OF THERMAL DUTY CYCLE TESTS.

MATERIAL	FLASH OXIDATION	CYCLE	NUMBER OF CYCLES	RT STRENGTH (KSI)	1650°F STRENGTH (KSI)	WEIGHT CHANGE (PERCENT)
RBN-122	NONE	A	5	$\bar{\sigma}$ = 35.2 S.D. = 4.5	$\bar{\sigma}$ = 37.3 S.D. = 6.5	Δwt = 0.24 S.D. = 0.07
RBN-122	2460°F/ 2 HOURS	A	5	$\bar{\sigma}$ = 44.7 S.D. = 1.0	$\bar{\sigma}$ = 50.7 S.D. = 3.5	Δwt = 0.28 S.D. = 0.09
RBN-122	2460°F 2 HOURS	A	25	$\bar{\sigma}$ = 36.7 S.D. = 2.4	$\bar{\sigma}$ = 52.0 S.D. = 1.8	Δwt = 0.23 S.D. = 0.12
NC-350	NONE	B	5	$\bar{\sigma}$ = 43.8 S.D. = 9.5	$\bar{\sigma}$ = 50.7 S.D. = 7.7	Δwt = 0.98 S.D. = 0.98
NC-350	2010°F/ 2 HOURS	B	5	$\bar{\sigma}$ = 35.2 S.D. = 4.2	$\bar{\sigma}$ = 62.9 S.D. = 4.9	Δwt = 0.68 S.D. = 0.14
NC-350	2010°F/ 2 HOURS	B	25	$\bar{\sigma}$ = 45.5 S.D. = 5.3	$\bar{\sigma}$ = 55.1 S.D. = 8.8	Δwt = 1.65 S.D. = 0.94

$\bar{\sigma}$ = AVERAGE FOUR-POINT FLEXURE STRENGTH
S.D. = STANDARD DEVIATION

TABLE 4-11. STRESS RUPTURE DATA FOR RBSN.

NC-350 RBSN				RBN 101 RBSN			
SERIAL NUMBER	TEMP. (°F)	STRESS (KSI)	TIME (HRS)	SERIAL NUMBER	TEMP. (°F)	STRESS (KSI)	TIME (HRS)
1337	1950	25	50	1781**	2250	25	0.2*
1333	1950	25	50	1782**	2250	25	50
1334	1950	35	35	3448**	2250	30	50
1335	1950	40	46.9*	3452**	2250	30	0.3*
1336	1950	45	0.02*	3454**	2250	30	50
1619	2250	40	50	3455**	2250	30	50
1621	2250	40	50	3456	2250	35	0.1*
1622	2250	40	50	3112***	2250	30	50
1623	2250	40	50	3113***	2250	30	1 MIN.*
2326	2250	30	50	3114***	2250	30	50
2327	2250	30	50	3115	2250	30	50
2328	2250	35	1*	3116***	2450	30	50
2329	2250	35	50	3117***	2450	30	50
2330	2250	35	0.4*	3118***	2450	30	50
1739	2250	25	50	3119***	2450	30	0.3*
1743	2250	25	50				
1748	2250	30	50				
1752	2250	30	0.08*				
1760	2250	30	50				

* FRACTURED
** AS-NITRIDED SURFACE
*** LONGITUDINALLY MACHINED

Test bars surviving stress rupture and creep testing for 50 hours were subsequently fractured in four-point flexure. The resulting strength was equivalent to the baseline strength of the materials, demonstrating that the stress rupture exposures had not degraded the RBSN materials.

4.3.6 CYCLIC FATIGUE OF RBSN

Cyclic fatigue testing of RBSN was conducted at IIT Research Institute under subcontract to Garrett.[49] The test procedures were previously discussed in Paragraph 4.1.5.

The fatigue test results for Norton NC-350 and ACC RBN101 RBSN are summarized in Table 4-12.[10] Very few failures occurred for the NC-350 and examination of the fracture surfaces revealed no indication of a fatigue mechanism. More

TABLE 4-12. CYCLIC FATIGUE DATA FOR RBSN MATERIALS.

NC-350, AS-NITRIDED				RBN 101, AS-NITRIDED				RBN 101, TRANSVERSE MACHINED			
SERIAL NO.	STRESS (KSI)	TEMP. (^{o}F)	CYCLES	SERIAL NO.	STRESS (KSI)	TEMP. (^{o}F)	CYCLES	SERIAL NO.	STRESS (KSI)	TEMP. (^{o}F)	CYCLES
3421	30	1950	301,400	3597	7*	1950	--	3033	25*	1950	170
3422	30	1950	301,300	3600	9*		50	3041	25		318,000
3423	35	1950	308,200	3601	10*		165	3042	30*		97,000
3424	35	1950	1,091,500	3604	10*		268	3274	20*	1950	20
1610	25*	2200	274,800	3598	10		1,000,000	3271	24*		23
1612	25	2200	303,000	3595	13.5*		20	3269	30		293,000
1629	25	2200	320,100	3462**	10	1950	311,000	3270	33*		47
1613	30	2200	302,300	3467**	10*		80	3284	20	1950	340,000
1614	30	2200	496,500	3459**	11*		18	3279	25*		527
1611	30	2200	324,900	3460**	20*		30	3603	25	1950	1,020,000
1630	30	2200	300,700	1788	20	2200	301,000	3596	25		313,000
1615	35*	2200	20,400	1789	25		377,000	3602	29*		125
1616	35	2200	363,900	1804	23*	2200	28	1772	20	2200	301,000
1631	35	2200	303,400	1800	25		300,000	1785	25		300,000
2325	25	2200	303,500	1803	29.5*		21	1793	30		311,000
2331	25	2200	304,600	1801	30		322,000	2987	25	2200	334,000
2335	25	2200	307,500					2996	30		300,000
2324	30*	2200	22,000					3026	25	2200	1,024,000
2332	30	2200	315,100					3028	30*		90
2336	30	2200	1,064,000								
2323	35*	2200	25								
2334	35*	2200	63,000								
2338	35*	2200	1,500								

* FRACTURED
** MATERIAL HAVING A POROUS SURFACE AND LOW BASELINE STRENGTH

failures occurred for the RBN 101 material, especially during early cycles while the load was being adjusted. The fracture surfaces showed no indication of a fatigue mechanism. The fracture origins were typically at flaws of a size range likely to cause fast fracture for the applied loads.

Specimens surviving the cyclic testing were subsequently fractured in four-point flexure. The resulting strength was comparable to the baseline strength of the materials.

The cyclic testing of the RBSN and hot-pressed Si_3N_4 materials in this program provided assurance that the materials would not fail in cyclic fatigue under the

TSE331C-1 engine operating conditions but did not determine their susceptibility to fatigue under other conditions. To do this would require a larger number of tests and refinements in the test setup. It would also be advisable to proof test the test bars prior to fatigue testing to minimize the confusion caused by overstress failures during the fatigue test.

4.4 PROPERTY SUMMARY

The material characterization studies indicated that the Norton NC-132 hot-pressed Si_3N_4 was acceptable for rotor blades and would have substantial property margin for 50 hours TSE331C-1 engine operation. The studies also indicated that the RBSN materials were acceptable for static structure components but that the strength margin was not as great as desired. Of further concern was the batch-to-batch and within-batch variability of the RBSN materials. The decison was made to progress to rig and engine testing but to pre-test each RBSN part in the static structure rig prior to engine testing.

5.0 NONDESTRUCTIVE EVALUATION

Due to the low fracture toughness and lack of ductility of ceramics, their strength is very sensitive to small internal and surface defects such as cracks, voids, inclusions and scratches. An applied tensile stress concentrates at the tip of microcracks associated with these defects and leads to macrocracks that can propogate to cause component failure. An important task of the DARPA/NAVY program was to evaluate nondestructive evaluation (NDE) techniques for detection of strength-limiting flaws in the candidate ceramic materials.[64]

The NDE program was conducted in three stages:

(1) Based upon component stress analysis, identify the critical flaw size for each material and prepare standards with known defects spanning the critical flaw size.

(2) Examine the standards by state-of-the-art and emerging NDE techniques to establish defect detection limits as a function of ceramic material, defect type and size, and NDE method.

(3) Apply these results to NDE of the ceramic engine components and evolve accept-reject criteria.

Figure 5-1 outlines the ceramic NDE program.

5.1 NDE STANDARDS

A variety of ceramic specimens containing known defects were prepared during the program to be used as NDE standards. These included step-block penetrameters, seeded billets, test bars and rotor blades with Knoop or Vickers indentations, and actual hardware containing cracks.

As the stress analysis was completed for each component, estimates of the critical flaw size requiring resolution by NDE were calculated for the highly-stressed regions of each component. These estimated critical flaw sizes for the rotor blades and stator vanes are summarized in Table 5-1. It is apparent that surface or near-surface defects in the attachment region of the rotor blade and in the trailing edge of

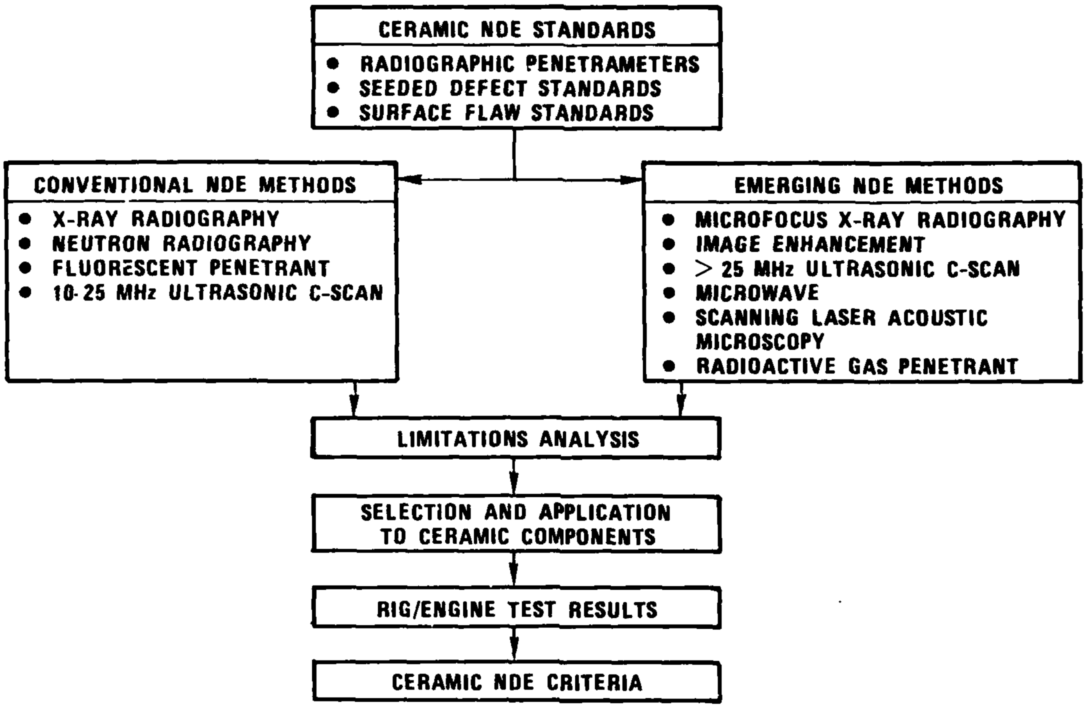

Figure 5-1. Ceramic NDE Program.

TABLE 5-1. ESTIMATED CRITICAL FLAW SIZE FOR THE TSE331C-1 ROTOR BLADES AND STATOR VANES.

HPSN ROTOR BLADES	ATTACHMENT, INCHES (MICRONS)	AIRFOIL, INCHES (MICRONS)
• SURFACE CRACKS	0.0014 – 0.0031 (35 – 80)	0.012 – 0.028 (300 – 700)
• SUBSURFACE SPHERICAL DEFECT	0.004 (100)	0.04 (1000)
RBSN STATOR VANES	TRAILING EDGE, INCHES (MICRONS)	OVERALL, INCHES (MICRONS)
• SURFACE CRACKS	0.002 – 0.006 (60 – 150)	0.008 – 0.0024 (200 – 600)
• SUBSURFACE SPHERICAL DEFECT	0.008 (200)	0.03 (750)

the stator vane are most critical and that NDE resolution in the 0.002-0.005-inch range is required.

5.1.1 STEP-BLOCK PENETRAMETERS

Step-block penetrameters were prepared from NC-132 hot-pressed Si_3N_4[2] and Ceramic Systems, Inc.* 2.6g/cm^3 RBSN[3] to comply with ASTM E94-68. The dimensions, as identified in Figure 5-2, were achieved by a combination of diamond grinding the surfaces and ultrasonic trepanning the holes. The 0.0008, 0.0012, and 0.0016-inch holes were too small to be accurately machined with the existing equipment and were not included in the HPSN penetrameter. Completed step-block penetrameters are shown in Figure 5-2.

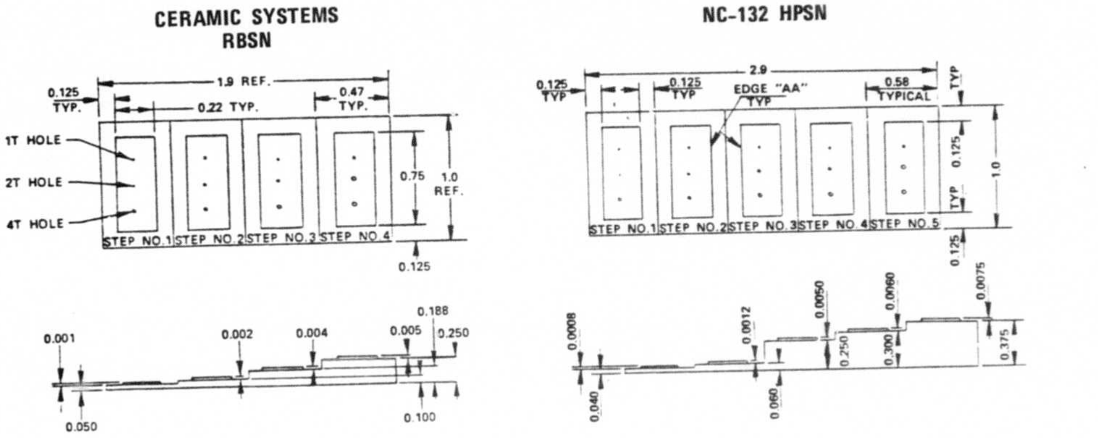

HOLE TYPE	HOLE DIAMETER - IN.			
	STEP NUMBER			
	1	2	3	4
1T 2T 4T	0.001 0.002 0.004	0.002 0.004 0.008	0.004 0.008 0.016	0.005 0.010 0.020
HOLE DEPTH-IN.	0.001	0.002	0.004	0.005

HOLE TYPE	HOLE DIAMETER - IN.				
	STEP NUMBER				
	1	2	3	4	5
1T	.0008 △	.0012 △	.005	.006	.0075
2T	.0016 △	.0024	.010	.012	.015
4T	.0032	.005	.020	.024	.030
HOLE DEPTH-IN.	.0008	.0012	.005	.006	.0075

△ = NOT MACHINED

RBSN STEP BLOCK PENETRAMETER **HPSN STEP BLOCK**

Figure 5-2. Step-Block Penetrameters of Candidate Ceramic Materials.

---

*A manufacturer of RBSN, located in Detroit, Michigan.

5.1.2 SEEDED-BILLET STANDARDS

Prior studies have shown that the strength-limiting flaws in Si_3N_4 are often inclusions or low-density regions that are traceable to fabrication steps such as powder processing, mold loading or sintering.[65,66] Examples are (1) tungsten carbide (WC) or iron (Fe) base alloy particles picked up in the powder during powder comminution and sizing, (2) boron nitride (BN) or graphite (C) particles picked up during mold loading (for hot pressed Si_3N_4), and (3) silicon (Si) or silicon carbide (SiC) either present in the original powder or retained in the microstructure as a separate phase during high-temperature densification. To evaluate the NDE detection capabilities for these types of process-related internal flaws, seeded billets of NC-132 hot-pressed Si_3N_4 and NC-350 reaction-bonded Si_3N_4 were procured from the Norton Company.[2,64] The types and sizes of the internal defects and their distribution in the billets are illustrated in Figure 5-3. The range in size was selected to span the estimated critical flaw sizes identified for HPSN and RBSN in Table 5-1.

5.1.3 SURFACE DEFECT STANDARDS

The objective was to prepare standards containing surface cracks of known dimensions. Petrovic et al.[67] and Lawn et al.[68] have shown that semicircular cracks

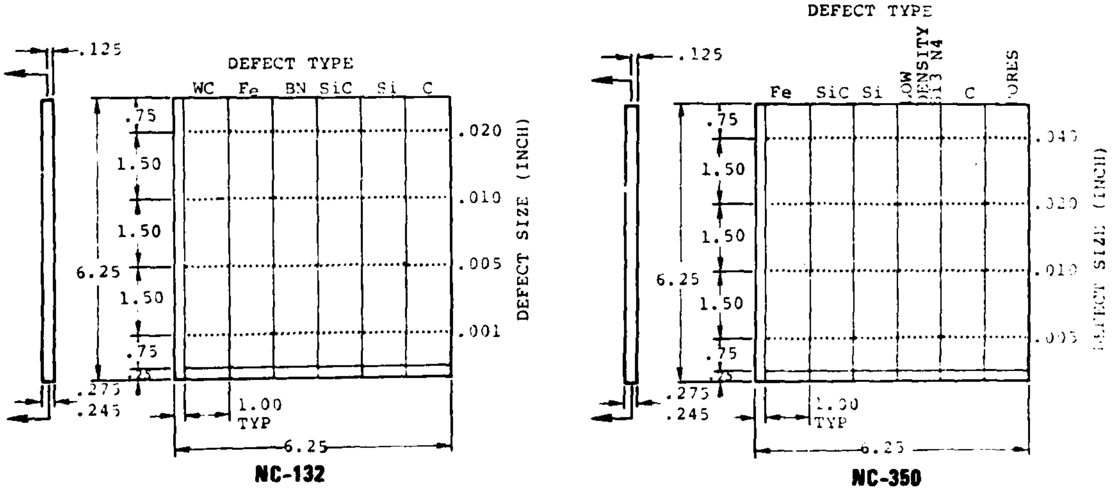

Figure 5-3. Seeded-Defect Standards Fabricated from (a) Hot-Pressed Silicon Nitride, and (b) Reaction-Bonded Silicon Nitride.

of visually measurable size can be produced by Vickers or Knoop microhardness indentations. To prepare NDE standards for this program, Vickers indentations at 1, 5, 10, 20, and 50 Kg loads were produced in HPSN test bars 0.125 by 0.250 by 3.0 inches. Indentations for 50 Kg and 10 Kg loads are shown in Figure 5-4. The crack can be seen extending from the points of the indentation. Some test bars with the 10 Kg indentation were surface-ground to remove the indentation, while leaving the subsurface crack.

The NDE standards with indentations were used mainly for evaluation of the scanning laser acoustic microscopy (SLAM) technique. To study the feasibility of applying SLAM to a complex shape, a HPSN rotor blade was used. Knoop indentations with loads of 2 and 3 Kg were made in the neck and dovetail regions of the blade attachment. The major axis of the indentations was oriented parallel to the blade attachment length and perpendicular to the machining direction.

5.1.4 COMPONENT STANDARDS

As the program progressed and ceramic hardware became available, individual components were encountered having well-defined defects such as inclusions, low-density areas, knit lines, and trailing-edge cracks. Examples of these were set aside as standards and were used in conjunction with the corresponding NDE records to define accept-reject criteria for subcontractor and in-house inspections.

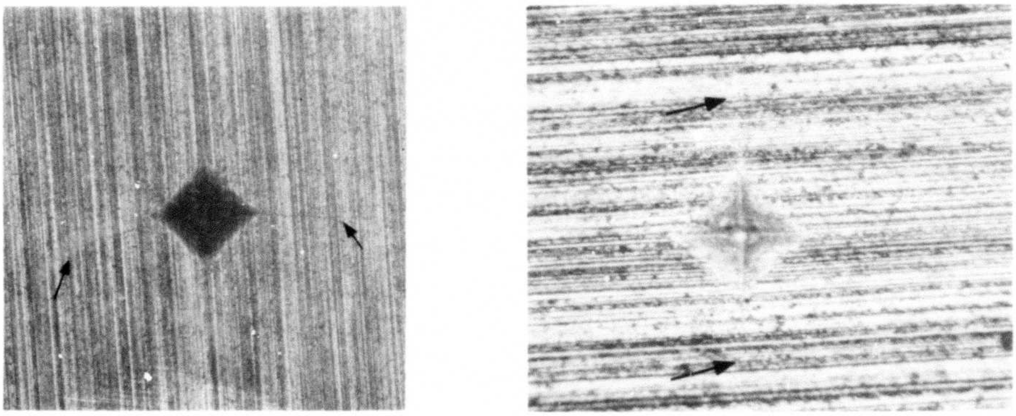

ARROWS INDICATE APPROXIMATE LENGTH OF CRACK

50 Kg INDENTATION **10 Kg INDENTATION**

Figure 5-4. Vickers Indentations in NC-132 Hot Pressed $S1_3N_4$. Arrows Indicate the Extent of the Surface Crack Produced.

5.2 EVALUATION AND DEVELOPMENT OF NDE TECHNIQUES

The NDE standards were used to determine the resolution-capabilities of state-of-the-art NDE methods such as conventional X-ray radiography, neutron radiography, ultrasonic C-scan, and dye penetrants. In general, the state-of-the-art techniques were not adequate to resolve defects in the critical flaw size range. This led to extension of the capabilities of these NDE techniques (e.g., transducer and setup modification of ultrasonic C-scan, utilization of microfocus X-ray radiography) and evaluation of emerging methods (e.g., computerized image enhancement of radiographs, microwave, SLAM). The following paragraphs describe the results of the evaluation and development of NDE techniques.

5.2.1 X-RAY RADIOGRAPHY

A Siefert 200-KV, 5-ma unit was used to obtain conventional X-ray radiographs. A Magnaflux 100-KV, 1-ma unit capable of achieving a 50-micron focal spot size was used to obtain microfocus X-ray radiographs. The step-block penetrameters were used to optimize the setup and equipment settings for conventional and microfocus X-ray radiography to obtain acceptable exposure levels (film density >2.0) as a function of the HPSN and RBSN material thickness.

The hot-pressed and reaction-bonded Si_3N_4 seeded billets were examined by the conventional and microfocus techniques.[69,2,3] The WC and Fe inclusions over the complete size range (including 0.001 inch) were detected by both methods. The largest C and void defects were also detected by both methods, but the microfocus system provided slightly better sensitivity. BN, Si, and SiC inclusions were not visible by either method for the hot-pressed Si_3N_4, but the largest ones were detected in the RBSN. Radiographic reversal prints (prints made directly by using the radiographic film as the negative) for the HPSN and RBSN seeded billets are shown in Figure 5-5. Some detail is lost during photographic reproduction so that some of the smaller defects that were visible on the film are not visible in the figure.

5.2.2 IMAGE ENHANCEMENT OF RADIOGRAPHS

Visual evaluation of a radiograph is subjective and is limited by the ability of the human eye to distinguish between various shades of gray. To obtain a less subjective interpretation of radiographs and improved contrast sensitivity, a computerized image enhancement system at Garrett was used.[69,2,3] The system is

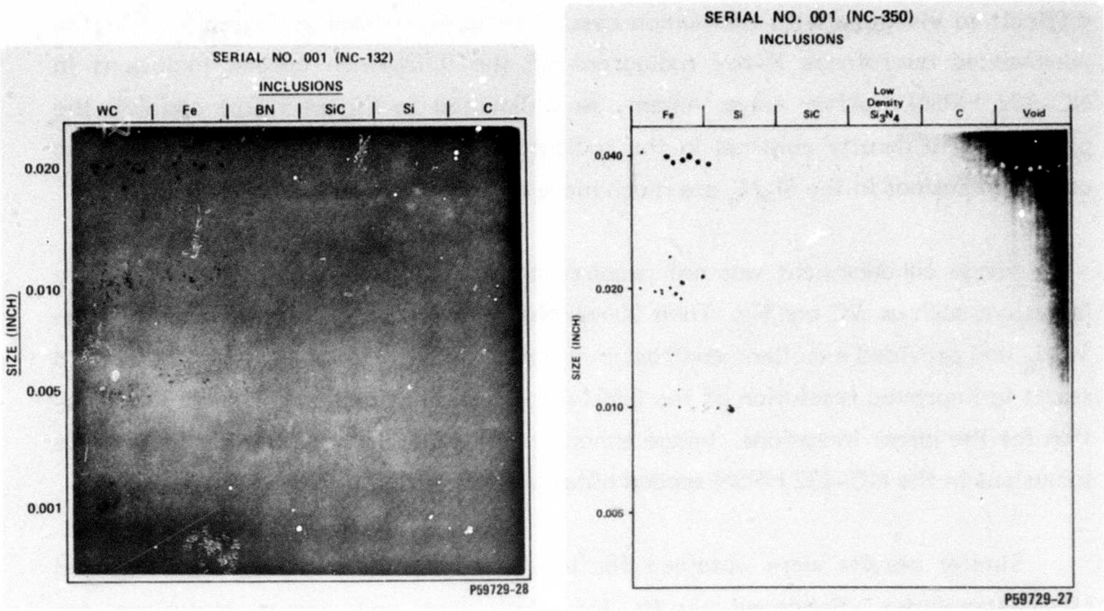

Figure 5-5. Radiographic Reversed Prints for NC-132 HPSN and NC-350 RBSN Seeded-Defect NDE Standards.

similar to those employed to study images from space exploration programs and satellite photographs. In the case of radiography, a television camera scans the back-lighted radiograph and transfers the image data to a digitizer. The digitizer divides the image into an array of 480 by 512 discrete picture elements, or pixels. Each pixel is assigned a gray-scale value ranging from 0 (black) to 255 (white). The typical human eye can distinguish only about two dozen gray levels in a radiograph. The digitized data is transmitted into a computer and manipulated by mathematical software programs and image-reconstruction techniques to produce an enhanced image, which is displayed on a standard black-and-white TV monitor.

To evaluate the effectiveness of image enhancement, constant density radiographs for each type of defect in the seeded billets were obtained at three X-ray exposure levels with the microfocus X-ray system. The focusing capability of the system allows examination of local areas and direct magnification of the image without loss in contrast. The microfocus X-ray radiographs were then evaluated with the use of the image-enhancement system.

As discussed earlier, carbon was difficult to detect by radiography. Carbon, silicon, and nitrogen are all low atomic weight elements and do not strongly absorb X-rays. Carbon in Si_3N_4 produces a low-contrast radiographic image that is difficult to visualize with the human eye. This is illustrated in Figure 5-6[2] by the unenhanced microfocus X-ray radiograph of the 0.020-inch carbon inclusions in NC-132 HPSN. After enhancement, as illustrated in Figure 5-6(b) and (c), the presence of a density contrast in the radiograph and the probable presence of the carbon inclusions in the Si_3N_4 are much more definitive.

Image enhancement was not required to detect the presence of high density inclusions such as WC and Fe. Their X-ray absorption was substantially greater than Si_3N_4 and provided excellent contrast in the radiograph. However, enhancement did result in improved resolution of the 0.001-inch inclusions and better shape information for the larger inclusions. Image enhancement results for the smaller WC and Fe inclusions in the NC-132 HPSN seeded billet are illustrated in Figure 5-7.

Similar results were obtained for image enhancement of the RBSN seeded billet standards. Enhanced results for small iron and carbon inclusions are illustrated in Figure 5-8.

Based upon the encouraging results with the seeded-billet standards, microfocus X-ray radiography and image enhancement were applied to TSE331C-1 engine components in the critical high-stress regions and in regions prone to contain fabrication defects. Some results for typical defects encountered in RBSN components are shown in Figure 5-9.

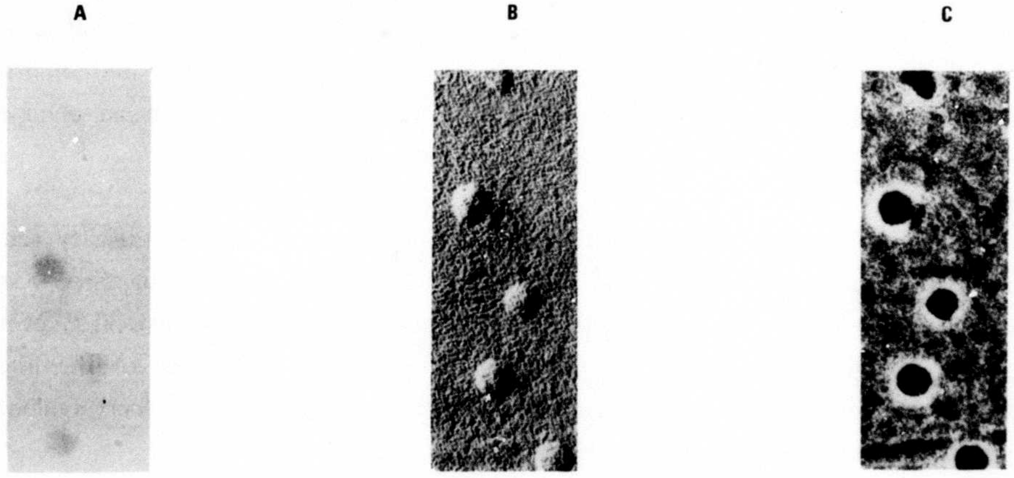

Figure 5-6. Radiographic Data for 0.020-Inch Carbon Inclusion in NC-132 HPSN. (a) Original Microfocus X-Ray Radiograph (b) Computerized Topographical Output (c) Computerized Edge Enhancement Output.

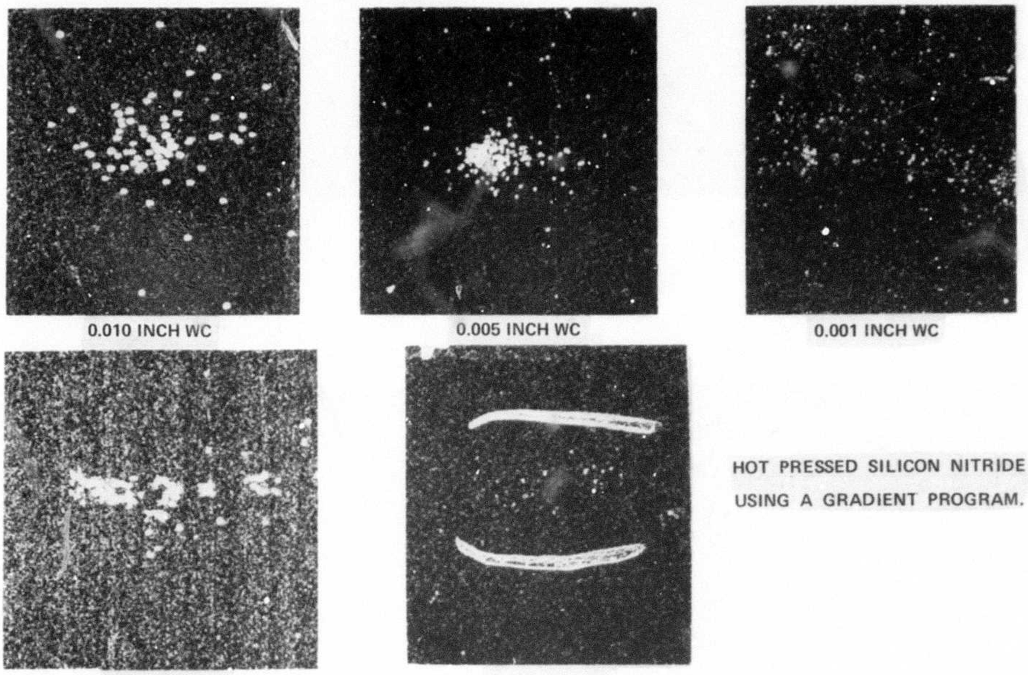
0.010 INCH WC

0.005 INCH WC

0.001 INCH WC

0.010 INCH Fe

0.001 INCH Fe

HOT PRESSED SILICON NITRIDE
USING A GRADIENT PROGRAM.

Figure 5-7. Image Enhancement of Tungsten carbide (WC) and Iron (Fe) Inclusions in the NC-132 HPSN Seeded Billet Standard.

5.2.3 ULTRASONIC NDE

X-ray radiography was effective for detecting high-density inclusions of critical flaw size and relatively large voids and cracks, but was not adequate for small low-density inclusions or voids. Ultrasonics was identified as an approach that would have a better chance of detecting these types of flaws. Ultrasonics uses acoustic waves that are perturbed by elastic variations within a material. They are reflected, refracted, and scattered at interfaces, structures, pores, density variations, and inclusions and therefore have potential for detecting a broader range of defects than can be detected by electromagnetic-waves such as X-rays.

The seeded-billet standards were used to evaluate various ultrasonic systems.[2,3,70] Initially, a conventional ultrasonic internal-gating technique was tried

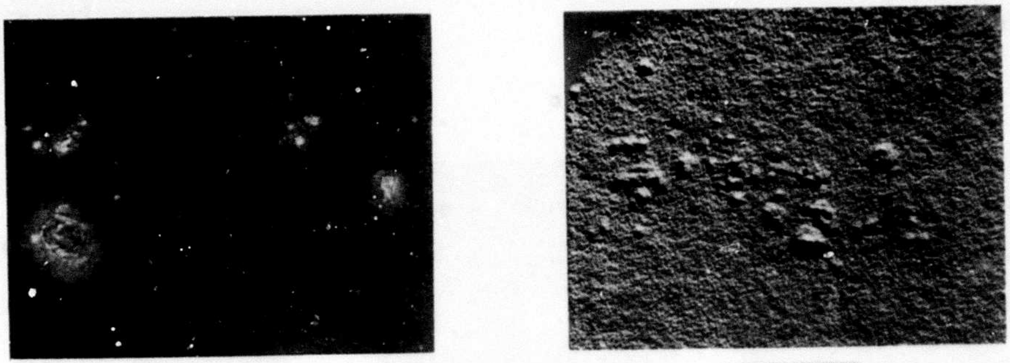

0.010 INCH

0.005 INCH

(A) IRON INCLUSIONS

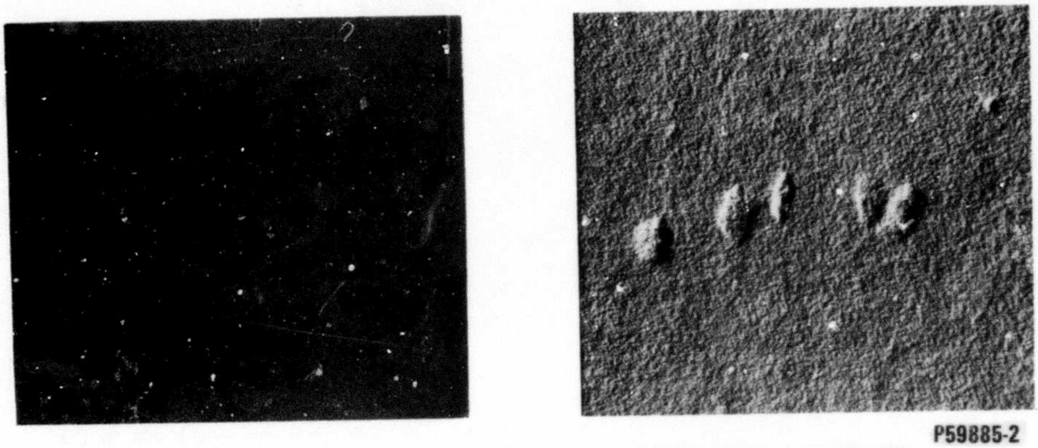

P59885-2

(B) CARBON INCLUSIONS - BOTH COMPUTERIZED OUTPUTS ARE OF 0.010 INCH CARBON.

Figure 5-8. Image-Enhanced Radiograph of Inclusions in the NC-350 RBSN Seeded Billet.

at Garrett. An Automation Industries C-scan system, capable of 25-MHz operation, and an immersion, spherically-focused transducer rated at 25 MHz with a focal length in water of 1.5 inches were used to examine the hot-pressed billets. Electronic gating within the material was used to display signals from defects whose amplitude exceeded a predetermined voltage threshold but produced poor indications of the subsurface inclusions on the recorded C-scans. The cathode ray tube (CRT) displays also indicated low reflected signal amplitudes from the inclusions.

An alternate method was subsequently employed that successfully detected a greater number of inclusions in the HPSN billets. Rather than electronic gating

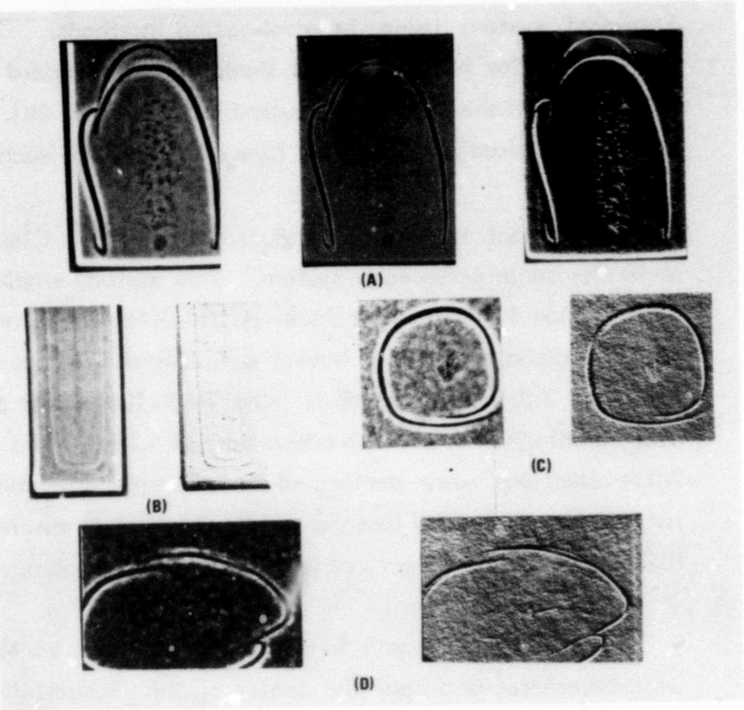

COMPUTERIZED OUTPUTS,
(A) CASTING VOIDS,
(B) CASTING LAMINATIONS
(C) SEGREGATED POROSITY AND,
(D) CASTING SHRINKAGE.

Figure 5-9. Image-Enhanced Radiographs of Flaws in Reaction-Bonded Silicon Nitride.

within the material, gating was set directly on the signal representing the back surface of the billet. In this manner, any subsurface anomaly that would reduce the ultrasonic energy reaching the back surface produced a reduction in the back surface signal amplitude. This technique, referred to as a loss-of-back-reflection, requires smooth and parallel front and back surfaces to negate the contribution of surface roughness and undulations. A machined billet thickness of 0.250 inch was required to simulate the nominal thickness of the highly stressed neck region in the HPSN rotor blades. Since the billets did not have sufficient stock to allow for total surface clean-up and still achieve a thickness of 0.250 inch, optimum ultrasonic surface conditions were compromised to retain a billet thickness of 0.250 inch.

The loss-of-back-reflection technique represented an improvment over the initial internal-gating technique but was still not optimum. The pulser/receiver unit was modified and recalibrated, and additional immersion transducers were procured.

An Aerotech Laboratories 25-MHz alpha transducer, having a 0.250-inch diameter element and a focal length in water of 1.5 inches, was selected based upon laboratory sensitivity experiments. The billets were then reevaluated with this improved system using internal-gating methods. The results are shown in Figure 5-10 for NC-132 HPSN seeded-billet standard serial number 001 and for NC-350 RBSN seeded-billet standard serial number 001. Both high-density and low-density inclusions in the critical flaw size range for each material were detected.

Additional effort was conducted at TRW in Cleveland, Ohio, using their 45 MHz ultrasonic pulse-echo system. This system employed a TRW-100 pulser, an Erdman Model 1177B pulser/receiver and defect gate, and an Aerotech Laboratories 45 MHz alpha transducer having a 0.25-inch piezoelectric element and a focal length of 2.0 inches in water. The TRW-100 pulser provides an output pulse of approximately 50 volts, with a rise time of 4.25 ns when loaded with this transducer. All evaluations were performed in an immersion pulse-echo mode, and C-scan recordings used a TRW internal defect standard to ensure that at least a 125-micron (0.005-inch) tungsten-carbide inclusion was detectable.

TRW evaluated both longitudinal and shear 45 MHz waves. The logitudinal waves were focused near the center of the seeded-billet. The shear waves were focused near the back surface at an incident angle of 11 degrees. The results are illustrated in Figure 5-11 for HPSN seeded-billet serial number 002. Shear waves provided greater sensitivity than longitudinal waves.

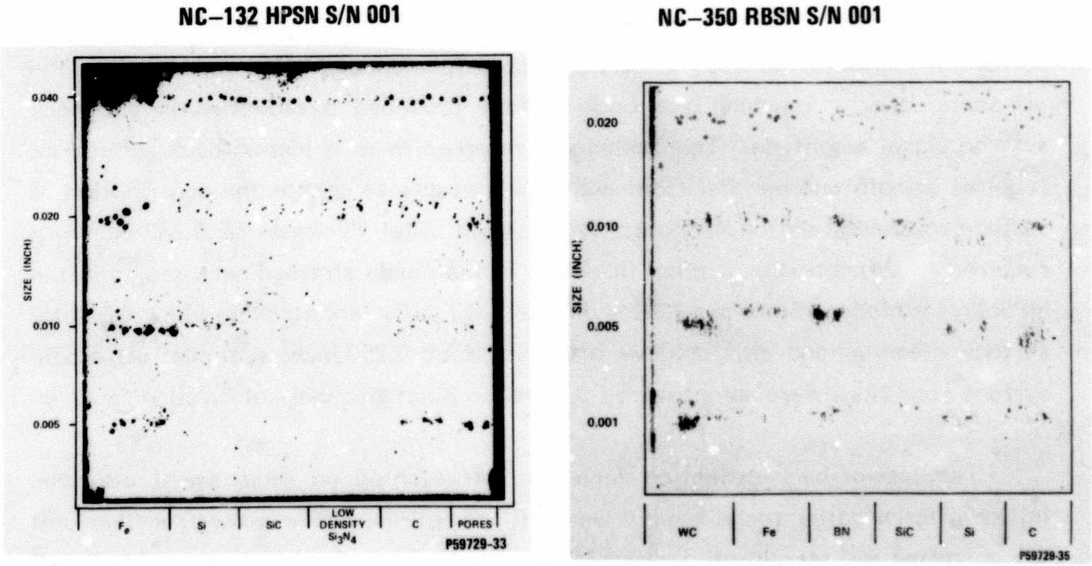
NC–132 HPSN S/N 001

NC–350 RBSN S/N 001

Figure 5-10. 25 MHz Ultrasonic C-Scans of HPSN and RBSN Seeded-Defect Billets Conducted at Garrett.

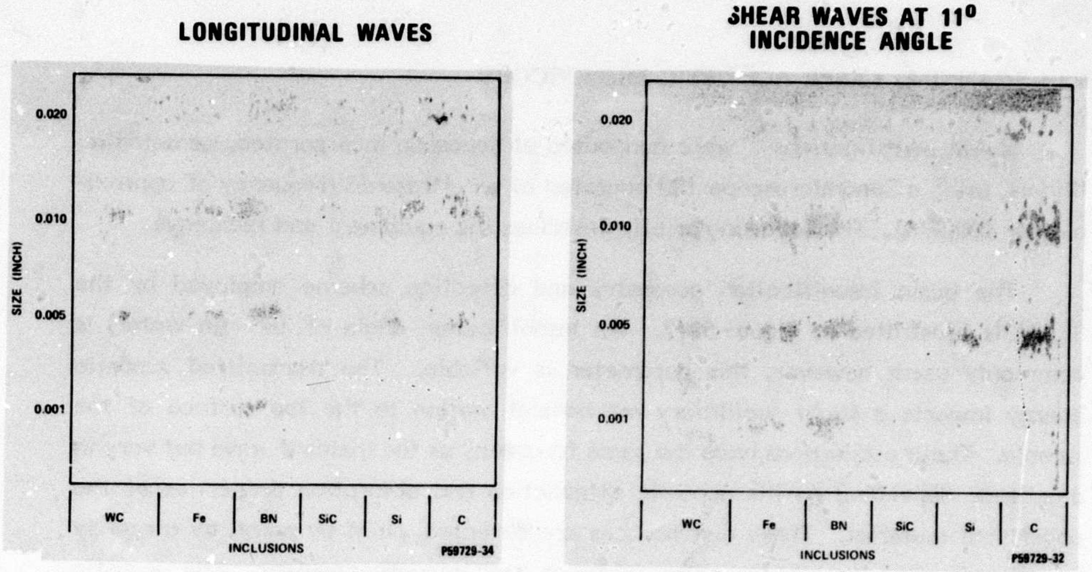

Figure 5-11. 45 MHz Ultrasonic C-Scans Conducted at TRW for HPSN Seeded-Defect Billet Serial Number 002.

Figures 5-10 and 5-11 suggest that ultrasonic NDE is superior to radiography. This would be the case if only flat billets with defects at their mid-plane and with machined surfaces were to be inspected. However, there are limitations to ultrasonic C-scan evaluation of turbine engine hardware. First, special contour-following fixtures and computerized data-handling systems are required for complex shapes. These were not available during the program and are only becoming available now. Second, conventional ultrasonic inspection cannot evaluate near-surface material. A dead zone exists near the specimen or component surface due to transducer ringing and electronic signal-damping. In HPSN, which has twice the sonic velocity of steel, the near-surface dead zone is substantial. For instance, assuming a pulse duration time of 2.5×10^{-5} second and a sonic longitudinal velocity of 11×10^{5} cm/sec, a dead-zone thickness of 0.054 inch exists. This is 54 percent of the thickness of a 0.100-inch section of HPSN.

Several approaches have potential for reducing or eliminating the near-surface dead zone, but they were not available during the NDE study conducted in this program. They include ultrasonic surface waves, scanning photoacoustic microscopy (SPAM),[71] scanning laser acoustic microscopy (SLAM),[72] highfrequency ultrasonics,[73] and microwaves.[74] NDE standards fabricated under this program were made available to other programs evaluating these new techniques. Some results for SLAM and microwaves are discussed below.

5.2.4 SCANNING LASER ACOUSTIC MICROSCOPY

SLAM investigations[72] were conducted at Sonoscan Incorporated, Bensenville, Illinois, using a Sonomicroscope 100 operated at an ultrasonic frequency of approximately 100 MHz. The following briefly describes the equipment and technique.

The basic insonification geometry and detection scheme employed by the SLAM is illustrated in Figure 5-12. An insonification angle of 10° (in water) is commonly used; however, this parameter is variable. The transmitted acoustic energy imparts a slight oscillatory mechanical motion to the top surface of the sample. These oscillations have the same frequency as the incident wave but vary in amplitude depending on the acoustic attenuation and absorption properties of the underlying material. These disturbances are detected, point by point, by a rapidly scanning focused laser beam which drives an opto-acoustic receiver. The acoustic image is then displayed on the TV monitor where the white regions correspond to areas of the sample with good acoustic transmission properties, while the darker areas of the micrographs are regions of higher ultrasonic attenuation due to increased scattering. If the sample has a good surface finish, an acoustic image can be obtained from the light specularly reflected directly from the surface. When this

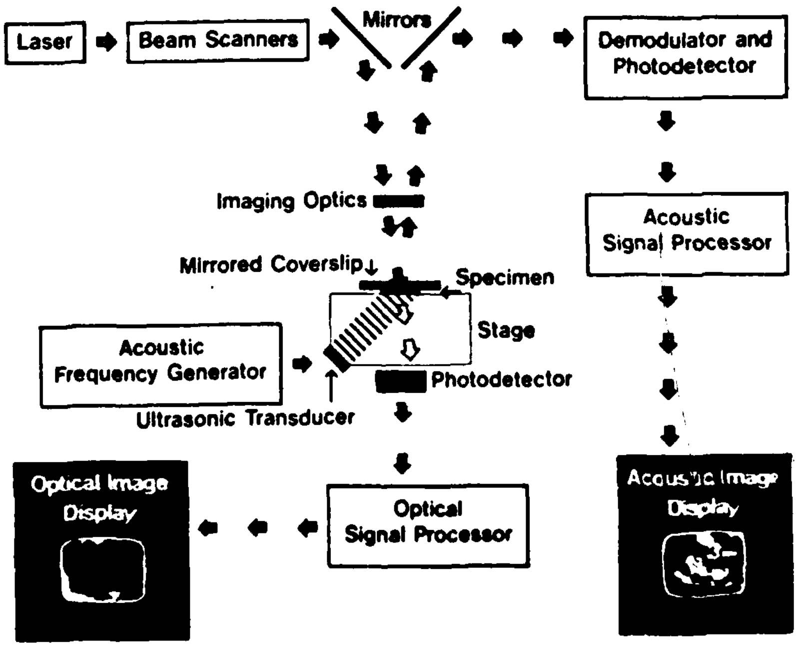

Figure 5-12. Simplified Block Diagram of the Sonomicroscope 100.

is not the case, a mirrored coverslip is placed in acoustic contact with the top surface of the sample, and light reflected from the coverslip is used to form the acoustic image.

The suface defect standards with 10Kg Vickers indentions described in Paragraph 5.1.3 were used for an initial evaluation of the SLAM technique. As shown in Figure 5-13, the indentation was easily detected by SLAM. Subsequently, 0.0017 inch (40 microns) was ground off the surface to remove the indentation mark but leave the surface crack extending inwards from the indentation. This was also detected by SLAM, as shown in Figure 5-14.

Figure 5-13. Frequency-Modulation Amplitude SLAM Photomicrograph of a 10 Kg Vickers Indentation in HPSN (25X Magnification).

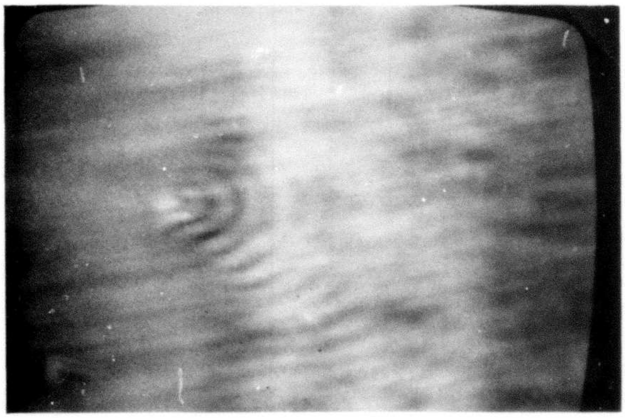

Figure 5-14. Frequency-Modulation Amplitude SLAM Photomicrograph of a 10 Kg Vickers Indentation in HPSN after Removal of 0.0017 Inches of Material (25X Magnification).

An HPSN turbine blade with 2Kg and 3Kg Knoop indentations in the attachment region was also evaluated by SLAM. The defects were not detected. Difficulties were encountered in fixturing, and it was not determined whether these precluded detection of the indentations or if the indentation sizes were below the level of detectability. Further studies would be necessary.

5.2.5 MICROWAVE NDE

The HPSN seeded-defect standard Serial No. 002 was provided to Stanford Research Institute for evaluation of their 98 GHz microwave system. Encouraging results were obtained, especially for the silicon inclusions which had been difficult to detect by other techniques.[6,70] Figure 5-15 illustrates the microwave C-scan results for the region of the seeded-billet containing silicon.

5.2.6 NEUTRON RADIOGRAPHY

Neutron beams behave in an opposite manner to X-rays and gamma rays with respect to their attenuation characteristics in materials. Neutrons pass through heavy metals with relative ease but are attenuated by light metals and non-metallic materials. The attenuation of a beam of neutrons is due to both neutron capturing by the nuclei in the material and scattering within the material.

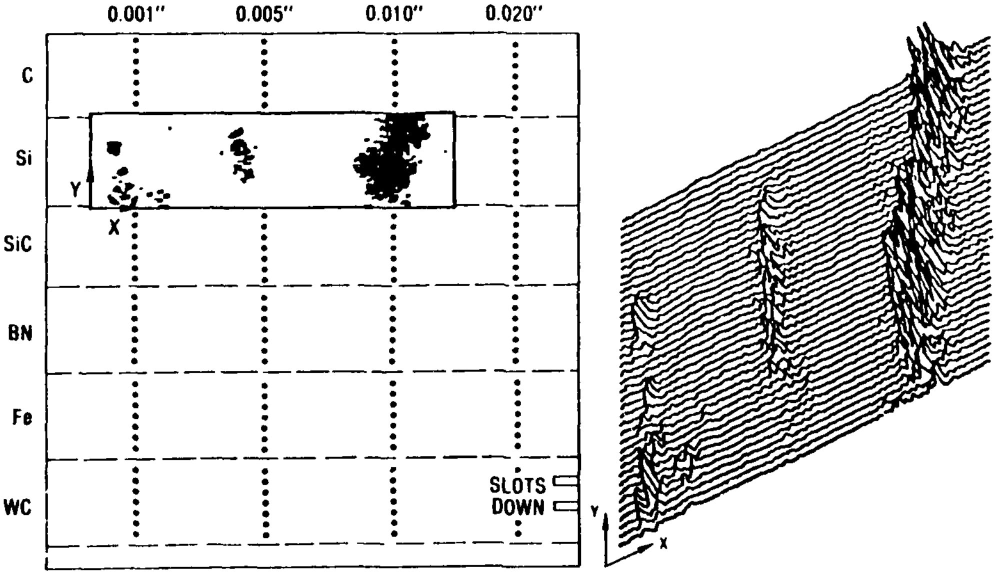

Excess Signal vs. Position

Amplitude vs. Position

Figure 5-15. Microwave Cross-Polarized-Transmission C-Scan of Silicon Inclusions in Hot-Pressed Silicon Nitride Seeded Billet (S/N 02), (Frequency = 98 GHZ).

Attenuation in silicon nitride--both hot-presssed and reaction-bonded--is significant and results in a low-contrast radiograph that makes subsurface inclusion detection very difficult.

Reversal prints for neutron radiographs of HPSN and RBSN seeded billets are shown in Figure 5-16.[2,69] Only boron nitride (BN) was detected in the HPSN standard. Boron has a high neutron absorption coefficient compared to Si_3N_4 and the other inclusions. Only the 0.04 inch voids and Fe inclusions were detected in the RBSN standard. These are indicated by arrows. The contrast was low on the original radiograph and did not reproduce well in the reversal print.

These observations indicated that neutron radiography does not have general utility for NDE of Si_3N_4.

5.2.7 FLUORESCENT PENETRANT

The use of conventional fluorescent dye penetrant was evaluated for HPSN and RBSN. Penetrants were not effective for low-density RBSN. The penetrant was absorbed uniformly by surface-connected porosity and resulted in fluorescence of the complete surface. Higher density RBSN ($\gtrsim 2.7$ g/cm^3) could be successfully inspected, but the technique was sensitive only for large cracks. Slightly smaller cracks could be detected for HPSN.[6] Examples of machining damage detected on rotor blades by dye penetrant are shown in Figure 5-17. These were inspected with P133, a Group-V-sensitivity penetrant from Uresco, Inc.

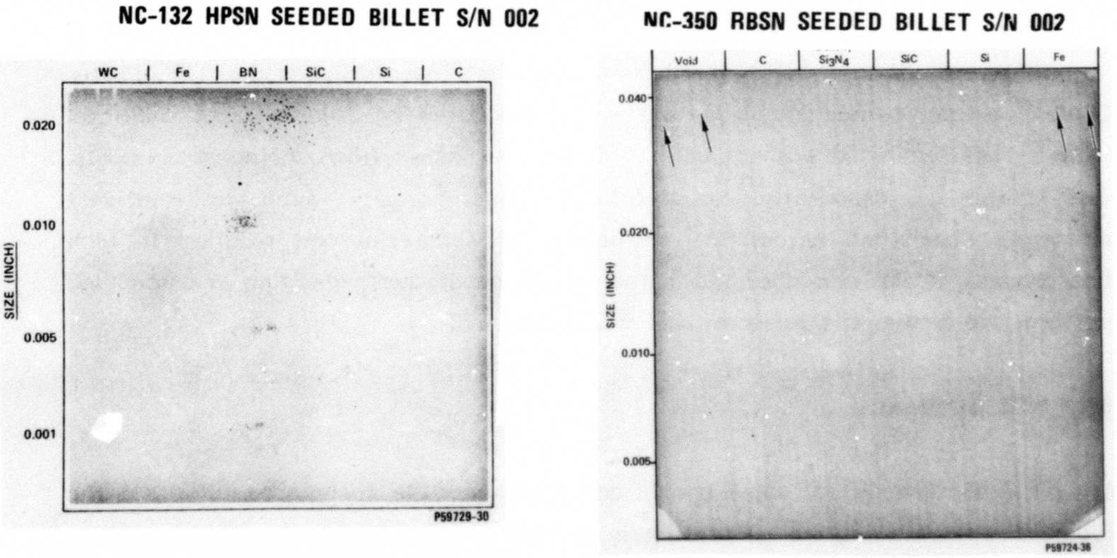

NC-132 HPSN SEEDED BILLET S/N 002

NC-350 RBSN SEEDED BILLET S/N 002

Figure 5-16. Neutron Radiographic Reversal Prints for HPSN and RBSN Seeded-Defect Standards.

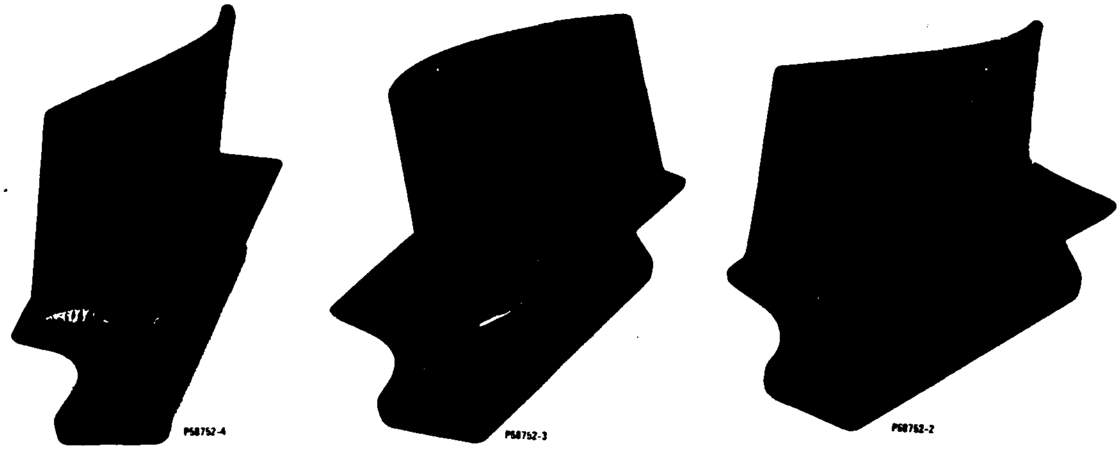

Figure 5-17. Machining Damage on HPSN Rotor Blades Detected by Dye Penetrant Inspection.

5.2.8 KRYPTON EMISSION TECHNIQUE

The krypton emission technique (KET) was evaluated for potential to detect finer surface cracks and flaws in HPSN than could be detected by dye penetrants. In KET, the part to be inspected is placed in a vacuum chamber. After evacuation, radioactive krypton gas is released into the chamber. This is absorbed on the surface, in cracks, and in surface-connected pores. The part is then exposed to atmospheric pressure air. The krypton gas is desorbed more rapidly from pore-free, crack free surfaces than from defects. The part is wrapped in photographic film, and the radiation from the residual krypton gas in the surface defects is allowed to expose the film to produce an auto-radiograph.

KET evaluation of HPSN test bars with Vickers indentations and of HPSN rotor blades containing machining damage were conducted at Qual-X, Inc., Hilliard, Ohio.[6] The technique was not able to detect the known flaws in the HPSN parts. The krypton gas apparently was absorbed by microporosity which was relatively uniformly distributed across the surface of the material and resulted in high background. It was also absorbed in the machining grooves, resulting in a speckled pattern. No further evaluation of KET was conducted.

5.2.9 NDE SUMMARY

The sensitivities of conventional and emerging NDE techniques to detect the types of defects likely to be present in ceramic engine hardware was determined using flat-plate standards containing known defects. The results for HPSN seeded-defect billets are summarized in Figure 5-18. Resolution of defects down to

DETECTED INCLUSIONS

WC	Fe	BN	SiC	Si	C	NDE METHOD
X	X	X			X	X-RAY
		X				N-RAY
X	X	X	X	X	X	ULTRASONIC

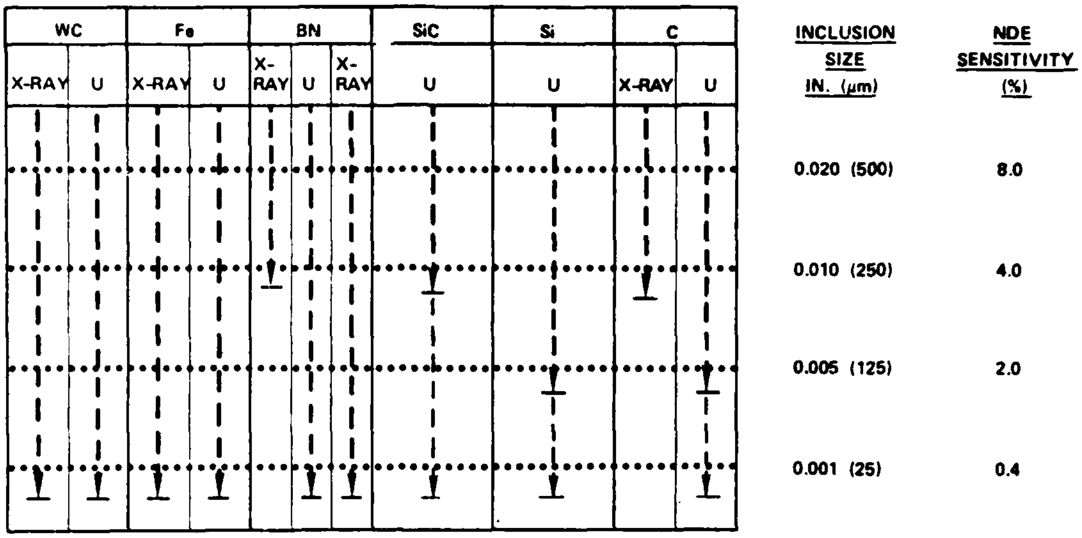

Figure 5-18. Summary of Defects Detected by Various NDE Methods for HPSN Seeded-Defect Billets.

0.005 inch was demonstrated. Resolution of clusters of 0.001-inch defects was also demonstrated, but further work will be necessary to verify if individual 0.001-inch defects can be routinely detected.

The complex geometry and thin trailing edges of rotor blades and stator vanes place limitations on NDE of engine hardware. Although ultrasonics has shown the best capability for detecting internal voids and low-density inclusions, it was not suitable for near-surface defects, and equipment was not available for handling contours and thickness gradients. Therefore, the major technique for inspecting engine hardware was microfocus radiography, supplemented by image enhancement of critical regions such as trailing edges. This was further supplemented by visual inspection, proof testing, and control of processing through use of specifications, certification procedures, and traceability records.

As an experience base was developed relating component inspection with rig testing and engine testing, radiographs were compiled defining preliminary accept-reject criteria for development hardware. These were provided to the AiResearch Casting Company to aid in their component inspection and were included in Appendix I of Reference 11.

The combination of process control, NDE, and proof testing proved adequate for qualifying hardware for rig and engine testing. No parts failed during the program from abnormal material defects that were not pre-detected by NDE.

6.0 RIG AND ENGINE TESTING

As described in previous sections, ceramic components were successfully designed, fabricated, and inspected. Rotor blades were spin proof tested prior to rig and engine testing. Simple proof tests of stator vanes and static structures were not as straightforward, so verification of these designs was dependent upon rig testing. Static structure component development and design verification was conducted by instrumented rig tests where flow and temperature conditions could be monitored and controlled more closely than in an engine. The second-stage stator and its supporting ceramic structure were evaluated first, followed by equivalent first-stage stator testing. In each case, the severity of conditions was increased incrementally, with disassembly and inspection of the components occurring after each test, until full design conditions of 1975°F for the second-stage stator and 2200°F for the first-stage stator were achieved. Hardware surviving these static rig tests was considered qualified for dynamic rig tests and engine tests. The following paragraphs describe the results of the static rig tests, the dynamic rig tests, and the engine tests.

6.1 SECOND-STAGE STATIC RIG TESTING

Static structure tests were conducted in a rig having a cross-section similar to the TSE331C-1 engine but adjustable through the use of spacers and other hardware to test individual stages.[4] The arrangement of the hot section for static tests of the second-stage stator is shown schematically in Figure 6-1.[5] The first-stage stator was replaced by a solid ring spacer, and the pressure drop was simulated by an orifice plate. A Z-spring provided an axial pre-load to hold the ceramic components in position, especially during the loose-tolerance room temperature condition.

A total of six second-stage stator rig tests were conducted, progressing in the following steps of increasing severity.

- Design airflow, 800°F air temperature
- Lightoff, design airflow, 1380°F
- Lightoff, design airflow, 1975°F
- Two hours cyclic endurance

Several problems associated with dimensional tolerances of the rig and with operating conditions differing from those predicted analytically for the engine were

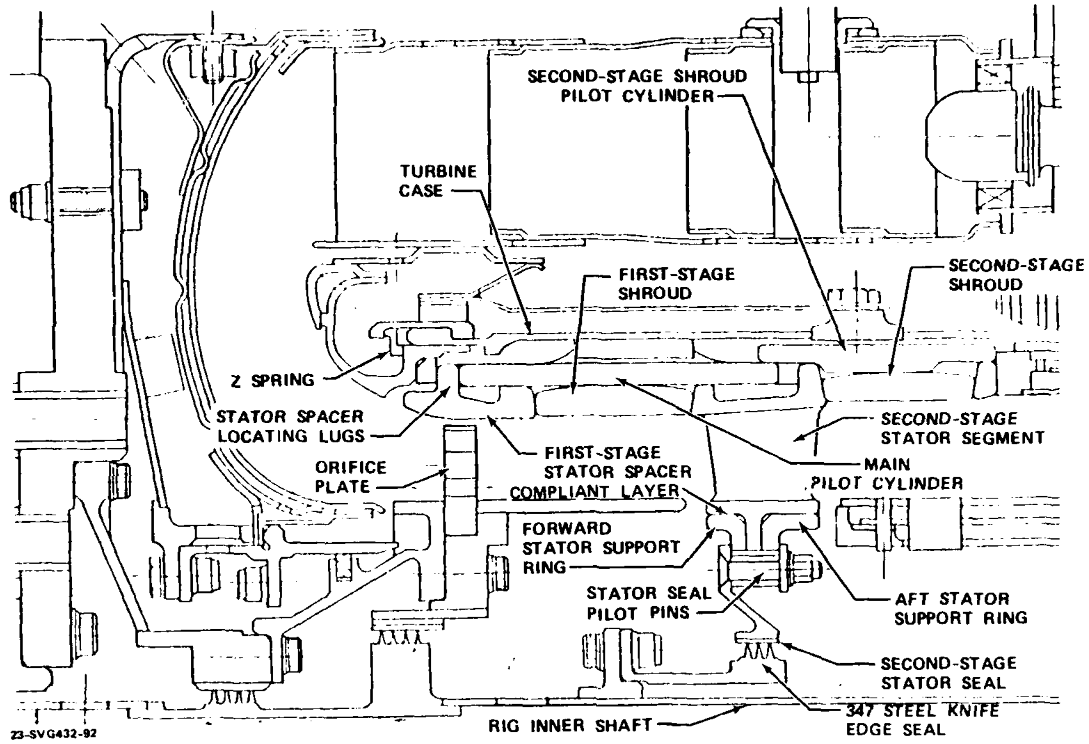

Figure 6-1. Second-Stage Stator Static Test Rig Configuration.

encountered during these tests.[6] Such problems are typical during the initial tests with a new rig. Unfortunately, these problems caused dimensional interferences that fractured or cracked some of the ceramic components. However, this provided a learning experience on the use of ceramic fracture analysis to differentiate between design and materials related problems and to locate the specific source of the problem. By locating the fracture origin in the ceramic component, it could be determined if the fracture was due to an overstress or to an unusually large defect in the ceramic. Also, by examining the configuration of the fracture surface and by observing the presence of witness marks (metal smudges, abrasion marks, etc.), it could be determined if the fracture was mechanically or thermally induced.

The sources of rig interferences were identified and resolved, and the rig was operated to an average second-stage stator inlet temperature of 1930°F with no damage to the ceramic components. A 5.2-hour test was then conducted in which the temperature was cycled between 1300°F and 1975°F, accumulating two hours at the maximum temperature.[9] All ceramic hardware survived except for the second-stage shroud retaining ring and two positioning rings on the first-stage rig spacer.

To avoid problems in later tests, the retainer ring was strengthened by increasing its axial length.

6.2 FIRST-STAGE STATIC RIG TESTING

The static structure rig for testing of first-stage stator vanes was similar to that shown in Figure 6-1, except that now a spacer ring replaced the second-stage vanes. A total of nine rig tests were conducted, employing a stepwise procedure similar to that used for second-stage tests.[6-8]

Two initial tests at full aerodynamic loading and 1400°F identified and resolved interferences associated with out-of-specification hardware. Damage to ceramic hardware included a chip on the trailing edge shroud of one stator vane, fracture of the forward, outer shroud antirotation lugs on eight vanes, and a circumferential crack in the second-stage turbine shroud support. The stator damage was traced to the interference conditions. The defect in the shroud support was an extensive circumferential crack which existed prior to nitridation (determined by the presence of white Si_3N_4 needles lining the fracture surface). The defect had not been detected by X-ray radiography because it was oriented perpendicular to the X-ray beam. It was not detected visually because it was coincident with an abrupt change in cross section. The NDE procedure was modified to detect this type flaw in subsequent parts.

The objective of the third first-stage stator rig test was to operate at design pressure and temperature (2200°F average). When the rig reached about 1400°F, the facility main air discharge valve malfunctioned by partially closing and restricting the rig airflow.[6] This resulted in a fuel-rich condition and a rapid temperature rise in excess of 250°F/second to a maximum temperature greater than 3000°F. Metal and ceramic parts were extensively damaged. Eleven stator vanes survived with minimal or no damage. The rest of the ceramic parts were damaged by thermal shock. An overtemperature control system was installed on the rig prior to further testing.

Test No. 4 achieved near-design conditions of 121 psia, 2200°F and 6.1 lb./sec. airflow. Disassembly of the rig revealed a number of cracked and chipped ceramic parts[7] as shown in Figure 6-2. Fractography indicated that the predominant cause of damage was tensile overload at regions of point contact, although the objective of the original engine and component design was to avoid point contact. However,

ARROW INDICATES FAILED OUTER PLATFORM ANTI-ROTATION LUGS

ARROW INDICATES FAILED INNER VANE PLATFORM

ARROW INDICATES CIRCUMFERENTIAL SEPARATION WHICH INITIATED AT AN OD SUPPORT LUG AND TERMINATED IN THE AXIAL DIRECTION ON THE FRONT AND REAR SURFACES

VIEW SHOWING AXIAL SEPARATIONS

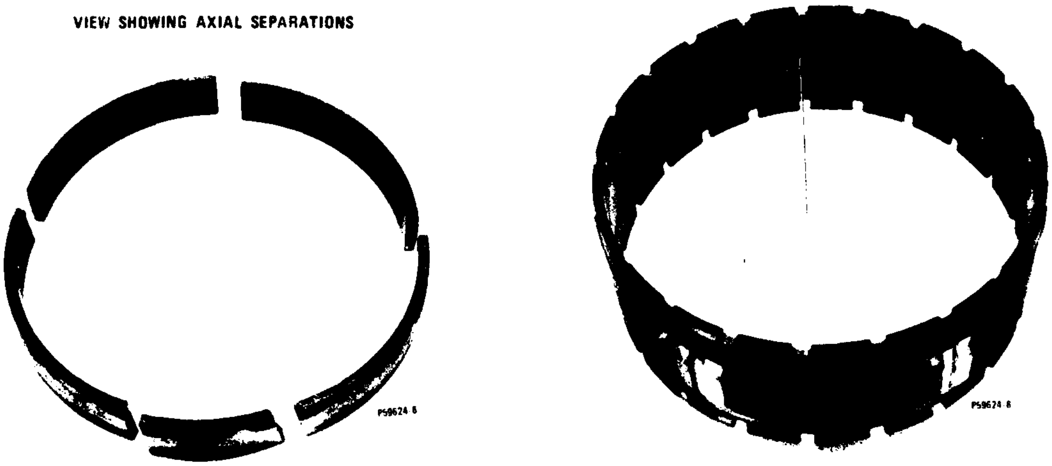

Figure 6-2. Cracked and Chipped Ceramic Hardware From the Fourth First-Stage Stator Rig.

in the rig with the available ceramic hardware, nonuniform temperature distribution, metal and ceramic component tolerance mismatches, and possible metal component thermal distortion, it was not possible to avoid this condition. Based upon the fractography data and mechanical analysis, the following items were identified for evaluation in subsequent rig tests:

- Additional radiusing of the anti-rotation lugs and stator inner platform external corners to avoid edge loading during relative thermal growth.

- Improved matching of the axial dimensions of stator vanes, better control of flatness at interfaces, and use of a metallic compliant interface layer between the stator vanes and the shroud; separate studies discussed in Paragraphs 7.1 and 7.2 were initiated to evaluate compatibility and friction characteristics of candidate compliant layers and interface dry film lubricants.

- Reduced radial interference between the support cylinder and the vanes and shrouds; use of a compliant interface layer.
- Redesign of the radial pilot interface between the metal support housing and the ceramic shroud support cylinder to incorporate a pin which can pivot to accommodate some cocking and misalignment; use of a lubrication surface on the pin to allow relative movement.
- Addition of a metal support to help center the ceramic shroud support cylinder relative to the metal housing, and installation of axial stops to prevent relative movement between the two ceramic support cylinders.

The above modifications were evaluated in first-stage stator rig tests Nos. 5 through 9.[8,9] The incidence of damage to ceramic components was sequentially decreased. In test No. 9, run at the design point of 2200°F, the only damage was a fractured rear shroud retaining ring and some spalling of the second-stage turbine shroud. The spalling was caused by a silicon-rich core in the RBSN shroud, requiring processing improvement at the vendor and a modified certification procedure. The ceramic assembly after test No. 9 is shown in Figure 6-3.

Test No. 9 used metal compliant layers at the stator platform ID and OD and at vane antirotation lugs. Platinum was evaluated as the compliant layer in an earlier rig test but apparently bonded to the RBSN at the high temperature and resulted in chips or pull-outs of the ceramic surface during cooling. Pre-oxidized HS-25 had a surface layer of cobalt oxide, which had excellent lubricating properties. Stainless steel (347) was also evaluated in earlier rig tests as a compliant layer for lower temperature surfaces. It did not have adequate compliance, so was used in later tests in a more compliant perforated condition.

6.3 TWO-STAGE STATIC STRUCTURE RIG TESTS

The single-stage rig testing identified key problems and solutions associated with high-temperature operation of the ceramic hardware but did not provide adequate simulation of the TSE331C-1 engine operating conditions. To provide a

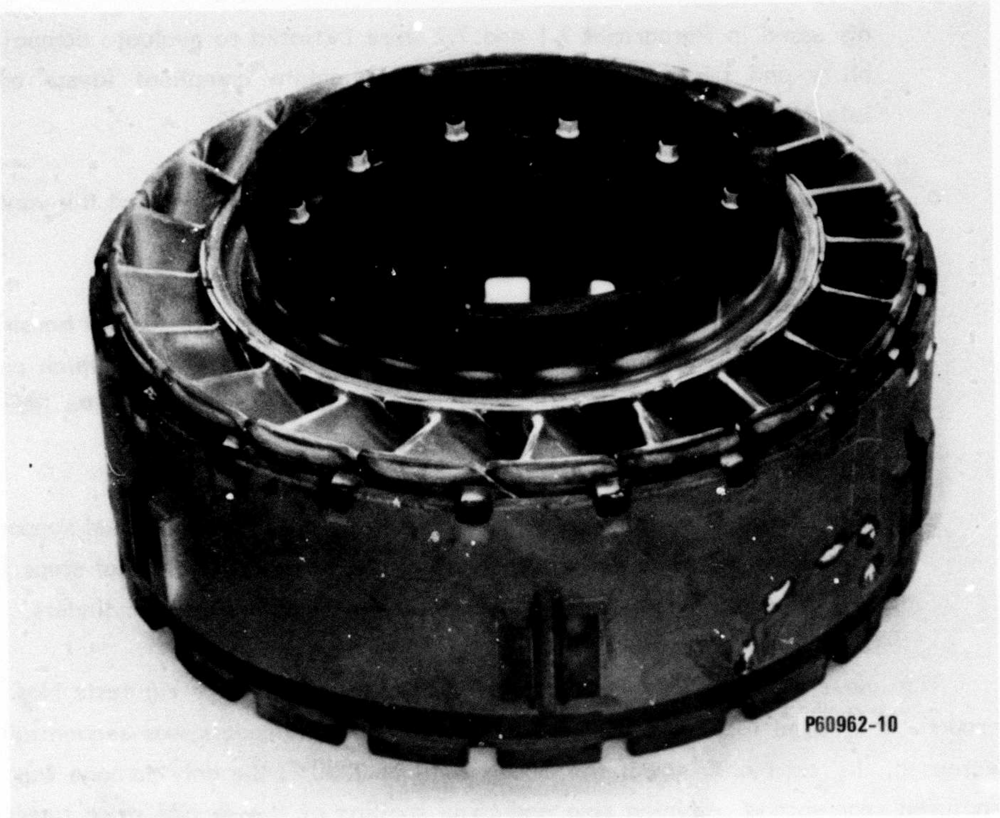

Figure 6-3. **Ceramic Assembly After First-Stage Stator Static Rig Test No. Nine to Design Aerodynamic Loading at 2200°F.**

better simulation and to obtain continued instrumented test experience, rig testing progressed to two stages of ceramic static hardware. This rig configuration is illustrated in Figure 6-4. A shielded shaft was included in the rig to simulate engine vibration. The objective was 10 hours operation at 1700°F and 145 psia (120 percent design pressure).

Three tests were conducted with the two-stage rig, the first without the rotating shaft to check out the rig. The second encountered a facility problem that resulted in a temperature > 2500°F for 85 seconds.[11] The temperature was then stabilized at 1700°F and the rig operated for 10 hours. Disassembly revealed severe overtemperature damage to the metal turning vane assembly (see Figure 6-4) along four well-defined combustor hot streaks. Several ceramic parts were fractured, all clearly associated with the hot streaks.

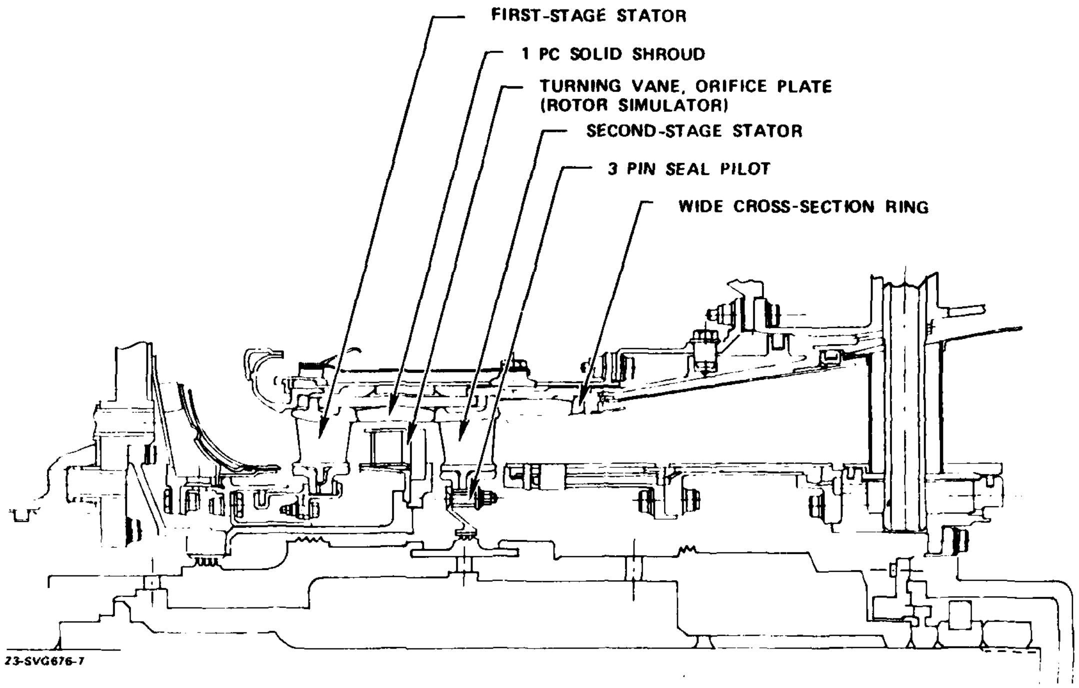

Figure 6-4. Two-Stage Rig Configuration.

The shaft assembly prevented reaching 120 percent design aerodynamic loads in the second test. The rig for the third test was rebuilt without the shaft assembly and operated at 1750°F, 145 psia and 6 lb/sec. for 10 hours. The test included two lightoffs and 22 cycles from 1250-1750°F at a transient rate of 250-350°F/sec. As shown in Figure 6-5, all ceramic hardware survived without damage.

6.4 DYNAMIC RIG TESTS

The objective of the first build of the dynamic turbine rig was to check out the second-stage rotor assembly, the dynamic turbine rig, and the test facility, and in particular to identify rig shaft criticals and to assure proper operation of the bearing/lubrication system. The test was run at ambient temperature and without the complication of elaborate instrumentation. The stator was a simplified integral metallic stator vane-shroud assembly. Second-stage ceramic blades previously proof-tested to 130 percent of design speed were used in the rotor assembly. The turbine was driven by flowing room-temperature air through the rig at minimum pressure loads and with minimum waterbrake loads to reduce the driving forces on the ceramic blades. The test was to be a series of slow accelerations working up to

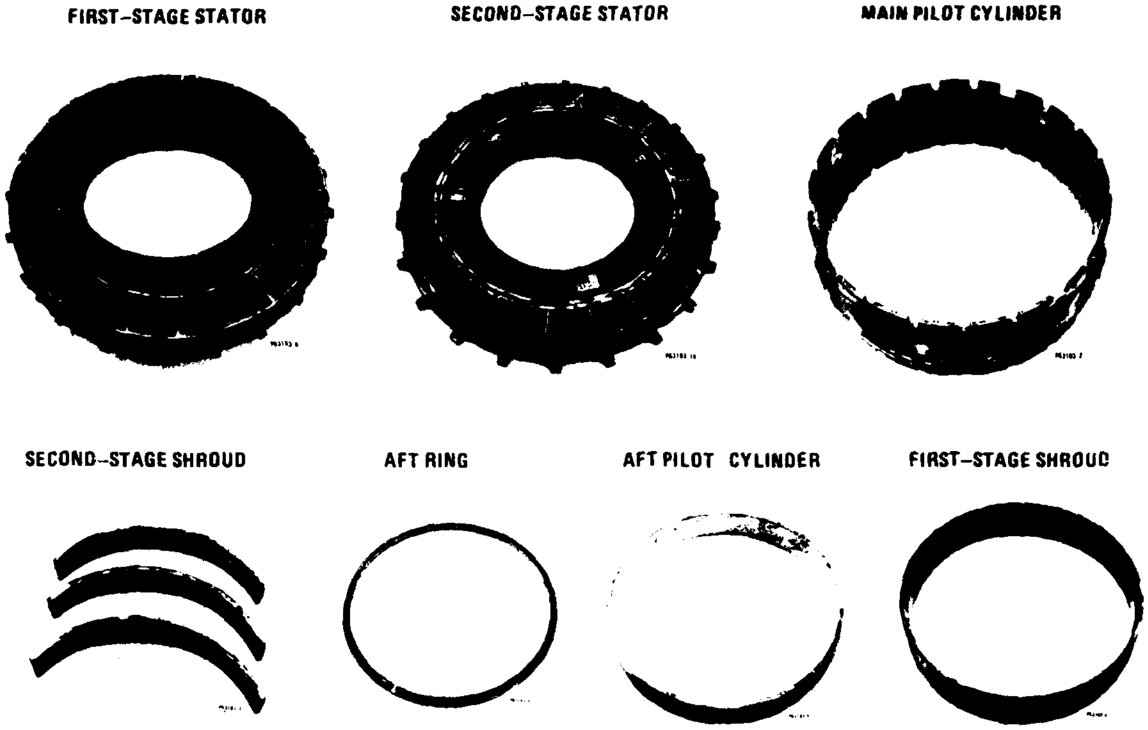

FIRST-STAGE STATOR

SECOND-STAGE STATOR

MAIN PILOT CYLINDER

SECOND-STAGE SHROUD

AFT RING

AFT PILOT CYLINDER

FIRST-STAGE SHROUD

Figure 6-5. Ceramic Components After 10 Hours (2 Light-Offs, 22 Transient Cycles) Two-Stage Static Rig Testing to 1750°F Average Inlet Temperature and 120 Percent Design Aerodynamic Loading.

a maximum speed of 90 percent (37,500 rpm). This speed limit of 90 percent was selected to avoid blade resonance with stator passing frequency, which was based on the predicted second-stage blade excitation diagram, Figure 6-6. This rig limit of 90-percent speed provided a margin greater than two standard deviations. Based on the rig and blade analysis, it was judged that the ambient rig test to 90-percent speed would be an adequate system checkout with little risk.

Assembly of the turbine rig was performed as designed. Seal and blade tip clearances were opened to eliminate the possibility of rubs. The rotating components were balanced well under limits, both individually and as a group.

The test cell systems and the rig operated well throughout the test. The test sequence consisted of accelerations to, and stabilizations at speeds of 5,000, 16,000, 25,000, 28,000, 34,000 and 37,000 rpm while monitoring rig vibrations and bearing temperatures. Shaft criticals were observed as predicted at 17,000 and 22,000 rpm with the vibration levels within acceptable limits. The bearing and lubrication systems functioned well, with the maximum bearing temperature reaching 120°F.

After one hour of total rig time and approximately 60 seconds into a slow acceleration from 36,000 rpm to 37,000 rpm, a distinct "pop" was heard from the test cell, and the rig immediately coasted down to zero rpm.[7] Shutdown was carried out, and the rig tailpipe was then removed for a visual inspection of the ceramic blades. It was observed that one blade had fractured in the attachment, and all others suffered airfoil damage (Figure 6-7). A comparison of speed and vibration traces showed that the change in vibration and the deceleration were coincident.

Visual inspection showed that one blade had a smooth fracture (shown previously in Figure 4-15 in Paragraph 4.1.8) below the platform adjacent to the contact zone, but not at the position analytically predicted to have the peak stress. As described in Paragraph 4.1.8, the fracture surface was different from any encountered previously in bend testing, tensile testing, thermal shock testing, impact testing or blade proof testing. The remaining blades all had jagged fracture surfaces above the platforms and appeared to have failed because of impact. The metallic second-stage turbine tip shroud had a single, well-formed blade indentation. The visual evidence thus suggested that one blade fractured for unknown reasons below the platform, hit the tip shroud and then impacted the other blades.

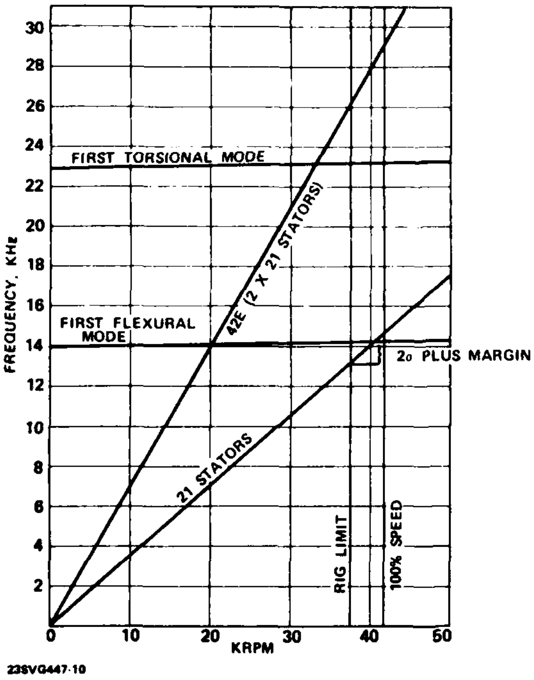

Figure 6-6. **Second-Stage Rotor Blade Vibration Diagram for the First Dynamic Rig Test.**

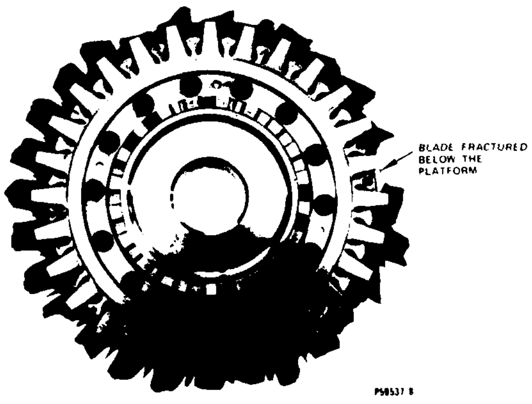

Figure 6-7. **Second-Stage Rotor After First Dynamic Rig Test.**

The following were evaluated as potential causes of the blade fracture:

- Vibration
- Foreign Object Damage
- Shaft Dynamics
- Axial or Radial Rub
- Dimensional Discrepancy
- Compliant Layer
- Proof Test Damage
- Handling

The evaluation included a detailed review of all test data, rig assembly data, material fracture surfaces, compliant layer and broach angle inspections plus additional proof tests, vibration-contact tests and refined stress analysis. The detailed procedures and results are described in Reference 7 and Paragraph 4.1.8 of this report. The conclusions were as follows: The blade failure was due to blade resonance at the stator passing frequency. The blade resonance frequency was lower than predicted (or previously measured on individual blades) due to irregularities in the broached superalloy attachment slot and inadequate compliancy of the HS-25 compliant layer to allow complete seating of the blade dovetail. This dropped the blade frequency to about 13,000 Hz, which was equivalent to the flexural mode of stator passing excitation at about 37,000 rpm.

A redesign of the stators was initiated. The number of vanes in the first-stage stator was reduced from 21 to 19 and in the second-stage stator from 21 to 17 to provide a greater margin between stator passing frequencies and blade resonance frequencies. In addition, it was decided that future broached attachment slots would be lapped to minimize irregularities and a softer compliant layer (platinum) would be evaluated.

Prior to receipt of redesigned stators, dynamic rig tests were continued with existing hardware using a partially bladed rotor with each blade strain-gauged. For as-broached slots, blade resonance started at 35,800 rpm for an HS-25 compliant layer and at 39,000 rpm with platinum. With redesigned stators and as-broached slots, blade resonance occurred at 43,600 rpm with HS-25 and 47,800 rpm with platinum. With lapped broach slots, both HS-25 and platinum yielded blade frequencies of approximately 47,800 rpm.

A total of seven dynamic rig tests were conducted, culminating in a final test at 1700°F and 45,000 rpm. This was conducted with a partially bladed rotor (10 blades), lapped slots, platinum compliant layers, and a 17-vane metal stator. Twenty-four cycles between 15,000 and 42,000 rpm were successfully completed. This demonstrated design and hardware suitability to begin full-scale engine testing.

6.5 ENGINE TESTING

Twenty-seven engine tests were conducted. The timing of these tests and rig tests is shown in Figure 6-8. Some engine tests were concurrent with rig tests; some were conducted with the 21/21 vane stator design (prior to delivery of the new 19/17 vane design hardware) with a speed limit of 35,000 rpm; and the final tests were conducted with the 19/17 vane design to the design condition of 2200°F/ 41,730 rpm. The following paragraphs will review the engine tests, with emphasis on the nature of the problems encountered.

6.5.1 21/21 VANE ENGINE TESTS

The objectives of the initial tests were to evaluate seal break-in, vibration, and lightoff conditions and to check for interference. The seals operated satisfactorily, and there was no indication of a vibration problem. However, an interference problem was identified during the first two tests. The metal inner transition liner was forced aft by the combustor or metal backbone during cooldown, placing high bending loads on the first-stage stator antirotation lugs. Corrective action involved increasing clearances between the inner transition liner, the combustor and the backbone and incorporating a Feltmetal compliant layer on the aft side of the lugs.

A second problem was identified which required more extensive development. The combustor lightoff characteristics were not optimum and resulted in hot starts and high temperature streaks. This was evaluated in engine Runs 3-7.

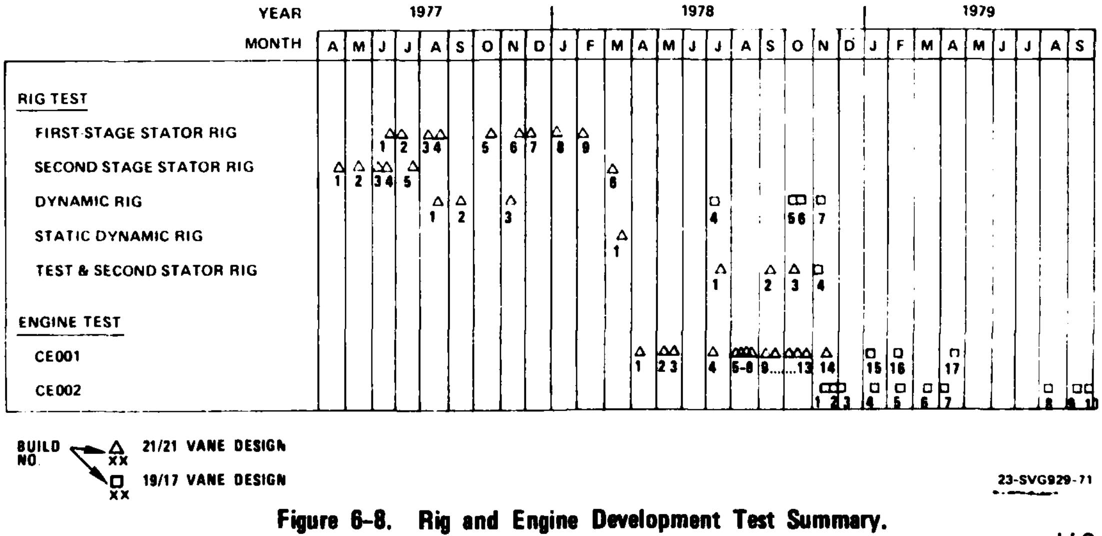

Figure 6-8. Rig and Engine Development Test Summary.

The objective of test No. 3 was to subject the engine to a two-hour run at 32,000 rpm and 1300°F average turbine inlet temperature. The engine start was accomplished with a peak average exit gas temperature (EGT) of 793°F. However, special high response tailpipe thermocouples indicated a peak temperature of 1422°F. The engine was operated at 28,000 rpm (ground idle) for 30 minutes, at 32,000 rpm/1300°F TIT for 70 minutes, 10 minutes at idle, followed by another 30 minutes at 32,000 rpm. After a total run time of 2 hours and 20 minutes, the facility overtemperature system sensed a sudden EGT increase and shut the engine down. A few seconds after rolldown initiated, severe breakage was heard.

Engine disassembly revealed that all ceramic components except the first-stage stator inner support rings had been destroyed.[10] Some of the debris is shown in Figure 6-9(a). All blade dovetails were still in place with all airfoil fractures of an impact nature [Figure 6-9(b)]. All but two stator vanes were in small fragments. The predominant fracture mode was impact as shown in Figure 6-9(c). Discoloration of the metal outer transition liner, shown in Figure 6-9(d), indicated the presence of five distinct hot streaks.

The initial cause of fracture in test No. 3 could not be conclusively determined by examination of the hardware and the recorded data from test instrumentation. Additional combustor rig tests verified the presence of a rapid temperature rise during light-off and of severe circumferential temperature gradients due to hot streaks. The engine was rebuilt for test No. 4 with extra instrumentation to obtain a better understanding of the temperature variations in the engine and of the transient conditions. This instrumentation included 12 thermocouples at the turbine inlet (T_4), 37 thermocouples at the exit of the second-stage turbine ($T_{4.5}$), 14 thermocouples at the tailpipe exit ($T_{5.2}$), accelerometers for the backbone and rear bearing, and a Kissler probe in the engine tailpipe.

Following routine seal break-in and vibration check, engine run No. 4 was begun. An engine start, using JP-5 fuel, was accomplished on the third attempt, and the engine accelerated to ground idle. Instrumentation recorded peak T_4 and $T_{5.2}$ temperatures of 2470°F and 902°F respectively during the startup transient with a T_4 temperature rise of 750°F/second. As soon as the data scan was taken, the engine was shut down without incident. Engine operating time was 3.5 minutes.

Disassembly of engine run No. 4 revealed one fractured second-stage stator vane, which was positioned in the engine at the worst hot streak. The fracture was

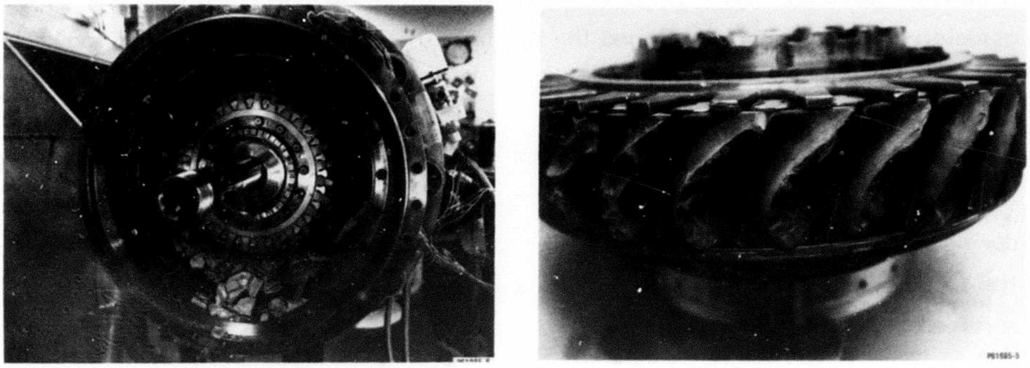

ENGINE TEARDOWN SHOWING DAMAGED CERAMICS

IMPACT DAMAGE ON ROTOR BLADES

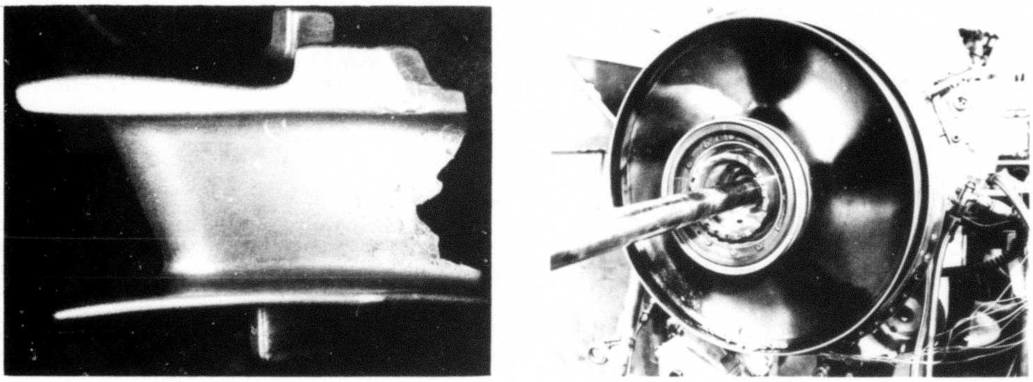

IMPACT DAMAGE ON STATOR VANE

HOT STREAKS ON TRANSITION LINER

Figure 6-9. Condition of Engine Hardware After Test Number Three in Engine Serial Number CE001.

identical to fractures induced previously in a torch thermal shock test apparatus. The fracture origin was at the trailing edge, and no material flaw was visible. All evidence indicated that the vane failed due to abnormally high thermal stress associated with the hot streak and the hot lightoff. The fractured vane is shown in Figure 6-10.

Additional combustor rig tests and lightoff tests in a metal turbine engine were conducted to identify options for decreasing the peak transient temperature during the engine start cycle. Promising start modifications were then evaluated in the CE001 ceramic engine in tests No. 5-9 using the ceramic hardware which had survived in test No. 4.[11]

Test No. 5 consisted of engine lightoff using JP-4 fuel (rather than JP-5), stabilizing at ground idle, and then shutting down. The peak transient TIT was 2150°F, which was 320°F cooler than the test No. 4 light-off. Disassembly revealed that all ceramic components were undamaged, so the engine was rebuilt with these parts and prepared for test No. 6. Test No. 6 consisted of an engine start with a 5 lb/hr reduction in start fuel flow. The peak TIT during the start transient was reduced to 1775°F. Teardown revealed all ceramic hardware to be in excellent condition.

The objective of test No. 7 was to perform a one-hour cycle consisting of lightoff, 15 minutes at ground idle, 30 minutes at 31,000 rpm and 15 minutes at ground idle. No problems were encountered. Peak T_4 during the start transient was

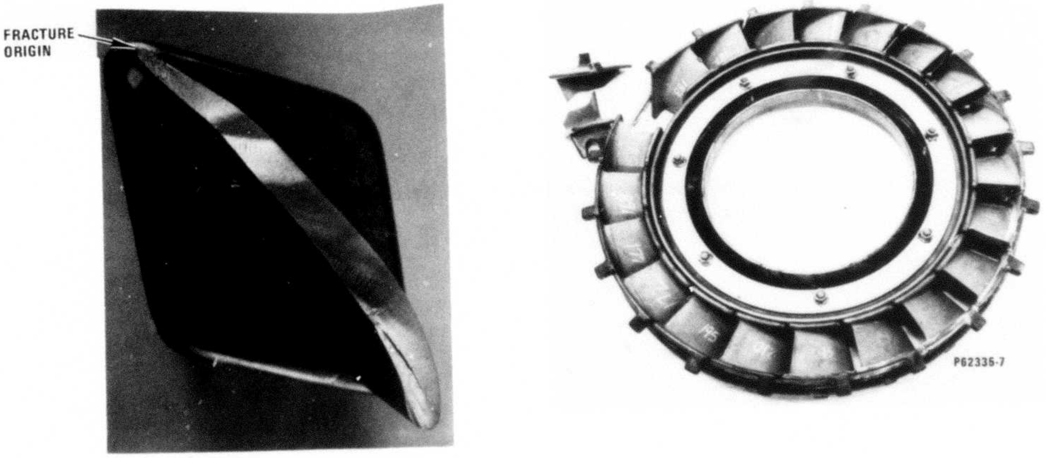

Figure 6-10. Single Vane Fractured by Thermal Shock Overstress in Engine CE001 Run Number 4.

1865°F. Upon disassembly, one first-stage vane was found to have a hairline crack beginning at the trailing edge but only extending partially through the vane. The vane was fractured by hand and the fracture surface evaluated. Energy dispersive X-ray identified Ti and Al on the fracture surface. TiO_2 had been injected as a trace powder in engine test No. 5 before shutdown. Al_2O_3 was injected during test No. 7. Since both TiO_2 and Al_2O_3 were detected on the fracture surface, it was likely that the crack initiated during test No. 4 or 5 and was not visually detected until after test No. 7. The characteristics of the crack indicated that it was caused by thermal shock.

The ceramic engine was rebuilt with the same ceramic hardware used in builds No. 4-7, except for replacements of the two stator vanes. Test No. 8 was then conducted. It consisted of three lightoffs. Peak TIT during the start transients were 2,000°F, 1740°F, and 1945°F. Disassembly revealed that all ceramic components were in excellent condition and acceptable for continued testing.

Test No. 9 consisted of a one-hour cycle to the 31,000 rpm condition. All hardware was suitable for continued testing.

Test No. 10 incorporated some hardware modifications. Solid first- and second-stage turbine rotor tip shrouds were used instead of the three-segment assemblies used previously. Three start cycles were performed during this test to further evaluate start parameters. Maximum T_4 temperatures recorded during these starts were 1840°F, 1650°F and 1535°F. All hardware was free of damage and suitable for continued testing.

Test No. 11 consisted of two one-hour cycles to 31,000 rpm. During both lightoffs, the peak TIT during the start transient was under 1700°F. All ceramic hardware was in excellent condition and was acceptable for further testing. This hardware subsequently survived five one-hour cycles in engine test No. 12 and five two-hour cycles in engine test No. 13, bringing the total engine time to about 20 hours and 23 lightoffs.[11] The ceramic hardware after this testing is illustrated in Figure 6-11.

Based upon the excellent results of engine tests No. 5 through 13, a final test with the 21/21 vane configuration was scheduled. Test No. 14 included two one-hour cycles to 1700°F/35,000 rpm with several speed cycles from ground idle to 35,000 rpm. The lightoffs were accomplished with a peak transient T_4 of 1840°F.

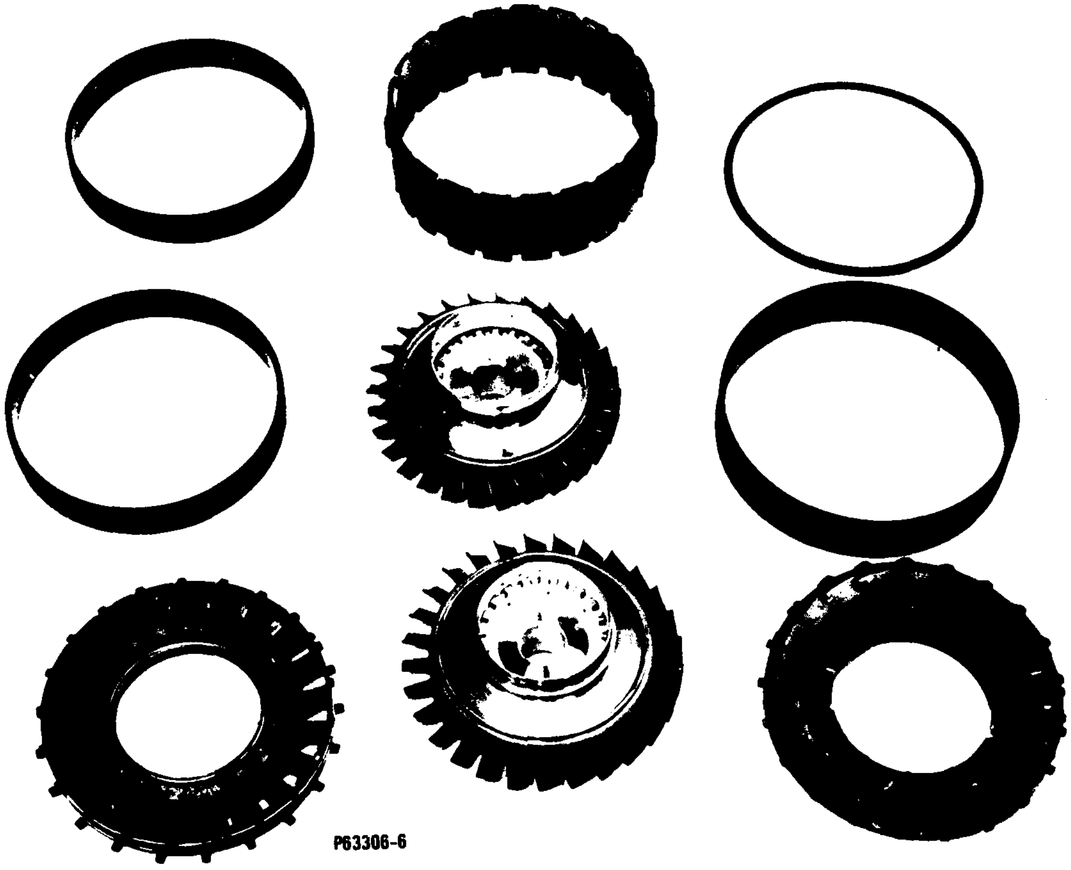

Figure 6-11. Ceramic Components After Accumulation of 20 Hours and 23 Light-Offs in Engine Tests Four Through Thirteen.

The engine ran as scheduled with no incidents.[12] Disassembly revealed that all the ceramic parts were in excellent condition except for a chip off one second-stage vane shroud and a cracked second-stage vane. These are illustrated in Figure 6-12. Fractography indicated that the fractures initiated at the interface between the vane and the turbine shroud and were caused by contact stress. The fracture surfaces showed no sign of exposure to combustion gases, suggesting that the fractures occurred during shutdown or disassembly.

6.5.2 19/17 VANE ENGINE TESTS

Testing of the 21/21 vane configuration ceased as soon as ceramic hardware for the 19/17 vane configuration was received. The new configuration was then tested in engines 002 and 001.

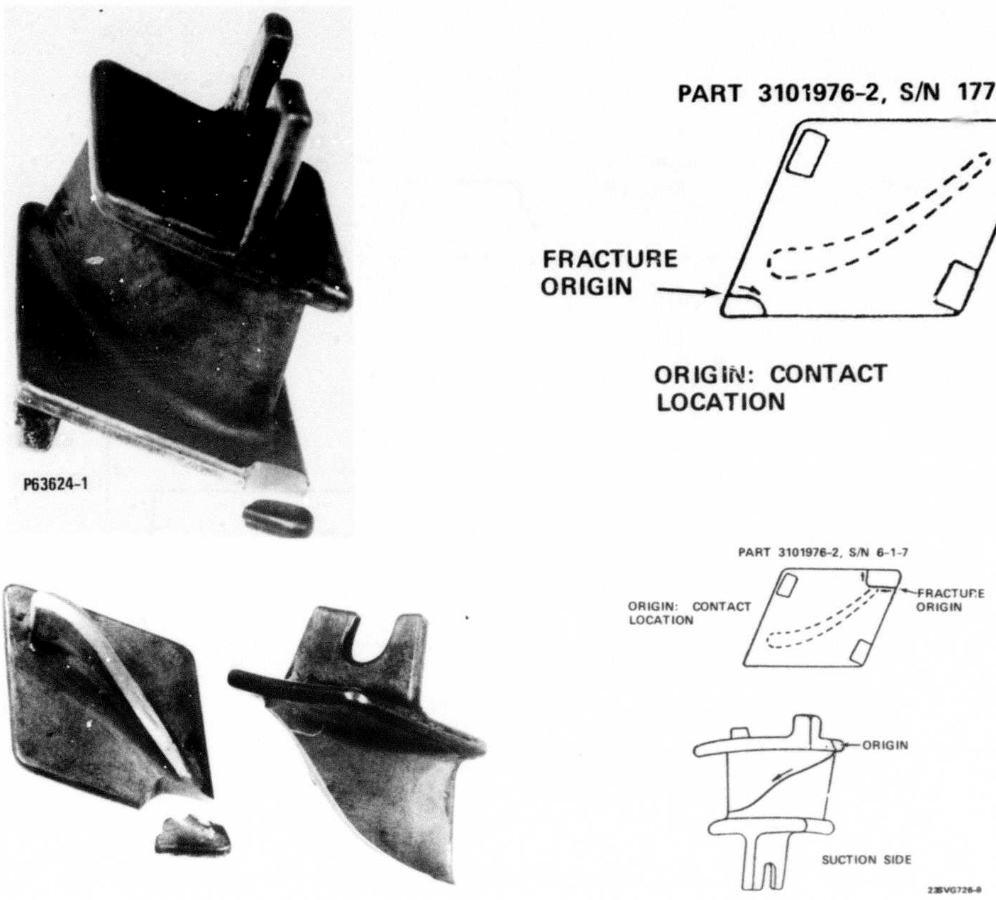

Figure 6-12. Contact-Initiated Damage on Two Stator Vanes From Engine Test 14. Arrows Show Direction of Crack Propagation.

Engine CE 002 had previously been used with metal hardware to optimize the light-off cycle. The new ceramic hardware was installed in this engine. As in the latter runs in CE 001, metallic compliant layers were used at many of the static structure interfaces. Test No. 1, consisting of a light-off with acceleration to ground idle, was accomplished with no difficulties.

The second CE 002 engine test with the 19/17 vane hardware was conducted to an average turbine inlet temperature of 1700°F and design speed of 41,730 rpm. The test cycle is illustrated in Figure 6-13. After ignition at 17.5 percent speed, the engine was stabilized at 65 percent speed, increased to full speed, and then to 1700°F. Al_2O_3, CaO and TiO_2 powders were injected into the engine airflow as tracers to aid in failure analysis should any ceramic parts fracture during the engine operation cycle.

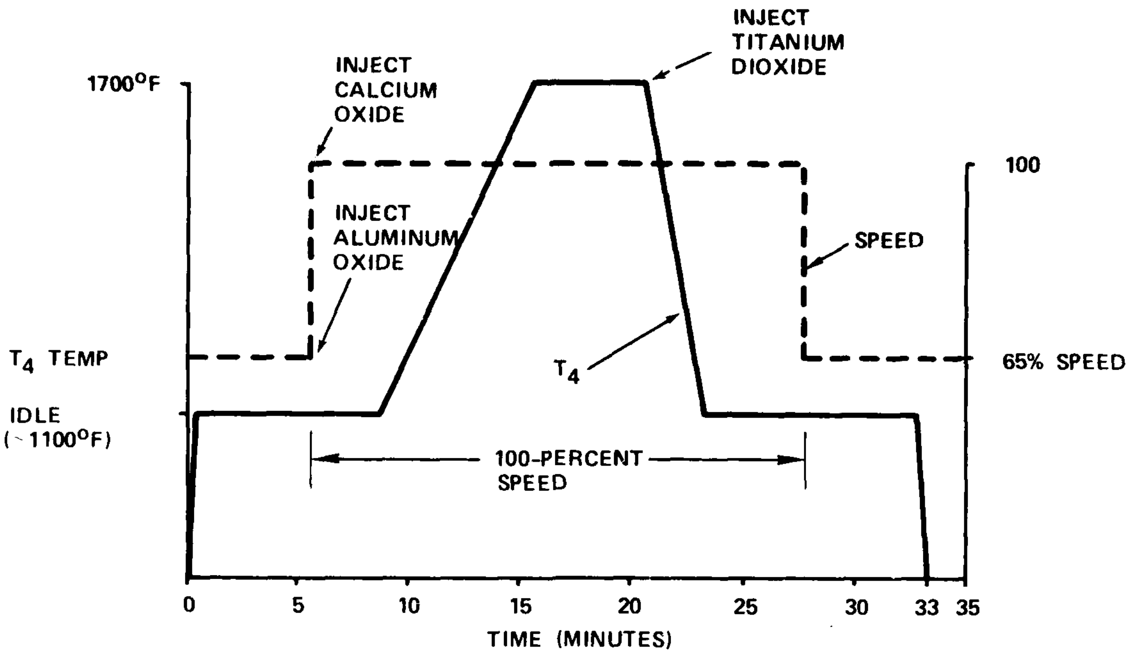

Figure 6-13. Test Cycle for Build 2 of Engine CE002 with the 19/17 Vane Configuration.

Engine CE 002, Build 2, operated smoothly and demonstrated that the 19/17 vane configuration solved the blade vibration problem encountered previously with the 21/21 vane configuration.[12] Engine disassembly revealed all ceramic hardware undamaged except for a small chip and crack on the ID corner of the first-stage turbine tip shroud. As shown in Figure 6-14, the damage occurred at the contact between the tip shroud and the first-stage stator pilot lug. Subsequent removal of the chip showed that the chip and crack initiated at the contact point and that no abnormal material defect was present. EDX analysis revealed the presence of Ti and Ca, indicating that the crack occurred while the speed was being increased to 100 percent. Several stator lug compliant layers were out of position. Evidence suggested that these out-of-position compliant layers caused cocking of the stator segments, resulting in point loading at the stator-to-shroud interface.

Prior to Engine CE 002, Build 3, the compliant layers were modified to ensure better positioning, and the shroud cross section was increased to decrease the chance of edge loading. The engine was then operated without incident to 41,730 rpm and 2214°F average turbine inlet temperature.

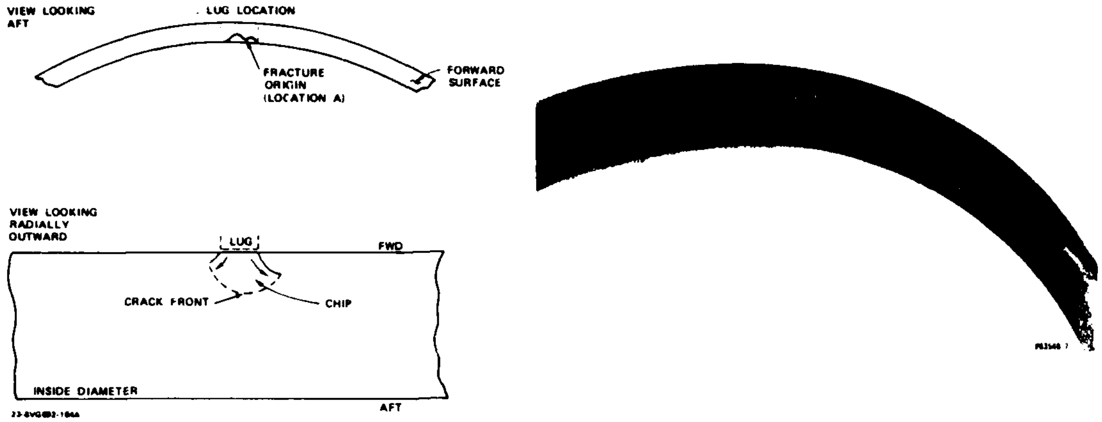

Figure 6-14. Photograph and Schematic Showing the Position and Orientation of the Small Crack on the First-Stage Tip Shroud.

The cycle consisted of one hour total time with 22 minutes above 1700°F. Disassembly revealed several chips on the first-stage rotor tip shroud very similar to the one encountered in Build 2. These were at shroud-stator lug interfaces and appeared to be due to localized high contact stress. The aft retainer ring also was damaged, containing two fractures that appeared to initiate in regions of point contact.

Build 3 demonstrated that the 19/17 vane ceramic hardware design could be operated for a single cycle to the program milestone conditions. However, further testing and modifications would be required to better understand the source of excessive contact loads and to demonstrate longer term and cyclic operation.

The next engine test was Build 15 of Engine CE 001. This was the first test with Engine 001 containing the 19/17 vane ceramic configuration. A two-hour test to 41,730 rpm and 1700°F average TIT was conducted, and the engine was shut down with no problems. One first-stage vane platform fractured at the point of contact with a surface bump on the adjacent compliant layer. The aft ring also fractured, with evidence that sticking had occurred between itself and the metal third-stage stator. Prior to the next test in Engine 001, a metal aft ring design was analyzed and the hardware fabricated. Additional modifications prior to Build 16 of Engine CE 001 included platinum paint on first-stage shroud contact faces, a wave spring (Z spring) with a longer stroke, improved cooling of the wave spring, and gold plating on the aft retainer ring.

Build 16 of Engine CE 001 was operated in a one-hour cycle to 41,730 rpm and 1700°F TIT. The test was conducted without incident, and all ceramic hardware survived without damage.[13]

Builds 4-6 of Engine CE 002 were scheduled to be one-hour runs to 41,730 rpm and 2200°F TIT to gain further experience at design point conditions. A premature shutdown from 2100°F/100-percent speed occurred during Test 4.[12] It was caused by an improper setting on the test cell overtemperature protection device and resulted in fracture of the second-stage ceramic turbine tip shroud and the first-stage stator seal and in permanent deformation of the metal axial thrust spring.

Damaged hardware were replaced, the axial stroke of the wave spring was increased, and the secondary cooling circuit was modified to avoid overtemperature of the wave spring. Engine CE 002, Test 5 was then run for one hour to full design speed and temperature, producing 925 shp.[13] Disassembly revealed that one first-stage vane platform was chipped at the interface with the first-stage shroud and that the main pilot cylinder was cracked. Fractography suggested that the vane platform was damaged by high local contact stress and that the main pilot cylinder fractured due to thermal shock, possibly with the crack initiating at contact damage. Although the precise time and cause of fracture were not determined, the evidence suggested that the damage may have initiated during engine Test 4 during the abnormal shutdown.

Prior to the next engine test (Build 6 in Engine CE 002), the first- and second-stage stator assemblies were match ground and radiused at the shroud contact. A one-hour test was successfully completed which reached 870 shp at 41,730 rpm and 2250°F TIT.[13] None of the ceramic hardware fractured. The only damage was several very small nicks on the ceramic aft retainer ring where a hot streak had melted the gold coating on the adjacent metal part.

The successful Build 6 run qualified the engine for two-hour duty cycle tests and for multiple starts. Three starts were conducted with engine CE 002 for Build 7.[13] The first encountered an overspeed, and the engine was shut down immediately. The second was a normal start with a full two-hour duty cycle in which 930 shp was achieved. Shutdown was normal. The third start was also normal. Fifty seven minutes into the cycle, after five minutes at 2200°F, the engine suddenly shut down. All ceramic parts were fractured except for the first-stage stator inner support rings. The cause of failure was not determined. All rotor blade dovetails were still in place with no fractures below the platforms, providing strong evidence that fracture did not initiate in the rotor.*

---

*Later contact studies suggest that surface damage at static structure interfaces caused by local biaxial stress concentrations propagated into cracks during cyclic engine operation and that a piece of RBSN fell into the turbine. This then resulted in widespread fracture due to wedging and impact. The contact studies are discussed in Section 7.0.

While replacement ceramic hardware was being prepared for Engine CE 002, Engine CE 001 was assembled as Build 17. Build 17 used match ground first- and second-stage stator vane assemblies with platforms radiused at shroud contact positions. The metal aft ring was coated with cobalt instead of gold. Compatibility studies had shown that the cobalt would oxidize and provide a low friction oxide surface. The objective of Engine CE 001 Test 17 was a two-hour cycle to 41,730 rpm and 2200°F. Forty-eight minutes into the cycle, while at full speed and approaching 2200°F, engine failure occurred and all ceramic parts fractured. The metal turbine-to-gearbox coupler sheared, and the prop shaft drive pins bent. One first-stage and one second-stage rotor blade fractured below the platform. The fracture surfaces are shown in Figure 6-15. The second-stage blade failed due to a tensile overload in bending. This likely resulted from a combination of the centrifugal load plus cantilevered bend loading due to impact. Much secondary cracking was present at the first-stage blade fracture, but the fracture origin was missing so that a precise cause could not be postulated. Neither blade fracture surface showed any evidence that vibration was involved. The remaining blades fractured above the platforms due to impact, as shown in Figure 6-16.

The output shaft drive pins were bent in a direction that indicated a stoppage in the engine rather than in the dynamometer. The torque required to bend these 1/2-inch diameter pins was sufficient to shear the coupler shaft. Based on the available

Figure 6-15. SEM Photomicrographs Showing the Fractured Surfaces of Blades that Fractured Below the Platform in Test 17 of Engine CE001.

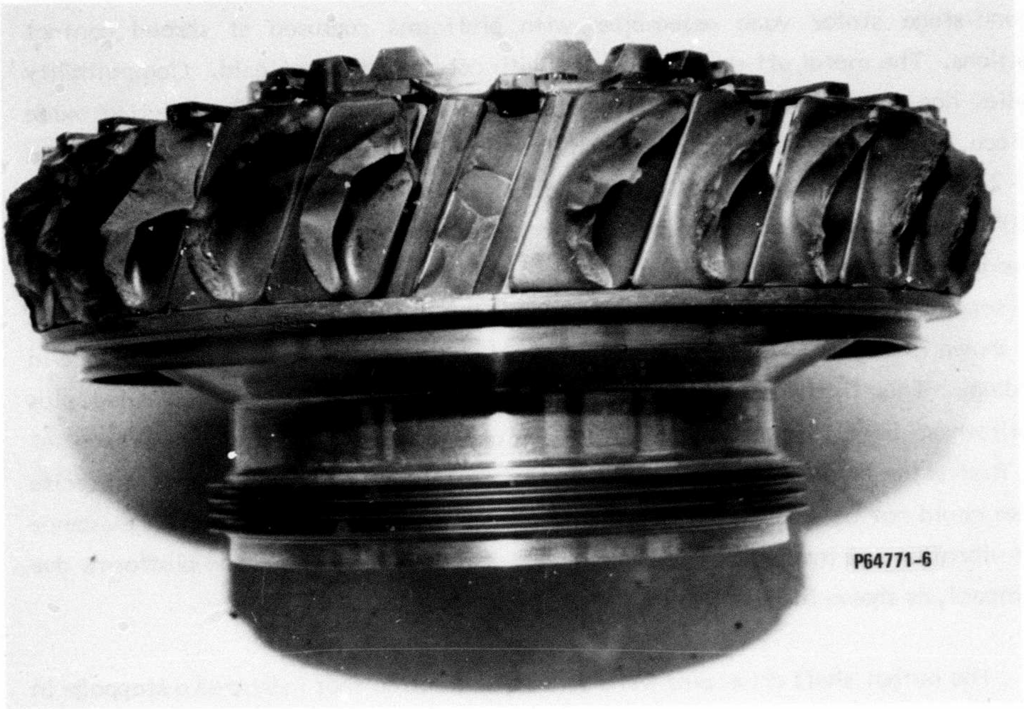

Figure 6-16. First-Stage Rotor After Engine Test CE001-17 Showing One Blade Fractured Below the Platform and the Rest Fractured by Impact Above the Platform.

evidence, the most plausible explanation was that a portion of the static structure broke loose and wedged between the metal turbine housing and the rotor. This would have caused an instantaneous speed change and generated enough torque to shear the shaft and bend the pins.

The next engine test was Build 8 in CE 002.[15] Prior to this test, the oxidation studies described in Paragraphs 4.3.3 and 4.3.4 were completed. These indicated that the Norton NC-350 RBSN was the most uniform RBSN and showed the least strength reduction during oxidation. They also indicated that a "flash" oxidation treatment of RBSN materials was beneficial. Therefore, for Engine CE 002 Test 8, all static-structure components (with the exception of the second-stage stator vanes, which were fabricated by ACC) were Norton NC-350, and all RBSN components were flash oxidized. The Norton NC-350 was oxidized 2 hours at 2012°F, and the ACC RBSN was oxidized two hours at 2460°F. In addition, photoetched HS-25 metal compliant layers were used at contact points along the outer flow path as shown in Figure 6-17.

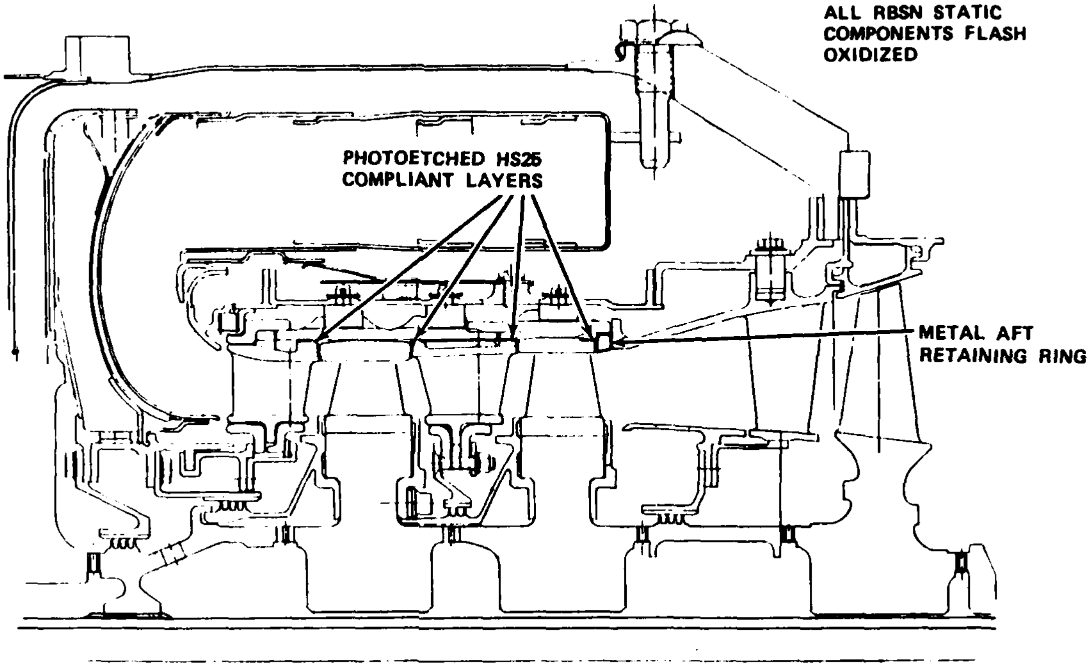

Figure 6-17. Engine Configuration for CE002 Test No. 8.

Test 8 consisted of a standard 2-hour cycle to full design conditions of 41,730 rpm and 2200°F. The test was run and shut down without incident. Disassembly revealed all ceramic components to be in the proper position, but several were damaged. A wedge-shape section was missing from the trailing edge of a first-stage stator vane. The fracture origin indicated the cause of fracture to be impact. Minor chipping or surface roughening type impact damage was present on 90 percent of the first-stage vanes and 30 percent of the second-stage vanes. No witness marks due to foreign materials were visible or detected by EDX analysis, suggesting that Si_3N_4 was the likely impacting material.

The second-stage tip shroud had two fractures which initiated at compliant layer tab locations. The compliant layer was distorted and showed signs of nonuniform loading. Review of dimensional data determined that the ID of the shroud was 0.025 inch oversize and would likely cause corner contact loading.

The final damaged part in run CE 002-8 was the main pilot cylinder. It had a crack that originated at a silicon-rich core at an outer pilot lug. The large silicon inclusion had been detected prior to engine assembly by both X-ray radiography and ultrasonic C-scan, but a better pilot cylinder was not available for the scheduled test.

Prior to Engine CE 002 Test 9, a new pilot cylinder was obtained, a second-stage shroud with the proper ID was machined, and the compliant layer configuration was modified to provide greater bearing surface. A two-hour cycle was conducted to full design conditions without incident. Disassembly revealed intact ceramic hardware but with chips on the shrouds and on vane platforms at contact points. The metal compliant layers did not prevent contact damage and in some cases appeared to contribute to it.

At this point in the program, the decision was made to attempt a single-cycle engine run of 10 hours and to base a go-forward decision upon the outcome. A number of modifications were selected for this engine build (Engine CE 002, Build 10). The second-stage shroud ID was further reduced in an effort to avoid edge loading with the stator platforms. Where build clearances allowed, compliant layers were eliminated. This decision was based upon the Test 9 results and preliminary data generated in the contact test apparatus (described in Section 7.0). The contact apparatus had revealed that coefficients of friction in excess of 0.8 could occur for ceramic interfaces with the HS25 compliant layers. The final compliant layer configuration is shown in Figure 6-18.

Engine light-off for Test CE 002-10 was accomplished smoothly, and acceleration to idle occurred without incident. Ten minutes were spent at idle followed by an acceleration to 100-percent speed and 1400°F T_4. Eighty minutes were spent at this condition followed by 6 hours 40 minutes at 1700°F T_4. A slow transient to 2200°F was then performed. After running 11 minutes at 2200°F, an engine failure occurred.

All ceramic parts except the first-stage inner support rings fractured into many small pieces. No blades were fractured below the platforms, suggesting that engine failure was not initiated by blade failure. However, all other parts were too fragmented to identify the source of initial fracture or to determine where in the engine test cycle the first damage initiated.

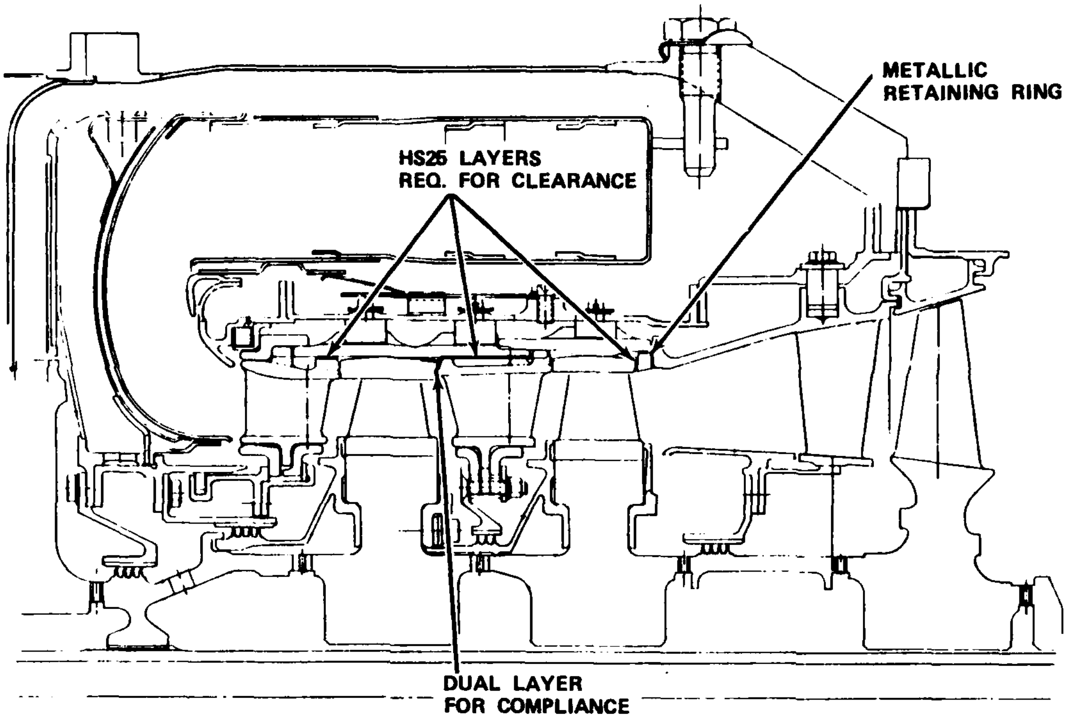

Figure 6-18. Compliant Layer Positions for Engine Test CE002-10.

6.6 RIG AND ENGINE TEST SUMMARY

A total of 19 static-structure rig tests were conducted, culminating in a successful 10-hour test to 1700°F average turbine inlet temperature and 120-percent design aerodynamic loading. This test included both stages of ceramic static structure hardware and consisted of a schedule containing two light-offs and 22 *transient cycles. None of the ceramic components were damaged.*

Initial dynamic rig testing detected a rotor vibration problem due to stator-passing excitation of the natural flexural vibration mode of a second-stage rotor blade. The stators were redesigned from a 21/21 to a 19/17 vane count to solve the problem, and the rotor was successfully operated in the dynamic rig to 45,000 rpm and 1700°F.

A total of 27 engine tests were conducted with mixed results. Most consisted of a successful light-off, smooth operation during a one- or two-hour cycle to design conditions of 2200°F TIT and 41,730 rpm, and successful shutdown. However, disassembly often revealed various levels of chipping or cracking of some of the static-structure components. Many tests were completely successful with no sign of damage to the ceramic components. The best of these were the series of Tests 8-13 in Engine CE 001 and 5-7 in Engine CE 002.

Tests 8-13 in CE 001 consisted of a series of light-offs and one- and two-hour runs with the 21/21 vane hardware to 31,000 rpm and 1700°F average TIT. A total of 23 light-offs and 20 hours test time were accumulated with no damage to the ceramic hardware. Tests 5-7 in Engine CE 002 consisted of one-hour and two-hour runs with the 19/17 vane hardware to 41,730 rpm and 2200°F average TIT. Shaft horsepower of 925, 870 and 930 shp respectively were recorded in these tests. This represents approximately 30 percent improvement over the baseline metal engine (715 shp).

In spite of these successful tests for individual cycles and for short sequences of cycles, reliable engine operation was not achieved. For example, the test following the above sequence at 41,730 rpm and 2200°F resulted in complete engine failure, even though it contained the same hardware that had operated successfully for several prior cycles. Three other complete engine failures occurred, each after the engine had been operating smoothly for some time.

The engine testing demonstrated that ceramic rotor blades and static-structure components can operate at the design conditions of 41,730 rpm and 2200°F average TIT and can produce substantial performance improvements over the baseline metal engine (30 percent increase in shp, 7 percent reduction in SFC). However, the engine testing also demonstrated that the ceramic components were failing on a delayed basis with an unknown failure mode. Evidence suggested that chipping and cracking due to contact stress at ceramic-ceramic and metal-ceramic interfaces was involved. As a result, the decision was made to suspend engine testing and to concentrate the remaining program funds on obtaining a better understanding of the mechanism of chipping and cracking at interfaces and to develop a solution for this problem.

7.0 CERAMIC CONTACT STRESS INVESTIGATION

As previously discussed, chipping or cracking at ceramic-ceramic and ceramic-metal interfaces was noted early in the rig test program. Intermittent materials tests were conducted in an effort to understand the problem and to determine a solution. The earliest investigations were compatibility tests of RBSN in contact with various metals and high-temperature lubricants at a range of loads and temperatures.[8] Promising material combinations were then selected for measurement of friction coefficients.[8-10] Finally, a special apparatus was designed to permit more accurate measurement of friction and to evaluate contact geometry, static-contact versus relative motion, time at temperature, and other variables that might affect interface integrity.[15]

7.1 COMPATIBILITY TESTS

Early rig tests indicated that surface damage due either to high point contact loads or adherence was the major recurring problem with ceramic components. Simple sandwich tests were initiated in a stress rupture furnace to identify metal compliant layers and high temperature parting agents that would be compatible with RBSN up to 2200°F.[8] Norton NC-350 RBSN and ACC RBSN were evaluated at temperatures of 1400, 1800, 2000° and 2200°F for 2 and 16 hours at a load of 1000 psi in contact with the materials listed in Table 7-1.

The test specimens consisted of 0.25-inch x 0.25-inch x 0.2-inch ceramic squares. One specimen face was machined with a 320-grit diamond grinding wheel and the other face was left in the as-nitrided condition, although it had also been machined with a 320-grit wheel in the green state prior to nitriding. Sheet metal compliant layer specimens were obtained in 0.005-inch and 0.010-inch thicknesses. Feltmetal compliant layer specimens were obtained in 0.040-inch thicknesses. All compliant layer specimens were cut into 0.5-inch x 0.5-inch squares for testing. Ultrasonically cleaned ceramic squares were stacked alternately up to ten layers thick with either a parting agent or compliant layer between the ceramic surfaces. The entire stack was placed in a furnace, dead-weight loaded at 1000 psi, and the furnace temperature increased to the test temperature. Upon completion of the test, the entire stack was allowed to cool under load to room temperature and then unloaded. Compliant layer deformation was measured with a micrometer, and surface adherence was noted by visual inspection.

TABLE 7-1. COMPLIANT LAYERS AND PARTING AGENTS EVALUATED.

PARTING AGENTS/LUBRICANTS	SHEET METAL
GRAPHITE	PLATINUM (Pt)
BORON NITRIDE	NICKEL (Ni)
PLATINUM PAINT	PLATINUM WITH ROUGH SURFACE
GOLD SPUTTERING	HS-25 (L-605)
NICKEL SPUTTERING	HS-188
HIGH TEMP NEVER SEEZ - NiO	HS-25-OXIDIZED
COPPER OXIDE	GOLD (Au)
GRAPHITE AND ALUMINA MIXTURE	310 STAINLESS
COBALT OXIDE	347 STAINLESS WITH PHOTOETCHED HOLES
HAFNIUM CARBIDE	
Y_2O_3 STABILIZED ZrO_2	FeCrALY
CALCIUM FLUORIDE	INCO 600
CORNING GLASS COMPOSITIONS 7570 7050, 7740, AND 1990	INCO 625 MA 956
FELTMETAL	**FLASH-COATED SHEET METALS**
FM 501 - 20-PERCENT DENSE	Pt WITH NiCo FLASH
FM 521 - 20-PERCENT DENSE	Ni WITH NiCo FLASH
HOSKINS 875 - 50-PERCENT DENSE	HS-25 WITH NiCo FLASH
FeNiCrAlY - 50-PERCENT DENSE	HS-25 WITH Cr FLASH *Ni WITH Cr FLASH*

The test results for 2000°F exposure are summarized in Table 7-2. The best results at 2000°F and above were obtained with pre-oxidized HS-25 sheet, cobalt oxide, bare RBSN surfaces, and Y_2O_3-stabilized ZrO_2 coating plasma-sprayed on an HS-188 surface. Also 310 and 347 stainless steel adhered on occasion but appeared satisfactory if pre-oxidized and used in conjunction with a parting agent such as gold, platinum, or cobalt oxide. The Feltmetals did not adhere but oxidized and deformed severely and embrittled.

7.2 INITIAL FRICTION MEASUREMENTS

This effort was initiated to determine the coefficient of friction of bare RBSN surfaces in contact from room temperature to 2000°F at normal stresses ranging from 500 to 1500 psi and to evaluate lubricants and interface layers which might reduce friction. Schematics of the test fixture and furnace arrangement are shown in Figure 7-1.

Norton NC-350 reaction-bonded Si_3N_4 with 320-grit machined and as-nitrided surfaces was used for the friction tests. After selecting the surface condition, the

TABLE 7-2. COMPATIBILITY OF RBSN AT 1100°C (2000°F) UNDER LOAD (COMPLIANT LAYER OR LUBRICANT).

	COMPLIANT LAYER	LUBRICANT
SEVERE REACTION	FeCrAlY - DELAMINATION HS-25/COBALT PLATED-MELTING AND REACTION HOSKINS 875-ADHERENCE MA956 - ADHERENCE, PULLOUTS PLATINUM - ADHERENCE NICKEL - EMBRITTLEMENT, CRUMBLING GOLD - MELTING, MECHANICAL BONDING 347 STAINLESS/PHOTOETCHED - ADHERENCE FELTMETAL 501 AND 521 - EMBRITTLEMENT, CRUMBLING	NICKEL OXIDE - ADHERENCE COPPER OXIDE - ADHERENCE BORON NITRIDE - GLAZED, ADHERENCE GRAPHITE - OXIDIZED GLASS NO. 7570, HIGH LEAD - GLASS/RBSN REACTION GLASS NO. 7050, BOROSILICATE - GLASS/RBSN REACTION GLASS NO. 7740, BOROSILICATE - GLASS/RBSN REACTION
POSSIBLE REACTION	INCO 625 - ADHERENCE 310 STAINLESS - ADHERENCE HS-188 - ADHERENCE HS-25 - ADHERENCE INCO 600 - ADHERENCE HOSKINS 875 FELT METAL - PULLOUTS PLATINUM PAINT (SINGLE SURFACE) - ADHERENCE	CALCIUM FLUORIDE - ADHERENCE GLASS NO. 1990, POTASH SODA LEAD - SLIGHT REACTION BETWEEN NO. 1990 AND RBSN
NO REACTION	HS-25 PRE-OXIDIZED Y_2O_3 STABILIZED ZrO_2	CoO in DTE-25 OIL

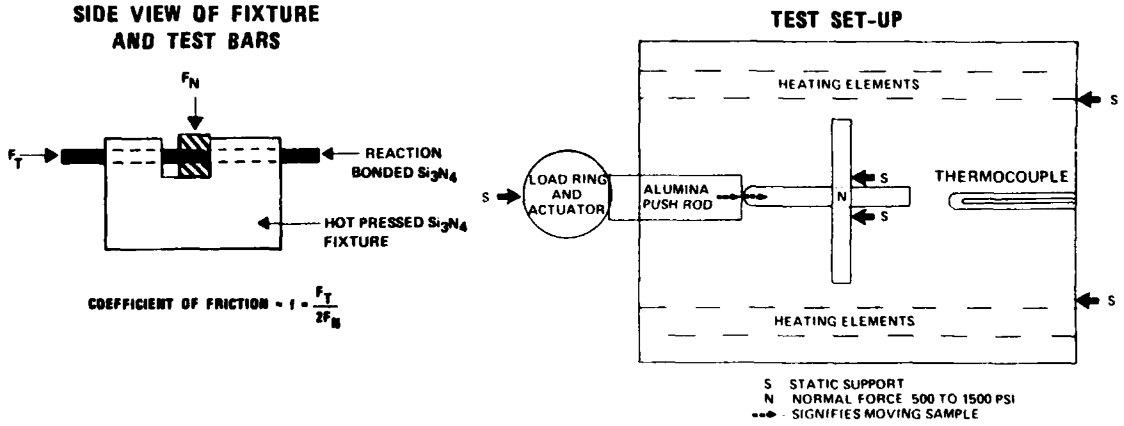

Figure 7-1. Schematic of Initial Friction Test Apparatus.

samples were coated with the candidate lubricant and tests were conducted at room temperature to ensure that the equipment was operational. The surfaces of the reaction-bonded Si_3N_4 were then recoated with lubricant and inserted into the fixture for the high-temperature tests. Furnace temperature was increased to 1400°F, and the temperature was allowed to stabilize for five minutes. Approximately six data points were obtained at each temperature, and the moving sample was repositioned through access ports in the furnace when necessary. The total test cycle, room temperature to 2000°F, required approximately two hours of test time.

The data from these initial friction tests are summarized in Table 7-3. The coefficient of friction of bare RBSN was greater than 0.5 at all temperatures and tended to increase at high temperature. Conventional dry lubricants such as graphite and boron nitride substantially reduced friction at low temperature but were not stable at high temperature. The graphite volatilized by oxidation and disappeared from the interface, while the boron nitride oxidized and left a glassy layer that bonded the RBSN together during cooling. Gold also substantially reduced friction but was limited in temperature capability and caused mechanical adherence upon cooling. Felpro C-200 and C-300 dry film lubricants also reduced friction at the lower temperatures, but resulted in reaction and bonding at high temperature. Cobalt oxide had a higher coefficient of friction than the Felpro lubricants but did not react with the RBSN at high temperature.

These initial friction studies indicated that sputtered gold was a good lubricant at lower temperatures and led to the use of gold on the aft retainer ring and on the positioning pins in contact with the main pilot cylinder. Photoetched, oxidized HS-25 with cobalt oxide was selected as the primary compliant layer material for the RBSN/RBSN static structure interface.

7.3 LATER FRICTION AND CONTACT STUDIES

As the program continued, it became apparent that the lubricants and compliant layers identified during the initial compatibility and friction studies were not solving the contact problem in the engine. The need for a more comprehensive study with a more versatile test apparatus was identified. Table 7-4 lists variables that could affect ceramic interface behavior and that needed to be assessed. It also lists the approaches selected to evaluate each variable.

TABLE 7-3. INITIAL FRICTION MEASUREMENTS FOR COATINGS, COMPLIANT LAYERS AND LUBRICANTS ON NC-350 RBSN.

MATERIAL	AVERAGE COEF. OF FRICTION/STANDARD DEVIATION AT VARIOUS TEMPERATURES			
	70°F	1400°F	1800°F	2000°F
BARE MACHINED RBSN	0.56/0.04	0.73/0.07	0.75/0.12	0.82/0.18
BARE AS-NITRIDED RBSN	0.86/0.08	0.63/0.06	0.64/0.15	0.08/-
UNFLUXED PLATINUM PASTE	0.27/0.04	0.42/0.04	0.72/0.04	-
<0.0001-INCH THICK SPUTTERED GOLD	0.76/0.05	0.49/0.06	-	-
0.0002-0.0004 INCH SPUTTERED GOLD	0.15/0.04	0.24/0.05	0.09/0.01	-
GOLD ON NICKEL SPUTTERED COATING	0.12/0.02	0.12/0.02	0.10/0.01	-
PLATINUM (Pt)	-	0.65/0.11	0.42/0.13	0.38/0.02
BORON NITRIDE (BN)	0.26/0.08	0.18/0.02	0.28/0.06	0.29/0.08
GRAPHITE (C)	0.16/0.03	0.06/0.01	0.57/0.16	0.70/0.13
COBALT OXIDE (ON MACHINED RBSN)	0.24/0.01	0.29/0.02	0.26/0.05	0.23/0.03
COBALT OXIDE (ON AS-NITRIDED RBSN)	0.50/0.05	0.36/0.02	0.43/0.11	0.52/0.03
GRAPHITE PLUS Al_2O_3	0.18/0.01	0.27/0.10	0.58/0.09	-
UNOXIDIZED HS-25 SHEET	0.34/0.02	0.40/0.02	0.39/0.03	-
HS-25 SHEET WITH COBALT OXIDE	0.20/0.01	0.16/0.03	0.42/0.09	0.64/-
OXIDIZED HS-25	0.30/0.01	0.42/0.04	0.39/0.06	-
PHOTOETCHED, OXIDIZED HS-25	0.24/0.01	0.47/0.0	-	-
FELPRO C-300 DRY FILM LUBRICANT	0.18/0.05	0.17/0.01	0.21/0.03	-
OXIDIZED HS-25 WITH FELPRO C-300	0.13/0.01	0.29/0.04	-	-
PHOTOETCHED, OXIDIZED HS-25 WITH C-200	0.17/0.01	0.34/0.01	RBSN BROKE	-
HOSKINS 875 SHEET	0.22/0.04	0.75/0.12	-	-
PHOTOETCHED, OXIDIZED HS-25 WITH C-300	0.19/0.02	0.44/0.01	RBSN BROKE	-
SPUTTERED GOLD WITH FELPRO C-300	0.18/0.04	0.30/0.06	RBSN BROKE	-

A new contact test apparatus was designed. As shown in Figure 7-2, it consisted essentially of a furnace, a leveraged dead-weight* load train for applying a normal force, and a test machine** for applying relative motion and recording the resulting tangential force.[14,75] The following typical test sequence describes the specimen configurations and the test procedure.

---

*Later replaced by a pneumatic cylinder load system.

**Model 1125 tension/compression test machine manufactured by the Instron Corp., Canton, MA.

TABLE 7-4. CERAMIC INTERFACE STUDIES

VARIABLES AFFECTING CONTACT	EVALUATION APPROACH
MATERIALS	
TEMPERATURE	
TIME AT TEMPERATURE	COEFFICIENT OF FRICTION, VISUAL INSPECTION, STRENGTH, FRACTOGRAPHY
PRE-OXIDATION	
LOAD	
POINT CONTACT	
LINE CONTACT	
AREA CONTACT	
RATE OF RELATIVE MOVEMENT	
CYCLES	
SURFACE FINISH	
CHEMICAL COMPATIBILITY	
COMPLIANT LAYERS	
LUBRICANTS	
SUPERIMPOSED BEND LOAD	
VIBRATION	

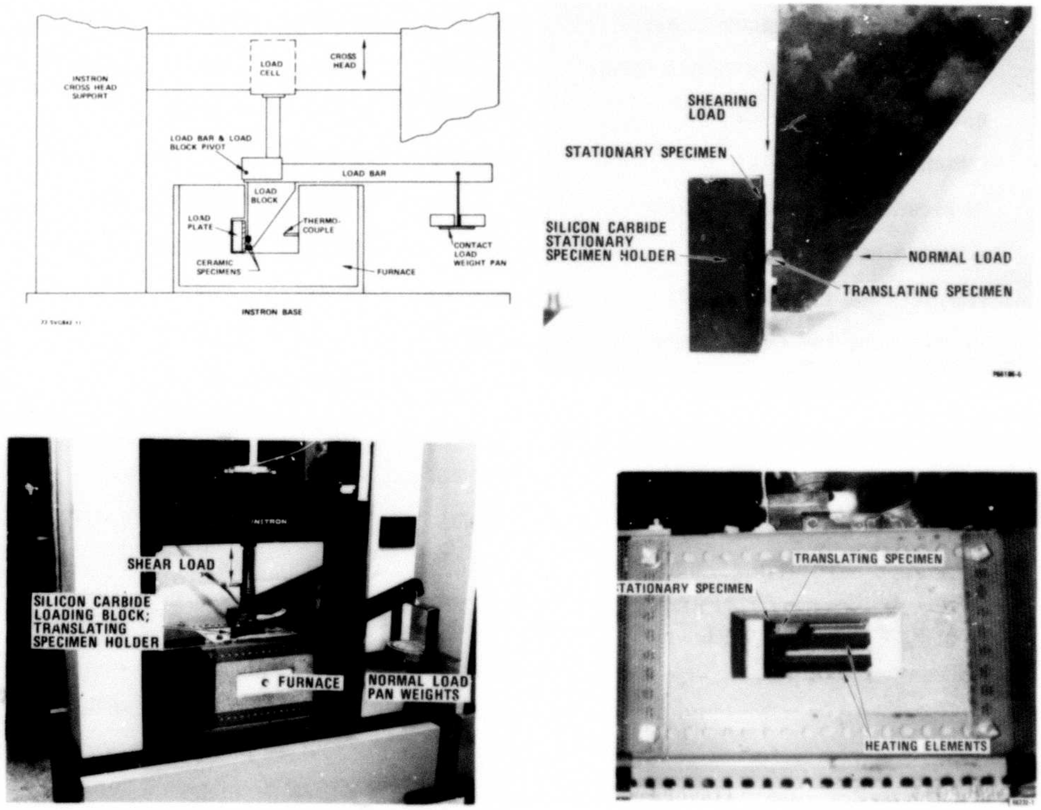

Figure 7-2. Schematic and Photographs of the Contact Test Apparatus.

Step 1 - Specimen Positioning - The two ceramic test bars are inserted into notches in the load plate and load block so that the long axes are perpendicular to each other. Both specimens are crowned on one surface and flat on the opposite surface. By selectively pairing the surfaces to be in contact, point loading, line loading or area loading can be achieved. Further test variation can be achieved by placing a compliant layer material or a lubricant between the two test bars. The specimen fixturing is made of hot-pressed SiC.

Step 2 - Heat to Test Temperature - The furnace is turned on and the specimens are heated to the selected test temperature. During this heating and the subsequent temperature soak, the Instron is set to maintain zero tangential force by automatically repositioning the crosshead to account for thermal expansion of the fixture.

Step 3 - Application of Normal Force - When the selected temperature has been reached, the deadweight loading is applied to provide the desired normal force at the specimen interface. The system previously has been calibrated by replacing the specimen and load plate with a load cell. The normal load is maintained at temperature for the selected time.

Step 4 - Application of Tangential Force - The load block and its ceramic specimen (referred to as the moving specimen) are moved, relative to the load plate and its ceramic specimen (referred to as the stationary specimen), by translating the Instron crosshead at a controlled speed (usually 0.02 inch per minute). The tangential force as a function of interface movement distance is plotted on the Instron chart recorder. From this data, the static and dynamic coefficients of friction are calculated. The test can be conducted with a single pass or in a cyclic mode.

Step 5 - Flexure Strength Measurement - The stationary test bar is removed from the load plate and strength tested at room temperature in four-point bending with the original contact surface in tension to determine if the contact conditions produced strength degradation. The test bars have a cross section of 0.125 x 0.250 inch and are tested in a self-aligning fixture with an outer span of 1.5 inch and an inner span of 0.75 inch.

Step 6 - Fractography - The contact area is compared with adjacent areas, and the fracture surface is compared with baseline test bars that have not been exposed to the contact conditions. These observations are correlated with friction and property data and with appropriate stress analyses in an effort to understand the mechanisms of contact damage.

Step 7 - Stress Analysis - The peak stress in the contact region is calculated for the measured load and friction conditions using a computer model developed under an Office of Navy Research (ONR) Program.[52]

The contact apparatus has been successfully used for exploring the effects of temperature, load, contact geometry, chemical compatibility, compliant layers, lubricants, surface finish and superimposed bend loads on friction and retained strength.[14-17]

The magnitude of the load, the mode of the load application (static-versus relative motion), and the coefficient of friction were identified as the dominant factors and will be described in the following paragraphs.

7.3.1 EFFECTS OF STATIC LOAD VERSUS RELATIVE MOTION

Results of initial testing of bare RBSN with and without relative motion for the point load condition* (0.25 inch radius crown on crown) are summarized in Figure 7-3. No surface damage was detected after static contact loads up to 308 lbs. The range in strength of these bars was the same as crowned baseline bars that had not been subjected to a static load (approximately 45 ksi). Most of the fracture origins were not located at the contact point.

When relative motion was added to the contact load, visible surface damage occurred and the average bend strength was reduced to 20 ksi. These reductions in strength occurred for applied normal loads of 24.7 and 57.3 lbs. The coefficient of friction was typically 0.8 or higher.

Figure 7-4(a) shows a typical scanning electron microscope (SEM) photomicrograph of a stationary RBSN test bar surface after a moving specimen was slid across it (from left to right) at 57.3 lbs normal load at room temperature. Arc-shaped cracks, similar to the partial ring cracks described by Lawn,[76] are present in the initial contact zone and were probably formed at the peak stress coincident with

---

*Measured contact width for the "point" contact configuration was typically 500-700 μm (0.020-0.028 inch).

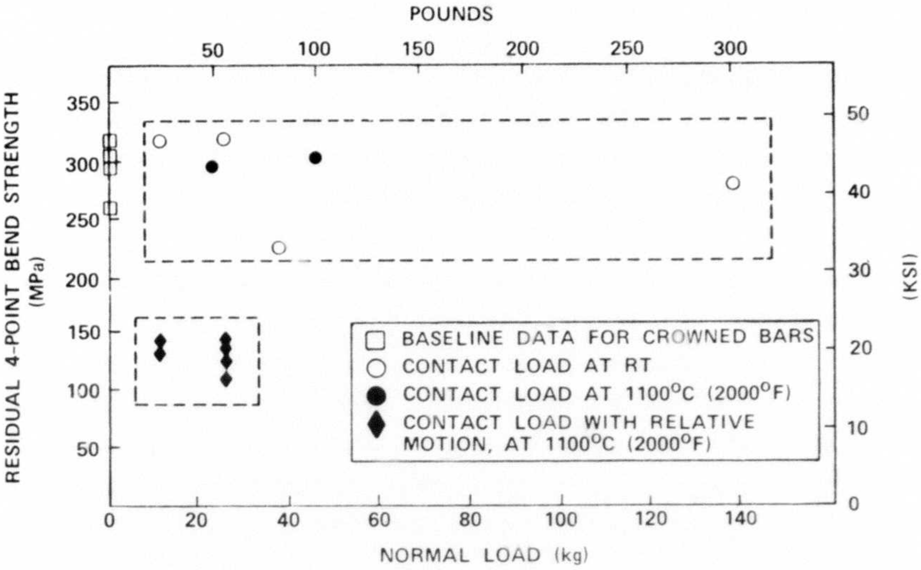

Figure 7-3. **Effect on Strength of Normal Contact Load (with and without Simultaneous Relative Motion).**

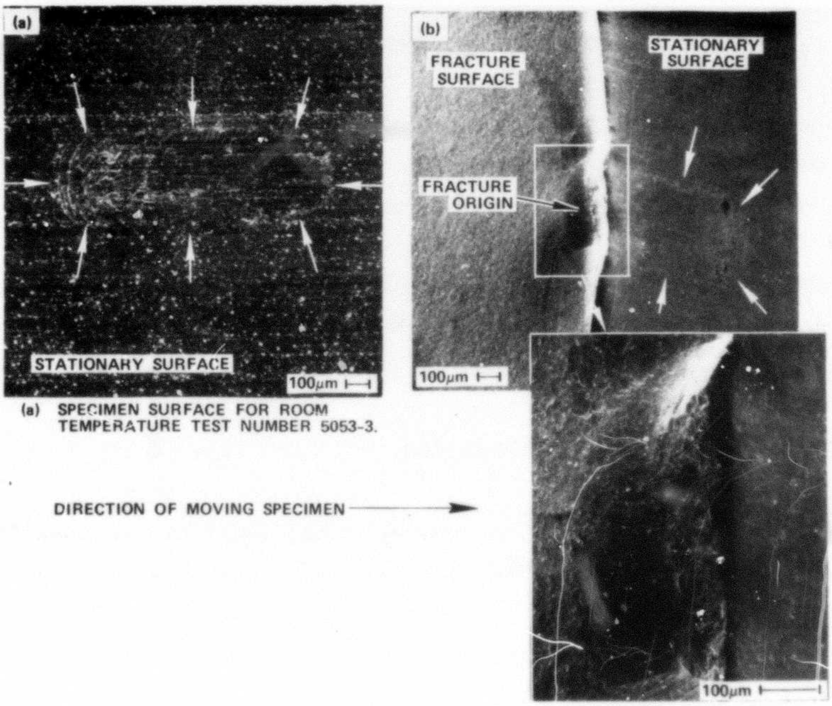

(a) SPECIMEN SURFACE FOR ROOM TEMPERATURE TEST NUMBER 5053-3.

(b) CONTACT SURFACE AND FRACTURE SURFACE OF 1100°C TEST NUMBER 5053-8.

P73688

Figure 7-4. **SEM Photomicrographs of Reaction-Bonded Si_3N_4 Stationary Test Bars After Contact Testing, Regions of Contact Outlined with Arrows.**

breakaway. Additional cracks are visible to the right of the partial ring cracks, but these are more irregular and appear to enter the material at a low angle. These occurred coincident with dynamic friction. As motion continued to the right, the frequency and apparent severity of cracks decreased.

Figure 7-4(b) shows the SEM photomicrograph of a typical fracture surface after bend testing. The fracture initiated at the test bar surface in the region of initial contact at a stress of 16.0 ksi. All fracture origins had similar appearance, i.e., a microcracked zone immediately under the contact width transitioning into a smooth bulbous or conical region. To estimate which of these regions represented the critical flaw during fracture, calculations were made on several specimens using the version of the Griffith equation proposed by Evans and Tappin[77] for an elliptical surface crack:

$$\sigma_f = \frac{Z}{Y}\left(\frac{2E\gamma}{c}\right)^{1/2}$$

where σ_f is the calculated fracture stress, c is the depth of the semi-elliptical surface crack, E is the elastic modulus, γ is the fracture surface energy, Y is a dimensionless parameter that depends on flaw position, specimen size and test procedure[78] (for pure bending with a flaw depth/specimen thickness ratio less than 0.01, Y = 2) and Z is a dimensionless parameter based on flaw shape.[24]

Better correlation between measured strength and calculated σ_f resulted when the microcracked region was selected as the critical flaw, i.e., measured σ = 16.0 ksi vs calculated σ_f = 16.3 ksi for the test bar shown in Figure 7-4(b).

7.3.2 MECHANISM OF CONTACT DAMAGE

A literature search and experimental studies under this program[17,75] and a literature search plus analytical studies under a parallel ONR program[52,79] have identified the probable source of contact damage in the TSE331C-1 ceramic demonstration engine. Stress distributions for various load configurations are shown in Figure 7-5.[80]

Figure 7-5a was initially analyzed by Hertz[81] and is commonly referred to as Hertzian loading. The symmetrical stress field is compressive directly under the contact zone and tensile adjacent to the contact zone. The tensile stress peaks at

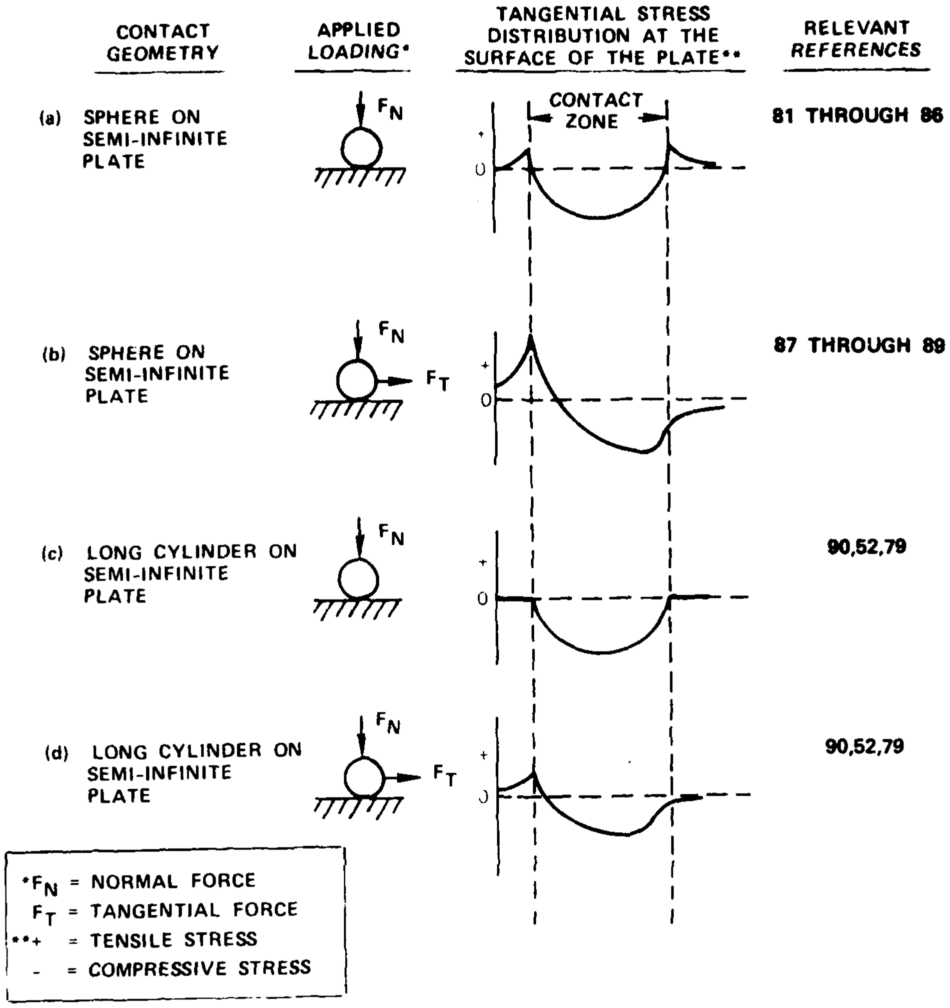

Figure 7-5. Contact Stress Distributions (Determined Analytically, Assuming Elastic Conditions) for Simple Contact Geometries for Normal and Biaxial Loading.

the edge of the circular contact zone and decreases with distance away from the contact zone.[82] Fracture initiates when the tensile stress becomes high enough to cause propagation of an existing material flaw at or near the surface adjacent to the contact zone. The crack initially forms a ring concentric with the contact zone. As the normal force is increased, the crack penetrates to greater depth following the stress contour in an outward sloping cone.[84-86]

The stress distribution for normal loading of a cylinder on a semi-infinite plate (Figure 7-5c) is similar to Hertzian loading except that no hoop tensile stress is present adjacent to the contact zone. Thus, under ideal contact, the contact stresses for a long cylinder on a plate will be compressive. However, for a short cylinder or for realistic conditions where surface asperities prevent ideal contact, localized tensile stresses are likely to be present.

Figures 7-5b and 7-5d show the stress distributions when a tangential force is present in addition to a normal force.[87,88] The stress distribution is skewed to produce a sharp tensile stress spike on the material surface at the trailing edge of the contact zone. The tensile spike for this biaxial loading is of much higher magnitude than the tensile stress in Hertzian loading (for a given normal force) and thus results in material surface damage at a much lower normal load.

Fracture or surface damage initiates under the same criteria for biaxial loading as for Hertzian loading; i.e., cracks propagate from existing flaws when the local tensile stress reaches a critical value dependent on the flaw size, the elastic modulus, and the fracture surface energy.

The magnitude of the tensile stress for sliding contact or biaxial loading is strongly dependent upon the coefficient of friction as shown in Figure 7-6.[52] The tensile stress is very localized, peaking at the surface at the trailing edge of the contact and rapidly diminishing beneath the surface.[52]

A parametric study[17] was conducted for line contact and point contact of RBSN using experimental data (load, contact area, friction-coefficient) from the contact apparatus tests and Finger's[52] computer program to estimate the localized surface tensile stress that might occur for TSE331C-1 ceramic static structure components under the worst case conditions of small-area contact and biaxial loading. Data for line contact over a normal load range of 10 to 50 pounds and a coefficient of friction range from 0 to 0.8 are summarized in Table 7-5. Assuming a material bend strength of 45 ksi, surface damage would be theoretically predicted at any load/coefficient of friction above 25 lbs/0.2 for a 1/16-inch contact radius and above 25 lbs/0.4 for a 1/4-inch contact radius. Although the theoretical conditions do not exactly simulate the experimental conditions, the correlation is excellent between predicted surface damage and measured surface damage (as determined by bend strength tests after contact motion).

Table 7-6 summarizes similar predictions for point contact conditions between RBSN surfaces assuming a contact length of 700 μm (0.028) as measured on actual contact surfaces by SEM. Finger's contact model of a radius on a plane does not simulate the actual crown-on-crown geometry but at least provides an order of magnitude estimate of the tensile stresses that can occur at the surface. The calculations predict that surface damage will occur for normal loads of 24.7 pounds and 57.3 pounds and for friction coefficients of 0.2 and 0.8.

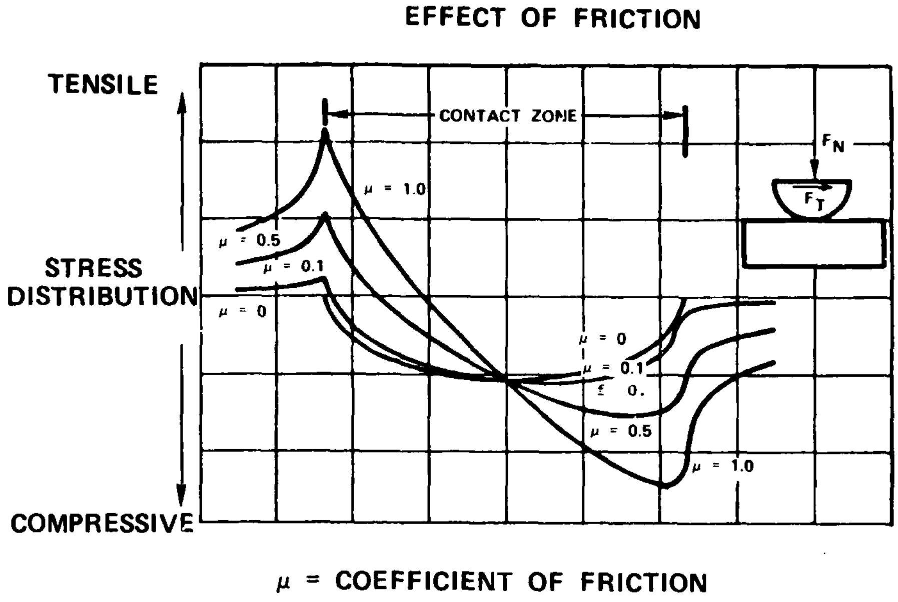

Figure 7-6 Effect of Friction on Stress Distribution for Biaxial Contact Loading.

The last two columns in Table 7-6 list the stress present 100 μm (0.004 inch) beneath the point on the surface where the stresses are maximum. The depth of 100 μm was selected because it coincided with the measured depth of surface damage for the point contact condition. For both normal loads at a friction coefficient of 0.2, the stresses at 100 μm depth are compressive. For 57.7 pounds normal load, at a friction coefficient of 0.8, the stress is still tensile but very low. The high surface tensile stresses undoubtedly cause surface damage, but the very rapid change in the stress field progressing inwards from the surface from a tensile to a compressive state limits the depth of damage and determines the level of material strength degradation. This explains why cracks do not propagate through the test bar during contact tests.

7.3.3 CONTACT TESTS WITH SUPERIMPOSED BENDING

The contact apparatus tests do not simulate the bend or tensile stresses that a component is exposed to during cyclic engine testing. To evaluate the effect of superimposed tensile stress, a special fixture was fabricated for use with the contact test apparatus; a schematic of the fixture is shown in Figure 7-7. A pin and shims are wedged behind the stationary test bar to place the contact side in tension.

The test results are summarized in Table 7-7.[17] Static loading did not result in fracture of the stationary specimen, even with superimposed bend loads greater than

TABLE 7-5. PREDICTED CONTACT STRESSES FOR RBSN UNDER LINE CONTACT WITH RELATIVE MOTION.

CONTACT RADIUS (IN.)	CONTACT NORMAL LOAD (LB)	MAXIMUM COMPRESSIVE STRESS (KSI)	MAXIMUM TENSILE STRESS AT SURFACE (KSI)			
			$\mu = 0$	$\mu = 0.2$	$\mu = 0.4$	$\mu = 0.8$
1/4	50	76.8	0	29.5	60.0	120.8
1/4	25	54.3	0	20.7	42.2	85.2
1/4	10	34.4	0	12.9	26.5	53.6
1/16	50	153.6	0	58.1	118.7	239.6
1/16	25	108.6	0	40.7	83.4	168.9
1/16	10	68.7	0	25.3	52.2	106.0

TABLE 7-6. PREDICTED CONTACT STRESSES FOR RBSN UNDER POINT CONTACT* WITH RELATIVE MOTION.

CONTACT RADIUS	CONTACT NORMAL LOAD (LB)	MAXIMUM COMPRESSIVE STRESS (KSI)	MAXIMUM TENSILE STRESS AT SURFACE (KSI)		MAXIMUM TENSILE STRESS AT 100 μm DEPTH (KSI)	
			$\mu = 0.2$	$\mu = 0.8$	$\mu = 0.2$	$\mu = 0.8$
1/4	57.3	245.7	96.2	389.4	-43.7	3.7
1/4	24.7	161.3	62.8	255.1	-21.5	-5.6

*700 μm x 265 μm (0.028 x 0.01 INCH) CONTACT AREA

20 ksi. However, as soon as relative motion was initiated, the specimen fractured. This testing verified that a combination of contact damage and superimposed or subsequent tensile loading could result in fracture and was a likely source of component failure in the engine. Use of a compliant layer at the interface, even though the coefficient of friction was high, prevented surface damage and fracture except for one case. This exception was for photoetched oxidized HS25 when the contact load was maintained during cooling. In this case, sticking of the HS25 to the Si_3N_4 apparently resulted in restraint of movement at the interface during cooling, which would produce near-surface shear stresses in the ceramic due to the large thermal expansion-difference between the Si_3N_4 and HS25.

7.3.4 EFFECT OF TEMPERATURE

Testing was performed with the contact apparatus to determine the effects of temperature and hold time at temperature. Figure 7-8 summarizes data for pre-

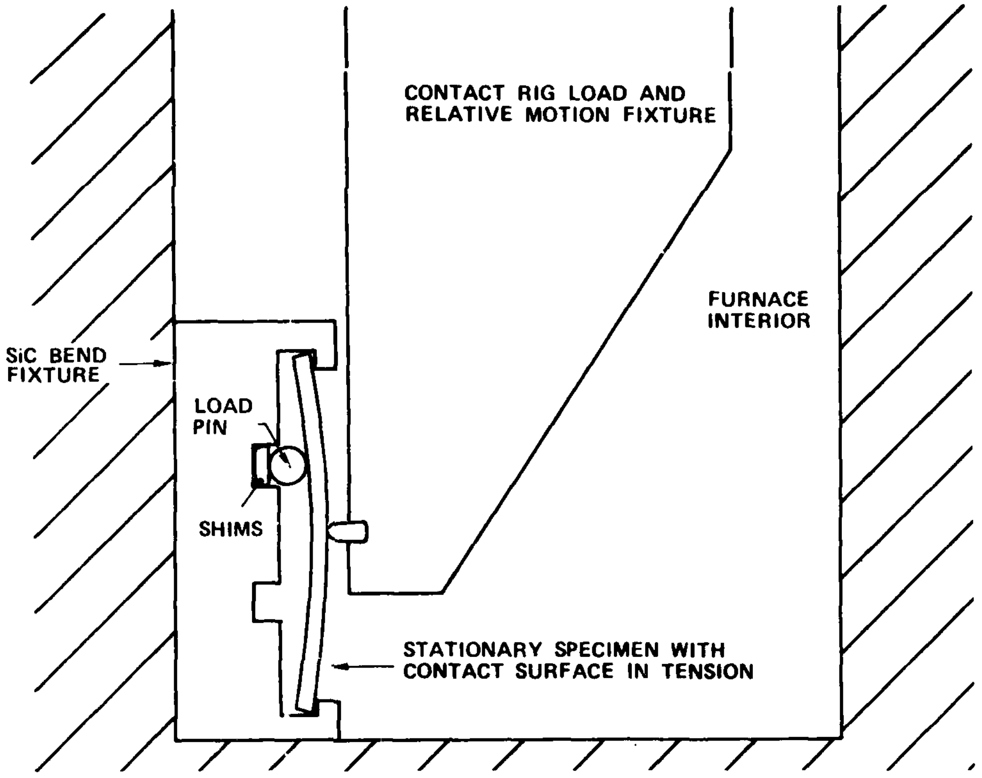

Figure 7-7. **Schematic of Fixture to Place the Stationary Test Specimen in Bending at the Contact Zone.**

oxidized (2012°F/2 hours) NC-350 RBSN tested at a normal load of 57.3 pounds. over the temperature range 1600°F to 2000°F. The coefficient of friction between the NC-350 specimens increased with increasing temperature. Visual inspection revealed microcracks on the contact surface of all the specimens and small chips on some of the specimens at each temperature. The residual four-point bend strength did not vary with respect to temperature. Flexure strengths for all temperatures tested ranged from 15 to 20 ksi, approximately half of the baseline strength. Similar results were obtained for RBSN that was not pre-oxidized, for other RBSN materials, and for lower normal loads of 10 and 25 pounds. Friction coefficients were similar for line contact, but less strength reduction resulted.

Hold time at temperature prior to initiating the relative movement had little effect at high loads (25-50 pounds) for point contact. The static coefficient of friction remained constant for hold times ranging from zero to 1.5 hours. Chipping occurred on some of the specimens at hold times of 0.5 and 1.5 hours. The residual room-temperature four-point flexure strength of the specimens at all hold times tested was approximately 50 percent of the material baseline flexure strength.

TABLE 7-7. SUMMARY OF CONTACT APPARATUS TEST WITH SUPERIMPOSED TENSILE STRESS.

MATERIAL	LUBRICANT	COMPLIANT LAYER	TEST CONDITION	SUPERIMPOSED BENDING LOAD (KSI)	CONTACT CONFIG	OBSERVATION	COEFFICIENT OF FRICTION
NC-350 RBSN	NONE	NONE	*BASELINE	20	POINT	BROKE DURING TEST	
				21		BROKE ON LOADING AT TEMPERATURE	- -
NC-350 RBSN	CoO/DTE-25	OXIDIZED HS25	*BASELINE, REMOVE CONTACT LOAD DURING COOLING	26	LINE	ROOM TEMPERATURE FLEXURE 52.3 KSI	1.21
				24		ROOM TEMPERATURE FLEXURE 48.3 KSI	1.18
NC-350 RBSN	CoO/DTE-25	OXIDIZED HS25	LOAD AT 75°F, 25 LBS, HEAT TO 1800°F/40 MIN, HEAT TO 2000°F/10 MIN, COOL TO ROOM TEMPERATURE WITHOUT RELEASING CONTACT LOAD	23	LINE	ROOM TEMPERATURE FLEXURE 54.6 KSI	- - -
		OXIDIZED AND PHOTO-ETCHED HS25		20		BROKE DURING COOL	- - -

*BASELINE TEST CONDITIONS
2000°F
1/2 HOUR HOLD AT TEMPERATURE
25 POUND NORMAL LOAD

Recent tests with SiC have shown that the coefficient of friction can increase to high levels (>1.3) at low normal loads (<3 lbs) at 2000°F.[79] This suggests that an adhesive or viscous surface mechanism is operative and may explain why chipping occurs on contact test specimens and on some engine components.

7.3.5 EFFECT OF LUBRICANTS

Results of the chemical compatibility study showed that the only lubricating material tested that did not react with RBSN at 2000°F was cobalt oxide in a DTE25 oil carrier. These two materials were used as a lubricant and carrier in the TSE331C-1 ceramic engine. Figure 7-9 shows the results of the static friction tests on bare NC-350 preoxidized specimens with and without CoO/DTE-25 lubricant. The CoO/DTE-25 lubricant reduced the static coefficient of fricton from 0.80-0.85 for bare surfaces to 0.18-0.25 for lubricated surfaces at 2000°F. Visual inspection of the contact area indicated that CoO/DTE-25 lubricant formed a protective smeared

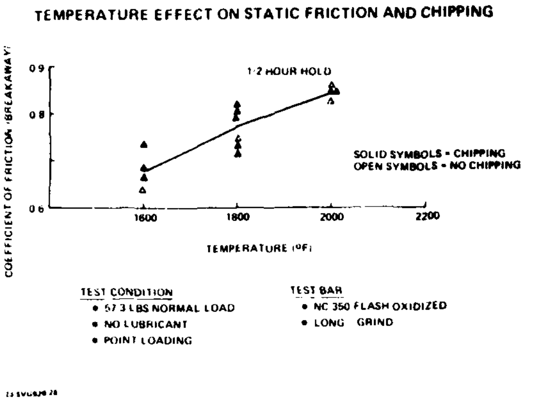

Figure 7-8. **Temperature Effect on Friction and Chipping.**

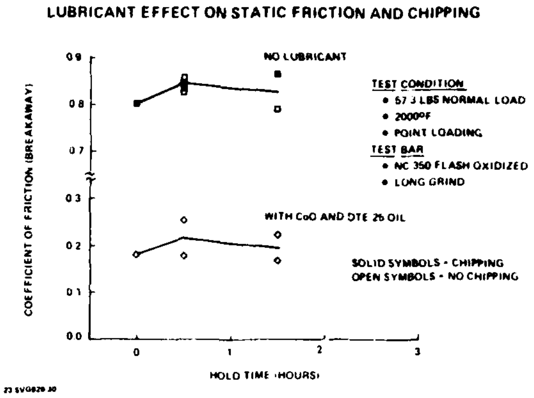

Figure 7-9. **Lubricant Effect on Friction and Chipping.**

surface layer so that the surfaces of the ceramic did not come in contact. However, in the flowing gas engine environment, the particulate CoO may blow off and not provide lubrication. Also contact apparatus tests have shown that the protective layer wears through under cyclic motion conditions.

7.3.6 EFFECT OF COMPLIANT LAYERS

Compliant layer tests were conducted for line contact conditions, by using a flat, stationary specimen and a crowned moving specimen with 0.010 inch thick metal sheet between the specimens. A standard test consisted of holding a normal load of 24.7 lbs for 0.5 hour at 2000°F followed by a relative movement of 0.06 inch. Strength and friction results are compared with those for bare and lubricated specimens in Figure 7-10.

HS25, HS188, MA956, cobalt- and chrome-plated HS25, and FeCrAlY were evaluated. Sticking occurred in many of these cases, often accompanied by formation of a broad, shallow chip, at the contact surface of the stationary ceramic specimen. Little or no sliding occurred between the metal layer and the ceramic specimens, the movement being accommodated by deformation and tearing of the compliant layer.

Figure 7-11(a) shows the surfaces of a typical chipped, RBSN stationary specimen and a torn HS25 compliant layer after exposure to the standard test conditions. The static coefficient of friction was 1.8, the dynamic coefficient ranged from 0.71 to 1.17, and the retained strength of the stationary RBSN specimen was 128 MPa (18.6 ksi). A shallow chip, one-third the width of the specimen in the center

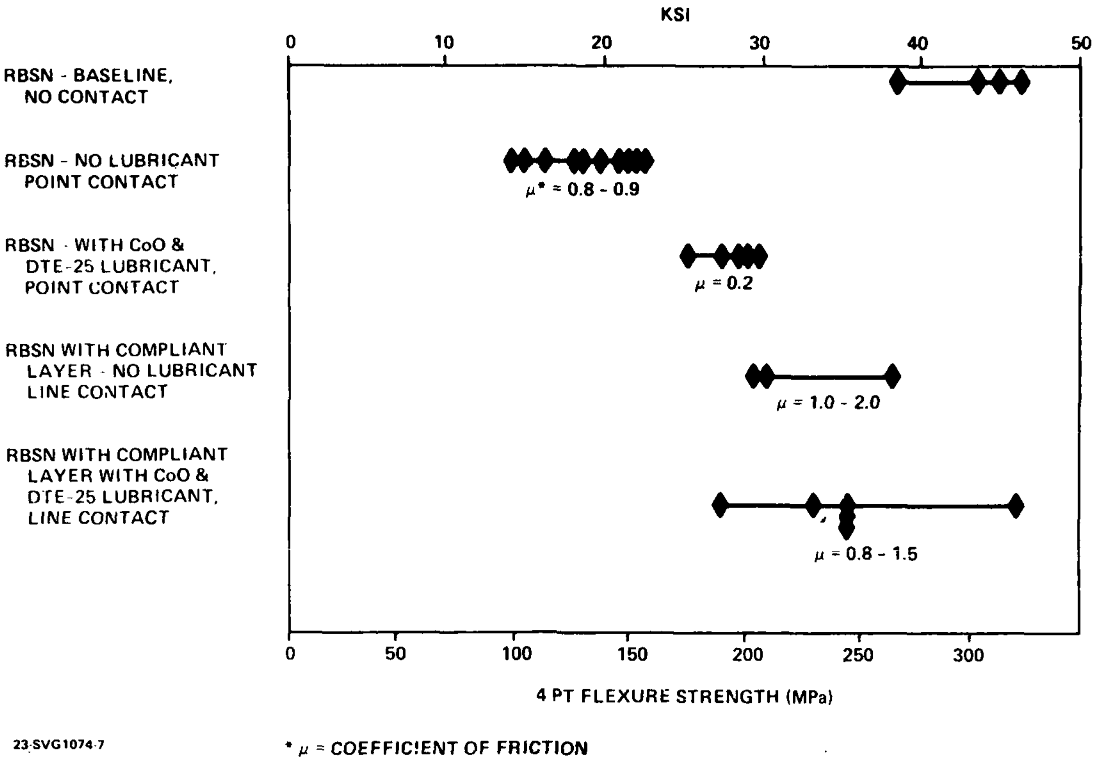

Figure 7-10. Retained Strength and Friction-Comparison for Bare RBSN, Lubricated RBSN and HS25 Metal Compliant Layer.

of the contact region is missing and adhered to the bottom side of the compliant layer. Examination at high magnification of a polished section through the chip and compliant layer showed intimate mechanical contact but no obvious chemical reaction or interdiffusion.

Similar chipping occurred in many of the contact rig compliant layer tests and also in some of the static compatibility tests. In most cases, the chip separated from the ceramic and adhered to the metal. Although a firm mechanism has not been defined, it would appear that bonding occurs at temperature and that the chip forms either at temperature or during cooldown, possibly due to thermal expansion mismatch between the ceramic and metal and because the local bonding and hydrostatic loading restrains the compliant layer from shearing. This would lead to near-surface tensile stresses in the ceramic that would likely cause formation of a broad, shallow chip.

Use of pre-oxidized HS25 resulted in less chipping and strength degradation of the RBSN. As shown in Figure 7-10 strengths were in the 30 to 40 ksi range

(a) HS25 COMPLIANT LAYER TEST, NO LUBRICANT

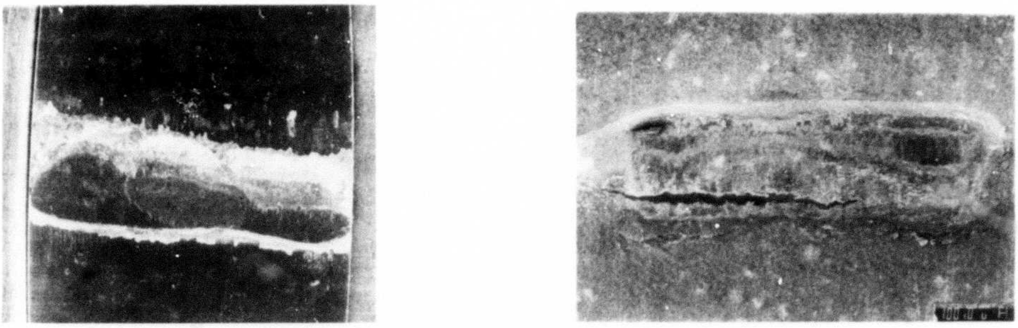

CERAMIC CONTACT SURFACE

COMPLIANT LAYER CONTACT SURFACE

(b) OXIDIZED HS 25 WITH CoO/DTE-25 LUBRICANT

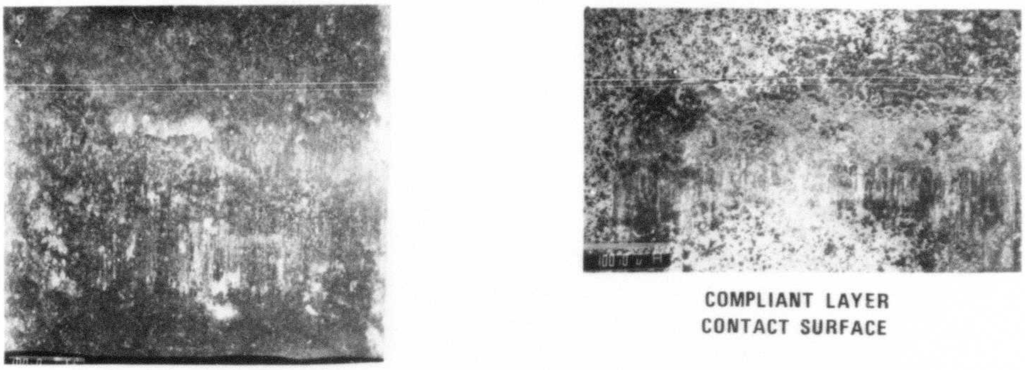

COMPLIANT LAYER
CONTACT SURFACE

CERAMIC CONTACT SURFACE

(c) OXIDIZED PHOTOETCHED HS25, NO LUBRICANT

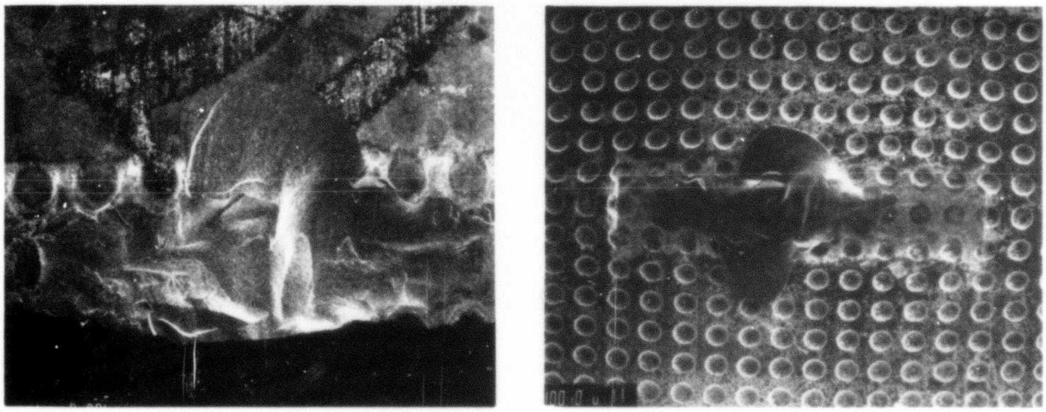

Figure 7-11. SEM Photomicrographs Showing the Surfaces of the RBSN and Compliant Layer After Contact Testing.

compared to 40 to 50 ksi for baseline test bars. The breakaway coefficient of friction was still around 1.0, but the dynamic coefficient of friction was only about 0.5. The pre-oxidation treatment produced a CoO surface layer on the HS25, which appeared to reduce sticking of the metal to the ceramic. Addition of particulate CoO in an oil carrier between the compliant layer and the ceramic further reduced strength degradation and friction.

Compliant layer tests were also conducted using HS25 with a pattern of photoetched indentations. This configuration was used in rig and engine testing and was initially selected because it was thought the perforations would increase compliancy. Some chips occurred at the interface with this photoetched HS25 during engine testing.

Figure 7-11(c) shows the results of a 2000°F contact test with NC-350 RBSN and oxidized photoetched HS25. The test was run in the contact apparatus but with a slightly different apprach than in previous tests. In this case, the normal load was maintained during heat-up and cooldown, but no relative motion was applied. However, a transverse force did occur due to thermal contraction of the fixturing. A large chip of NC-350 at the line of contact adhered to the photoetched HS25. The retained strength was only 15 ksi.

7.3.7 ALTERNATE MATERIALS

The objective of the interface study was to obtain an understanding of and devise a solution for the contact problems encountered by RBSN components in the DARPA/NAVY ceramic demonstration engine. Most of the studies were conducted with RBSN materials, specifically Norton NC-350 (shaped by isostatic pressing and machining) and AiResearch Casting Company RBN122 (shaped by injection molding). A few additional tests were conducted with alternate materials having lower porosity, better surface finish, and higher strength in an effort to further understand the controlling mechanisms of contact surface damage. The data for these limited tests are compared in Table 7-8 with data for the RBSN materials under lubricated and unlubricated conditions.

In general, the higher density (less porous) materials had lower coefficient of friction in the unlubricated condition, about the same coefficient of friction in the lubricated condition, and greater retained strength. Some chips or pull-outs resulted with the αSIC and some self-lubrication with the Refel Si-SiC.

7.4 CONTACT STUDY CONCLUSIONS AND RECOMMENDATIONS

Two mechanisms were identified which could cause surface damage at ceramic-ceramic and ceramic-metal interfaces:

TABLE 7-8. COMPARISON OF CONTACT TEST RESULTS FOR ALTERNATE MATERIALS AND RBSN.

MATERIAL	LUBRICANT	DENSITY g/cm^3	BASELINE STRENGTH ksi	STATIC COEFFICIENT OF FRICTION	RETAINED STRENGTH ksi	TYPICAL SURFACE FINISH μin rms
NC-350 RBSN	NONE	2.50	47.8	0.80	19.0	
	CoO + DTE-25			0.20	28.0	
RBN-101 RBSN	NONE	2.72	33.5	0.70	18.0	10
RBN 104 RBSN	NONE	2.78	45.1	0.42	27.7	
	CoO + DTE-25			0.36	38.7	
SINTERED αSiC	NONE	3.12	45.8	0.45	32.1	6
	CoO + DTE-25			0.20	48.1	
NCX-34 HPSN	NONE	3.35	121.0	0.61	89.9	7
	CoO + DTE-25			0.27	143.9	
REFEL Si-SiC	NONE	3.09	55.4	0.62	80.1	4
	CoO + DTE-25			0.40	53.2	

TEST CONDITIONS: 57.3 LB NORMAL LOAD, POINT CONTACT, 2000°F 1/2 HR HOLD, 0.060 INCH RELATIVE MOVEMENT.

SOURCE OF MATERIALS: SINTERED α SiC, CARBORUNDUM CO., NIAGARA FALLS, NEW YORK

HOT PRESSED NCX-34 Si_3N_4 8 PERCENT Y_2O_3, NORTON CO., WORCESTER, MASS.

REFEL REACTION-SINTERED SiC, PURE CARBON CO., ST. MARYS, PA.

(1) High localized tensile stresses resulting from biaxial loading at the interface

(2) Adhesion at high temperature, leading to restraint during cooling

Biaxial stress distributions could occur at interfaces in the TSE331C-1 ceramic engine from several sources:

(1) Contact surfaces not normal to the load path

(2) Component misalignment due to a combination of tolerance mismatch and cantilevering of the static-structure from the OD

(3) Restraint of sliding during heating or cooling due to high friction or adhesion

(4) Combination of axial aerodynamic loads and thermally-induced radial relative motion

Contact-induced surface damage was likely produced during the initial engine run or cycle, probably during peak aerodynamic loading at maximum temperature, or during cooldown due to component restraints. The transient thermal tensile stresses during subsequent engine runs or cycles then resulted in crack extension, which ultimately led to component fracture. This hypotheses is compatible with rig and engine test results.

The contact study determined the nature of the interface problem and identified possible directions for solution. These are summarized in Table 7-9. Use of compliant layers at engine interfaces was evaluated but was not successful by itself. Redesign of the engine appeared to be necessary to decrease contact loads and to provide better control over load paths. A major redesign was not within the scope of the program. Fortunately a ceramic development program (AFWAL Contract F33615-77-C-5171, Ceramic Components for Turbine Engines) utilizing the same baseline engine as the TSE331C-1 was begun about the time that contact stress was recognized as a key problem.[24, 25, 91] The decision was made not to redesign the DARPA/NAVY engine but rather to incorporate the experience gained through engine testing and contact studies into the AFWAL engine design and to test that engine as a second-generation design.*

---

*The AFWAL program resulted in a second-generation engine with substantially reduced contact loading. The RBSN static structure components have been operated under severe cyclic conditions to >2300°F average turbine inlet temperature with no sign of contact-induced damage.

TABLE 7-9. DIRECTIONS FOR SOLUTION OF THE CONTACT PROBLEM.

DECREASED FRICTION	DECREASED CONTACT LOAD
LUBRICANT DEVELOPMENT	MODIFIED ENGINE DESIGN
SURFACE COATING	MODIFIED CONTACT GEOMETRY
BETTER SURFACE FINISH	COMPLIANT LAYER
ALTERNATE MATERIAL	DAMAGE-TOLERANT MATERIAL
HIGHER STRENGTH, NONPORUS CERAMIC	

8.0 CERAMIC-BLADED ROTOR TEST PROGRAM

As described in the prior section, the RBSN static structure contact damage problem prevented cyclic operation of the ceramic demonstration engine. However, the HPSN ceramic rotor blades had performed without difficulty (after redesign of the stator to avoid vibrational excitation of the rotor). To permit additional durability testing of the rotor blades, an add-on effort was initiated in July 1980 using a modified Garrett T76 engine containing cooled metal static structure components.

8.1 ENGINE MODIFICATION

An Uprate T76 engine was made available by NAVAIR and Garrett. The Uprate T76 is a growth version of the T76-G-10* and has a maximum stator inlet temperature capability of 2124°F. The objective was to replace the first-stage metal rotor blades with hot-pressed Si_3N_4 blades and provide additional cooling for critical metal hardware to operate the engine at 2200°F average turbine inlet. The specific goal was 15 hours of cyclic engine testing.

Analysis was conducted to estimate flow path temperature and pressures, to define stress distributions for the first-stage disk and coverplates, to determine the turbine tip clearance, and to develop cooling flows for maintaining metal temperature within acceptable levels. It was determined that the metal temperature of static structure components could be controlled within acceptable levels for the short test time through increased cooling flows. The second-stage rotor could be used without airfoil cooling but would have a stress rupture limitation and would require careful temperature monitoring. Its temperature at the critical section would be 1680°F (compared to 1525°F for the Uprate T76) which would reduce the stress rupture life to about 40 hours.

The following hardware modifications were required:

- o First Stage Rotor Blades. Existing ceramic blades from the TSE331C-1 engine were modified to make them compatible with the Uprate T76 hardware design. Specifically, the fore and aft faces of the dovetail and platform of each blade were machined to change the broach angle. Also the airfoil tips were crowned to provide acceptable tip clearance.

---

*The T76-G-10 was the original baseline model for the ceramic TSE331C-1

- First-Stage Rotor Assembly. A new assembly of disk, coverplates, compliant layers, and ceramic blades replaced the all-metal assembly. Sheet metal platform seals were used to seal the gaps between the blade platforms. Two compliant layers were used around the blade dovetail: a 0.005-inch platinum layer adjacent to the ceramic parts, and a 0.002-inch oxidized HS25 layer between the platinum and the Waspalloy disk.

- Second-Stage Rotor Assembly. A new rotor was procured. The rotating seal design was altered to allow for the larger first-stage disk.

- First-Stage Stator Assembly. The number of vanes was reduced from 22 to 19 in order to avoid a resonance problem with the ceramic blades. Thirty percent more cooling air was required for 2200°F TIT operation to avoid an increase in metal temperature. The trailing edge cooling slots were moved upstream 0.2 inch along the airfoil.

- Second-Stage Stator Assembly. Both the inner and the outer leading edges of this assembly were machined back to prevent a possible rub with the ceramic blades since the blades were located further aft than their metal counterparts.

- Combustor System. A low-carbon combustor from a civil derivative of the T76 was used. Fuel nozzles, igniters and combustor deswirl vanes were modified to be compatible with this combustor.

- First Stage Turbine Shroud Segment. The arc lengths of these segments were shortened by 0.005 inch to insure that they would not grow together and buckle.

The ceramic blades were modified without difficulty. Following machining, they were heat treated at 1800°F for 50 hours (to minimize the effects of machining damage) and then proof tested in the whirl pit at 130 percent design speed. Thirty nine blades were proof tested with one failure. Twenty five blades were selected for engine use.

Instrumentation was installed on the engine in the locations shown in Figure 8-1. Cavity temperatures, cavity pressures and metal temperatures are

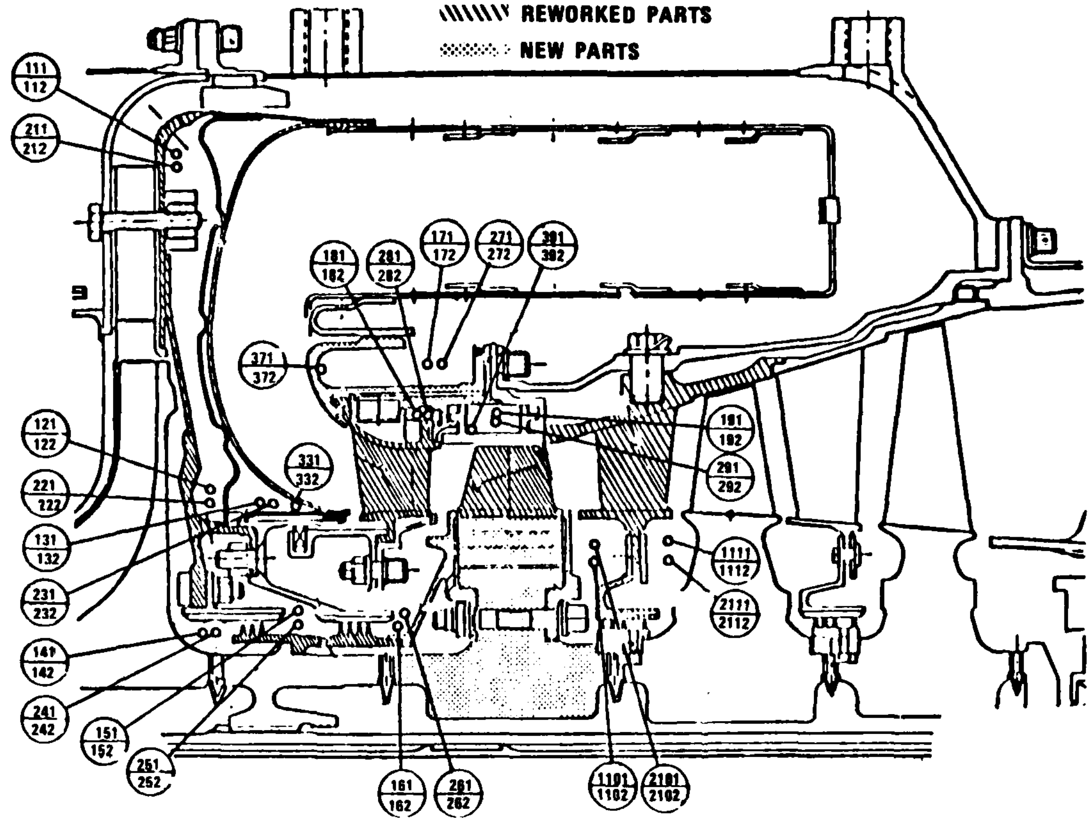

Figure 8-1. Modified Version of the Uprate T76 Showing Instrumentation Positions.

indicated by master numbers whose first digit is respectively a "1," "2" or "3." Temperatures and pressures required continuous monitoring since some of the metal components were being operated near their property limits.

8.2 ENGINE TEST RESULTS

Two 7-1/2 hour engine tests were conducted using the duty cycle illustrated in Figure 8-2. The only major difference between the two tests involved the start procedure. The first test used the start procedure developed for the TSE331C-1 DARPA ceramic engine which calls for acceleration to 17 percent speed with an air turbine starter before initiating fuel flow and ignition. The second test start procedure was similar except that fuel flow and ignition were initiated at 10 percent speed, which is the standard start procedure for the conventional metal engine.

The 15 hours of cyclic testing were completed with no problems. An average turbine inlet temperature of 2220°F was achieved yielding a power output of 1184 shp

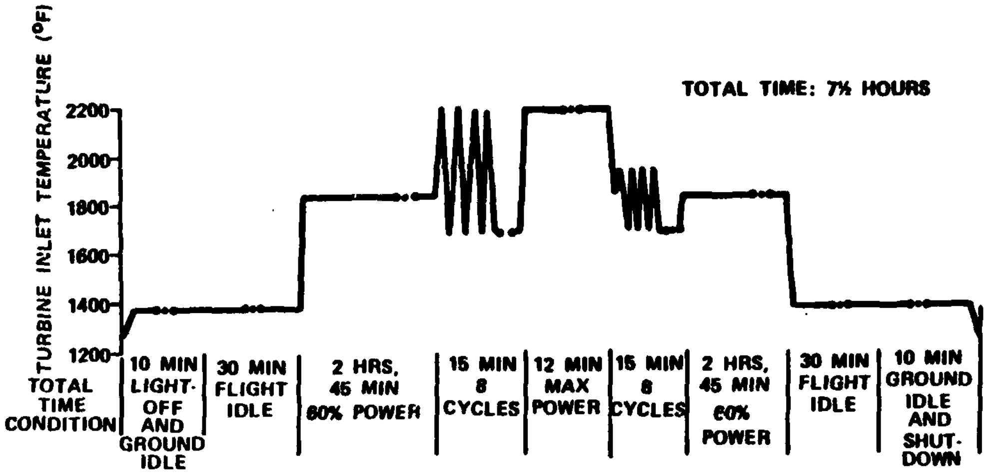

FIGURE 8-2. DARPA/NAVY CERAMIC-BLADED ROTOR ENGINE TEST DEMONSTRATION CYCLE.

and a specific fuel consumption of 0.523 lb/hr-hr. Peak temperature, based on a combustor pattern factor of 0.195, was 2520°F. The testing clearly demonstrated that the ceramic blades and the inserted-blade rotor configuration could operate under a normal engine start-up procedure and severe cycling.

9.0 CONCLUSIONS AND RECOMMENDATIONS

The feasibility of using ceramic components to achieve substantial improvements in the performance of gas turbines for limited-life applications has been demonstrated. The effort leading up to this demonstration has involved technology advancement along a broad front, including design methodology, material characterization, complex shape ceramic component fabrication, NDE, and proof testing. Perhaps a major contribution has been improved understanding of the failure mechanisms, both design and materials oriented, that must be overcome for ceramics to be used reliably in gas turbine and other heat engines.

The following are recommendations for further development of ceramics for gas turbine engines:

- Conduct iterative ceramic process development to achieve improved properties and reliability
- Integrate these improved ceramic materials into a low-contact-stress engine design (such as the second generation TSE331C engine)
- Reduce rotor tip clearances to optimize engine performance; as part of this effort, develop and demonstrate an abradable shroud
- Conduct longer term tests with the ceramic-bladed Uprate T76 engine
- Operate the ceramic-bladed Uprate T76 engine in a vehicle
- Demonstrate cyclic engine operation and the durability of an all-ceramic hot section such as the second generation design currently being developed under the AFWAL program.

10.0 REFERENCES

1. K. M. Johansen, N. R. Nelson, and F. B. Wallace, Garrett Report No. 76-212188(1), Ceramic Gas Turbine Engine Demonstration Program Interim Report No. 1, June 1976, Contract N00024-76-C-5352.

2. N. R. Nelson and F. B. Wallace, Garrett Report No. 76-212188(2), Ceramic Gas Turbine Engine Demonstration Program, Interim Report No. 2, Sept. 1976, Contract N00024-76-C-5352.

3. N. R. Nelson and F. B. Wallace, Garrett Report No. 76-212188(3), Ceramic Gas Turbine Engine Demonstration Program, Interim Report No. 3, Dec. 1976, Contract N00024-76-C-5352.

4. N. R. Nelson and F. B. Wallace, Garrett Report No. 76-212188(4), Ceramic Gas Turbine Engine Demonstration Program, Interim Report No. 4, March 1977, Contract N00024-76-C-5352.

5. N. R. Nelson and F. B. Wallace, Garrett Report No. 76-212188(5), Ceramic Gas Turbine Engine Demonstration Program, Interim Report No. 5, May 1977, Contract N00024-76-C-5352.

6. N. R. Nelson and F. B. Wallace, Garrett Report No. 76-212188(6), Ceramic Gas Turbine Engine Demonstration Program, Interim Report No. 6, Sept. 1977, Contract N00024-76-C-5352.

7. J. E. Harper and F. B. Wallace, Garrett Report No. 76-212188(7), Ceramic Gas Turbine Engine Demonstration Program, Interim Report No. 7, Nov. 1977, Contract N00024-76-C-5352.

8. J. E. Harper and F. B. Wallace, Garrett Report No. 76-212188(8), Ceramic Gas Turbine Engine Demonstration Program, Interim Report No. 8, Feb. 1978, Contract N00024-76-C-5352.

9. J. E. Harper and F. B. Wallace, Garrett Report No. 76-212188(9), Ceramic Gas Turbine Engine Demonstration Program, Interim Report No. 9, May 1978, Contract N00024-76-C-5352.

10. J. E. Harper and F. B. Wallace, Garrett Report No. 76-212188(10), Ceramic Gas Turbine Engine Demonstration Program, Interim Report No. 10, Aug. 1978, Contract N00024-76-C-5352.

11. J. E. Harper and F. B. Wallace, Garrett Report No. 76-212188(11), Ceramic Gas Turbine Engine Demonstration Program, Interim Report No. 11, Nov. 1978, Contract N00024-76-C-5352.

12. J. E. Harper and F. B. Wallace, Garrett Report No. 76-212188(12), Ceramic Gas Turbine Engine Demonstration Program, Interim Report No. 12, Feb. 1979, Contract N00024-76-C-5352.

13. J. E. Harper and F. B. Wallace, Garrett Report No. 76-212188(13), Ceramic Gas Turbine Engine Demonstration Program, Interim Report No. 13, May 1979, Contract N00024-76-C-5352.

14. J. E. Harper and F. B. Wallace, Garrett Report No. 76-212188(14), Ceramic Gas Turbine Engine Demonstration Program, Interim Report No. 14, Aug. 1979, Contract N00024-76-C-5352.

15. J. E. Harper and F. B. Wallace, Garrett Report No. 76-212188(15), Ceramic Gas Turbine Engine Demonstration Program, Interim Report No. 15, Nov. 1979, Contract N00024-76-C-5352.

16. C. R. Dins and F. B. Wallace, Garrett Report No. 76-212188(16), Ceramic Gas Turbine Engine Demonstration Program, Interim Report No. 16, Feb. 1980, Contract N00024-76-C-5352.

17. D. W. Richerson, L. J. Lindberg, and C. R. Dins, Garrett Report No. 76-212188(17), Ceramic Gas Turbine Engine Demonstration Program, Interim Report No. 17, May 1980, Contract N00024-76-C-5352.

18. J. W. Fairbanks and R. W. Rice, eds., "Proceedings of the 1977 DARPA/ NAVSEA Ceramic Gas Turbine Demonstration Engine Program Review," MCIC Report MCIC-78-36, March 1978.

19. F. B. Wallace, A. J. Stone, and N. R. Nelson, "ARPA/Navy Ceramic Engine Program," Ceramics for High Performance Applications - II, Brook Hill Publishing Co., Chestnut Hill, Ma., 1978, 593-624.

20. D. W. Richerson, J. J. Schuldies, T. M. Yonushonis, and K. M. Johansen, "ARPA/NAVY Ceramic Engine Materials and Process Development Summary," Ibid., 625-650.

21. F. B. Wallace, et al., "Silicon Nitride Turbine Blade Development," Ceramics for Turbine Engine Applications, AGARD-CP-276, 1980, pp. 5-1 to 5-12.

22. J. E. Harper, "ARPA/NAVAIR Ceramic Gas Turbine Engine Demonstration Program" Ceramics for High Performance Applications - III, to be published in 1982 by Plenum Press, New York.

23. D. W. Richerson, et al., "Material, Design and Test Aspects of Ceramic Component Development" ASME Paper 81-GT-179, 1981.

24. K. M. Johansen, "Ceramic Components for Turbine Engines," Garrett Report 21-2794(03), Phase I Technical Report, Nov. 15, 1978, Prepared under AFWAL Contract No. F33615-77-C-5171.

25. K. M. Johansen, "Ceramic Components for Turbine Engines," Garrett Report 21-2794(12), Tenth Interim Quarterly, Dec. 5, 1980, Prepared under AFWAL Contract No. F33615-77-C-5171.

26. N. R. Nelson and D. J. Tree, Reference 18, pp.19-40.

27. "Reliability of Ceramics for Heat Engine Application," Chapter 2, National Material Advisory Board Report NMAB-357, 1980.

28. A. Paluszny and W. Wu, "Probabilistic Aspects of Designing with Ceramics," Journal of Engineering for Power, Vol. 99, No. 4, Oct. 1977, pp. 617-630; also ASME paper 77-GT-41.

29. D. J. Tree and H. L. Kington, Reference 18, pp. 41-75.

30. H. L. Kington, C. R. Dins, L. J. Meyer, and D. J. Tree, Reference 18, pp. 77-116.

31. G. S. Calvert, "Design, Fabrication and Spin Testing of Ceramic Blade-Metal Disk Attachment," Pratt and Whitney Aircraft, Contract NAS3-19715, October-December 1975.

33. R. A. Soloman, J. G. Zimmerer, and K. M. Johansen, Reference 18, pp. 151-186.

34. M. W. Robare and D. W. Richerson, Reference 18, pp. 291-311.

35. D. W. Richerson and M. W. Robare, "Turbine Component Machining Development," The Science of Ceramic Machining and Surface Finishing-II, NBS Special Publication 562, 1979, pp. 209-220.

36. M. L. Torti, S. H. Baker, S. Tuffs, and B. A. Olson, Reference 18, pp. 341-363.

37. D. G. Miller and C. R. Booher, "Brittle Material Design, High Temperature Gas Turbine Stator Vane Development and Static Rig Tests," AMMRC CTR 76-32 Vol. II, Dec. 1976.

38. C. R. Dins, T. M. Yonushonis, L. P. Wynn, and H. L. Kington, Reference 18, pp. 449-491.

39. J. A. Mangels, "Development of Injection-Molded Reaction-Bonded Si_3N_4," in Ceramics for High Performance Application-II (J. J. Burke, E. N. Lense, and R. N. Katz, eds.) Brook Hill Publ. Co., Chestnut Hill, MA., 1978, pp. 113-130.

40. H. Gersh, D. Mann, M. Rorabaugh, and J. Schuldies, Reference 18, pp. 313-340.

41. A. Ezis and J. M. Nicholson, "Method of Manufacturing a Slip Cast Article," U.S. Patent No. 4,067,943.

42. A. Ezis and J. T. Neil, "Fabrication and Properties of Fugitive Mold Slip-Cast Si_3N_4," Bull. Amer. Ceram. Soc., 58 [9],883.

43. E. A. Fisher, J. R. Baer, and C. F. Johnson, Reference 18, pp. 365-380.

44. H. R. Baumgartner, Reference 18, pp. 273-284.

45. L. Lindberg, D. Richerson, D. Carruthers, and H. Gersch, "Oxidation Stability of Advanced Reaction-Bonded Si_3N_4 Materials," to be published in the Bull. of the Amer. Ceram. Soc.

46. D. W. Richerson, Reference 18, pp. 187-191.

47. D. W. Richerson, T. M. Yonushonis, and G. Q. Weaver, Reference 18, pp. 193-217.

48. Reference 10, Attachment 2.

49. Reference 10, Attachment 1.

50. T. M. Yonushonis and K. E. Hofer, Reference 18, pp. 235-245.

51. D. W. Richerson and T. M. Yonushonis, Reference 18, pp. 247-271.

52. D. G. Finger, "Contact Stress Analysis of Ceramic-to-Metal Interfaces," Final Report, ONR Contract N00014-78-C-0547, September 1979.

53. G. Q. Weaver, "Characterization of an Optimized Si_3N_4 - Y_2O_3 Material," Presented at the American Ceramic Society, 29th Pacific Coast Regional Meeting, Nov. 3, 1976.

54. D. W. Richerson, "Effects of Impurities on the High Temperature Properties of Hot Pressed Silicon Nitride," Bulletin, American Ceramic Society, July, 1973.

55. R. Kossowsky, "Creep and Fatigue of Si_3N_4 as Related to Microstructure" in Ceramics for High Performance Application, edited by J. J. Burke, A. E. Gorum and R. N. Katz, Brook Hill Publishing Co., 1973.

56. G. E. Gazza, "Effect of Y_2O_3 Additions on Hot Pressed Si_3N_4," Bulletin, American Ceramic Society, Vol. 54, No. 9, 1975.

57. F. F. Lange, S. C. Singhal, and R. C. Kusnicki;, "Phase Relations and Stability Studies in the Si_3N_4-Y_2O_3 Preudoternary System" Bull. Amer. Ceram. Soc. 60 [5-6] pp. 249-252, 1977.

58. W. D. Carruthers, D. W. Richerson, and K. W. Benn, "3500-Hour Durability Testing of Commercial Ceramic Materials," NASA CR-159785, July 1980, pp. 48-63.

59. R. W. Davidge, and G. Tappin, "Thermal Shock and Fracture in Ceramics," Transactions, British Ceramic Society, Vol. 66, No. 8, 1967.

60. D.P.H. Hasselman, "Unified Theory of Thermal Shock Fracture Initiation and Crack Propagation in Brittle Ceramics," Journal, American Ceramic Society, Vol. 52, No. 11, 1969.

61. C. Zener, Elasticity and Anelasticity of Metals, Chapter 6, University of Chicago Press, Chicago, Ill., 1948.

62. G. Q. Weaver, H. R. Baumgartner, and M. L. Torti, "Thermal Shock Behavior of Sintered Silicon Carbide and Reaction-Bonded Silicon Nitride," Symposium on Special Ceramics, 6th, Stoke-on-Trent, England, July, 1974.

63. T. M. Yonushonis and D. W. Richerson, Reference 18, pp. 219-234.

64. J. J. Schuldies and D. W. Richerson, Reference 18, pp. 381-402.

65. R. Kossowsky, "Defect Detection in Hot-Pressed Si_3N_4," in Ceramics for High Performance Applications (J. J. Burke, A. E. Gorum, and R. N. Katz, eds.), Brook Hill Publishing Co., Chestnut Hill, MA. (1974) pp. 665-685.

66. H. R. Baumgartner and D. W. Richerson, "Inclusion Effects on the Strength of Hot-pressed Si_3N_4," Fracture Mechanics of Ceramics, Vol. I, Ed. by R. C. Bratt, D. P. H. Hasselman and F. F. Lange, 1973.

67. J. J. Petrovic, L. A. Jacobson, P. K. Talty, and A. K. Vasudevan, "Controlled Surface Flaws in Hot Pressed Si_3N_4," J. Am. Ceram. Soc. 58, 113 (1975).

68. B. R. Lawn, A. G. Evans, and D. B. Marshall, "Elastic/Plastic Indentation Damage in Ceramics: the Median/Radial Crack System," J. Am. Ceram. Soc. 63, (1980) pp. 574-581.

69. J. J. Schuldies and W. H. Spaulding, Reference 18, pp. 403-428.

70. J. J. Schuldies and T. Derkacs, Reference 18, pp. 429-448.

71. L. J. Inglehart, R. L. Thomas, and J. Schuldies, "Photoacoustic Microscopy of Ceramic Engine Hardware," J. of NDE, Vol. I, No. 4, 1980.

72. Reference 10, Appendix I.

73. A. G. Evans, G. S. Kino, P. T. Kuri-Yakub, and B. R. Tittman, "Failure Prediction in Structural Ceramics," Mater. Eval. 35 (4), (1977), p. 85.

74. A. J. Bahr, "Microwave Techniques for the Nondestructive Evaluation of Ceramics," AMMRC Contract DAAG46-76-C-0048, Final Technical Report, June 1977.

75. D. W. Richerson, W. D. Carruthers, and L. J. Lindberg, "Contact Stress and Coefficient of Friction Effects on Ceramic Interfaces" in Surfaces and Interfaces in Ceramic and Ceramic-Metal Systems, J. Pask and A. Evans, eds., Plenum Press, 1981, pp. 661-676.

76. B. R. Lawn, "Partial Cone Crack Formation in a Brittle Material Loaded with a Sliding Spherical Indenter," Proc. Roy. Soc. Lond. A299, 307 (1967).

77. A. G. Evans and G. Tappin, Proc. Br. Ceram. Soc. 20 (1972), pp. 275-297.

78. W. F. Brown and J.E. Srawley, ASTM Special Tech. Publ. No. 410 (1966).

79. D. W. Richerson, D. G. Finger, and J. M. Wimmer, "Analytical and Experimental Evaluation of Biaxial Contact Stress," in Fracture Mechanics of Ceramics, Vol. 5 (edited by R. C. Bradt et al.) Plenum Press, 1982.

80. D.W. Richerson, "Contact Stresses at Ceramic Interfaces," in Nitrogen Ceramics II (edited by F. C. Riley) Nordhoff Int. Publishers, 1982.

81. H. Hertz and J. Reine Angew, Math 92, 156 (1881); Reprinted in English in "Hertz's Miscellaneous Papers," Chapter 5, 6, Macmillan and Co., Ltd London, 1896.

82. F. C. Roesler, Proc. Phys. Soc. Lond. B69, 981 (1956).

83. F. C. Frank, and B. R. Lawn, Proc. Roy. Soc. Lond. A299, 191 (1967).

84. T. R. Wilshaw, J. Phys. D: Appl. Phys., Vol. 4, 1567-81 (1971).

85. B. R. Lawn, and D. B. Marshall in Fracture Mechanics of Ceramics, Vol. 3 (ed. by R. C. Bradt, D.P.H. Hasselman and F.F. Lange), (1978), Plenum Press, New York, pp. 205-229.

86. B. R. Lawn, S.M. Wiederhorn, and H. H. Johnson, J. Amer. Ceram. Soc. 58 (9-10) (1975), pp. 428-32.

87. G. M. Hamilton and L.E. Goodman, J. Appl. Mech. 33 (1966), pp. 371.

88. B. R. Lawn, Proc. Roy. Soc. Lond. A299, 307 (1967).

89. D. R. Gilroy and W. Hirst, J. Phys. D; Appl. Phys. 2, 1784-7 (1969).

90. J. O. Smith and C.K. Liu, "Stresses Due to Tangential and Normal Loads on an Elastic Solid with Application to Some Contact Stress Problems," J. Appl. Mech., pp 157-166, June, 1953.

91. K. M. Johansen, D. W. Richerson, and J. J. Schuldies, "Ceramic Components for Turbine Engines," Phase II Technical Report, February 29, 1980, Garrett Report Number 21-2794(08), prepared for AFWAL under contract F33615-77-C- 5171.

REPORT DISTRIBUTION

No. of Copies	To
	Director, Defense Advanced Research Projects Agency
	1400 Wilson Boulevard, Arlington, Virginia 22209
2	ATTN: Dr. Van Reuth
1	Major L. Jacobson
	Code AIR-536 Naval Air Systems Command
	Washington, D.C. 20362
5	ATTN: A. Rezetta
	Office of the Under Secretary of Defense for Research and Engineering
	The Pentagon, Washington, D.C. 20301
1	ATTN: Mr. J. Persh
2	Commander, Defense Technical Information Center, Cameron Station
	Building 5, 5010 Duke Street,
	Alexandria, Virginia 22314
1	National Technical Information Service, 5285 Port Royal Road
	Springfield, Virginia 22161
	Battelle Columbus Laboratories, Metals and Ceramics Information Center
	505 King Avenue, Columbus, Ohio 43201
1	ATTN: Mr. Winston Duckworth
1	Dr. D. Niesz
1	Dr. R. Wills
	Chief of Naval Research, Arlington, Virginia 22217
1	ATTN: Code 471
1	Dr. A. Diness
1	Dr. R. Pohanka
	Naval Research Laboratory, Washington, D.C. 20375
2	ATTN: Mr. R. Rice
	Headquarters, Naval Air Systems Command, Washington, D.C. 20360
1	ATTN: Code 5203
1	Code MAT-042M
	Commander, Naval Weapons Center, China Lake, California 93555
1	ATTN: Mr. F. Markarian
	Naval Sea Systems Command, Department of the Navy
	Washington, D.C. 20362
1	ATTN: Code SEA 0331
1	Code SEA 0253

REPORT DISTRIBUTION

No. of Copies	To
1	Naval Ship Engineering Center, Philadelphia Div. Philadelphia, PA. 19112 ATTN: Code SEC 6734
1	Naval Air Propulsion Center Trenton, N.J. ATTN: T. Elsasser
1	Office of Naval Research Washington, D.C. 20360 ATTN: Code 471
1	Chief of Naval Research, Department of the Navy Arlington, VA 22217 ATTN: Code 472
1	Superintendent, U.S. Naval Academy Annapolis, MD 21402 ATTN: Technical Library
1	Chief of Naval Operations, Department of the Navy Washington, D.C. 20350 ATTN: OP-03FG
1	Naval Surface Weapons Center White Oak, MD 20910
1	Deputy Chief of Staff, Research Development and Acquisition Pentagon Bldg., Washington, D.C. 20310 ATTN: Dr. C. Church
1	U.S. Army Research and Technology Labs. DAVDL, Moffatt Field, Calif. ATTN: Dr. R. Carlson
1 1 1 1 1	Director, Army Materials and Mechanics Research Center Watertown, Massachusetts 02172 ATTN: DRXMR-PL DRXMR-WD Dr. R. Katz Dr. E. Lenoe Dr. E. Wright
1	Deputy Chief of Staff, Research, Development, and Acquisition Headquarters, Department of the Army, Washington, D.C. 20310 ATTN: DAMA-CSS, Dr. J. Bryant

REPORT DISTRIBUTION

No. of Copies	To
	Commander, Army Research Office, P.O. Box 12211, Research Triangle Park, North Carolina 27709
1	ATTN: Information Processing Office
1	Dr. J. Hurt
1	Dr. P. Parrish
	Commander, U.S. Army Tank-Automotive Research and Development Command, Warren, Michigan 48090
1	ATTN: Dr. P. Glance
1	Mr. E. Hamperian
1	Dr. R. Mundt
1	DRDTA-UL, Technical Library
	Commander, U.S. Army Aviation Research and Development Command P.O. Box 209, St. Louis, Missouri 63166
1	ATTN: DRDAV-EXT
1	Technical Library
1	B. Titus DRDAV-M Bldg. 105
	Commander, U.S. Army Mobility Equipment Research and Development Command, Fort Belvoir, Virginia 22060
2	ATTN: DRDME-EM, Mr. W. McGovern
	Director, Eustis Directorate, U.S. Army Research and Technology Laboratory, DAVDL-ATL-A, Fort Eustis, Virginia 23604
1	ATTN: Mr. J. Lane
1	Mr. G. Eliot
	Commander, U.S. Air Force Office of Scientific Research, Building 410 Bolling Air Force Base Washington, D.C. 20332
1	ATTN: Capt. Wax
	Commander, U.S. Air Force Wright Aeronautical Laboratory Wright-Patterson Air Force Base, Ohio 45433
1	ATTN: Dr. N. Tallan AFML
1	Dr. H. Graham AFML
1	Dr. R. Ruh AFML
1	Hank Johnson AFML
1	Mr. E. Lindner AFWAL-POTA
1	Mr. W. Troha AFWAL-POTC
1	Mr. D. Zabierek AFWAL-POTC
1	Aero Propulsion Labs, Mr. R. Marsh
	National Aeronautics and Space Administration Washington, D.C. 20546
1	ATTN: Mr. G.C. Deutsch - Code RW
1	Mr. C. Bersch
1	AFSS-AD, Office of Scientific and Technical Information

REPORT DISTRIBUTION

No. of Copies	To
	National Aeronautics and Space Administration, Lewis Research Center
	21000 Brookpark Road, Cleveland, Ohio 44135
1	ATTN: J. Accurio, USAMRDL
1	Dr. H.B. Probst, MS 49-1
1	Dr. T. Miller, MS 49-1
1	S. Grisaffe
1	H. Rohlik, 77-2
1	G. Weden, 5-3
1	R. Evans, MS 49-2
	National Aeronautics and Space Administration, Headquarters
	Washington D.C., 20546
1	ATTN: J. Gangler
1	J. Kerrebrock
	National Aeronautics and Space Administration, Langley Research Center
	Hampton, Virginia 23665
1	ATTN: Mr. J. Buckley, Mail Stop 387
1	Science and Technology Division, Library of Congress
	Washington, D.C. 20540
	Department of Energy, Division of Transportation, 20 Massachusetts Avenue
	N.W., Washington, D.C. 20545
2	ATTN: Mr. Robert Schulz (TEC)
1	Mr. S. Kramer
	Department of Transportation, 400 Seventh Street
	S.W., Washington D.C. 20590
1	ATTN: Mr. M. Lauriente
1	Mechanical Properties Data Center, Belfour Stulen Inc., 13917 W. Bay
	Shore Drive, Traverse City, Michigan 49684
	National Bureau of Standards
	Washington, D.C. 20234
	ATTN: Dr. S. Wiederhorn
1	Dr. J.B. Wachtman
1	Dr. N. Tighe
	National Research Council, National Materials Advisory Board
	2101 Constitution Avenue, Washington, D.C. 20418
1	ATTN: D. Groves
1	R.M. Spriggs

REPORT DISTRIBUTION

No. of Copies	To
	National Science Foundation
	Washington, D.C. 20550
1	ATTN: B. Koepke
	Jet Propulsion Laboratories, California Institute of Technology
	4800 Oak Grove Dr., Pasadena, CA 91103
1	ATTN: Marc Adams
1	R. Smoak
1	J. Zwissler
	Electric Power Research Institute, 3412 Hillview Ave., P.O. Box 10412
	Palo Alto, CA 94304
1	ATTN: Wate Bakker
	Gas Research Inst., 8600 W. Bryn Mawr Ave.
	Chicago, Ill. 60631
1	ATTN: C. Dobos
	Solar Energy Research Inst., 1536 Cole Blvd.
	Golden, Colo. 80401
1	ATTN: T. Coyle
	Department of Energy, 20 Massachusetts Ave.,
	Washington, D.C. 20545
1	ATTN: J. Fairbanks
	Los Alamos Scientific Laboratory, P.O. Box 1663
	Los Alamos, N.M. 87545
1	ATTN: Dr. J. Petrovic, Group CMB-5
1	H. Sheinberg, Group D, M/S 770
	Oak Ridge National Laboratories, P.O. Box X
	Oak Ridge, Tenn. 37830
1	ATTN: J.A. Carpenter
1	V. Tennery
	Lawrence Radiation Laboratory
	Livermore, CA. 94550
1	ATTN: Ceramics Dept.
	The Aerospace Corporation, P.O. Box 92957
	Los Angeles, California 90009
1	ATTN: Dr. Louis Rubin
	AiResearch Casting Company, 2525 West 190th Street
	Torrance, California 90505
1	ATTN: Mr. K. Styhr

REPORT DISTRIBUTION

No. of Copies	To
	AiResearch Manufacturing Company, 2525 West 190th St.
	Torrance, CA 90505
1	ATTN: Dr. D. Kotchick
	Alfred University
	Alfred, N.Y.
1	ATTN: Dr. D. Rossington 14802
	Carborundum Company, Research and Development Division
	P.O. Box 1054, Niagara Falls, New York, 14302
1	ATTN: Dr. J.A. Coppola
1	Dr. M. Srinivasan
1	Dr. R. Phoenix
	Caterpillar Tractor Company, Technical Center, Building F
	Peoria, Illinois 61602
1	ATTN: Mr. A.R. Canady
	Ceramic Finishing Company, P.O. Box 498
	State College, Pennsylvania 16801
1	ATTN: Dr. H.P. Kirchner
1	Ceradyne, Inc., 3030 South Red Hill
	Santa Ana, CA 92705
1	Coors Porcelain Company, Research Department
	17750 West 32nd Avenue, Golden, Colorado 80401
	Corning Glass Works, Research Department
	Corning, New York 14832
1	ATTN: Mr. J. Lanning
	Cummins Engine Company
	Columbus, Indiana 47201
1	ATTN: Mr. R. Kamo
	Deposits and Composites, Inc., 1821 Michael Faraday Drive
	Reston, Virginia 22090
1	ATTN: Mr. R.E. Engdahl
	Eaton Corporation, Research Center, 26201 Northwestern Highway
	Southfield, Michigan 48076
1	ATTN: Dr. L. Eltinge

REPORT DISTRIBUTION

No. of Copies	To
	Ford Motor Company, Scientific and Engineering Labs
	2000 Rotunda Dr., Dearborn, MI. 48121
1	ATTN: E.A. Fisher
1	J. Harwood
1	A. McLean
	General Electric Company, Research and Development Center, Box 8
	Schenectady, New York 12345
1	ATTN: Dr. R.J. Charles
1	Dr. C.D. Greskovich
	General Electric Company, Valley Forge Space Center
	Box 8555, Philadelphia, PA. 19101
1	ATTN: Mr. L.R. McCreight
	General Motors Corporation, AC Spark Plug Division
	Flint, Michigan 48556
1	ATTN: Dr. M. Berg
	General Motors Corporation, Detroit Diesel Allison Division
	P.O. Box 894, Indianapolis, Indiana 46206
1	ATTN: Dr. P. Heitman
1	D.M. Herman
	Georgia Institute of Technology, EES
	Atlanta, Georgia 30332
1	ATTN: Mr. J.D. Walton
	GTE Laboratories, Waltham Research Center, 40 Sylvan Road
	Waltham, Massachusetts 02154
1	ATTN: Dr. C. Quackenbush
1	Dr. W.H. Rhodes
1	Dr. D.T. Smith
	IIT Research Institute, 10 West 35th Street
	Chicago, Illinois 60616
1	ATTN: Mr. S. Bortz, Director, Ceramics Research
1	Dr. D. Larsen
	Martin Marietta Laboratories, 1450 South Rolling Road
	Baltimore, Maryland 21227
1	ATTN: Dr. J. Venables

REPORT DISTRIBUTION

No. of Copies	To
	Massachusetts Institute of Technology, Department of Metallurgy and Materials Science, Cambridge, Massachusetts 02139
1	ATTN: Prof. R.L. Coble
1	Prof. H.K. Bowen
1	Prof. W.D. Kingery
1	Prof. R. Cannon
	Norton Company
	Worcester, Massachusetts 01606
1	ATTN: Dr. N. Ault
1	Dr. M.L. Torti
	Pennsylvania State University, Materials Research Laboratory, Materials Science Department, University Park, Pennsylvania 16802
1	ATTN: Prof. R. Roy
1	Prof. R.E. Tressler
1	Prof. R. Bradt
	Pratt and Whitney Aircraft, P.O. Box 2691
	W. Palm Beach, Florida 33402
1	ATTN: Mr. M. Mendelson, Mail Stop B-08
	Program Development Consultants, 25 Schalren Drive
	Latham, New York 12110
1	ATTN: Dr. Robert Harmon
	Teledyne CAE, 1330 Laskey Rd.
	Toledo, Ohio 43697
1	ATTN: R. Beck
	Rockwell International Science Center, 1049 Camino Dos Rios
	Thousand Oaks, California 91360
1	ATTN: Dr. F. Lange
	San Fernando Labs, 10258 Norris Ave.
	Pacoima, CA 91331
1	ATTN: R. Holzl
	Standard Research International, 333 Ravenswood Ave.
	Menlo Park, California 94025
1	ATTN: Dr. P. Jorgensen
1	Dr. D. Rowcliffe
	United Technologies Research Center
	East Hartford, Connecticut 06108
1	ATTN: Dr. J. Brennan
1	Dr. F. Galasso

REPORT DISTRIBUTION

No. of Copies	To
	University of California, Department of Materials Science and Engineering
	Hearst Building, Berkeley, California 94720
1	ATTN: Dr. D. Clarke
1	Prof. A.G. Evans
	University of Florida
	Department of Materials Science and Engineering
	Gainesville, Florida 32601
1	ATTN: Dr. L. Hench
	University of Massachusetts, Department of Mechanical Engineering
	Amherst, Massachusetts 01003
1	ATTN: Prof. K. Jakus
1	Prof. J. Ritter
	University of Michigan
	Ann Arbor, Michigan 48104
1	ATTN: Prof. Edward E. Hucke, Materials and Metallurgical Engineering
1	Dr. Maurice J. Sinnot, Department of Chemical and Metallurgical Engineering
	University of Washington, Ceramic Engineering Division, FB-10
	Seattle, Washington 98195
2	ATTN: Prof. J.I. Mueller
1	Prof. R. Taggert
1	Prof. R.J.H. Bollard
	V.P.I., Department of Materials Engineering
	Blacksburg, Virginia 24061
1	ATTN: Prof. D.P.H. Hasselman
	Westinghouse Electric Corporation, Research Laboratories
	Pittsburgh, Pennsylvania 15235
1	ATTN: Dr. R.J. Bratton

Garrett Turbine Engine Company

111 So 34th St
P O Box 5217
Phoenix
Arizona 85010
602-267-3011

June 10, 1982

Refer to:
C:MCJ:2125:061082

Commander
Naval Air Systems Command
Department of the Navy
Washington, D.C. 20361

Attention: A. R. Rezetta
(AIR-5362B)

Subject : Contract No. N00024-76-C-5352
"CERAMIC GAS TURBINE ENGINE
DEVELOPMENT PROGRAM"
Transmittal of Final Report

Gentlemen:

The enclosed reports are submitted in accordance with DD Form 1423, Sequence Item No. A00B, B00A and C00A, subject contract, for your review and files.

Should there be further questions or information required, please contact either the undersigned or Mr. W. W. Trombley, Representative for The Garrett Corporation located at Suite 520, Cafritz Bldg., 1625 Eye Street, N.W., Washington, D.C. 20006, telephone number (202) 331-1873.

GARRETT TURBINE ENGINE COMPANY
A Division of The Garrett Corporation

MC Johnson

M. C. Johnson
Sr. Contract Manager

MCJ:mg
Enclosure: Ceramic Gas Turbine Engine
Demonstration Program
Document No. 21-4410
Dated May, 1982
(Five Copies)

Via : The Garrett Corporation
Washington, D.C. 20006
Attn: Mr. W. W. Trombley

cc : See Attached Distribution List

A Division
of The Garrett
Corporation

DISTRIBUTION LIST

C:MCJ:2125:061082

Defense Contract Administration
Services Management Area
3800 North Central Avenue
Phoenix, AZ 85012
Attn: Lee C. Holcomb
(Letter Only)

Naval Air Propulsion Test Center
P. O. Box 7176
1440 Parkway Avenue
Trenton, NJ 08628
Attn: Code PE-4
(One Copy)

Commander
Defense Technical Information
Center, Cameron Station
Bldg. 5, 5010 Duke Street
Alexandria, VA 22314
(Two Copies)

Defense Advanced Research
Projects Agency
1400 Wilson Blvd.
Arlington, VA 22209
Attn: Dr. Van Reuth (Two Copies)
Major L. Jacobson (One Copy)

Office of the Under Secretary
of Defense for Research & Eng.
3D1089 Pentagon
Washington, D.C. 20301
Attn: Mr. J. Persh (One Copy)
Mr. R. M. Standahar (One Copy)

National Technical Information
Service
5285 Port Royal Road
Springfield, VA 22161
(One Copy)

Battelle Columbus Laboratories
Metals and Ceramics Info. Center
505 King Avenue
Columbus, OH 43201
Attn: Mr. W. Duckworth
Dr. D. Niesz
Dr. R. Wills
(One Copy Each)

Chief of Naval Research
Arlington, VA 22217
Attn: Code 471 (One Copy)
Dr. A. Diness (One Copy)
Dr. R. Pohanka (One Copy)

Naval Research Laboratory
Washington, D.C. 20375
Attn: Mr. R. Rice (Two Copies)

Headquarters
Naval Air Systems Command
Washington, D.C. 20360
Attn: Code 5203 (One Copy)
Code MAT-042M (One Copy)

Commander
Naval Weapons Center
China Lake, CA 93555
Attn: Mr. F. Markarian
(One Copy)

Naval Sea Systems Command
Department of the Navy
Washington, D.C. 20362
Attn: Code SEA 0331 (One Copy)
Code SEA 0253 (One Copy)

DISTRIBUTION LIST

C:MCJ:2125:061082

Naval Ship Engineering Center
Philadelphia Division
Philadelphia, PA 19112
Attn: Code SEC 6734 (One Copy)

Office of Naval Research
Washington, D.C. 20360
Attn: Code 471 (One Copy)

Superintendent
U. S. Naval Academy
Annapolis, MD 21402
Attn: Technical Library
(One Copy)

Naval Surface Weapons Center
White Oak, MD 20910
(One Copy)

Director
Army Materials and Mechanics
Research Center
Watertown, MA 02172
Attn: DRXMR-PL
DRXMR-WD
Dr. R. Katz
Dr. E. Lenoe
Dr. E. Wright
(One Copy Each)

Deputy Chief of Staff
Research, Development, and
Acquisition Headquarters
Department of the Army
Washington, D.C. 20310
Attn: DAMA-CSS, Dr. J. Bryant
(One Copy)

Naval Air Propulsion Center
P. O. Box 7176
Trenton, NJ 08628
Attn: T. Elsasser (One Copy)

Chief of Naval Research
Department of the Navy
Arlington, VA 22217
Attn: Code 472 (One Copy)

Chief of Naval Operations
Department of the Navy
Washington, D.C. 20350
Attn: OP-03FG (One Copy)

Deputy Chief of Staff
Research Development and Acquisition
Pentagon Bldg.
Washington, D.C. 20310
Attn: Dr. C. Church (One Copy)

U. S. Army Research and
Technology Laboratories, DAVDL
Moffatt Field, CA
Attn: Dr. R. Carlson
(One Copy)

Commander
Army Research Office
P. O. Box 12211
Research Triangle Park, NC 27709
Attn: Information Processing Office
Dr. J. Hurt (One Copy)
Dr. P. Parrish (One Copy)

DISTRIBUTION LIST

C:MCJ:2125:061082

Commander
U. S. Army Tank-Automotive
R&D Command
Warren, MI 48090
Attn: Dr. P. Glance
Mr. E. Hamperian
Dr. R. Mundt
DRDTA-UP, Technical Library
(One Copy Each)

Commander
U. S. Army Aviation R&D Command
P. O. Box 209
St. Louis, MO 63166
Attn: DRDAV-EXT (One Copy)
Technical Library (One Copy)
B. Titus, DRDAV-M, Bldg. 105
(One Copy)

Commander
U. S. Army Mobility Equipment
R&D Command
Fort Belvoir, VA 22060
Attn: DRDME-EM, W. McGovern
(Two Copies)

Director
Eustis Directorate
U. S. Army Research and Technology
Laboratory, DAVDL-ATL-A
Fort Eustis, VA 23604
Attn: Mr. J. Lane (One Copy)
Mr. G. Eliot (One Copy)

Commander
U. S. Air Force Office of
Scientific Research
Building 410
Bolling Air Force Base,
Washington, D.C. 20332
Attn: Captain Wax
(One Copy)

Commander
Department of the Air Force
Wright Aeronautical Laboratory
Wright-Patterson Air Force Base,
OH 45433
Attn: Dr. N. Tallan, AFML
Dr. H. Graham, AFML
Dr. R. Ruh, AFML
Hank Johnson, AFML
Mr. E. Lindner, AFWAL-POTA
Mr. W. Troha, AFWAL-POTC
Mr. D. Zabierek, AFWAL-POTC
(One Copy Each)

Department of the Air Force
Aero Propulsion Laboratory
Wright-Patterson Air Force Base,
OH 45433
Attn: AFAPL/TBP/D. Campbell
Mr. R. Marsh
(One Copy Each)

National Aeronautics and Space
Administration
Washington, D.C. 20546
Attn: Mr. G. C. Deutsch - Code RW
Mr. C. Bersch
AFSS-AD, Office of Scientific
and Technical Information
(One Copy Each)

DISTRIBUTION LIST

C:MCJ:2125:061082

NASA-Lewis Research Center
21000 Brookpark Road
Cleveland, OH 44135
Attn: J. Accurio, USAMRDL
Dr. H. B. Probst, MS 49-1
Dr. T. Miller, MS 49-1
S. Grisaffe, MS 105-1
H. Rohlik, MS 77-2
G. Weden, MS 5-3
R. Evans, MS 49-2
J. Acurio, MS 302-2
C. Blankenship, MS 105-1
(One Copy Each)

NASA Headquarters
600 Independence Avenue, S.W.
Washington, D.C. 20546
Attn: J. Gangler
J. Kerrebrock
(One Copy Each)

NASA-Langley Research Center
Hampton, VA 23665
Attn: Mr. J. Buckley,
MS 387 (One Copy)

Science and Technology Division
Library of Congress
Washington, D.C. 20540
(One Copy)

Department of Energy
Division of Transportation
20 Massachusetts Avenue, N.W.
Washington, D.C. 20545
Attn: Mr. Robert Schulz (TEC)
(Two Copies)
Mr. S. Kramer (One Copy)

Department of Transportation
400 Seventh Street, S.W.
Washington, D.C. 20590
Attn: Mr. M. Lauriente (One Copy)

Mechanical Properties
Data Center
Belfour Stulen Inc.
13917 W. Bay Shore Drive
Traverse City, MI 49684
(One Copy)

National Bureau of Standards
Washington, D.C. 20234
Attn: Dr. S. Wiederhorn (One Copy)
Dr. J. B. Wachtman (One Copy)
Dr. N. Tighe (One Copy)

National Research Council
Nat'l Materials Advisory Board
2101 Constitution Avenue
Washington, D.C. 20418
Attn: D. Groves (One Copy)
R. M. Spriggs (One Copy)

National Science Foundation
Washington, D.C. 20550
Attn: B. Koepke (One Copy)

DISTRIBUTION LIST

C:MCJ:2125:061082

Jet Propulsion Laboratories
Calif. Institute of Technology
4800 Oak Grove Drive
Pasadena, CA 91103
Attn: Marc Adams (One Copy)
R. Smoak (One Copy)
J. Zwissler (One Copy)

Electric Power Research Institute
3412 Hillview Avenue
P. O. Box 10412
Palo Alto, CA 94304
Attn: Wate Bakker (One Copy)

Gas Research Inst.
8600 W. Bryn Mawr Avenue
Chicago, IL 60631
Attn: C. Dobos (One Copy)

Solar Energy Research Inst.
1536 Cole Blvd.
Golden, CO 80401
Attn: T. Coyle (One Copy)

Department of Energy
20 Massachusetts Avenue
Washington, D.C. 20545
Attn: J. Fairbanks (One Copy)

Los Alamos Scientific Laboratory
P. O. Box 1663
Los Alamos, NM 87545
Attn: Dr. J. Petrovic, Group CMB-5
(One Copy)
H. Sheinberg, Group D, M/S 770
(One Copy)

Oak Ridge National Labs.
P. O. Box X
Oak Ridge, TN 37830
Attn: J. A. Carpenter (One Copy)
V. Tennery (One Copy)

Lawrence Radiation Laboratory
Livermore, CA 94550
Attn: Ceramics Dept. (One Copy)

The Aerospace Corporation
P. O. Box 92957
Los Angeles, CA 90009
Attn: Dr. L. Rubin (One Copy)

AiResearch Casting Company
2525 West 190th Street
Torrance, CA 90505
Attn: Mr. K. Styhr (One Copy)

AiResearch Manufacturing Co.
2525 West 190th Street
Torrance, CA 90505
Attn: Dr. D. Kotchick (One Copy)

Alfred University
Alfred, NY
Attn: Dr. D. Rossington 14802
(One Copy)

DISTRIBUTION LIST

C:MCJ:2125:061082

Carborundum Company
Research & Development Div.
P. O. Box 1054
Niagara Falls, NY 14302
Attn: Dr. J. A. Coppola
Dr. M. Srinivasan
Dr. R. Phoenix
(One Copy Each)

Ceramic Combustor Heat Exchanger
3412 Hillview Avenue
P. O. Box 14012
Palo Alto, CA 94304
Attn: Dr. A. Cohn
EPRI Program Manager
(One Copy)

Ceradyne, Inc.
3030 South Red Hill
Santa Ana, CA 92705
(One Copy)

Corning Glass Works
Research Department
Corning, NY 14832
Attn: Mr. J. Lanning (One Copy)

Deposits and Composites, Inc.
1821 Michael Faraday Drive
Reston, VA 22090
Attn: Mr. R. E. Engdahl
(One Copy)

Ford Motor Company
Scientific and Engineering Labs
20000 Rotunda Drive
Dearborn, MI 48121
Attn: E. A. Fisher
J. Harwood
A. McLean
(One Copy Each)

Caterpillar Tractor Company
Technical Center
Building F
Peoria, IL 61602
Attn: Mr. A. R. Canady
(One Copy)

Ceramic Finishing Company
P. O. Box 498
State College, PA 16801
Attn: Dr. H. P. Kirchner
(One Copy)

Coors Porcelain Company
Research Department
17750 West 32nd Avenue
Golden, CO 80401
(One Copy)

Cummins Engine Company
Columbus, IN 47201
Attn: Mr. R. Kamo (One Copy)

Eaton Corporation
Research Center
26201 Northwestern Highway
Southfield, MI 48076
Attn: Dr. L. Eltinge (One Copy)

General Electric Company
Research and Development Center
Box 8
Schenectady, NY 12345
Attn: Dr. R. J. Charles
Dr. C. D. Greskovich
(One Copy Each)

DISTRIBUTION LIST

C:MCJ:2125:061082

General Electric Company
Valley Forge Space Center
Box 8555
Philadelphia, PA 19101
Attn: Mr. L. R. McCreight (One Copy)

General Motors Corporation
Detroit Diesel Allison Division
P. O. Box 894
Indianapolis, IN 46206
Attn: Dr. P. Heitman (One Copy)
D. M. Herman (One Copy)

GTE Laboratories
Waltham Research Center
40 Sylvan Road
Waltham, MA 02154
Attn: Dr. C. Quackenbush
Dr. W. H. Rhodes
Dr. D. T. Smith
(One Copy Each)

Lehigh University
Bethleham, PA 18015
Attn: Dr. Richard M. Spriggs
F.A. Cer. S., F.I. Ceram. IISS
V.P. - Administration &
Professor of Metallurgy and
Materials Science
(One Copy)

Norton Company
Worcester, MA 01606
Attn: Dr. N. Ault (One Copy)
Dr. M. L. Torti (One Copy)

Pennsylvania State University
Materials Research Laboratory
Materials Science Department
University Park, PA 16802
Attn: Prof. R. Roy (One Copy)
Prof. R. E. Tressler (One Copy)
Prof. R. Bradt (One Copy)

General Motors Corporation
AC Spark Plug Division
Flint, MI 48556
Attn: Dr. M. Berg (One Copy)

Georgia Institute of Technology
EES
Altanta, GA 30332
Attn: Mr. J. D. Walton
(One Copy)

IIT Research Institute
10 West 35th Street
Chicago, IL 60616
Attn: Mr. S. Bortz, Director,
Ceramics Research
Dr. D. Larsen
(One Copy Each)

Martin Marietta Laboratories
1450 South Rolling Road
Baltimore, MD 21227
Attn: Dr. J. Venables (One Copy)

Massachusetts Institute of Technology
Department of Metallurgy and
Materials Science
Cambridge, MA 02139
Attn: Prof. R. L. Coble (One Copy)
Prof. H. K. Bowen (One Copy)
Prof. W. D. Kingery (One Copy)
Prof. R. Cannon (One Copy)

Pratt and Whitney Aircraft
P. O. Box 2691
W. Palm Beach, FL 33402
Attn: Mr. M. Mendelson,
Mail Stop B-08
(One Copy)

GARRETT TURBINE ENGINE COMPANY

DISTRIBUTION LIST

C:MCJ:2125:061082

Program Development Consultants
25 Schalren Drive
Latham, NY 12110
Attn: Dr. R. Harmon (One Copy)

Teledyne CAE
1330 Laskey Road
Toledo, OH 43697
Attn: R. Beck (One Copy)

Rockwell Int'l Science Center
1049 Camino Dos Rios
Thousand Oaks, CA 91360
Attn: Dr. F. Lange (One Copy

San Fernando Labs
10258 Norris Avenue
Pacoima, CA 91331
Attn: R. Holzl (One Copy)

Standard Research International
333 Ravenswood Avenue
Menlo Park, CA 94025
Attn: Dr. P. Jorgensen (One Copy)
Dr. D. Rowcliffe (One Copy)

United Technologies Research Center
East Hartford, CT 06108
Attn: Dr. J. Brennan (One Copy)
Dr. F. Galasso (One Copy)

University of California
Dept of Materials Science & Eng
Hearst Building
Berkeley, CA 94720
Attn: Dr. D. Clarke (One Copy)
Prof. A. G. Evans (One Copy)

University of Florida
Dept of Materials Science & Eng
Gainesville, FL 32601
Attn: Dr. L. Hench (One Copy)

University of Massachusetts
Dept. of Mechanical Eng.
Amherst, MA 01003
Attn: Prof. K. Jakus (One Copy)
Prof. J. Ritter (One Copy)

University of Michigan
Ann Arbor, MI 48104
Attn: Prof. E. E. Hucke (One Copy)
Dr. M. J. Sinnot (One Copy)

University of Washington
Ceramic Engineering Division
FB-10
Seattle, WA 98195
Attn: Prof. J. Mueller (Two Copies)
Prof. R. Taggert (One Copy)
Prof. R. Bollard (One Copy)

V.P.I.
Department of Materials Engineering
Blacksburg, VA 24061
Attn: Prof. D. P. H. Hasselman
(One Copy)

Westinghouse Electric Corporation
Research Laboratories
Pittsburgh, PA 15235
Attn: Dr. R. J. Bratton (One Copy)

Warren Associates
22230 Bassett Street
Canoga Park, CA 91303
Attn: Mr. J. Warren (One Copy)

Westinghouse Electric Corporation
Power Generation Systems Division
Lester, PA 19113
Attn: Mr. C. Booher, Jr., MS A-605
(One Copy)